Quantum optics with single atoms and single photons

Thesis by

Quentin A. Turchette

In Partial Fulfillment of the Requirements

for the Degree of

Doctor of Philosophy

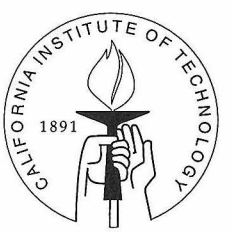

California Institute of Technology

Pasadena, California

1997

(Submitted May 20, 1997)

Acknowledgements

I could never have done all the work presented in this thesis without the continual help of my fellow labmates. Thanks to Olivier Carnal, Mike Chapman, Nikos Georgiades, Christina Hood, Wolfgang Lange, Hideo Mabuchi, Eugene Polzik, Gerd Rempe, Rob Thompson, and Dave Vernooy. Special thanks go to Christina who breathed new life and energy into an old experiment, Rob who took me in as a youngster, and Hideo whose insistence on making things better than marginal was the perfect complement to my style. Extra-special thanks go to Jeff Kimble. I could not have asked for a more attentive, knowledgeable and kind advisor, nor can I imagine a better graduate career than I had, thanks largely to Jeff and the fine group that he has assembled.

Abstract

An atom strongly coupled to a high-finesse resonator forms a microscopic optical system in which the interaction of single atoms with single photons has significant consequences. This is in contrast to a typical optical system in which a field composed of many photons interacts with a medium consisting of many atoms. This unique optical system has been used in studies of the fundamental matter-radiation interaction on the single quantum level, in quantum computation, and in real-time, high-position-resolution detection of single atoms.

Contents

Acknowledgements iii

Abstract iv

Preface xvii

I The One-Dimensional Atom and its Applications 1

1 Introduction 2

1.1 The atom-field interaction I 3

1.1.1 Ideal cavity coupled to a non-decaying atom 3

1.1.2 Real cavity coupled to a decaying atom 4

1.1.3 Two limits 8

1.1.3.1 The bad-cavity limit 8

1.1.3.2 The strong-coupling limit 10

1.2 The critical parameters 10

1.3 The atom-field interaction II: nonlinearity 13

1.3.1 The optical bistability state equation 13

1.3.2 Comparison of the quantum and semiclassical theories 17

1.3.2.1 The bad cavity 19

1.3.2.1.1 Discussion of n_s vs. n_0 23

1.3.2.2 Strong coupling 24

1.3.3 Discussion of $\langle a^\dagger a \rangle$ vs. $|\langle a \rangle|^2$ 26

2 One-Dimensional Atom 31

2.1 Description of the experiment 32

2.1.1 The cavity 32

2.1.1.1 Cavity parameters 32
2.1.1.1.1 Cavity losses in brief 32
2.1.1.1.2 Discussion of g_0 33
2.1.1.1.3 More on losses 35
2.1.1.2 The cavity realized 37
2.1.1.2.1 Overview of cavities used 37
2.1.1.2.2 Mirror technology and cavity construction . 38
2.1.1.2.3 Measuring the cavity length 41
2.1.1.2.4 Measuring the cavity line-width 42
2.1.1.2.5 Locking the cavity 46
2.1.2 The light 48
2.1.2.1 Laser and its lock 48
2.1.3 The atoms 50
2.1.3.1 Cs in the abstract 50
2.1.3.2 Real atoms from a thermal beam 52
2.1.3.3 Fluctuations 55
2.1.4 Probe beam generation 62
2.1.5 Detection 65
2.1.5.1 Photon counting 65
2.1.5.2 Heterodyne detection 65
2.1.5.3 Direct comparison of heterodyne and photon counting 74
2.1.6 Summary of the probe generation and detection chain 74
2.2 Data 76
2.2.1 Extremely brief recapitulation of experimental strategy 76
2.2.2 Linear transmission spectrum 76
2.2.3 On the determination of $\bar{N}$ 82
2.2.4 Nonlinear measurements 88

3 One-D atom with squeezing **93**

3.1 Background and motivation 95

3.1.1 Why do it? 95

3.1.2 What is squeezed light? 98

3.1.3 The DOPO in brief 101

3.2 Theory of squeezing and atoms 103

3.2.1 Free-space atom and squeezing 103

3.2.2 Atom in cavity and squeezing[1] 104

3.2.2.1 Broadband limit 105

3.2.2.2 Narrow-band squeezing 106

3.2.2.3 Phase-sensitive transmission 108

3.3 Experiment 112

3.3.1 Generating the squeezing 112

3.3.2 Getting the squeezing into the cavity 116

3.3.3 Measurements of probe transmission spectra with squeezing . 119

3.3.4 Measurements of phase-sensitive transmission 128

3.3.4.1 Driving through M_1 *vs.* driving through M_2 141

4 Quantum Phase Gate **142**

4.1 Quantum computation 143

4.2 The Quantum Phase Gate 146

4.3 Experimental QPG 147

4.3.1 The atom-cavity phase 147

4.3.1.1 The $g_- \to 0$ approximation 147

4.3.1.2 Converting the intracavity phase to a polarization rotation 149

4.3.2 One-atom waveplate. 150

4.3.3 Nonlinear conditional phase 156

4.3.4 Truth table 159

4.3.5 Issues 170

II Nonlinear Spectroscopy in the Strong Coupling Domain **172**

5 Nonlinear Spectroscopy **173**

5.1 Introduction 173

5.2 Quantum and semiclassical theory of the atom-cavity system 175

5.2.1 Preliminaries: Structure of the atom-cavity system 175

5.2.2 Weak excitation: linear regime 180

5.2.3 Strong excitation: nonlinear regime 181

5.3 Semiclassical simulations, or, What exactly is a 1 atom effect? 184

5.3.1 Description 184

5.3.2 Linear simulations 185

5.3.3 Nonlinear simulations 191

5.3.4 Comments on comparison of simulated and experimental data 193

5.4 Pump-probe experiment 198

5.4.1 Apparatus 198

5.4.2 Linear results 200

5.4.3 Nonlinear results 203

5.5 Conclusions and the future 212

6 Other data in the strong coupling regime **214**

6.1 Optical bistability with very few atoms 214

III Alternative Atom Sources **216**

7 Cavity QED with slow atoms **217**

7.1 Introduction 218

7.1.1 The new time scales 218

7.1.2 The idea of the experiment 219

7.2 The experiment 220

7.3 Atom transits 231

8 Would-be cavity QED with fast atoms **238**

8.1 Why fast atoms? 239

8.2 Getting the atoms where we want them 241

8.3 The gratings and the OLGA 246

8.4 Near-field imaging with two transmission gratings for submicrometer localization of atoms 250

8.4.1 Abstract 250

8.4.2 Introduction 251

8.4.3 Outline of the problem 252

8.4.4 Theoretical framework 255

8.4.5 Patterns and their visibilities behind two gratings 260

8.4.6 Numerical simulations for a realistic experimental setup 267

8.4.7 Conclusions 271

9 Would-be cavity QED with stopped atoms **274**

9.1 Attainable atom-cavity parameters 275

9.1.1 Atom 275

9.1.2 Cavity 276

9.1.3 Trap parameters 276

9.1.4 Mechanical parameters 281

9.2 Apparatus 281

9.3 Some calculations on expected results 284

9.3.1 Fixed ion assumed 284

A Complicated expressions for $\gamma_{x,y,z}$ and $\Omega_{y,z}$ **286**

B Experimental parameters code **290**

B.1 Cavity Parameters: cavityq.mcd 290

B.1.1 The bad cavity 290

B.1.2 The falling atoms cavity 293

B.1.3 The proposed ion trap cavity 296

B.2 Heterodyne Efficiency Calibration: beat.mcd 300
B.3 Intracavity Photon Number from Beatnote: phot.mcd 301

Bibliography **302**

List of Figures

1.1 The Jaynes-Cummings ladder. 4
1.2 Real and imaginary parts of the eigenvalues as a function of coupling strength 7
1.3 Transmission spectrum of the weakly-driven atom-cavity in the bad cavity limit 9
1.4 Transmission spectrum of the weakly-driven atom-cavity in the strong-coupling limit 11
1.5 Progress in the critical numbers 14
1.6 Input-output for the bad cavity regime 20
1.7 Saturation of the bad cavity 22
1.8 Saturation of the bad cavity, with $b = 8/3$ 25
1.9 Input-output for a strong coupling atom-cavity system 27
1.10 Saturation of the strong coupling cavity 28
1.11 Comparison of $\langle a^\dagger a \rangle$ and $|\langle a \rangle|^2$ for a bad-cavity 29
1.12 Comparison of $\langle a^\dagger a \rangle$ and $|\langle a \rangle|^2$ for strong-coupling 30

2.1 The cavity parameters 34
2.2 The cavity mount 40
2.3 The empty cavity 43
2.4 The normalization 44
2.5 The empty cavity raw data 45
2.6 The cavity-lock optical schematic 47
2.7 Schematic diagram of the FM saturation laser lock 49
2.8 Noise-eater 50
2.9 The Cs D2 line 51
2.10 A guide to the Cs D2 line transitions from the $F = 4$ ground state. . 52

2.11 The beam 53
2.12 Histograms of N_g 59
2.13 Spectra breakdowns 60
2.14 Comparison of the averaged and optimal spectra 61
2.15 Probe field generation schematic 64
2.16 A balanced heterodyne detector 66
2.17 Heterodyne detector schematic 69
2.18 Calibration of the UDT power meter 72
2.19 Comparison of photon flux from the heterodyne and from photon counting 75
2.20 Summary of the experimental optical apparatus. 77
2.21 Transmission of the atom-cavity for $\bar{N} = 1.5$ 79
2.22 Raw data for Figure 2.21 80
2.23 Normalized transmission spectra for several values of $\bar{N}$ 83
2.24 Transmission with and without optical pumping 85
2.25 Intracavity atom number $\bar{N}$ vs. fluorescence intensity I_F 87
2.26 Strong-field spectrum 89
2.27 Saturation curve, on resonance 90
2.28 Saturation curves for various detunings 92

3.1 Squeezing on free atom, squeezing on 1-D atom 94
3.2 A cascaded quantum system 98
3.3 Ball and stick diagrams 99
3.4 The effect of broadband squeezed vacuum on the transmission spectrum 107
3.5 Widths for various kinds of light 108
3.6 The idea of the phase-sensitive transmission measurement 110
3.7 Envelope of amplitude modulation as a function of gain 113
3.8 Envelope of amplitude modulation as a function of gain, larger reference 114
3.9 Envelope of amplitude modulation as a function of gain, still larger reference 115

3.10 The cavity buildup and reflection vs. C 118
3.11 The squeezing on atom-cavity experimental schematic 119
3.12 The probe spectrum with squeezed light excitation 123
3.13 The probe transmission spectrum with thermal light excitation 124
3.14 The difference spectrum Δ_s with squeezed light excitation 125
3.15 The difference spectrum Δ_t with thermal light excitation 126
3.16 Averaged difference spectra 127
3.17 The effect of diminishing efficiency η 129
3.18 The phase-sensitive transmission measurement apparatus 130
3.19 The signal from the DSA 132
3.20 Amplitude fractional modulation vs. OPO gain 135
3.21 Amplitude fractional modulation vs. coherent reference power 136
3.22 Amplitude fractional modulation vs. probe frequency 137
3.23 Amplitude fractional modulation vs. number of intracavity atoms . . 138
3.24 Phase-sensitive transmission theory with data 140

4.1 The three relevant atomic levels for conditional logic 148
4.2 Saturation of the atom-cavity transmission for polarized pump beams of opposite helicity. 149
4.3 Measuring the atom-cavity phase 152
4.4 Transmission through the phase-measuring apparatus 153
4.5 Constructing the atom-cavity phase 154
4.6 Modulus and phase of the atom-cavity transmission spectrum 155
4.7 The conditional phase measurement setup 157
4.8 Phase of the transmission spectrum as the pump power is varied . . . 158
4.9 Saturation of the phase 159
4.10 The slope reveals the conditional phase term 166
4.11 Phase saturation for a different set of detunings 167
4.12 Swapping the slopes 168
4.13 Pump and probe on opposite sides of resonance 169

5.1 Comparison of level structure of the first two excited states 178
5.2 Occurrences of mode volume (V_g) occupation N_g 187
5.3 Breakdown of the contributions 188
5.4 Nonlinear spectra for optimally coupled atoms 192
5.5 Histogram of N_e, M_e and η_e 194
5.6 Histogram of N_e, M_e and η_e 195
5.7 Spectra associated with something 196
5.8 Schematic of the experimental apparatus 199
5.9 Linear spectrum for $\bar{N} \approx 1.0$ atoms measured by photon counting . . 201
5.10 Linear spectrum for $\bar{N} \approx 1.1$ atoms measured by heterodyne detection 202
5.11 Sequence of nonlinear probe spectra for $\bar{N} \approx 4.2$ atoms 205
5.12 Sequence of nonlinear spectra for $\bar{N} \approx 1.1$ atoms 207
5.13 Linear and nonlinear spectra as the number of atoms is varied 208
5.14 Difference spectra with semiclassical theory overlaid 211
5.15 Plot of difference peak position *vs.* number of intracavity atoms . . . 213

6.1 Optical bistability for $\bar{N} \approx 7$ 215

7.1 Falling atoms 221
7.2 Transmission of the probe as the atom passes through the gaussian waist 222
7.3 The transmission spectrum for fixed drive field corresponding to $n_s Y =$ 1 on resonance 223
7.4 The transit contrast as a function of empty cavity drive 225
7.5 The drive field which will just send the with atom signal into the shot noise 227
7.6 S/N in various bandwidths 229
7.7 Monitoring the falling atoms 230
7.8 The cold atoms cavity mount 232
7.9 Atom transits 233
7.10 Another trap drop 235
7.11 Individual transits 236

8.1 The adiabatic fast passage scheme for state preparation 240
8.2 Plane wave single-grating simulations 243
8.3 Plane wave single-grating simulations 244
8.4 Plane wave single-grating simulations 245
8.5 Making the gratings 247
8.6 SEM photo of a grating 248
8.7 SEM close-up of a grating 249
8.8 OLGA, the seeded supersonic Caesium wonder 250
8.9 Two possible setups to localize atoms 253
8.10 General two-grating setup 254
8.11 Transmission function $t(x)$ for an idealized grating 258
8.12 Self-images behind two gratings 263
8.13 Results of the numerical simulations 270
8.14 Numerical result for a finite width in the velocity distribution 271
8.15 More of that 272

9.1 Yb^+ partial term scheme 277
9.2 The trap electrodes 280
9.3 Position wavefunction for a cooled ion 282
9.4 The ion-trap/cavity-mount apparatus. 283
9.5 Quantum simulation of the transmission spectrum for coincident probe and cavity 285

List of Tables

2.1 Cavities used in this research 38

7.1 The new world order 219

8.1 The two sets of parameter values used for the numerical calculations . 268

Preface

This thesis covers research in quantum optics in which single atoms and single photons interacting with each other produce observable laboratory consequences. This statement is not as trivial as it may at first seem: after all, no one would dispute that in an atomic dipole excitation from the ground state to the excited state, a single photon leaves the field and is absorbed by the atom. However, it is surprisingly difficult to design and perform an experiment in which this unquestionable process, *as it occurs between single entities* is at all relevant. In the vast majority of optics experiments, an "optical field" interacts with an "atomic medium" such that the concept of the quantum and its associated dynamics is largely lost. Indeed, one could make a reasonably convincing argument that this is still the case even for some of the data presented in this thesis. Whether the atomic-medium/optical-field description or the single-photon/single-atom picture is appropriate, we have unquestionably created a system in which there is never more than one photon in the optical field and never more than one (on average) atom interacting with it. It may be the parenthetical "on average" that forces us ultimately to accept the atomic-medium/optical field description, but the fact that the single quantum does matter is certainly evident in many of the experiments that I will discuss. The elimination of the "on-average" caveat is the subject of the closing chapters of this thesis and is just beginning to become laboratory reality.

Our simple single-quantum quantum-optical system is realized in a cavity quantum electrodynamic (QED) environment consisting of an atom strongly coupled to one of the electromagnetic modes of a nearly lossless optical resonator. With it, we have been able to study fundamental aspects of the matter-radiation interaction, and in fact to realize (quantum) optical devices which were heretofore unattainable. As an example of the former, we have investigated the nonlinear interaction of an atom with both the quantized electromagnetic field of the cavity itself and an externally

applied nonclassical squeezed electromagnetic field. As examples of the latter, we have realized Kerr-type optical nonlinearities in a single atom medium, induced by a single photon, which we have utilized in a demonstration of a simple quantum logic transformation, and we have demonstrated an efficient, real-time single-atom detector.

For our lab, the route towards the micro-optical has been via cavity QED. The basic idea of cavity QED is to put an atom in a high-quality-factor electromagnetic resonator in order to alter controllably its environment. When I began the work presented in this thesis, cavity QED was already a mature field with many of the fundamental ideas thoroughly investigated both on paper and in the laboratory. Since the days of Purcell's first prediction that an atom coupled to a resonant cavity would have a different rate of spontaneous emission than one in free space [1] and the analysis of the basic quantum theory of the interaction by Jaynes and Cummings [2], research in cavity QED has progressed remarkably. The pioneering proof-of-principle experiments of Drexhage with dyes on mirrors [3] paved the way for the many significant experiments realized since. Stand-out experiments include but are certainly not limited to: the observation of collapse and revival [4], observation of antibunching and sub-poissonian statistics [5, 6], observation of single-atom vacuum-Rabi splitting [7] (perhaps the culminating achievement in "old-style" cavity QED), and evidence of nonlinear peaks in a Jaynes-Cummings system [8]. It was clear when I began my work and still is, that cavity QED has passed the demonstrative phase and is ready to be utilized as a tool in the study of a variety of topics in quantum optics, and more broadly, in areas of physics which have not traditionally been within the domain of quantum optics, such as information theory. I would thus like to divide the history of experimental cavity QED into two broad "epochs": the phase in which the underlying principles were demonstrated and the subsequent phase in which these principles and technologies are being applied. This thesis spans the two epochs, including one major demonstrative-type experiment and several other experiments which are among the early research in the "tool-like" phase of cavity QED. We are, of course, not alone in this progression of mind-set, with recent results

outside of our group utilizing cavity QED in a one-atom (perhaps) laser [9], and to study decoherence of quantum superposition states [10].

While we are not alone within the world of cavity QED, nor are we alone in the general physics community. There are several areas of physics where there is interest in isolating and manipulating single quanta, with perhaps the most notable being an ion trap system in which a single ion is trapped and cooled to the ground state of the trapping potential and the resulting quantum motion is manipulated with exquisite control [11]. Here the single quanta are ions and phonons. Other areas which are progressing towards the regime in which interactions between single quanta are important include: wavefunction superposition in atomic hydrogen [12], manipulation and tracking of single atoms via scanning-tunneling microscopy [13, 14], cavity QED in exitonic systems [15], single electron tunnelling junctions and transistors [16, 17] and quantum dots [18]. This list is not meant to be exhaustive and the references within the cited works should be consulted as well.

Having provided a brief discussion of motivation, history and context for the work presented in this thesis, I will now introduce its structure. As an aside, I feel that it is important to justify the need for such a complete document. First, in today's scientific world, the main mode of communication is a brief report in a (hopefully major) journal and a 15 minute presentation at a large conference. The unfortunate consequence of this is that no one but those directly involved knows how a given experiment is actually performed. Such detail is necessarily absent from a four-page PRL. Even with the moderately lengthy discussions to be found here, anyone else would be hard-pressed to reproduce the experiments to confirm or refute the conclusions. This thesis is a small effort towards correcting this regrettable situation. Second, I have worked on at least 4 experiments which remain unpublished. At least they will appear here for the record. Finally, this is likely to be the last thesis from our group with any reference to the good old days of hard-core beam-type cavity QED experiments. There are some not-so-pretty details of this that must not be left behind and are here documented.

Part I covers our research in the bad-cavity limit of cavity QED. We have devel-

oped a system which we have dubbed the "one-dimensional atom" since it interacts efficiently with the standard 1-D laser fields common to an optics laboratory and lends itself to efficient photo-interrogation of single-atom effects with standard optical techniques. We have studied the linear and non-linear properties of the 1-D atom and utilized a single-photon nonlinearity to confirm the truth-table of a simple quantum logic gate. We have also used the 1-D atom to investigate the textbook quantum optical system of an atom illuminated with squeezed vacuum. Within Part I, Chapter 1 introduces the basic theory and computations with a brief discussion of the differences between a semiclassical and fully quantum theory. Chapter 2 presents the 1-D atom as an experimental entity with discussions of the apparatus, various parameters and linear and nonlinear spectroscopic data. Chapter 3 presents the theory and experiment on the interaction of squeezed light and the 1-D atom. Chapter 4 introduces the concept of quantum computation and describes our experimental foray into this fascinating, brand-new, and very in-vogue discipline.

I return to an earlier experiment in Part II, which describes our research searching for the elusive extra peaks in a spectroscopic study of the nonlinear response of the atom-cavity system as predicted by the (simple) Jaynes-Cummings model. The specific details of the experiment are extremely important here so they are described in some detail. Our efforts to observe a departure from semiclassical predictions are described.

Part III discusses our efforts to control not only the quantum *internal* degrees of freedom of the atom-cavity system, but also the quantum *external* degrees of freedom. A fundamental complication in the experiments of Parts I and II is our lack of knowledge of the position and arrival time of individual atoms within the cavity mode. Control over the center-of-mass is imperative to correct this situation, and also leads to interesting interactions between the cavity-field state and the atomic-position state which are now both quantum variables. The central result of Part III, Chapter 7, describes our recent experiments in cavity QED with ultra-cold (slow) atoms, culminating with the observation of single atoms passing through the cavity mode in real-time. This is a significant achievement which is paving the way for the

future of cavity QED in our group. Chapter 8 describes a different approach to the atomic-localization issue, which uses a fast, low-dispersion atomic beam and physical atom-optical elements. Chapter 9 describes an experiment in progress in which we are attempting to use a trapped ion for cavity QED. The great advantage is the extremely precise control over the center-of-mass degree of freedom offered by the ion trap.

Part I

The One-Dimensional Atom and its Applications

Chapter 1 Introduction

The one-dimensional atom is realized within the context of cavity quantum electrodynamics (cavity QED). In broad terms, cavity QED is the study of the quantized interaction between the electromagnetic field and matter in boundary conditions different from free space. In the regime of cavity QED that is the focus of this research, novel optical effects occur in which the electromagnetic field consists of only one photon and the atomic medium consists of only one atom. This is in marked contrast to typical optical systems, such as a laser, in which the intracavity field consists of 10^{12} photons and the active medium has an inversion involving 10^{13} atoms. In this thesis, there is an emphasis on the capabilities that such a system offers for measurements in quantum optics, such as investigations of the fundamental nature of the atom-field interaction, and quantum logic.

The ideal system is quite simple: an atom is coupled via an allowed electric dipole transition to a single mode of a highly reflective optical cavity. In a very qualitative sense, when the rate of coherent interaction between the cavity field and the atom is comparable to or larger than the rate of decay of the atom via spontaneous emission and (in some cases) the rate of decay of the cavity field via a lossy mirror, a new entity is created which has novel properties that can differ significantly from those of the independent uncoupled subsystems. Remarkably, the isolation thereby implied does not deny the experimentalist a detailed look at the dynamics and structure of the composite atom-cavity system. The interaction is controlled by the presence of the cavity to such an extent that the observer can learn a great deal with a photodetector monitoring the output of the cavity. This gives the 1-D atom great power as a tool for investigating fundamental physical concepts and as a constituent of unique quantum devices.

1.1 The atom-field interaction I

1.1.1 Ideal cavity coupled to a non-decaying atom

The Hamiltonian for a single two-state atom interacting with a single electromagnetic mode (of a cavity, e.g.) is:

$$H_{tot} = H_a + H_c + H_{int} \tag{1.1}$$

where

$$H_a = \hbar\omega_a\sigma_z/2 \tag{1.2}$$

$$H_c = \hbar\omega_c a^\dagger a \tag{1.3}$$

$$H_{int} = \hbar g_0 \left[a^\dagger\sigma_- + a\sigma_+\right]. \tag{1.4}$$

H_a, H_c, H_{int} are the atomic, field, and interaction Hamiltonians, respectively, written in the dipole and rotating-wave approximations. The field creation and annihilation operators are given by a and $a^\dagger$, $\sigma_\pm$ are the atomic raising and lowering operators, and σ_z is the atomic inversion operator, with eigenvalues ± 1. The atomic transition frequency is ω_a, the field frequency is ω_c. The atomic-dipole/field interaction rate is given by g_0. The spectrum of eigenvalues for the case of coincident atom and cavity frequencies $\omega_a = \omega_c \equiv \omega$ is given by the so-called Jaynes-Cummings ladder [2] shown in Figure 1.1. The eigenvalues are $E_n^\pm = n\hbar\omega \pm \hbar g_0\sqrt{n}$ where n is the number of quanta in the cavity mode. The first excited states are given by $|\pm\rangle = 1/\sqrt{2}\,[|g\rangle|1\rangle \pm |e\rangle|0\rangle]$ with eigenvalues $\pm\hbar g_0$ where $|g\rangle$ is the uncoupled atomic ground state, $|e\rangle$ is the uncoupled atomic excited state and $|n\rangle$ is the uncoupled field state. The time evolution governed by Eq. 1.1 exhibits an exchange of energy between the cavity field and the atom, known as the vacuum-Rabi oscillation. The corresponding evolution in the frequency domain is characterized by a splitting of the normal-mode frequencies of oscillation by frequency $\pm g_0$ from the uncoupled (and coincident) atom and cavity resonances.

There are numerous interesting effects associated with the simple Hamiltonian 1.1

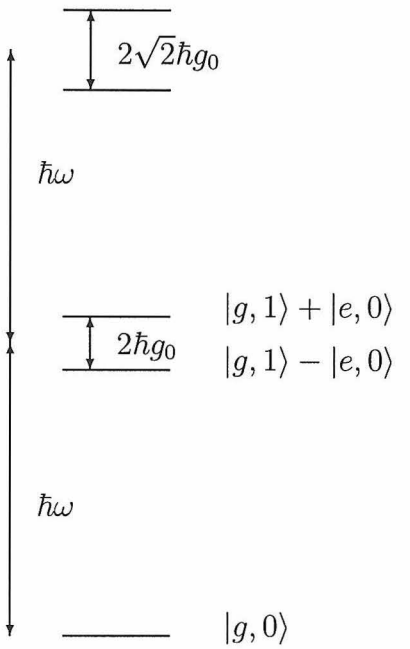

Figure 1.1: The Jaynes-Cummings ladder. Note that the figure is not to scale and that only the ground and first two excited states are shown.

such as collapse and revival of the Rabi oscillations for a cavity field initially prepared in a coherent state [19]. For our purposes, however, there is not much more to say about this ideal case, with the exception of the following. The splitting of the first excited state can be explained with a semiclassical description of radiation, whereas that of the second and higher excited states is a prediction only of the quantum theory. This is the basis for the experiments described in Part II. I will return to this point in much greater detail there.

1.1.2 Real cavity coupled to a decaying atom

It has been one of the main thrusts of cavity QED to attain conditions in which the Jaynes-Cummings Hamiltonian 1.1 is a good approximation to the "real" system. By real, I mean that the atomic excited state decays via spontaneous emission at a rate $\gamma_{\parallel} \equiv A$, with A the Einstein-A coefficient, and that the cavity decays via transmission through one of its mirrors at a rate κ. It is certainly a noble goal to

reach the ideal, but in reality this path ignores a wealth of opportunity in cavity QED which is the consequence of a "nonideal" system. Thus, we will encounter frequently the dissipative rates κ and $\gamma_{\|}$ which together with the coherent rate g_0 describe completely any realizable optical cavity QED system.

With the inclusion of dissipation, the atom-cavity system obeys a set of Heisenberg equations of motion for the field and atomic operators given by:

$$\begin{aligned} \dot{\hat{a}} &= -\kappa(1+i\Theta)\hat{a} + g_0\hat{\sigma}_- + \varepsilon e^{-i(\omega_p-\omega_0)t} \\ \dot{\hat{\sigma}}_- &= -\gamma_\perp(1+i\Delta)\hat{\sigma}_- + g_0\hat{a}\hat{\sigma}_z \\ \dot{\hat{\sigma}}_z &= -\gamma_{\|}(\hat{\sigma}_z+1) - 2g_0(\hat{a}^\dagger\hat{\sigma}_- + \hat{a}\hat{\sigma}_+). \end{aligned} \tag{1.5}$$

Here ε denotes a coherent driving field at frequency ω_p, $\Theta = (\omega_c - \omega_0)/\kappa$ is the cavity detuning and $\Delta = (\omega_a - \omega_0)/\gamma_{\|}$ is the atomic detuning from the fixed reference frame ω_0, which defines the rotating frame for Eqs. 1.5.[1] κ is the cavity field decay rate and $\gamma_\perp$ is the transverse atomic decay. For pure radiative decay $\gamma_\perp = \gamma_{\|}/2$; for a homogeneously broadened medium, $\gamma_\perp > \gamma_{\|}/2$. Note that $\gamma_{\|}$ is in general the decay rate to modes other than the single cavity mode. However, for our cavities, $\gamma_{\|}$ is essentially the same as for an atom in free space since we operate in the limit that the solid angle f subtended by the cavity mode is small ($f \approx 7 \times 10^{-6}$).

Much of the goal of cavity QED theory is to predict the rich dynamics and structure dictated by Eq. 1.5. To aid in this task, I will start with some simplifications to the full equations. I begin with the case of weak drive field $\varepsilon \ll g_0, \gamma_\perp, \kappa$ and consider only expectation values of the operators. In the weak-field limit there is allowed only one excitation in the system, so that the identity $\langle a\sigma_z\rangle = -\langle a\rangle$ holds. Additionally, since the excitation is small, the atomic excited state remains unoccupied, so that $\langle\sigma_z\rangle = -1$. This weak-field approximation is similar to the typical semiclassical approximation in which joint-operator moments are factored. For an informative discussion of this topic see Ref. [21]. In any event, what is formally equivalent to a

[1]The equations of this section are consistent with those of Ref. [20] but the notation, while appearing the same is actually a bit different.

semiclassical approximation is valid for the weak-field case. It takes the form:

$$\dot{\beta} = -\gamma_\perp(1+i\Delta)\beta - g_0\alpha \tag{1.6}$$

$$\dot{\alpha} = -\kappa(1+i\Theta)\alpha + g_0\beta + \varepsilon e^{-i\Omega_p t} \tag{1.7}$$

with $\Omega_p = \omega_p - \omega_0$ and $\alpha \equiv \langle a \rangle$, $\beta \equiv \langle \sigma_- \rangle$. If we take Eqs. 1.6 and 1.7 as a description of a linear black box which transforms an input field ε to some steady-state output field $\kappa\alpha_{ss}$ then the associated complex transmission function is

$$T(\Omega_p) = \frac{\kappa\alpha_{ss}}{\varepsilon} = \frac{\kappa\left[-i\Omega_p + \gamma_\perp(1+i\Delta)\right]}{(\lambda_+ - i\Omega_p)(\lambda_- - i\Omega_p)}. \tag{1.8}$$

Note that ε does not appear in the rhs of Eq. 1.8—this is the definition of a linear transformation: an increase in input power merely produces the same increase in output power. $T(\Omega_p)$ is characterized by the eigenvalues $\lambda_\pm$ which are roots of the quadratic

$$f(\lambda) = [\lambda + \kappa(1+i\Theta)][\lambda + \gamma_\perp(1+i\Delta)] + g_0^2. \tag{1.9}$$

For the case of coincident atom, cavity, and drive frequencies, the eigenvalues are:

$$\lambda_\pm = -\left(\frac{\kappa+\gamma_\perp}{2}\right) \pm \left[\left(\frac{\kappa-\gamma_\perp}{2}\right) - g_0^2\right]^{\frac{1}{2}}. \tag{1.10}$$

Figure 1.2 shows the eigenvalues $\lambda_\pm$ as a function of coupling strength g for fixed κ and $\gamma_\perp$. Imλ reveals the energy structure of the coupled system, while Reλ describes the decay rates. As the coupling is increased, Imλ eventually splits, showing a trend towards the linear relationship of $E_1^\pm$ of the Jaynes-Cummings model. Reλ begins as the uncoupled atom and cavity decay rates, trending towards the averaged decay rate $(\kappa+\gamma_\perp)/2$ (which, incidentally can be slower than the natural atomic decay rate [22, 23]).

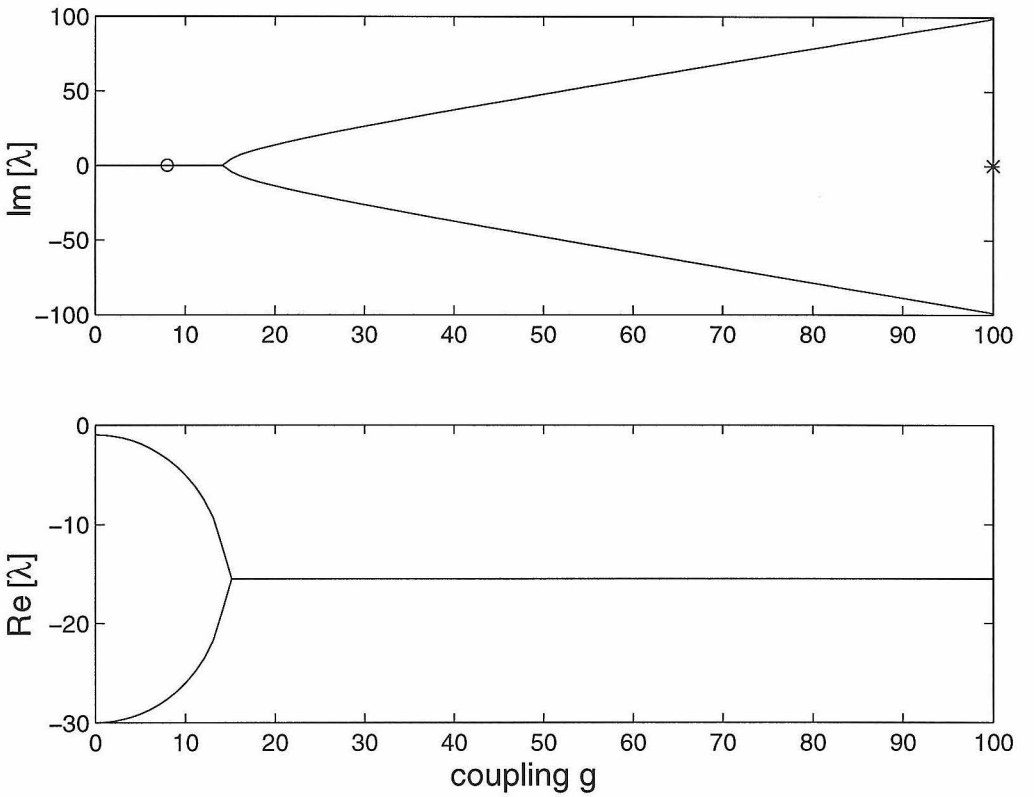

Figure 1.2: Real and imaginary parts of the eigenvalues ($\Delta = \Theta = 0$) as a function of coupling strength g with $\gamma_\perp = 1$ and $\kappa = 30$. All quantities are in the same arbitrary frequency units. The 'o' and '$*$' mark parameter sets discussed in Section 1.1.3.

1.1.3 Two limits

It is instructive and relevant to consider limiting values of the three rates g_0, κ, $\gamma_\perp$. I will restrict the discussion to the two limits with associated experiments in this thesis. These are the bad-cavity limit and the strong-coupling limit.

1.1.3.1 The bad-cavity limit

In the so-called "bad-cavity" limit, cavity decay is the dominant rate, while coherent cavity processes evolve significantly faster than spontaneous emission. For purposes of this thesis, the bad-cavity regime is specified by $\kappa \gg g_0^2/\kappa \gg \gamma_\perp$ and resides towards the leftmost side of Figure 1.2 before Imλ splits. The eigenvalues have zero imaginary part and reduce to:

$$\lambda_+ = -\gamma_\perp(1+2C_1) \tag{1.11}$$

$$\lambda_- = -\kappa\left(1-2C_1\frac{\gamma_\perp}{\kappa}\right) \tag{1.12}$$

where

$$C_1 = \frac{g_0^2}{2\kappa\gamma_\perp} \tag{1.13}$$

is the single-atom cooperativity parameter. In the bad-cavity limit, there is a separation of time scales such that the atom and cavity each retain their essential character. There are, however important modifications due to the coupling. There is cavity-enhanced atomic decay at rate $-\lambda_+ = \gamma_\perp(1+2C_1)$ and a slight atom-inhibited cavity decay at rate $-\lambda_- = \kappa(1-g_0^2/\kappa^2)$. The bad cavity limit has a somewhat more formal definition in the optical-bistability literature. I will call this the "strict" bad-cavity limit, to distinguish it from my bad-cavity limit $\kappa \gg g_0^2/\kappa \gg \gamma_\perp$. In the strict bad cavity limit $(\kappa/\gamma_\perp, g/\gamma_\perp) \to \infty$ with C_1 constant [24] so that $-\lambda_- \to \kappa$. The regime specified by Eqs. 1.11 and 1.12 is the limit in which we are interested, because of the strong effect of the cavity on a single atom (reflected in the factor $(1+2C_1) \gg 1$ for large C_1), and because the atom and cavity retain distinct identities due to the separation of time scales between $\gamma_\perp$ and κ. Note that this is the domain in which

the experiments of Refs. [3, 25, 26, 27, 28, 29, 30] were performed. I have indicated the location of a bad cavity system with a 'o' in Fig. 1.2 and show its associated weak-field transmission spectrum in Fig. 1.3. The weak-field transmission spectrum represents the response of the atom-cavity to a weak drive (probe) field $\varepsilon e^{-i\Omega_p t}$ as in Eq. 1.7 and is given by $T(\Omega_p)$ in Eq. 1.8

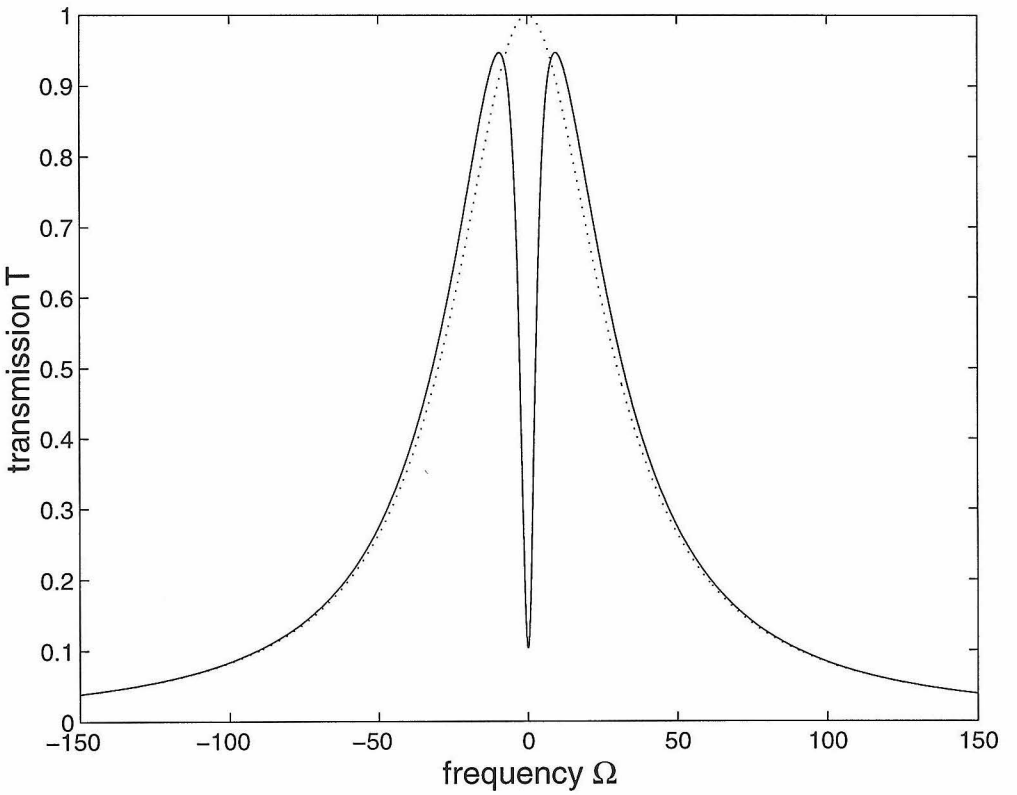

Figure 1.3: Transmission spectrum of the weakly driven atom-cavity in the bad cavity limit. Note that the parameter set for this graph is indicated by the 'o' in Fig. 1.2. $\gamma_\perp = 1$, $\kappa = 30$, $g_0 = 8$, $C_1 \approx 1$. The solid curve is $T(\Omega)$ from Eq. 1.8 with $\Delta = \Theta = 0$. The dashed line is the empty cavity $T(\Omega, C_1 = 0 = g_0)$.

As a final note, the on-resonance transmission of a weak probe (for zero detunings $\omega_a = \omega_c$) with an atom in the cavity is $1/(1+2C_1)^2$ compared to the empty cavity transmission. That is,

$$\frac{|T(\text{with atom, } \Omega_\text{p} = 0)|^2}{|T(\text{no atom, } \Omega_\text{p} = 0)|^2} = \frac{1}{(1+2C_1)^2}. \tag{1.14}$$

This is not an approximation of any sort; it is valid for all values of g_0, κ, $\gamma_\perp$. This can be seen from Eq. 1.8 with Eq. 1.10.

1.1.3.2 The strong-coupling limit

Alternative to the bad-cavity limit is the true strong coupling regime, $g_0 \gg (\kappa, \gamma_\perp)$ for which the eigenvalues exhibit the well-known normal-mode (vacuum-Rabi) splitting (and associated oscillatory behavior in the time domain) due to the imaginary component of $\lambda_\pm$:

$$\lambda_\pm \simeq -\frac{(\kappa + \gamma_\perp)}{2} \pm i g_0. \tag{1.15}$$

This is the regime in which the Jaynes-Cummings model is most closely realized. An observable normal-mode splitting will be present only if $g_0 > (\kappa + \gamma_\perp)/2$. The strong coupling regime occupies the extreme right of the graphs in Figure 1.2; the parameter set indicated by the '$*$' has the weak field transmission spectrum shown in Figure 1.4, which clearly shows the split vacuum-Rabi peaks characteristic of the Jaynes-Cummings model. Note that I will sometimes use the term "strong-coupling" to mean $g_0/\gamma_\perp \gg 1$, independent of the cavity decay. I do this, because I consider strong coupling to be just that—strong coupling between the atom and the cavity mode. This is a concept that is independent of the cavity losses, as neither g_0 nor $\gamma_\perp$ depend on κ. However, there is an accepted term for the limit $g_0 \gg (\kappa, \gamma_\perp)$ which I here call the "true" strong-coupling limit. I will try to make it clear in which sense I mean strong-coupling when I use the term.

1.2 The critical parameters

The discussion thus far has not emphasized the distinction between "mush" (the atomic medium) interacting with a welding laser (the optical field) and single atoms interacting with single photons. In order to distinguish mush, which we presume to be uninteresting, from the single quantum, which we know to be interesting, I will now introduce the critical parameters of cavity QED. Simply stated, the critical

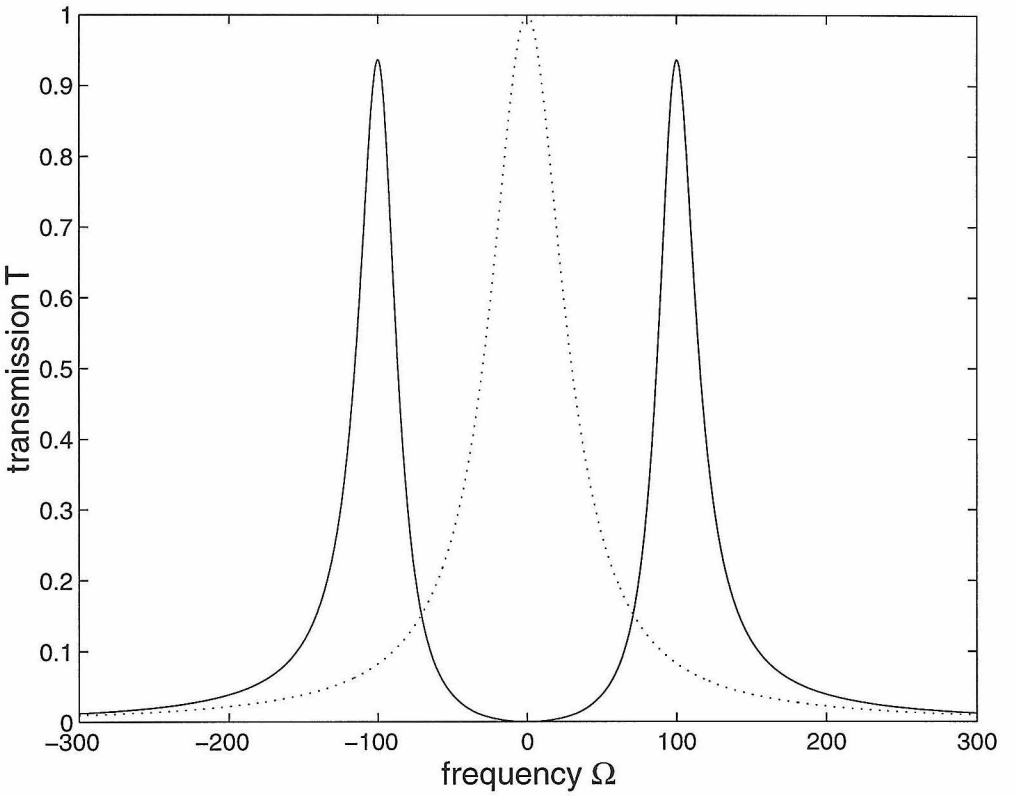

Figure 1.4: Transmission spectrum of the weakly driven atom-cavity ($T(\Omega)$ from Eq. 1.8) in the strong coupling limit. Note that the parameter set for this graph is indicated by the '$*$' in Fig. 1.2. $\gamma_\perp = 1$, $\kappa = 30$, $g_0 = 100$, $C_1 \approx 167$. The dashed line is the transmission spectrum of the empty cavity ($T(\Omega, g_0 = 0)$).

parameters stipulate the number of quanta fundamentally involved in the matter-field dynamics. From $g_0, \kappa, \gamma_\perp$ we form two dimensionless numbers: the critical (or saturation) photon number

$$n_0 \equiv \frac{\gamma_\perp \gamma_\parallel}{4g_0^2} b \text{ (also called } m_0), \tag{1.16}$$

where b is a geometrical factor ($b = 8/3$ for a Gaussian standing-wave cavity mode), and the critical atom number

$$N_0 \equiv \frac{2\kappa\gamma_\perp}{g_0^2} = \frac{1}{C_1}. \tag{1.17}$$

These critical numbers effectively divide the parameter space of cavity QED in a manner appropriate to the types of experiments in which we are interested. In particular, we can ignore bad cavities, good cavities, strong coupling, weak coupling and all the rest of cavity QED's categorization attempts. Simply put, in order for an atom-cavity system to be "interesting" from our perspective, it must be the case that:

$$N_0,\ n_0 \ll 1. \tag{1.18}$$

This can be justified in words in several different ways, depending on what is deemed interesting for a particular experiment. So, if the critical atom number N_0 is below unity, I can say that *a single atom*:

- removed from or inserted into the cavity, even in the presence of many atoms, can have a dramatic effect on the cavity field.
- can be used to switch a property of the cavity field.
- can be efficiently addressed with well controlled in-going or out-going fields.
- can be easily detected if it is in the cavity.

And likewise, if the critical photon number n_0 is below unity, then *a single photon*:

- can saturate the atomic response.

- induces a strong nonlinearity in the intracavity medium.
- can control a property of another photon via the intracavity medium.

As I proceed, it will become clear which description is most useful for a given experiment.

As a final word on the critical numbers, the progress over the last 1.5 decades towards sub-unity critical numbers has been remarkable. To demonstrate this, I have plotted in Figure 1.5 those cavities which have been constructed for use in cavity QED experiments in our labs during that time. Even within my all-too-brief tenure (1991–1997), almost 2 orders of magnitude have been traversed.

1.3 The atom-field interaction II: nonlinearity

I have thus far presented theory valid in the weak field. In this limit, there is no difference between a semiclassical and quantum theory. The more interesting aspects of the atom-cavity system are found not in the weak-field limit, but rather when the system is driven with "strong" fields. Of course, strong in this case can still mean only a few photons or less, if $m_0 \ll 1$. Available analytic quantum theory (e.g., Ref. [21]) in the strong drive regime is useful, but limited in scope. The best option is usually to directly simulate a very simple system, such as one stationary atom localized to the maximum of the cavity field. On the other hand, the semiclassical theories [31] are extremely well developed and can handle rather complicated scenarios, closer to real experiments. Of course, the semiclassical equations model the real system incorrectly, since a real system can be in a regime handled only by a true quantum theory. Indeed, this is the regime towards which we strive. In this section, I will discuss techniques for and results of various approaches to treating the strong-drive case.

1.3.1 The optical bistability state equation

When the radiation field is treated semiclassically (the joint operator moments are factored), the atom-cavity system is described completely by the well-known input-

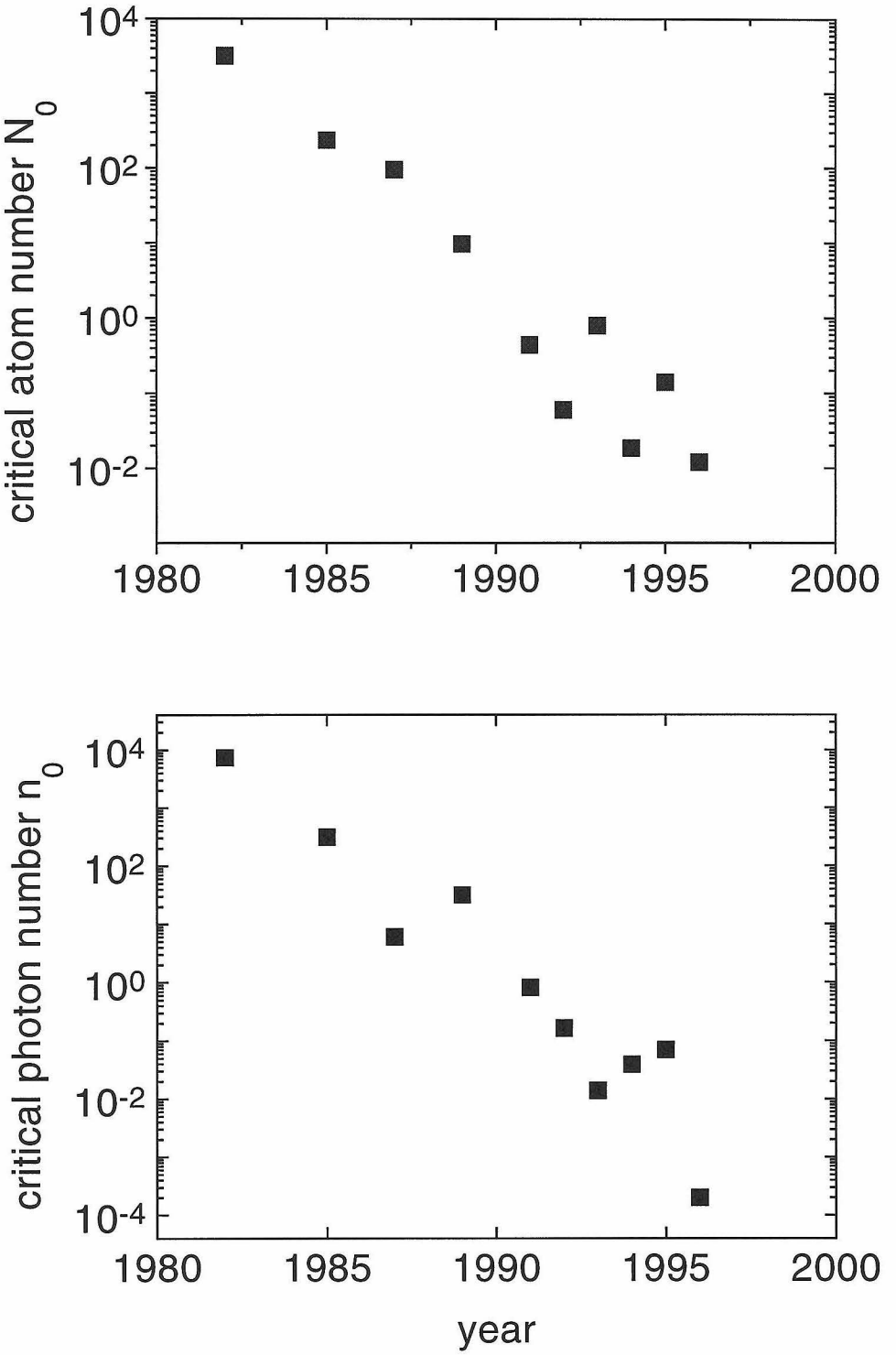

Figure 1.5: Progress in the critical numbers.

output state equation of optical bistability [31, 32]:

$$y = x\left[\left(1+\frac{2C}{1+\delta^2+x^2}\right)+i\left(\phi-\frac{2C\delta}{1+\delta^2+x^2}\right)\right], \tag{1.19}$$

for input field y and output field x. Here, $C = N_e C_1$ where N_e is the "effective number of intracavity atoms," $N_e \equiv \sum_{i=1}^{N_s} |\psi(r_i)|^2$ where $\psi(x_i, y_i, z_i) = \exp(-(x_i^2 + y_i^2)/w_0^2)\sin(kz_i)$ is the Gaussian-standing wave mode amplitude for the i^{th} atomic site, and the sum is over all N_s sites comprising the atomic sample, with w_0 the cavity waist and $k = 2\pi/\lambda_a$ the cavity wavenumber. Note that for atoms on the top of the Gaussian ($x_i = y_i = 0$) and at the antinodes of the standing-wave ($kz_i = p\pi/2$), N_e represents the actual number N of atoms in the cavity, but for atoms distributed over all parts of the Gaussian-standing-wave mode, N_e is an effective number of intracavity atoms representing the collective coupling of the sample. The detunings δ and ϕ are now defined with respect to the probe frequency ω_p (which is itself detuned from the reference frequency ω_0).

$$\delta = \frac{\omega_a - \omega_p}{\gamma_\perp} \tag{1.20}$$

$$\phi = \frac{\omega_c - \omega_p}{\kappa}. \tag{1.21}$$

This is not always the most useful frequency notation, but simple algebra will convert this to the fixed detunings Δ and Θ of Eq. 1.5. The fields x and y are related to previously defined quantities by

$$\langle a \rangle \leftrightarrow \sqrt{n_0}x \tag{1.22}$$

$$y = \sqrt{n_0}\frac{\varepsilon}{\kappa}, \tag{1.23}$$

where ε is the drive field from Eq. 1.5. In the sense that I will consider x and y, the correspondence of Eq. 1.22 is not to be taken literally; x and y are semiclassical quantities, calculated from Eq. 1.19 while the expectation value of the field operator is a quantum quantity calculated from a full solution to Eqs. 1.5. The correspondence

of Eq. 1.23 is, however, literal since ε is a classical driving field. The output flux of photons is $2n_0|x|^2\kappa \leftrightarrow 2|\langle a\rangle|^2\kappa$. I will also use the corresponding scaled powers $X = |x|^2$ and $Y = |y|^2$.

For resonant atom, cavity and laser probe, that is, $\omega_a = \omega_c = \omega_p$, or, $\delta = \phi = 0$ (the absolute square of) Eq. 1.19 reduces to

$$Y = X\left[1 + \frac{2C}{1+X}\right]^2. \tag{1.24}$$

Unfortunately, Eqs. 1.19 and 1.24 give expressions for the input field Y in terms of the output field X. For weak fields ($X \ll 1$) the state equation is easily invertible and leads to Eq. 1.8, but for strong fields numerical inversion is usually the best approach (aside from rotating the graph of Y *vs.* X by 90°, which is often fine). For $C > 4$ the input-output relation is bistable [31].

The regime of validity of the semiclassical bistability state equation is limited to large values of the critical parameters (we speak of $1/N_0, 1/m_0 \ll 1$ so that quantities may be expanded in terms of these small parameters). In this case the collection of atoms behaves as a classical optical medium with susceptibility χ and $C \to \alpha_0 l/T$ where α_0 is the absorption coefficient ($\alpha_0 \propto \mathrm{Im}\chi$ [33]), l is the cavity length and T is the cavity transmission. For this regime Eq. 1.19 is valid for all drive fields y and any value of C. To connect this to the discussion of Section 1.1, note that the cooperativity parameter $C = C_1 \sum_{i=1}^{N_s} |\psi(r_i)|^2 \equiv C_1 N_e$ as above. The Heisenberg equations (1.5) for atom i must be modified to:

$$\begin{aligned}
\dot{\hat{a}} &= -\kappa(1+i\Theta)\hat{a} + \sum_{i=1}^{N_s} g_i\hat{\sigma}_-^i + \varepsilon e^{-i(\omega_p-\omega_0)t} \\
\dot{\hat{\sigma}}_-^i &= -\gamma_\perp(1+i\Delta)\hat{\sigma}_-^i + g_i\hat{a}\hat{\sigma}_z^i \\
\dot{\hat{\sigma}}_z^i &= -\gamma_\parallel(\hat{\sigma}_z^i + 1) - 2g_i(\hat{a}^\dagger\hat{\sigma}_-^i + \hat{a}\hat{\sigma}_+^i),
\end{aligned} \tag{1.25}$$

where $g_i \equiv g_0|\psi(r_i)|$. Now the g_0 which appears throughout Section 1.1 should be replaced by $g \to g_0\sqrt{N_e}$ where g_0 is the maximum value of the coupling (on a site where $|\psi|$ is maximum).

In the limit in which a large coupling strength is achieved via large N ($C \gg 1$, $C_1 \ll 1$ or $g_0 N_e^{1/2} \gg \kappa, \gamma_\perp$; $g_0 \ll \kappa, \gamma_\perp$), the bistability state equation 1.19 and a fully quantum solution of Eqs. 1.25 will yield the same results [21]. However, if the single particle coupling is large ($C_1 \gg 1$, $g_0 \gg \kappa, \gamma_\perp$) Eq. 1.19 will not, in general, be a valid approximation.

1.3.2 Comparison of the quantum and semiclassical theories

Eq. 1.19 depends only on the atom-cavity parameter C. The quantum equations depend on $g, \kappa, \gamma_\perp$ explicitly. In the weak field this does not matter, in the strong field, it will. A question not yet considered is in what cases will the state equation come close to the "correct" answer. This is an important and relevant question, since it is often much simpler to use the classical equations and it is definitely easier to model a real experiment in the semiclassical limit (regardless of the issue of whether the experiment is itself "in" the semiclassical or quantum regimes). I will merely try to answer the question by example. In order to compare levels of approximation, I will single out one property which is of paramount import. This property is the nonlinear behaviour of the system, that is, the input-output relation or the saturation behaviour with a strong driving field, where for simplicity I consider only the case of resonant excitation. To compare directly the quantum and semiclassical predictions, I must relate x and y as they appear in the semiclassical state equation to ε and $\langle a \rangle$ from the quantum picture via Eqs. 1.22, 1.23. While it is not strictly true that $n_0 X = \langle a^\dagger a \rangle$, I will use this association often. The difference between $\langle a^\dagger a \rangle$ and $|\langle a \rangle|^2$ is subtle and not particularly relevant for the topics covered here, or for the parameter regimes of most of the experiments; I will discuss this issue at greater length in Section 1.3.3.

I will perform the quantum/semiclassical comparison in a situation appropriate to a single atom localized to the strong part of the cavity field mode with cooperativity $C_1 \gg 1$ (and coupling $g_0 \gg \kappa, \gamma_\perp$) in the quantum case, and many atoms localized to the strong parts of the field mode such that $C = C_1$, $C = N C_1^{\text{semiclass}}$, $C_1^{\text{semiclass}} \ll 1$, $N \gg 1$ in the semiclassical case. In both of these cases, $b = 1$ is the appropriate

geometrical factor in the saturation photon number, so for convenience, I will define a new saturation photon number,

$$n_s = \frac{\gamma_\perp \gamma_\parallel}{4g_0^2}. \tag{1.26}$$

The localized-one-atom case is the only scenario handled in a straightforward fashion by the quantum calculations,[2] so the comparison reduces to the question of how best to model the single atom case with the semiclassical equations, which are in reality incapable of handling the job in its full generality. This photon-number scaling will be discussed at greater length in Section 1.3.2.1.1.

The strong-field quantum calculation is simply a numerical evaluation of the evolution of the system density matrix, taken to steady state.[3] The evolution of the system density matrix is described by ($\hbar = 1$):

$$i\dot{\rho} = \mathcal{L}\rho, \tag{1.27}$$

in which $\mathcal{L}$ is the superoperator whose action on ρ is:

$$\mathcal{L}\rho = [H_0, \rho] - \sum_j \frac{i}{2}\left(L_j^\dagger L_j \rho + \rho L_j^\dagger L_j - 2L_j \rho L_j^\dagger\right) \tag{1.28}$$

where H_0 is the free evolution Hamiltonian with a drive field, $H_0 = H_{tot} + i\varepsilon(a - a^\dagger)$ (H_{tot} from Eq. 1.1) and the L_j are the decay or "jump" operators which characterize decay into the environment. For the atom-cavity system:

$$L_c = \sqrt{2\kappa}a \tag{1.29}$$

$$L_a = \sqrt{2\gamma_\perp}\sigma_- \tag{1.30}$$

where L_c describes decay of system excitation out the cavity and L_a describes decay of excitation via atomic spontaneous emission.

[2]The quantum calculations get prohibitively large for more than 1 atom.

[3]The calculations are performed using the Matlab Quantum Optics Toolbox developed by Sze Tan. Hideo Mabuchi developed the code for the steady-state calculations.

In steady-state, $\dot{\rho} = 0$ while preserving the usual trace condition $\mathrm{Tr}(\rho) = 1$. Solution of this system of equations gives the steady state density matrix ρ_{ss} from which $\langle a^\dagger a \rangle_{ss}$ and other expectation values can be calculated via $\langle \hat{O} \rangle = \mathrm{Tr}(\hat{O}\rho)$. Most of what I use in this thesis, and indeed, almost everything done in cavity QED is in the steady-state limit.

1.3.2.1 The bad cavity

The regime in which we are most interested has $C_1 \approx 1$ and $n_s \ll 1$, so I will start here.

Rice and Carmichael [24] have derived quantum expressions for the steady-state operator moments in the strict bad cavity limit. Essentially, the cavity decay rate is sufficiently faster than all other rates that it can be adiabatically eliminated, leaving the atomic operators expressed as field operators, allowing solution of Eq. 1.5. The only result I need is:

$$n_s x^2 \equiv \langle a^\dagger a \rangle_{ss} = n_s y^2 \frac{1+y^2}{(1+2C_1)^2 + y^2}. \tag{1.31}$$

This provides a middle ground between the full quantum calculation and the semiclassical state equation. It is not valid for all drive strengths, since eventually the Rabi frequency associated with the drive field becomes too fast relative to cavity decay and the field elimination is no longer valid.

The input-output curves predicted from the semiclassical state equation and the quantum simulation are shown in Fig. 1.6 for a system in the bad-cavity limit. The differences are not especially pronounced.

Another way to present the same quantities is via the saturation curve. The saturation curve is more useful in this thesis, since it is directly related to a measurement which we make frequently. Taking X as a function of C, I define the *normalized transmission* as

$$T_n \equiv \frac{|x(C)|^2}{|x(C=0)|^2} \equiv \frac{X_{wa}}{X_{na}} = \frac{X}{Y} \tag{1.32}$$

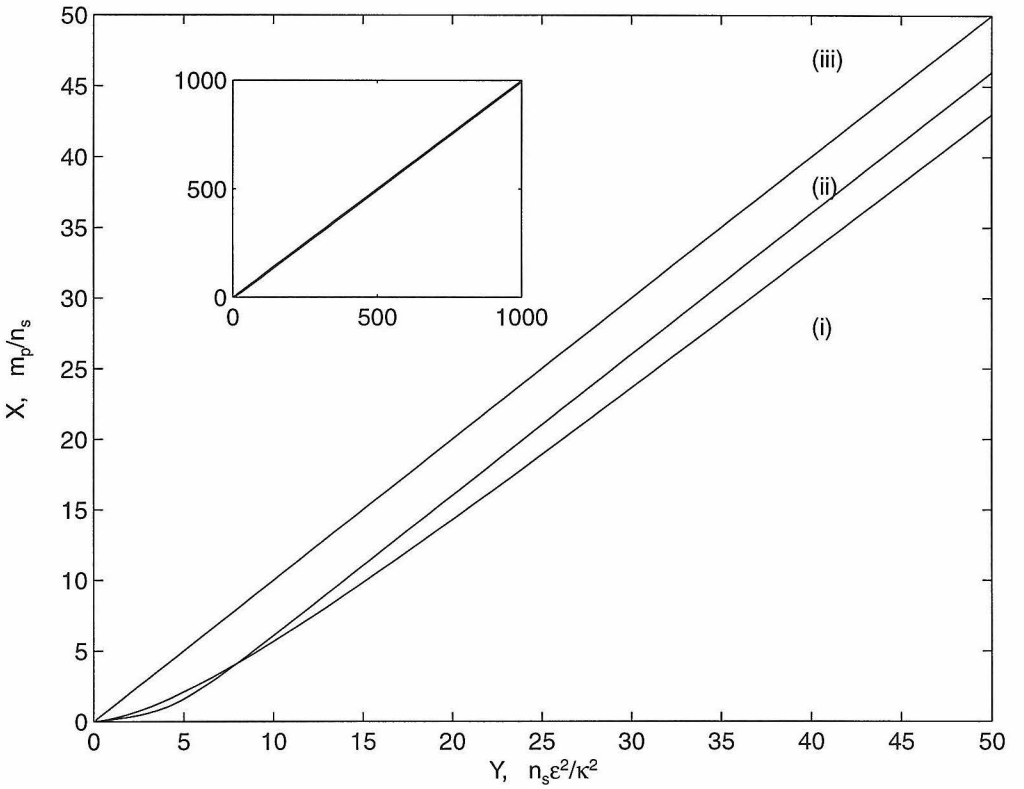

Figure 1.6: Input-output for the bad cavity regime. The curves are from (i) a quantum simulation (Eq. 1.28, supplemented by Eqs. 1.22 1.23) which gives $m_p/n_s = \langle a^\dagger a \rangle / n_s$ vs. $n_s\varepsilon^2/\kappa^2$ and (ii) the optical bistability state equation 1.19 which gives X vs. Y. Curve (iii) is the empty cavity $X = Y$. The inset has the same axis quantities but shows a larger drive range (out to approximately 10 intracavity photons). The prediction of Eq. 1.31 has been left out, but is nearly indistinguishable from the quantum curve. The parameters are: $g_0/2\pi = 20$ MHz, $\kappa/2\pi = 80$ MHz, $\gamma_\perp/2\pi = 2.5$ MHz, $C_1 = 1$, $N = 1$, $n_s = 0.008$.

or, for the quantum case

$$T_n \equiv \frac{\langle a^\dagger a \rangle_{ss}^{\text{atom}}}{\langle a^\dagger a \rangle_{ss}^{\text{no atom}}}. \tag{1.33}$$

This is simply the ratio, for a fixed strength driving field, of the transmission of the cavity with and without intracavity atoms. It removes any necessity for absolute knowledge of the input field strength or the empty-cavity peak transmission. Note that T_n can be displayed as a function of drive power (or intracavity photon number) for fixed probe frequency, or of probe frequency for fixed drive strength. The *saturation curve* treats T_n as a function of intracavity photon number *in the presence of an atom* $\langle a^\dagger a \rangle_{ss}^{\text{atom}} \equiv m_{p,wa}$. The saturation curve for the bad cavity system with $C_1 = 1$ and $n_s = 0.008$ is shown in Fig. 1.7. Note that the saturation curve starts out flat in the linear regime $m_{p,wa} \ll m_0$, then curves up and saturates to the empty cavity transmission for very strong drive fields. The differences between the semiclassical and quantum results are again not exceptionally pronounced. The main feature is that the quantum case saturates more quickly than the semiclassical case initially, but is then overtaken at higher drive powers.

The idea that the linear properties in the bad-cavity regime are well described semi-classically is important in this thesis, since they provide a convenient basis for comparison with experimental data. The absolute comparison between the quantum and semiclassical results for the nonlinear case is not as relevant. In many places I do make use of the far simpler semiclassical equations rather than performing a full blown quantum calculation, but not in any way that is essential to the conclusions of any experiment. Indeed it is not at all obvious that the full quantum calculation is any better at making predictions about the experiment, since the actual experiment is vastly more complicated than any simple (classical or quantum) model can possibly handle. After all is said and done, the onus is on the experimentalist to devise operationally significant measurements which in their interpretation do not rely on any particular theory.

Of course, simply because the result of one particular measurement is to some reasonable accuracy equally well described by several models, this does not mean that the

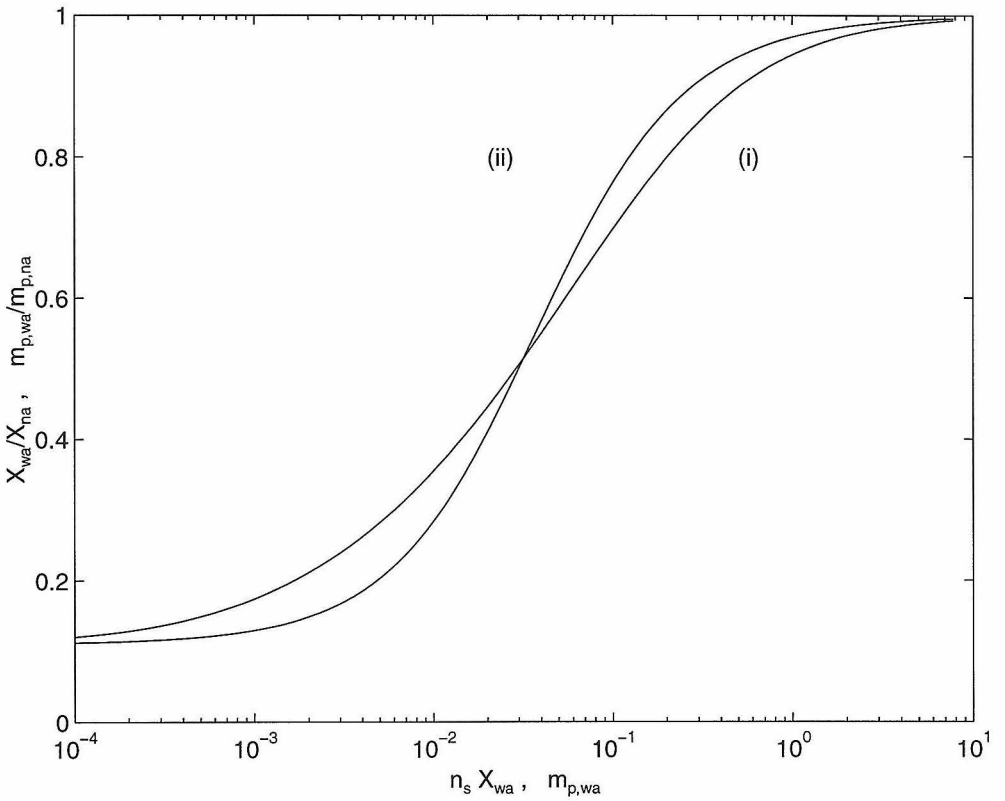

Figure 1.7: Saturation of the bad cavity from (i) a full quantum simulation (Eq. 1.33) which plots $m_{p,wa}/m_{p,na}$ vs. $m_{p,wa}$ and (ii) the optical bistability state equation (Eq. 1.32) which plots $X_{wa}/X_{na} = X/Y$ vs. $n_s X$. Same parameters as in Figure 1.6.

underlying physics does not respect the "correct" theory (in this case the full quantum theory). Rather, other measurements are required to explore those properties which are in fact demonstrably different in the quantum and semiclassical predictions. Although we have made several experimental attempts, such measurements have proven to be elusive and have essentially not been made in any direct way. Nevertheless, there is evidence that the underlying quantum mechanics is indeed relevant to some of the observations that we have made.

1.3.2.1.1 Discussion of n_s vs. n_0 If instead of individual atoms localized and fixed in space, the atoms are spread over the cavity mode, then the saturation behaviour of the system is described more properly by n_0 than n_s. That is, the system saturates at a larger (by $b = 8/3$) intracvaity photon number than in the localized atom case, for the same value of effective atom number N_e. This is relevant for the direct comparison of the quantum and semiclassical results. In order to get the semiclassical and quantum curves on the same abscissa, I have employed the following procedure. To avoid inverting Eq. 1.24, I choose a value of X and from it, compute the drive Y that would have produced this value of X. I then drive the quantum simulation with $\varepsilon = \sqrt{\kappa^2 n_s Y}$. The quantum simulation produces $m_{p,wa} = \mathrm{Tr}(\rho a^\dagger a)$. For the case of the empty cavity, $X_{na} = Y$, which is obvious both from the definition of X and Y and from Eq. 1.24 with $C = 0$. For the empty cavity quantum case, I likewise drive the quantum simulation with ε, setting $g_0 = 0$ to produce the no-atom intracavity photon number $m_{p,na}$. I have used the saturation photon number n_s, which is appropriate for a fixed atom localized on a maximum of the intracavity field. In our experiments, the atom is not fixed to any one position within the cavity. In fact "one atom" is really an average over many multi-atom realizations (in the sense of N_e), with each realization achieving a slightly different value of the coupling due to the exact distribution of atoms within the Gaussian standing-wave (I will discuss this much more further on, particularly in Section 2.1.3.3). When the atom (or atoms) is (are) distributed uniformly over the Gaussian mode volume $\psi(r)$, the saturation of the atom-cavity can be significantly more complicated than Eqs. 1.32 and 1.33

allow. Semiclassically, the weak-field response and the initial saturation behavior (fairly weak fields) can account for this through the geometrical factor $b = 8/3$ in n_0 which comes from an integration of the state equation over the Gaussian radial field distribution [34]. This has the net effect of moving the saturation curves in Figure 1.7 to the right by an amount b: it is harder to saturate "mush" spread out over the mode volume than a single atom localized at the field maximum. This is not surprising, as the de-localized mush samples all parts of the field, both strong and weak. The quantum theory really cannot take the atom "smearing" into account in any simple way, in any regime of drive field.

Despite this, in almost all of what follows, I will use a definition of n_0 with $b = 8/3$, as I did in section 1.2, and I will use it even in regimes where it is not strictly meant to be used. In order to compare a semiclassical prediction with a quantum prediction in this light, I plot the two results (quantum and semiclassical) in Figure 1.8. It is important to note that this is not in any way a direct comparison of quantum and classical theory for identical circumstances (that is shown in Fig. 1.7). It is, rather, a comparison of a quantum calculation for one stationary atom on an antinode of the field with some C_1 and a semiclassical prediction for a conglomerate atomic system spread out over the cavity mode volume with $C = C_1$. In an actual comparison to experimental data taken with an atomic distribution, **both** curves could be moved to the right by $b = 8/3$. This is partially valid semiclassically, and of unknown validity quantum-mechanically (though it is probably not too far from the truth, especially in the bad-cavity limit). If all of this seems mysterious at this point, it will become clearer as the actual experiments are described.

1.3.2.2 Strong coupling

Fig. 1.9 shows the input-output curves for a system in the strong coupling limit. Clearly there are some differences between the two predictions. The semiclassical curve exhibits the bistability expected since $C = 10$ for the parameters that I have chosen. It is no surprise that the quantum answer is not bistable, as I have plotted a single-valued photon number expectation value. The bistability is revealed in a

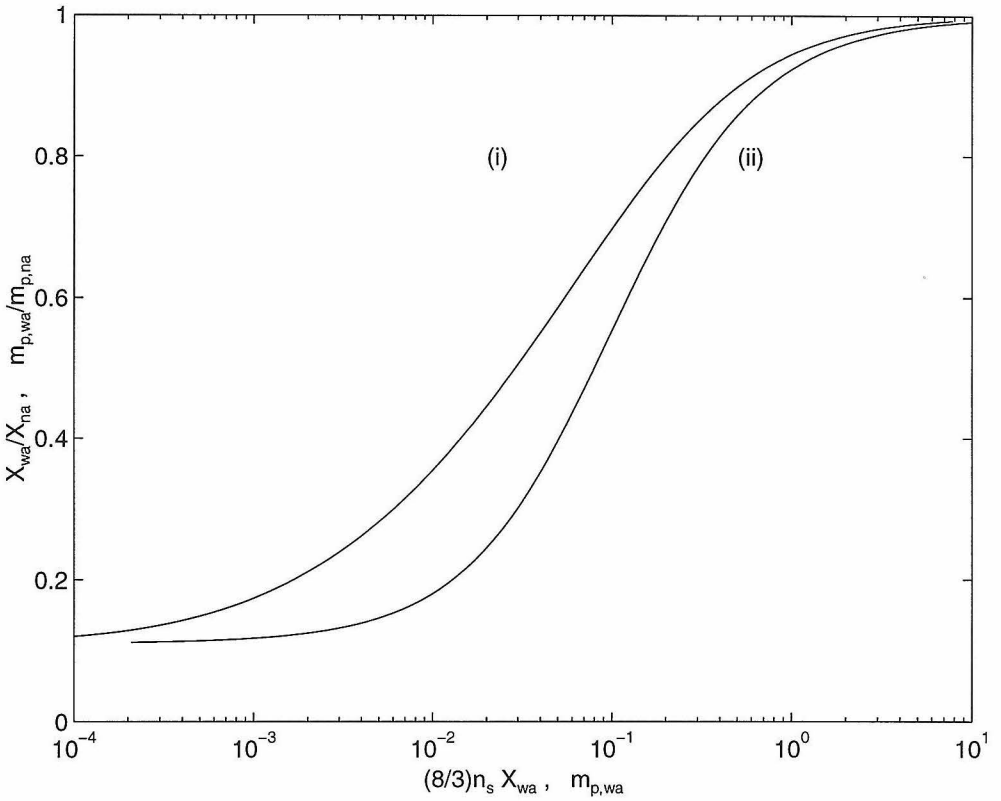

Figure 1.8: Same as Figure 1.7 with an adjustment to the semiclassical abscissa of $b = 8/3$. The semiclassical x-axis is $\kappa^2 n_0 |x|^2$. (i) Quantum simulation. (ii) State equation. Note that the curves have swapped sides relative to Figure 1.7.

bimodal photon number distribution [35] which is lost in the expectation value. Note even for very large drive fields Y, that X never quite reaches the empty cavity value. In saturation, the atom scatters photons at a constant, fixed rate, which causes the X vs. Y curve to never quite reach the empty cavity curve. This can also be seen by expanding Equation 1.24 for large X. It is seen from this that $X = Y - 4C$, so that the effect is more noticable for large C. Additionally, the semiclassical theory predicts a much smaller discrepancy than does the quantum theory. This was also noted in Ref. [36].

As in the bad cavity case, it is initially easier to saturate the quantum case than would be expected from the semiclassical guess. In this regime, the reason becomes clear: the semiclassical curve follows the lower branch of the bistability curve for weak drives. Only when the semiclassical curve reaches the turning point and jumps to the upper branch, does it become relatively easier to saturate. This is seen quite clearly in the saturation curve of Fig. 1.10.

1.3.3 Discussion of $\langle a^\dagger a \rangle$ vs. $|\langle a \rangle|^2$

As a final consideration, I will examine the differences between quantum calculations of intracavity intensity based on the photon number operator $\langle a^\dagger a \rangle$ and the modulus-square of the field operator $|\langle a \rangle|^2$. I mention this point because it could be relevant in the context of photo-detection. Photon counters respond to $\langle a^\dagger a \rangle$, while unit efficiency homodyne (and heterodyne) detection provides a measure of $\langle a \rangle$. Will the two types of detection on cavity output yield different results? Coherent states are eigenvalues of the anninilation operator, so $\langle \alpha | a^\dagger a | \alpha \rangle = |\alpha|^2 = |\langle \alpha | a | \alpha \rangle|^2$, and therefore it may be expected that the two methods will lead to identical results. The semiclassical state equation does not distinguish between field operator expectations and photon number operator expectations: the intensity is simply the square of the field. On the other hand, the Jaynes-Cummings Hamiltonian clearly prefers photon basis states. Not surprisingly, the answer for a real system, including dissipation probably lies somewhere between these two possibilities. Again, I will only investigate the question

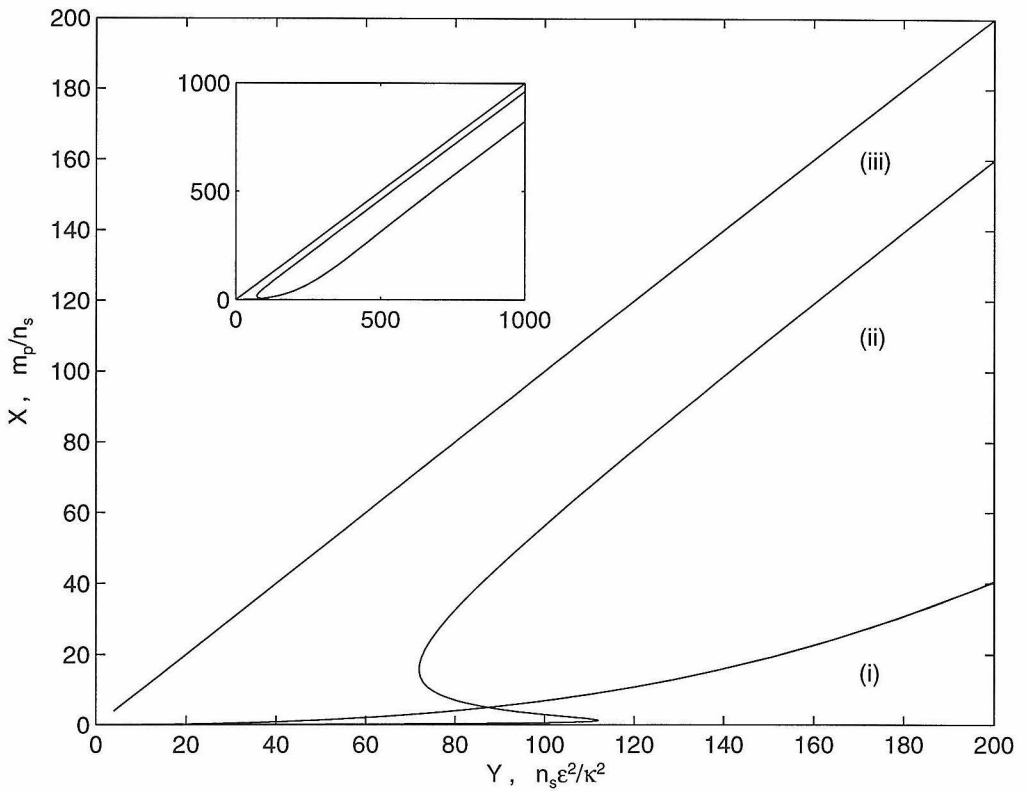

Figure 1.9: Input-output for a strong coupling atom-cavity system from (i) a quantum simulation (ii) optical bistability state equation with (iii) the empty cavity. The parameters are: $g/2\pi = 20$ MHz, $\kappa/2\pi = 8.4$ MHz, $\gamma_\perp/2\pi = 2.5$ MHz, $C = 9.5$. Note the bistability in the semiclassical prediction. Note also that these parameters come from those of Figure 1.6 with κ chosen 1 order of magnitude smaller. See Figure 1.6 for a further explanation of the graph axes.

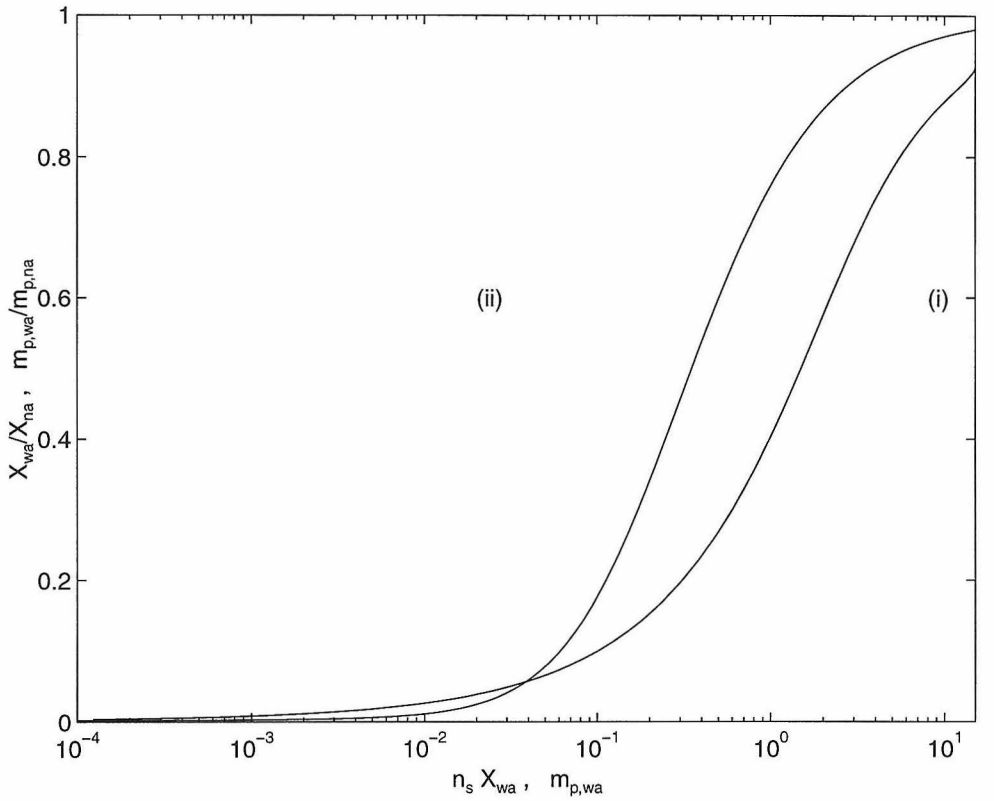

Figure 1.10: Saturation of the strong coupling cavity from (i) a quantum simulation (ii) optical bistability state equation. Same parameters as in Figure 1.9. See Figure 1.7 for a further explanation of the graph axes.

by example, looking at the resonant input-output curves. These are shown in the bad-cavity limit (same parameters as Section 1.3.2.1) in Figure 1.11 and the strong-coupling limit (same parameters as Section 1.3.2.2) in Figure 1.12. In the bad cavity, it is seen that the two answers are similar throughout the range of drive fields shown. In weak field, the answers are identical. In the strong-coupling case, however, the answers are significantly different away from weak field. This system is closer to the Jaynes-Cummings model and shows signs of the non-classical interaction between an atom and a quantized cavity field. In this regime, care must be taken in correctly accounting for differences in the two types of detection.

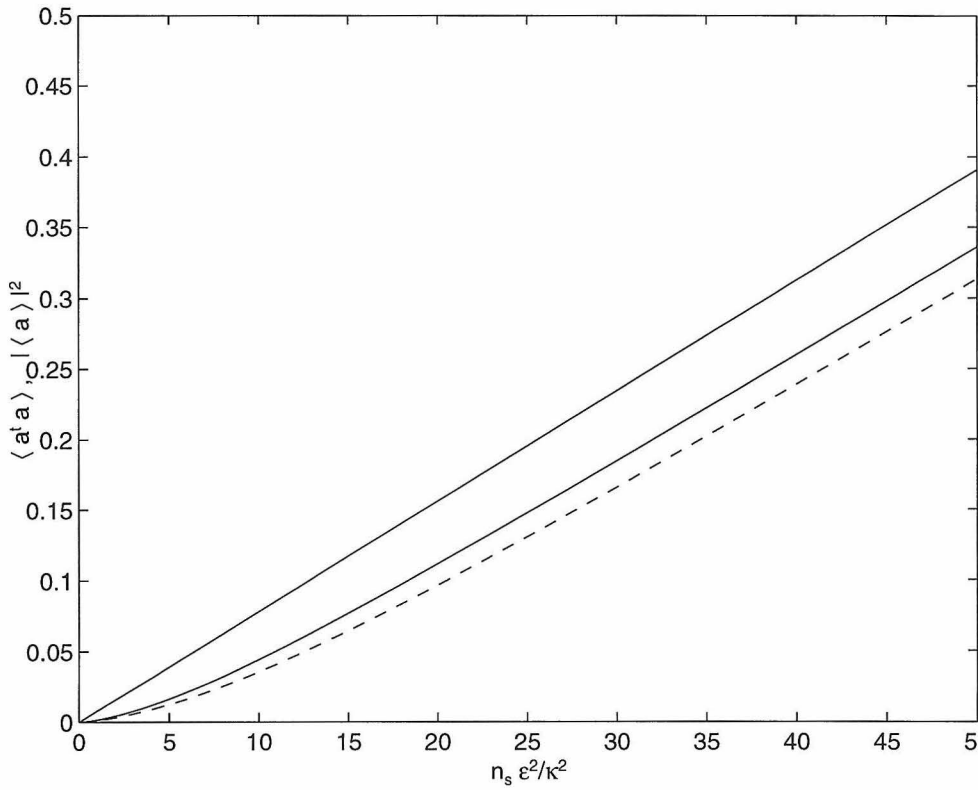

Figure 1.11: Comparison of intracavity intensity via two schemes in the bad cavity limit. The solid curve is a calculation of $\langle a^\dagger a \rangle$, while the dashed curve is a calculation of $|\langle a \rangle|^2$ for identical parameters. The straight solid line is the empty cavity. Same parameters as in Figure 1.6.

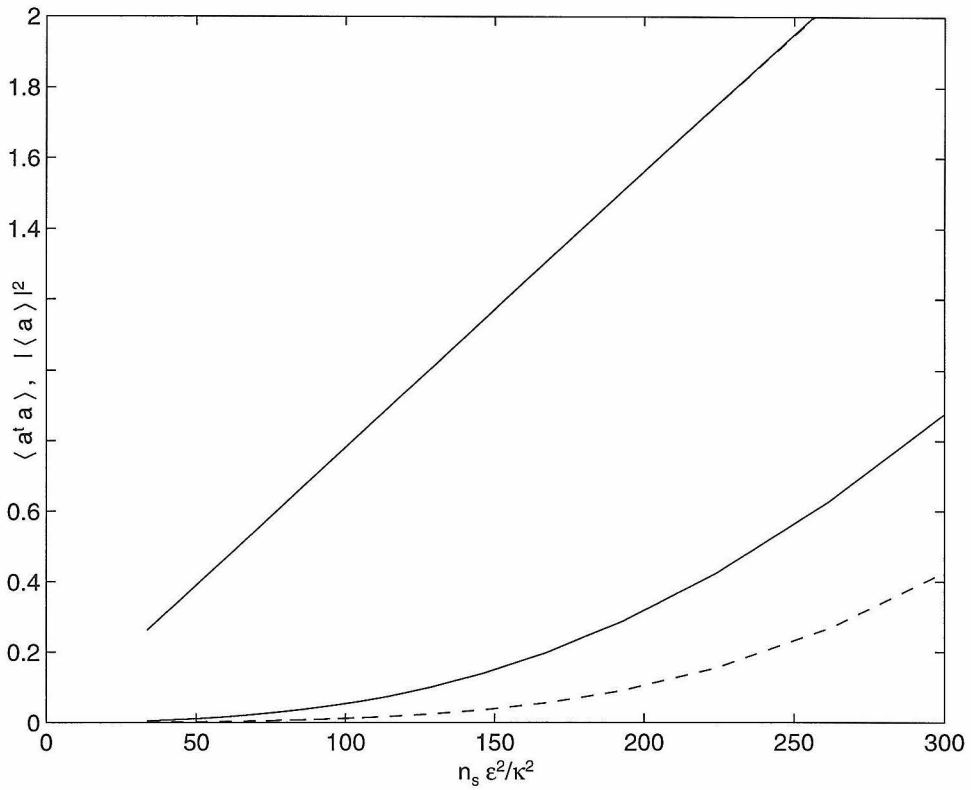

Figure 1.12: Comparison of intracavity intensity via two schemes in the strong coupling limit. The solid curvee is a calculation of $\langle a^\dagger a \rangle$, while the dashed curve is a calculation of $|\langle a \rangle|^2$ for identical parameters. The straight solid line is the empty cavity. Same parameters as in Figure 1.9.

Chapter 2 One-Dimensional Atom

"A cavity QED system in the bad cavity limit" is a lengthy and technically accurate (in my definition) description of the central subject of this thesis. It is not, however, a particularly illuminating description. On the other hand, the name "one-dimensional atom" embodies the key elements of this system—namely, it is relatively easy to probe with beams of light (along $\hat{z}$) and in so doing, we will not lose any photons to unmonitored, inaccessible "dimensions" (along $\hat{x}$ and $\hat{y}$). We have seen in Section 1.1.3.1 that in the bad cavity limit, the atom essentially behaves like an atom with a modified decay rate. As long as $g_0^2/\kappa > \gamma_\perp$, (coherent interaction rate > spontaneous emission rate) interaction with the cavity mode dominates the evolution of the modified atom and it becomes one-dimensional in the same sense that the cavity mode supports a "one-dimensional" paraxial Gaussian beam. It is an unfortunate misnomer in this case to call κ the cavity decay—decay implies a loss of information. Rather, here, cavity decay occurs into a channel which is easy (both in principle and in practice) to monitor with high efficiency.

It is useful at this point to introduce a quantity that is commonplace in the semiconductor diode trade, that is, β, the fraction of spontaneous emission emitted into the cavity mode. Laser manufacturers are interested in this quantity because the more spontaneous emission captured by the cavity, the more laser power for a given supply power—more laser photons for the buck. We are interested in β because it keeps the photons in the controllable and measurable channel. To derive an expression for β in the bad cavity limit is a trivial matter. The total rate of spontaneous emission is the sum of spontaneous emission out the sides of the cavity, that is, $\gamma_\perp$, and the emission into the cavity g_0^2/κ. The sum is of course $\gamma_\perp(1+2C_1)$ as we have already seen. Thus

$$\beta = \frac{g_0^2/\kappa}{\gamma_\perp + g_0^2/\kappa} = \frac{2\gamma_\perp C_1}{\gamma_\perp(1+2C_1)} = \frac{2C_1}{1+2C_1}. \tag{2.1}$$

For the experiment to be described in this chapter $C_1 \sim 1$, so $\beta \sim 2/3$. Thus radiation emitted by the atom is most likely to contribute to the cavity output field, which we detect with near unit efficiency, and rarely ends up in modes other than the single cavity mode.

To put our value of $\beta = 2/3$ in perspective, I will now consider other achievements in β of which I am familiar. In atomic optical cavity QED experiments in which Eq. 2.1 is valid, $\beta = 0.2$ [30, 37], $\beta = 0.03$ [38] and $\beta = 0.3$ [39] have been achieved. These three experiments attain these values by use of large solid angle cavities, so that many modes each weakly coupled to the atom generate a large spontaneous emission alteration, as opposed to our approach in which one strongly coupled mode generates the radiative alterations. In the semiconductor laser world, $\beta = 10^{-5}$ is common [40] while $\beta = 0.23$ is one of the largest values (obtained in a microdisk laser [41]). For plane-wave Fabry-Perot resonators (flat mirrors) which are most commonly used in laser diodes, the theoretical maximum value is $\beta = 1/2$ [15]. In microwave cavity QED experiments $\beta \approx 1$ is readily attained [26, 25, 42], but there is no direct access to the cavity field.

My coworker in the early phases of this experiment was Rob Thompson—before he went ahead and left me by graduating. In the later phases, and especially for the nonlinear measurements Christina Hood did a great deal of work.

2.1 Description of the experiment

2.1.1 The cavity

2.1.1.1 Cavity parameters

2.1.1.1.1 Cavity losses in brief Needless to say, in cavity QED, the cavity is preeminent. Relevant parameters for our cavities are shown in Figure 2.1. To make a cavity suitable for cavity QED experiments, the mirror reflectivity must be very high and the losses at the mirrors should be dominated by transmission. There are three contributions to the losses: transmission $T_{1,2}$, absorption $A_{1,2}$ and scattering $S_{1,2}$. I

will not differentiate between the "bad" loss mechanisms A and S, but instead lump them together as "losses" $L_{1,2} = A_{1,2} + S_{1,2}$. I will call $\mathcal{L} = L_1 + L_2 + T_1 + T_2$ the total losses even though it could consist of both good and bad contributions. Legitimate cavity QED demands that $\mathcal{L} \ll 1$ so that a photon is stored for an appreciable time and once radiated by an atom has a good chance of being reflected by the cavity to be reabsorbed by the atom. This is an essential aspect of the altered environment of cavity QED. The demand that $L_{1,2} \ll T_{1,2}$ is on the other hand, a criterion solely for the type of cavity QED in which we are interested. That is, we demand that all the light in the cavity eventually leak out into a channel that we can detect. Scattering losses and absorption losses are not of this type. In this sense, scattering and absorption losses are similar to spontaneous emission losses out the sides of the cavity, which we also do not detect (though in principle we could but in practice with very low efficiency). Spontaneous emission can in many situations be avoided via the use of some clever tricks, but mirror scattering or absorption losses cannot be circumvented.

2.1.1.1.2 Discussion of g_0 The second demand on the cavity is on its mode volume. Roughly speaking, the aim of cavity QED is to create as large an electric field *per photon* as possible so that a single photon can saturate the atomic response. This is accomplished by "confining" the photon to a small volume V_m. This is clear from the expression for the magnitude of the electric field $\mathcal{E}$ of a photon of frequency ω: $\mathcal{E} = \sqrt{\hbar\omega/(2\epsilon_0 V_m)}$ where ϵ_0 is the permittivity of the vacuum. Equivalently, we have seen that g_0 should be "large". Since $\hbar g_0$ is the energy of interaction between a single photon and the atom, $\hbar g_0 = \mu\mathcal{E}$ where μ is the atomic dipole moment matrix element (taken to be real). This gives:

$$g_0 = \left(\frac{\mu^2 \omega_a}{2\hbar\epsilon_0 V_m}\right)^{1/2}, \tag{2.2}$$

for an atomic transition at frequency ω_a. The smaller the mode volume, the larger g_0 becomes. For convenience, I can re-express Eq. 2.2 by replacing μ with the

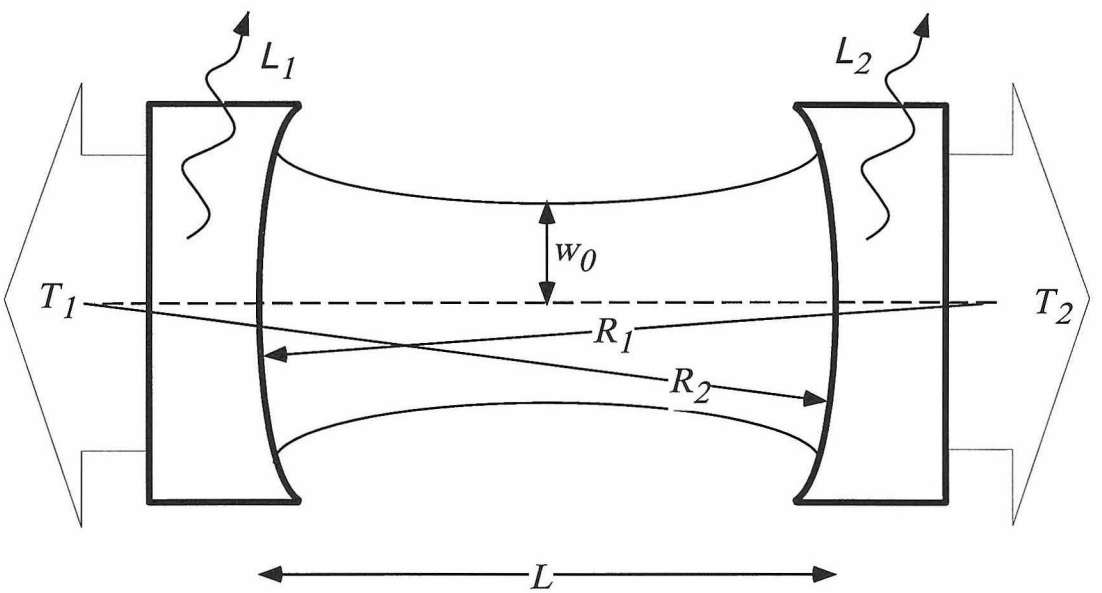

Figure 2.1: The cavity parameters. $L_{1,2}$ are scattering and absorption losses in the mirror coatings. $R_{1,2}$ are the mirror radii of curvature. $T_{1,2}$ are the individual mirror transmissions. L is the cavity length, w_0 is the waist of the fundamental Gaussian cavity mode.

appropriate expression in terms of $\gamma_{\|}$, $\mu^2 = \gamma_{\|} 3\pi\epsilon_0\hbar c^3/\omega_a^3$ and arrive at a final (useful) expression for g_0:

$$g_0 = \left(\frac{3c\lambda_a^2\gamma_{\|}}{8\pi V_m}\right)^{1/2} \tag{2.3}$$

where λ_a is the wavelength of the atomic transition. To calculate g_0, we must have an expression for the mode volume V_m. This is straightforward for a Fabry-Perot cavity geometry supporting the fundamental Gaussian mode and will merely be quoted here, after the definition of a few convenient quantities. The cavity is conveniently parameterized by the so-called cavity g-factors (no relation to the coherent coupling strength g_0; the notation is unfortunate for us, but widely accepted). They are:

$$g_i = 1 - \frac{l}{R_i} \tag{2.4}$$

where l is the cavity length and R_i is the radius of curvature of the i^{th} mirror. The mode volume for the TM_{00} mode of a Gaussian standing wave cavity is given by:

$$V_m = \frac{\pi}{4} w_0^2 l \tag{2.5}$$

where w_0 is the Gaussian waist, given by

$$w_0^2 = \frac{l\lambda}{\pi}\sqrt{\frac{g_1 g_2\left(1 - g_1 g_2\right)}{\left(g_1 + g_2 - 2g_1 g_2\right)^2}}. \tag{2.6}$$

Combining expressions 2.6, 2.5, 2.4, 2.3 gives g_0 in terms of the measured quantity l (more on this below), the known quantities R_i (known from the mirror supplier) and atomic quantities λ_a and $\gamma_{\|}$.

2.1.1.1.3 More on losses Now I will provide more detail on cavity losses, in a new notation. The cavity finesse $\mathcal{F}$ is defined by

$$\mathcal{F} = \frac{\pi\sqrt{r_1 r_2 e^{-\delta_0/2}}}{1 - r_1 r_2 e^{-\delta_0/2}} \tag{2.7}$$

where $r_{1,2}$ are the *amplitude* reflectivities at each mirror and δ_0 is the *round trip* internal cavity losses in *power* (due to an intracavity medium, scattering and absorption losses at both mirrors, dust, etc.). I will now introduce the common δ-notation wherein $r_i^2 = e^{-\delta_i} \approx 1 - \delta_i$ for sufficiently small losses $\delta_i \ll 1$. With this definition, δ_1 is the power transmission of the first mirror, δ_2 is the power transmission of the second mirror and δ_0 is the *total* absorption + scattering loss in power due to *both* cavity mirrors. This definition of δ_0 is consistent with Siegman (Ref. [43]) and reflects the fact that there is no *cavity* measurement which can assign the internal loss to one or the other of the mirrors. Additionally, I define the total cavity losses $\delta_c = \delta_1 + \delta_2 + \delta_0$. With these definitions the cavity finesse can be written ($\mathcal{F} \gg 1$)

$$\mathcal{F} = \frac{2\pi}{\delta_c} \tag{2.8}$$

which is the expression that is actually used. The finesse can also be expressed as the ratio of the cavity free-spectral range $\nu_{\mathrm{FSR}} = c/2l$ to the cavity full-width-at-half-maximum $\nu_{\mathrm{FWHM}} = 2\kappa/2\pi$ by $\mathcal{F} = \nu_{\mathrm{FSR}}/\nu_{\mathrm{FWHM}}$. The finesse is also roughly the average number of round trips that a photon in the empty cavity makes before leaking out.

It is useful to know the on-resonance build-up, reflection and transmission of the cavity in terms of $\delta_{0,1,2}$. These are all given in [43], but are here repeated for completeness and subsequent reference. The quantities are given as ratios of transmitted (or reflected, or circulating) intensity to *incident intensity on mirror* M_1.

$$\frac{I_{\mathrm{trans}}}{I_{\mathrm{inc}}} = \frac{4\delta_1\delta_2}{\delta_c^2} \tag{2.9}$$

$$\frac{I_{\mathrm{refl}}}{I_{\mathrm{inc}}} = \frac{(\delta_2 + \delta_0 - \delta_1)^2}{\delta_c^2} \tag{2.10}$$

$$\frac{I_{\mathrm{circ}}}{I_{\mathrm{inc}}} = \frac{4\delta_1}{\delta_c^2}. \tag{2.11}$$

If the finesse is known (or measured) the δ's are in principle completely constrained by measuring both Eqs. 2.9 and 2.10. In practice it is often more reliable to measure

the reflectivity of the cavity from both sides. If one of the δ_i's is very small relative to the other, it is difficult to get an accurate measure of the small one.

As an important aside, I will derive an effective δ_A—the effective atom-caused intracavity losses—in terms of C_1. I start from Eq. 2.9 and the fact that the weak-field transmission of a bad-cavity-with-atom is attenuated by $1/(1+2C_1)^2$ (see Eq. 1.14). The atom is treated strictly as a loss mechanism (it is not, since the dipole is excited and re-radiates out-of-phase) that causes photons in the cavity to be scattered out of the cavity or absorbed. The resulting expression (for $\delta_0 = 0$) is $\delta_A = 2(\delta_1 + \delta_2)C_1$, so that the total losses are now $\delta_c = \delta_1 + \delta_2 + \delta_A$. This is consistent with the "semiclassical" definition $C = \alpha_0 l\mathcal{F}/2\pi$ where α_0 is the absorption coefficient of the intracavity medium [32]. It is true only when the atom, cavity and incident probe frequencies are coincident.

The task of the cavity designer is typically to make g_0 large yet keep κ "reasonable" ($C_1 \geq 1$). This is a task of tradeoffs. The route to large g_0 is via small mode volume which is achieved via two possibilities: short length, or tight radius of curvature R. It is useful to point out some scalings. For a symmetric radii, near-planar cavity, $w^2 \propto \sqrt{lR}$ so $g_0 \propto l^{-3/4}R^{-1/4}$. As for the cavity linewidth, keeping κ small requires large finesse and a long cavity. Of course, $\kappa \propto \mathcal{F}^{-1}l^{-1}$. For fixed radius of curvature and finesse, eventually κ dominates over g_0 as the cavity is made shorter. For the true strong-coupling regime this becomes a problem, but for the bad-cavity regime, it is relatively easy (nowadays) to get the parameters just right, especially at long optical wavelengths.

2.1.1.2 The cavity realized

2.1.1.2.1 Overview of cavities used Having discussed the cavity parameters, I will now describe the cavities that my co-workers and I have used in various experiments. To start, in Table 2.1, I list the parameters of four cavities.

Note that most of the cavities are "one sided," that is, the transmission of one of the mirrors is much larger than that of the other. This is a practical design issue which allows all of the cavity leakage to occur in one direction, so that the most

#	$\mathcal{F}$	$l[\mu m]$	(δ_1, δ_2)	$(R_1, R_2)[cm]$	$\frac{1}{2\pi}(g, \kappa, \gamma_\parallel)[MHz]$	(N_0, m_0)	ref.
1	8×10^4	1100	(1, 75)	(17, 17)	(3.1, 0.9, 5)	(0.5,0.8)	[7]
2	3×10^5	346	(1, 15)	(17, 17)	(7.2, 1.2, 5)	(0.06,0.16)	[44]
3	1.8×10^4	56	(1, 350)	(100, 45)	(20, 75, 5)	(0.9,0.02)	[45]
4	2×10^5	108	(15, 15)	(100, 100)	(11, 3.5, 5)	(0.14,0.07)	[46]

Table 2.1: Cavities used in this research.

information about the intracavity field emerges in one direction. (Take the ratio of Eq. 2.9 and 2.11 to get: $I_{\text{trans}} = \delta_2 I_{\text{circ}}$.)

For all of Part I cavity # 3 is used. In addition to the parameters quoted in Table 2.1, this cavity has $w_0 = 33$ μm, $V_m = 5 \times 10^4$ μm^3, $\nu_{\text{FSR}} = 2,760$ GHz. For additional atom-cavity parameters see Appendix B.1.1.

2.1.1.2.2 Mirror technology and cavity construction The mirror technology itself is becoming fairly routine. Transmissions as low as $\delta_i = 10$ ppm with $\delta_0/2 \approx 1$ ppm are common. $\delta_1 = 1$ ppm on $\delta_0/2 = 0.5$ has been obtained. The mirrors are multi-layer (up to 80 layers for super-high finesse) dielectric coatings deposited on super-polished substrates of either BK7 or fused-silica. More information about the mirror coating materials and techniques can be found in Ref. [47].

The cavity mount for cavities 1–3 is shown schematically in Figure 2.2. This is not a new mount, it is explained in more detail elsewhere [48], but briefly: Each mirror is mounted (glued) in a macor cup which is in turn mounted (glued) to a tubular piezoelectric transducer (PZT), which itself is mounted (glued again) into a brass holder. Each of these assemblies is glued into an invar tube, thereby forming the "cavity mount." This assembly is placed in the vacuum chamber on a bed of viton o-rings and lead sheet for vibration isolation. The lead offers excellent mass and damping characteristics for passive vibration isolation, but is a non-ideal vacuum material. Nonetheless adequate pressures on the order of 10^{-6}–10^{-7} torr were attained. The cavity was aligned to the atomic beam (more on the beam in Section 2.1.3.2) by sighting down the vacuum tube with an army surplus surveyor's telescope.

Control over the nominal length of the cavity during construction was marginal, but adequate. The glue which is in contact with the mirror must be a very small drop,

as stresses in the substrate impart small birefringence on the mirror coatings, which for large finesse cavities, can be a real problem. Even with precautions, birefringence is still present. The alignment criterion is fairly strict for long radius-of-curvature mirrors. Essentially, the cavity mode is formed along a line which connects the centers-of-curvature of the two mirrors. If the line does not happen to intersect the coated regions of both mirrors, the cavity will not support modes. If the line intersects the outer area of the mirrors, it is likely that the finesse will not be high, since the mirror coatings are only of optimal quality near the center. This has not been tested in any quantitative way, but is the present folklore. The long arm associated with long-radius mirrors makes alignment critical. Because the cavity mount has no degrees of freedom, the assembly process was a bit of a trial and error procedure in which a cavity would be glued together, and one would then hope it actually supported high-finesse modes.

To facilitate the construction of a cavity, the following technique was developed. The first mirror is glued into its holder and the holder glued into the invar tube. The second mirror then is placed into its holder, the rest of the mount lowered over this mirror while the mirror faces are brought into contact with each other. The second mirror is then glued in place. The cavity is separated and reassembled with foil spacers inserted between the brass holder and the invar tube, to choose a satisfactory length. The whole assembly is then glued together. This absurd procedure managed to produce mostly functional cavities. The idea of contacting the mirrors, horrid as it may seem, is salvaged by the curvature of the mirrors. When the edges of the mirrors are touching there is still space between the actual coated surfaces. The indentation of the curved surfaces is given by $d_{\mathrm{ind}} = R - \sqrt{R^2 - r^2}$ where R is the radius of curvature and r is the substrate radius. For a 1 m curved mirror on the typical 7.75 mm substrates the indentation is 7.5 μm. There shouldn't be anything at all on the surface of the mirrors anyway, so this is a completely adequate spacing. All cavity assembly is done in a laminar-flow clean-hood. Mirror cleaning is done with standard techniques and solvents.

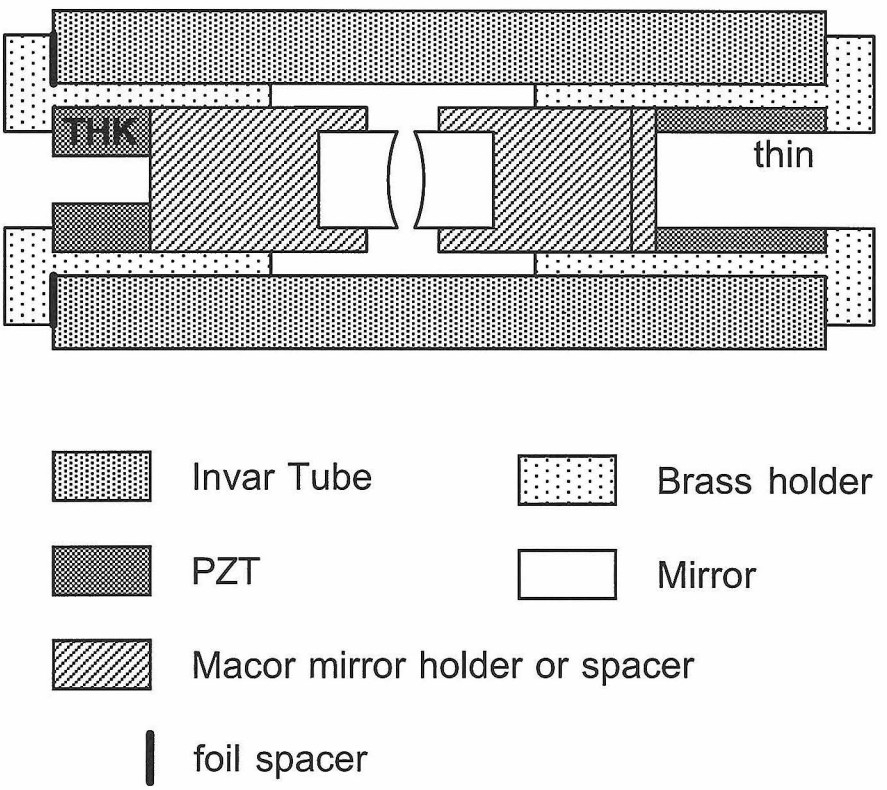

Figure 2.2: The cavity mount. After Ref. [48].

2.1.1.2.3 Measuring the cavity length The cavity length can be measured by a simple, powerful, and accurate method. Because the cavities are so short, the free-spectral-range is extremely large—several nm. The length can thus be derived from a direct measure of ν_{FSR}. The cavity length is scanned over a free-spectral-range (a length $\lambda/2$ where λ is the laser wavelength) by the thin PZT. The position of the modes within the scan ramp is noted, and the laser is tuned in wavelength (by the birefringent filter of our laser (Coherent 899)) until the modes are walked through a free-spectral-range and reappear in the same position as the previous modes, which corresponds to ± 1 additional half-wavelengths in the cavity. On the wavemeter, the original wavenumber (to an accuracy of 0.01 cm^{-1}) $\sigma_1 \equiv 1/\lambda_1$ and the subsequent wavenumber $\sigma_2 \equiv 1/\lambda_2$ are recorded. The cavity supports a longitudinal mode when the round-trip phase returns to 2π, so, $2\pi\sigma_1 2l + \phi_1 = 2\pi p$ and $2\pi\sigma_2 2l + \phi_2 = 2\pi(p+1)$ where p is an integer and ϕ_1 is the phase shift at the mirror coatings at λ_1 and ϕ_2 is the phase shift at the mirror coatings at λ_2. For very short cavities, λ_1 and λ_2 can differ by several nm (12 nm for $l = 50$ μm), which can be outside of the mirror coating bandwidth, so that $\phi_{1,2}$ could be considerably different. If we neglect this possible complication, then the cavity length is given simply by $2l = 1/(\sigma_1 - \sigma_2)$. We can measure $\sigma_{-2,-1,0,+1,+2}$, etc., several times (on both sides of the mirror coating center wavelength $1/\sigma_0$ to mitigate effects of $\phi_{1,2}$) to determine the exact number of half-wavelengths in the cavity. The time between wavelength measurements must be as short as possible to avoid drift in the length of the cavity due to thermal effects. Thirty seconds or so is usually good enough.

Another, sometimes useful method of measuring the length takes advantage of the transverse mode structure of the cavity. The transverse mode spacing is given by

$$\nu_{\mathrm{TM}} = \frac{\cos^{-1}\sqrt{g_1 g_2}}{\pi}\frac{2\pi c}{2l}. \tag{2.12}$$

Inverting this and making the short cavity approximation gives,

$$l = \frac{R_1 R_2}{R_1 + R_2}\left[\frac{\nu_{\mathrm{TM}}}{\nu_{\mathrm{FSR}}}\pi\right]^2. \tag{2.13}$$

$\nu_{\rm TM}$ and $\nu_{\rm FSR}$ are measured as voltages on the PZT. Something causes this method to be inaccurate by $\pm 50\%$ typically. Whether it is nonlinearity in the PZT scan or a failure of the Fresnel approximation (which is assumed in Eq. 2.12, and almost everywhere else) is not known. This technique is only used as a gross indicator of the length, and in cases where the cavity is not sufficiently short to resolve the difference in adjacent longitudinal mode wavelength, a direct technique (such as with a ruler and a microscope) must supplement it. (Of course, for very long cavities with $\nu_{\rm FSR} \sim 10$–100 MHz, it again becomes easy to measure $\nu_{\rm FSR}$ by e.g. application of rf sidebands to the optical beam.)

2.1.1.2.4 Measuring the cavity line-width As a practical matter, when a cavity is first assembled very little is known of it. The first task is to measure the length, as described above. The next will be to measure its line-width ($\kappa/2\pi$). From the manufacturer, we know $\delta_{1,2}$ to 10–20% , but δ_0 is unknown. If we trust $\delta_{1,2}$ then a measure of the length and the line-width is enough to tell us whether δ_0 is acceptable. If we want more information, then we must look to Eqs. 2.9 and 2.10 and make the appropriate measurements. The line-width is determined by the following measurement. We quickly scan the laser across the cavity resonance (at a rate of ≈ 10 MHz/ms) while simultaneously recording the hyperfine structure of the excited state from an auxiliary Cs cell, for a frequency marker. The cavity transmission is collected on a PMT (the "locking PMT" of Fig. 2.6) and $\nu_{\rm FWHM}$ is read from the signal stored on a digital oscilloscope over many repetitions. This measurement determines $2\kappa/2\pi = \nu_{\rm FWHM}$.

The measured transmission of the empty cavity is shown in Figure 2.3. The data taking process is described at length in subsequent sections, but briefly, the data is compiled by slowly stepping the frequency of a rf sideband across the cavity resonance and detecting the output on a balanced heterodyne photo-receiver. (Probe beam generation is described in Section 2.1.4 and detection is described in Section 2.1.5.) The data in Figure 2.3 are not as they appear directly out of the experiment. There is a normalization procedure to correct deficiencies in the apparatus. The data of Fig.

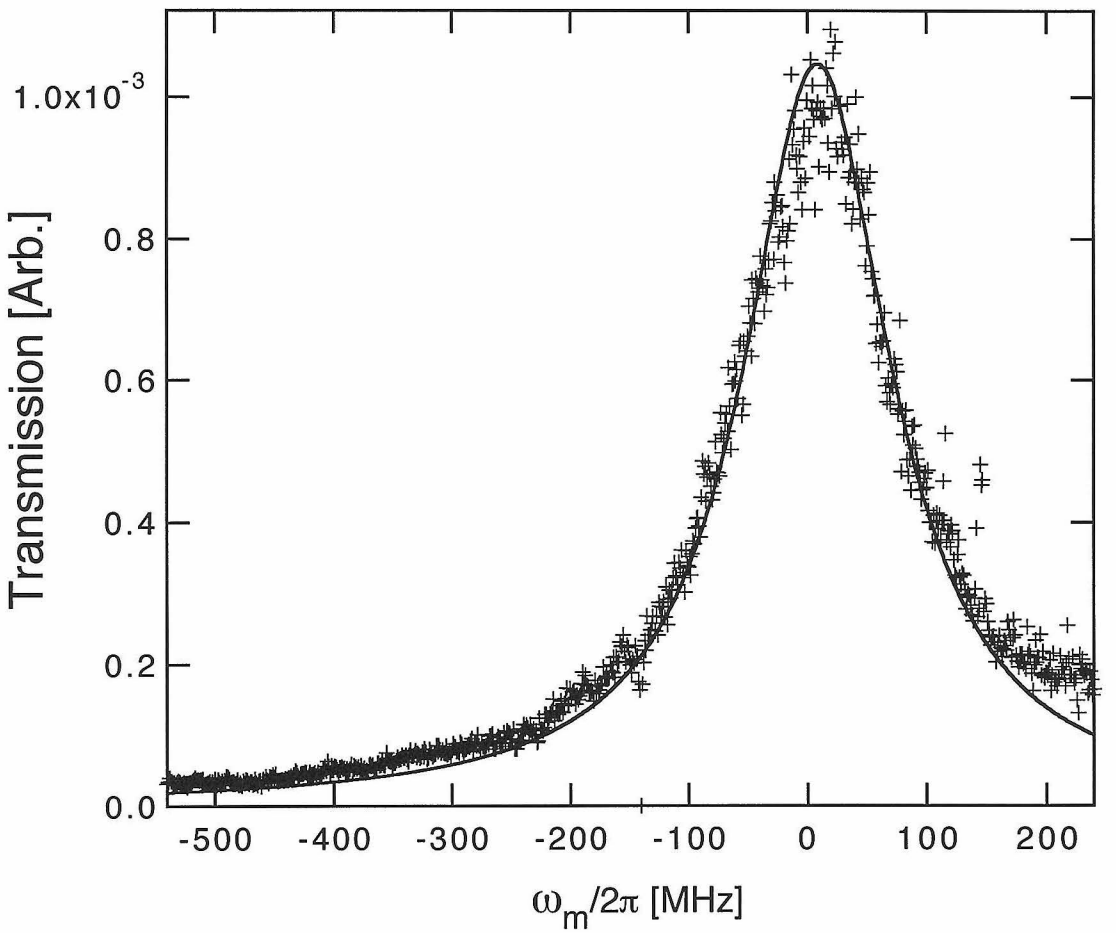

Figure 2.3: The empty cavity transmission. The '+' are the data and the solid line is from Eq. 1.8 with $g_0 = 0$, $\Delta = \Theta = 0$, $\kappa/2\pi = 75$ MHz (fixed by the measurements described in the text) and an adjustable height.

2.3 have been normalized to the measured response function $R(\omega_m)$ of our apparatus, which is determined by removing the cavity from the light path and performing the same frequency step with the same probe generation and the same detection chain (both optical and electrical). (The probe generation and detection chain is summarized in Section 2.1.6.) $R(\omega_m)$ is not constant over the 800 MHz scan range, due to efficiency of rf-sideband generation, the response of the photodetectors, and cable rf responses. Great care was taken to assure that, while $R(\omega_m)$ has significant structure over the scan range, this structure did not change from day to day. The normalization curve is shown in Figure 2.4—it coincidentally looks remarkably like the empty cavity itself, shifted off a bit. It is not symmetric about 0 MHz because there is nothing special about 0 MHz in the probe generation (see Section 2.1.4 and 2.1.6).

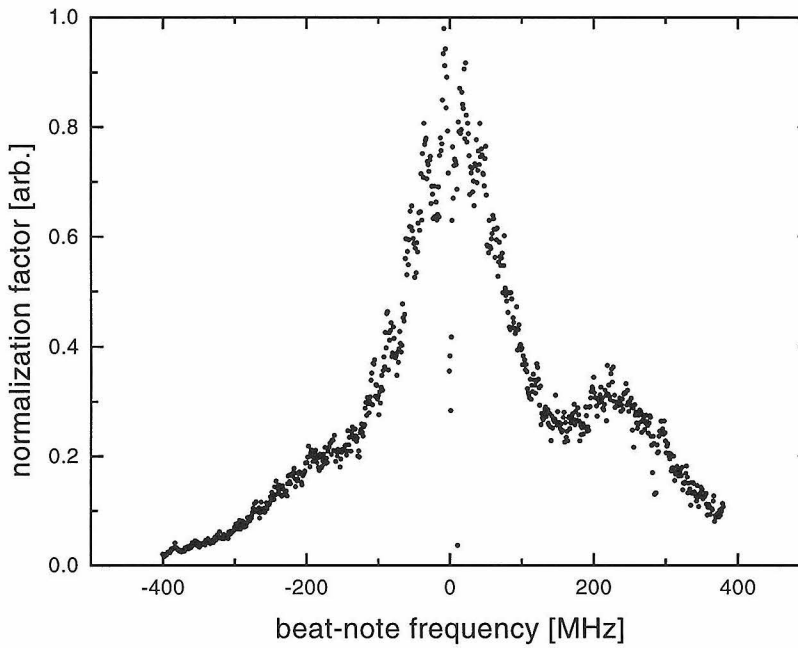

Figure 2.4: The normalization. The frequency scale is in terms of the beat-note frequency from the heterodyne, which is offset from the atomic resonance by 140 MHz.

To complete the entire raw-data-to-PRL-graph path, I show the empty cavity

scan as it actually appears in the lab in Figure 2.5. The sharp dip at 0 frequency is due to a roll-off in photodiode amplification below 5 MHz in the photodetectors, also seen in the normalization. After normalization of the data in Figure 2.5 by the normalization curve in Figure 2.4, Figure 2.3 magically appears. Note that the solid curve in Figure 2.3 is not a fit to the data, but rather a height-adjusted Lorentzian with width determined from the laser-scan measurements described above. Determining the width from data such as that shown in Fig. 2.3 proves to be too inconsistent to be of value for anything but confirmation of the width at the 20% level. However, for short scans over just the (enhanced) atomic bandwidth, which will be prominent later, $R(\omega_m)$ is nearly constant and normalization is not a major concern. In fact, most of the data acquisition procedure is designed to work around the need for normalization.

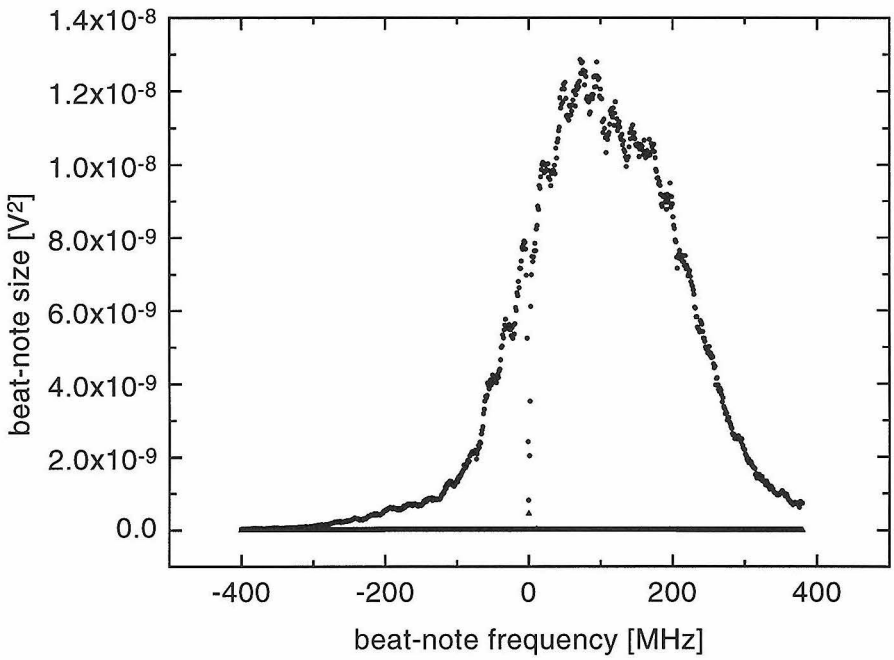

Figure 2.5: The empty cavity raw data, before normalization. The frequency scale is in terms of the beat-note frequency from the heterodyne, which is offset from the atomic resonance by 140 MHz. The cavity center is actually at 140 MHz, though this is difficult to see before normalization.

2.1.1.2.5 Locking the cavity The cavity is not sufficiently passively stable to maintain its length to the required accuracy for the necessary measurement time, so it must be actively servoed. In general, a high finesse cavity is ultra-sensitive to vibration. To see this, consider the following. The length of the cavity on resonance is a half-integral number of wavelengths, $l = n\lambda = nc/\nu$ so, $\nu = nc/l$, where ν is the frequency of resonant light. If the length is changed by some external disturbance, then the corresponding change in supported frequency is $\Delta\nu/\Delta l = -nc/l^2 = -n/l2\nu_{\mathrm{FSR}} = -2\nu_{\mathrm{FSR}}/l$. If we demand that the cavity stay within some fraction f of its linewidth, that is, $\Delta\nu = f\nu_{\mathrm{FWHM}}$ then $\Delta l = -f\lambda\nu_{\mathrm{FWHM}}/2\nu_{\mathrm{FSR}}$, or, $\Delta l = -f\lambda/2\mathcal{F}$. If the finesse is large, this can be a fairly impressive limit. For example, for cavity #3 locked to 10% of its linewidth, $\Delta l \sim 10^{-11}$ m. However, the statement is somewhat artificial, since this cavity would still be locked in absolute terms to only $\Delta\nu \sim 10$ MHz.

The cavity is servoed to constant length by monitoring and maximizing its transmission to a strong "lock" beam (see Fig. 2.6). The lock is achieved by a low-frequency phase-sensitive servo. The thick PZT on the cavity mount is dithered with a small-amplitude sine-wave at 80 kHz. Normally the PZT would have no response at this frequency, but a) we search for a mechanical resonance to enhance the effect and b) it does not take much displacement to make a perceptible change in transmission. The thick PZT is used because it has low sensitivity to any noise present on the driving electronics. The transmission of the cavity to the lock beam is monitored by a PMT (see Figure 2.6). The PMT current is driven through a 10kΩ resistor which feeds a SRS lock-in (post-processing time constant 1 ms) which demodulates the dithered signal, giving a sharp zero-crossing at cavity center as an error signal. The error signal is amplified, inverted, and lowpassed at 2 Hz and sent to the thin PZT to correct the length. The dither on the cavity is an effective modulator for the transmitted light (FM for resonant light, AM for off-resonant light), which is the basis of the technique. However, it is undesirable to fracture too much of the light into the 80 kHz sidebands from the dither. The 80 kHz sidebands on the locking beam can be easily seen on the heterodyne detectors, and an effort was made to always keep the sidebands more than 20 dB down from the carrier. (Actually, even -20 dB translates to a fairly large

cavity length excursion.)

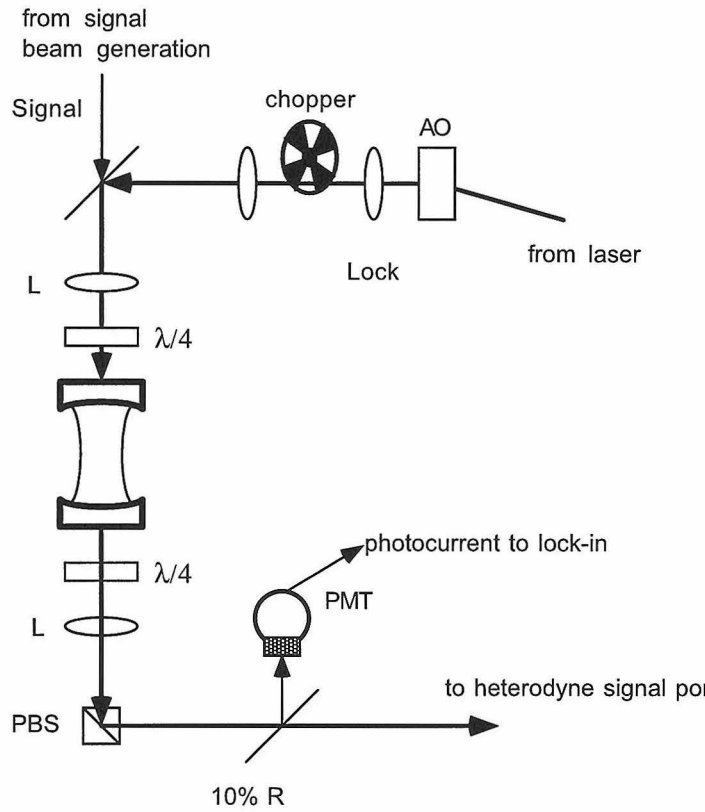

Figure 2.6: The cavity-lock optical schematic. AO: acousto-optic modulator. PMT: photo-multiplier tube. PBS: polarizing beam-splitter. $\lambda/4$: quarter-wave-plate. L: lens.

We have seen that weak-field corresponds to $\bar{n} \equiv \langle a^\dagger a \rangle \ll m_0$, which produces a low flux of photons out the cavity. For good S/N in the cavity lock, it is necessary to use a much stronger beam to servo-lock the length of the cavity. This lock beam is resonant with the atoms, since for nearly all measurements we want the cavity and atoms at the same frequency ($\omega_a = \omega_c$). In order to avoid the effects of the much stronger locking beam, which would easily saturate the atomic response, it is chopped on and off, with a fifty percent duty cycle at a frequency of 3 kHz. During the "off" portion of the lock cycle, the data is accumulated. The data window has a duty cycle of 30%, with the data "on" centered at the lock "off" to avoid any possible transient

effects due to the lock beam, and to let the lock photons leak out of the cavity. This is not a completely trivial statement. If we are performing a weak field measurement with $\bar{n} \sim 10^{-6}$ intracavity photons, and the lock beam has $\bar{n} \sim 10^{3}$, then we must wait a time t given by $e^{-t/\tau} = 10^{-9}$, where τ is the cavity lifetime. Surely 20 lifetimes is safe, corresponding to several micro-seconds. We typically wait 10 μs. Similarly, the the technique for chopping the lock-beam proved to be extremely important, with a satisfactory "off" state only achieved via a tightly focused beam through a mechanical chopper. Two amplitude modulators each consisting of an EO-polarizer pair proved to have insufficient attenuation, and oddly enough, the off state of a typical video-driver AO controller provides insufficient attenuation of the first-order deflected beam.

2.1.2 The light

2.1.2.1 Laser and its lock

The laser is an Ar^{+}-pumped Titanium:Sapphire laser. An early laser was an in-house design, described elsewhere [48] while later we switched to a Coherent 899. Stabilization to the Cs atomic resonance was achieved via a common FM saturation spectroscopy technique, with the error signal fed directly back to the laser cavity length. Laser linewidth of the 899 was never measured with great care, but estimates from the in-loop error signal give between 50–100 kHz, and a direct beat-note comparison with the old Ti:Saph concurred with this value. The FM laser lock is completely standard [49, 50, 51], so I will leave it at the level of the unexplained Figure 2.7. The only detail to note is that with the pump beam downshifted by the double-pass AO driven with rf frequency $\Delta/2$, the laser will be locked $\Delta/2$ above the transition frequency.

In addition, the light directly from the Ti:Saph is rather noisy, with ≈10–20% intensity fluctuations out to ≈ 400 Hz. To quiet this, we used a simple EO-polarizer combination noise eater. This is shown in Figure 2.8.

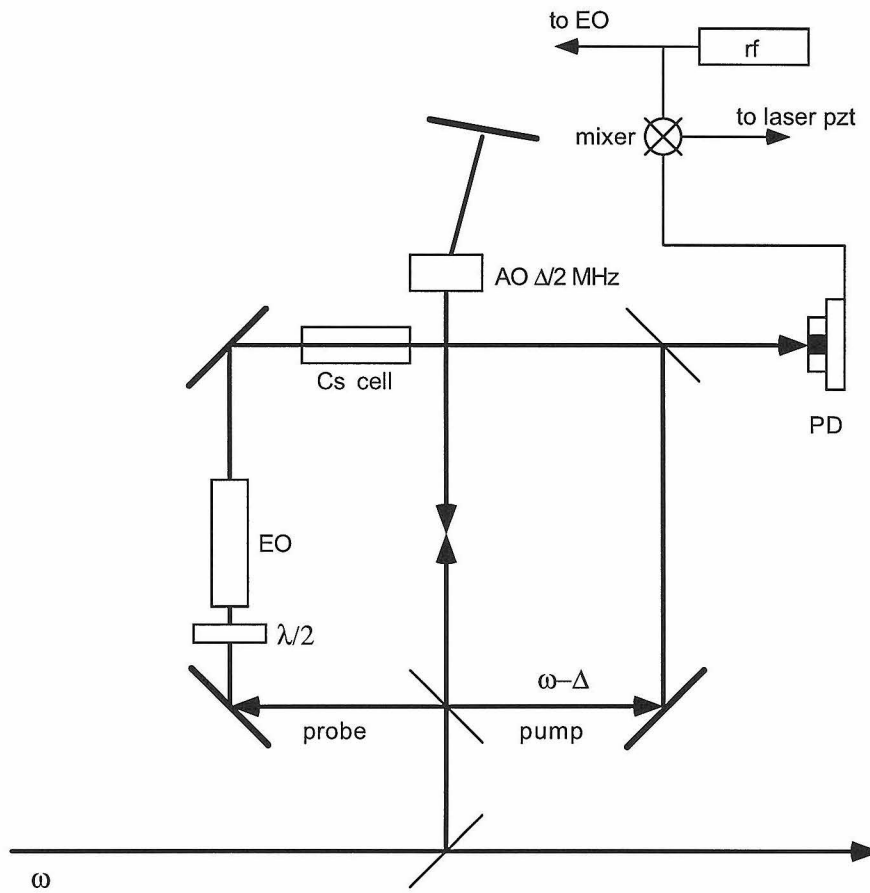

Figure 2.7: Schematic diagram of the FM saturation lock. $\lambda/2$: half-wave-plate. PD: photodiode. EO: electro-optic modulator.

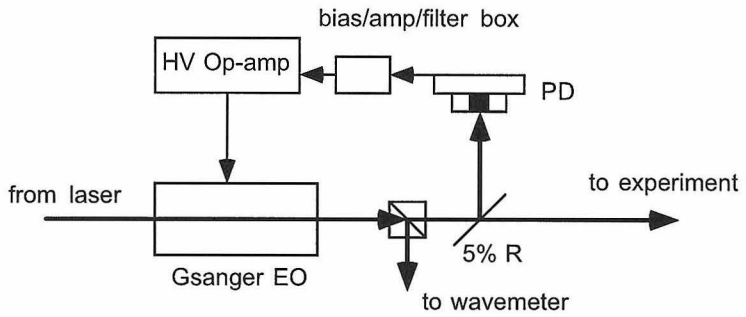

Figure 2.8: Noise-eater. The EO is aligned as a polarization rotator. The through-port of the polarizing beam-splitter is amplitude quiet, while the other port is "noise-enhanced" and is sent to the wavemeter.

2.1.3 The atoms

2.1.3.1 Cs in the abstract

The hyperfine levels of the 852 nm Cesium D2 line ($6S_{1/2} \rightarrow 6P_{3/2}$) are shown in Figure 2.9 along with the transition amplitudes for the various Zeeman sublevels within the $F = 4 \rightarrow F' = 5$ transition. We use the closed transition $m_F = 4 \rightarrow m'_F = 5$ (σ^+ circular polarization) within this manifold. I have alluded to the parameters of this transition, with $\gamma_{\|}/2\pi = 5$ MHz and corresponding excited state lifetime $\tau_a = 1/\gamma_{\|} = 32$ ns. Of course, the advantage of this transition is that it is a two-state transition which in the ideal case cycles indefinitely, without interruptions via decays to other levels. The atoms are optically pumped into the $F = 4, m_F = 4$ level just prior to their entry into the cavity. The degree to which all atoms are optically pumped is important, since the effective coupling is decreased for transitions other than the $m_F = 4 \rightarrow m'_F = 5$ by the transition weight. The effect of imperfect optical pumping and the measurement of the efficiency of the optical pumping will be discussed in Section 2.2.3. The positions of the resonances of the saturation signal (see Figure 2.7 for the optical apparatus) are shown in Figure 2.10, along with the actual laser frequency and the AO frequency to shift back to the frequency of the

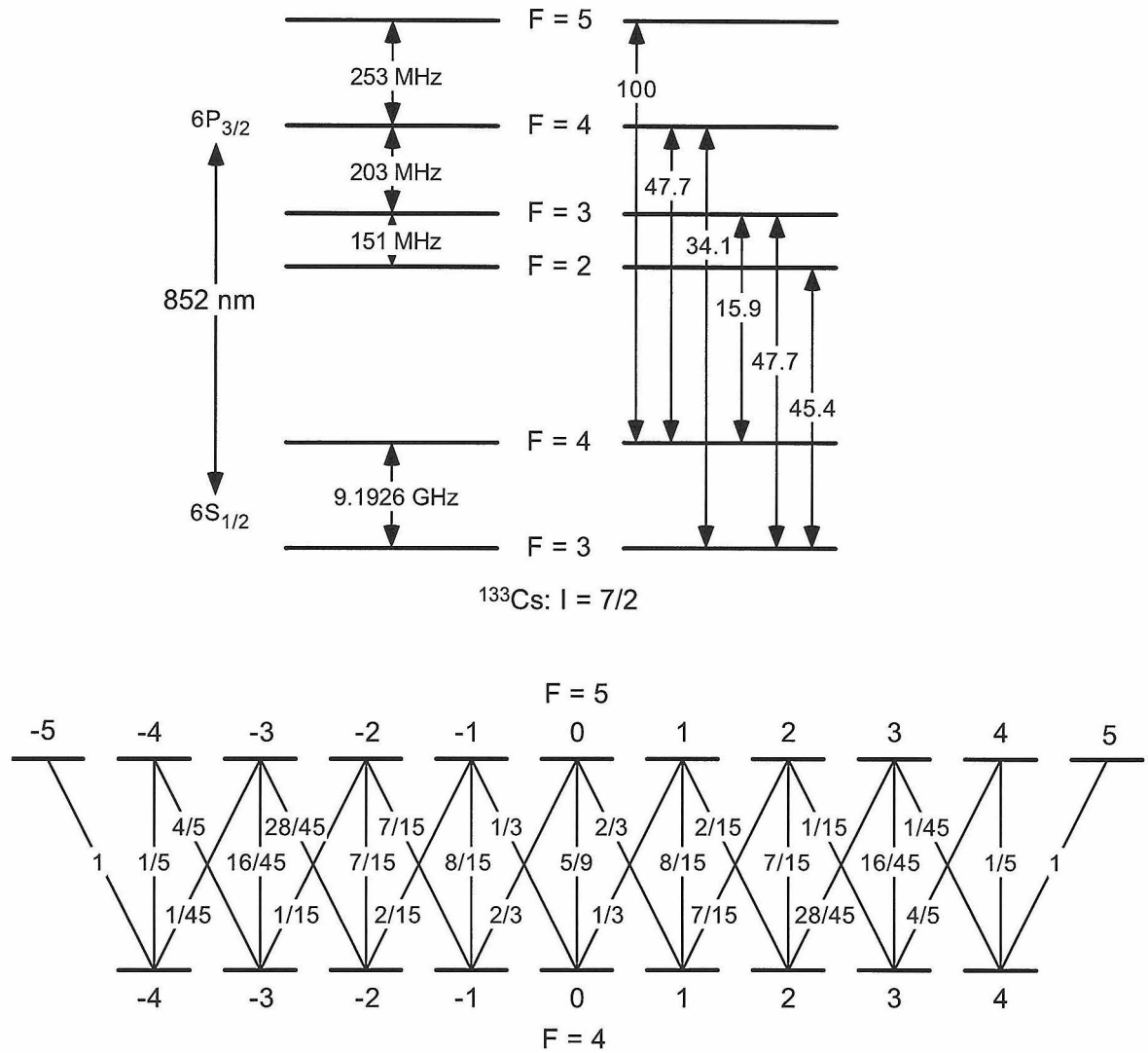

Figure 2.9: The Cs D2 line at 852.360 nm. Upper left, hyperfine level spacings. Upper right, relative transition strengths. Lower, magnetic sublevels for the $F = 4 \rightarrow F' = 5$ transition with transition amplitude coefficients (note that the $\sqrt{\ }$ around each fraction has been omitted).

$F = 4, F' = 5$ transition. The laser is locked via the $F = 4, F' = 3/F = 4, F' = 5$ crossover resonance which is 228 MHz red of the $F = 4, F' = 5$ transition. The saturation AO from the fm saturation lock detunes the pump beam by -88×2 MHz, so that the laser frequency is locked at $\nu_{\rm LO} = \nu_a - 140$ MHz where the frequency of the $F = 4, F' = 5$ transition is ν_a.

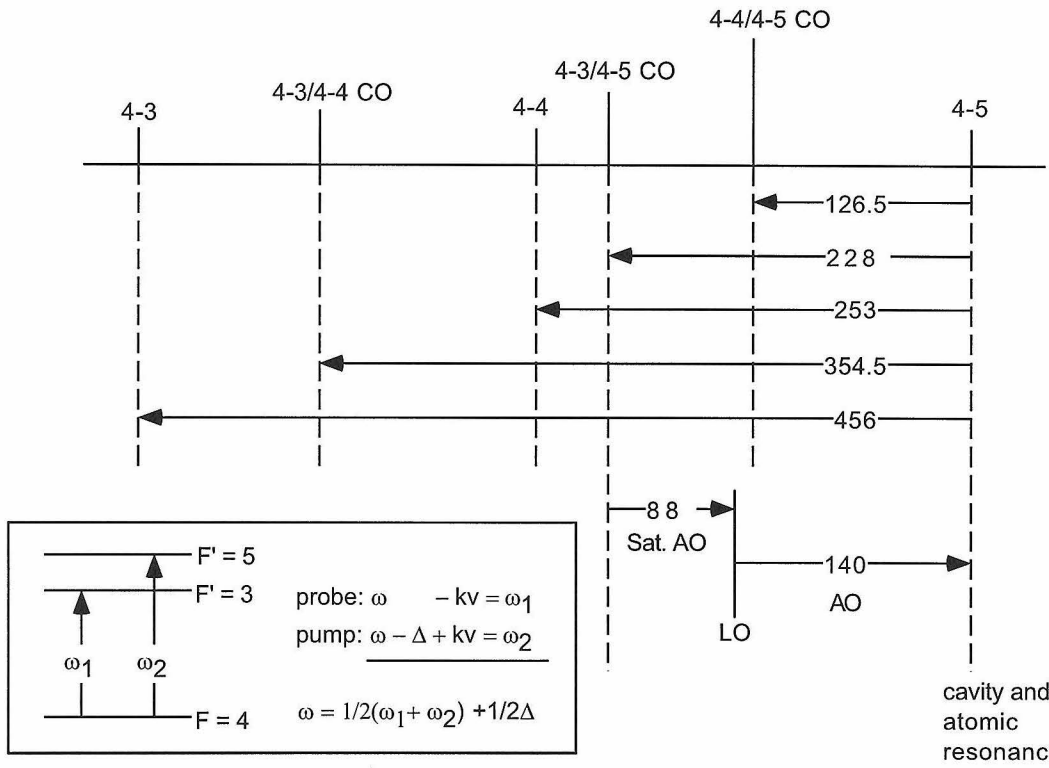

Figure 2.10: A guide to the Cs D2 line transitions from the $F = 4$ ground state. CO: cross-over resonances. The heights of the lines vaguely resemble what might be expected in the lab. The resonance used for the laser lock is the $F = 4, F' = 3/F = 4, F' = 5$ crossover resonance. The inset is a guide to locate the laser frequency in the saturated absorption set-up where Δ is the *double-pass* saturation AO frequency downshift ($\Delta = 88\times$ 2 MHz, also shown in Fig. 2.7).

2.1.3.2 Real atoms from a thermal beam

The experiment is not performed with one single atom sitting stationary at an antinode of the cavity field, but rather with a thermal beam of atoms crossing the cavity mode at a fast rate. Figure 2.11 gives the general idea. The transit time of the atoms

across the cavity mode waist is about 7 atomic lifetimes, so that each atom to a good approximation reaches an equilibrium with the cavity field (remember atomic decay is the slowest rate in our atom-cavity system $\kappa > g^2/\kappa > \gamma_\perp$).

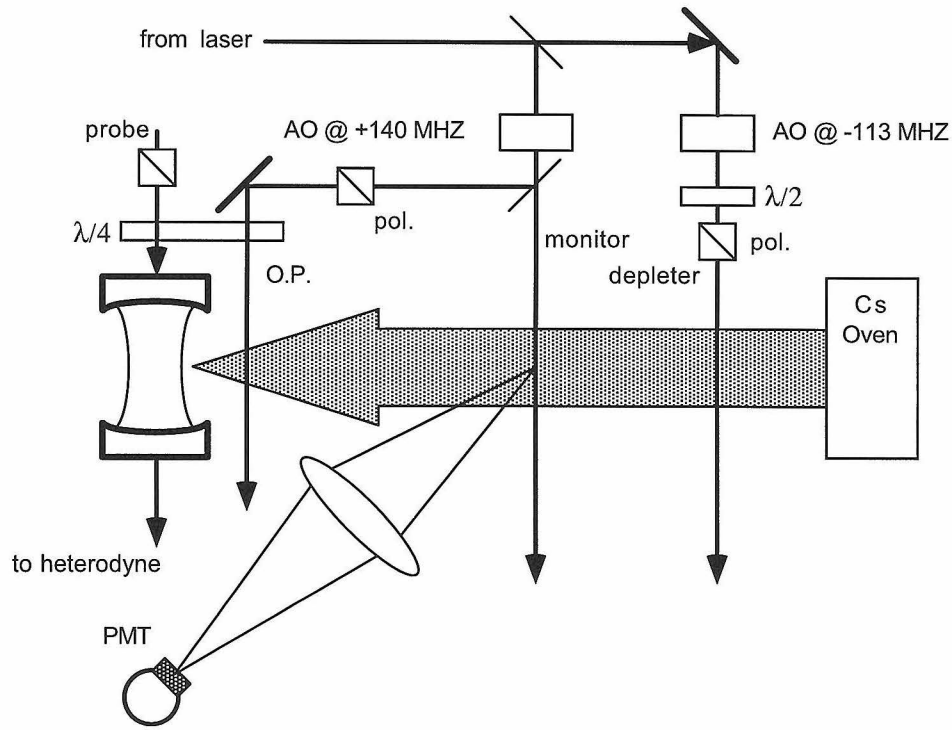

Figure 2.11: The beam. O. P.: optical pumping. 'pol.': polarizer. The half-waveplate/polarizer combination in the "depleter beam" is a variable attenuator.

The atoms are optically pumped into the $F = 4, m_F = 4$ ground state before entering the cavity, as I have already stated. There is a small magnetic field along the cavity axis to define the quantization axis. Two conditions must be met in order that the two-state atoms defined by the optical pumping be the same type of two-state atoms probed within the cavity: The magnetic fields at the two locations must be parallel and in the same plane and the circular polarization of the light in the optical pumping beam must be the same helicity as the light in the cavity. To guarantee that these two conditions are met, two precautions are taken. First, the optical pumping is performed no more than 1 cm from the cavity axis, to assure B-field direction uniformity. Second, both the cavity probing beam and the optical pumping beam

(OP) originate as the same linear polarization, through two polarizers whose axes are carefully aligned to one another, and both beams are converted to circular at the same quarter-wave plate just in front of the cavity (see Figure 2.11). That the linear polarizations of each beam are well aligned is confirmed by removing the quarter waveplate, redirecting the optical pumping beam (with a minimal number of carefully aligned turning optics) along the probe path, crossing the OP polarizer against the probe polarizer for maximum extinction (typically 100:1), and then rotating the OP polarizer back by 90°. Thus, if the probe circular polarization is good (with the quarter waveplate reinserted, see Section 2.1.4), then the OP polarization will also be good and will be an exact replica. Using the same quarter-wave plate also eliminates any need to know in an absolute sense the helicity of the light.

The number of atoms in the cavity mode volume is controlled in two ways. The rough method is with the temperature of the oven. The temperature ranged from 8 to 12 mV on a Type-K thermocouple. It is pointless to convert this to a temperature, because there is no way of knowing how faithfully this represented the actual temperature of the Cs in the reservoir. With the hottest temperature usable (judged by how quickly the oven would fail) we were just barely able to get 2 atoms, on average in the cavity mode. The fine control of the atom number was done with the so-called "depleter" beam (see Fig. 2.11). The depleter beam controls the intracavity atom number by exciting atoms from the $6S_{1/2}, F = 4$ ground-state to the $6P_{3/2}, F' = 4$ excited state, from which they can decay into the $6S_{1/2}, F = 3$ ground state 9.1 GHz away from the $6S_{1/2}, F = 4$ ground state (see Fig. 2.10). Atoms in the $F = 3$ ground state are effectively lost to the experiment. The power of the depleter beam determines the number of cycles an atom makes on the $F = 4, F' = 4$ transition (the branching ratio from the $F' = 4$ excited state to the $(F = 3)$ ground state is 34%), and therefore controls the number of atoms in the "correct" $(F = 4)$ ground state. The fluorescence from the atomic beam is monitored on a PMT about 8 inches from the cavity and 4 inches from the oven pinhole.

The atomic beam actually delivers many atoms in the physical space between the mirrors. In principle, the fundamental mode of the cavity extends to the edges of the

cavity mirror substrates. This creates a rather large volume, which contains far more than one atom at any instant of time. Additionally, the number of atoms between the cavity mirrors is constantly fluctuating due to the Poissonian statistics of a stream of thermal atoms. Needless to say, this situation differs dramatically from the ideal situation that we would like to attain. Careful attention must be paid to this detail in any analysis of the intracavity physics. I have already discussed the idea of an effective number of intracavity atoms N_e in Section 1.3.1. The actual experimental situation is more complicated still, because the detection process averages over many different realizations of N_e to create a composite atom number $\bar{N}$. We will only probe the same physics as the ideal case of one atom fixed to the maximum of the cavity field when it turns out that the distribution giving rise to $\bar{N}$ is dominated by cases in which only one of the many atoms is located within a region of the cavity field in which the coupling is "large" and the other atoms in the sample contribute just a "small amount." I will have much more to say about this in Part II, but I will now discuss the general idea.

2.1.3.3 Fluctuations

Life would be so much simpler if the complications discussed in this section were peripheral to the main subject. Unfortunately this is not the case. The problems of atomic beam fluctuations are, to a greater or lesser extent, present in all the experiments of Parts I and II and have almost exclusively detrimental effects. Much of the formalism presented here was developed by Jeff Kimble, Rob Thompson and myself for the experiment to be described in Part II, but is applicable to the present experiment as well. The notation and tone of this section may be more in line with those of Part II because it is largely plagiarized from there (and a paper in progress [44]).

At the most fundamental level, our experiment is a complex quantum mechanical system consisting of a beam of atoms interacting with a single cavity mode. Ideally, we would like to make predictions of the outcomes of particular measurements on such a system. Quantum mechanically, this is a challenging task. To model our

experiment requires keeping track of a phenomenally large amount of information. For example, even when there is on average less than 1 atom in the cavity mode volume, the response of all "spectator" atoms—those atoms which are weakly coupled due to their location on the skirts of the Gaussian beam waist, or those atoms which are near the nodes of the standing wave field—must be taken into account. Indeed, counterintuitively, it is these very atoms which smooth the otherwise much larger fluctuations in cavity transmission that would occur if one and only one atom were popping in and out of the cavity mode, and hence allow useful observations of single atom effects. But these spectator atoms make a full quantum mechanical simulation extremely costly.

Our initial approach has been to develop a semiclassical model which accounts for fluctuations in number and position of atoms within the cavity mode but which approximates transit time effects by a simple modification of $\gamma_\perp$ (as discussed in Section 2.2.3). The model is equivalent to a full quantum treatment in the weak field linear regime, but is only a semiclassical approximation for strong excitation. The semiclassical model starts with the modified Maxwell-Bloch equations for the cavity field $\hat{a}$, the atomic polarization $\hat{\sigma}_l^-$ and inversion $\hat{\sigma}_l^z$ which are given as follows for the l^{th} atom in a sample of N_s atoms:

$$\begin{aligned}
\langle \dot{\hat{a}} \rangle &= -(\kappa + i\Theta)\langle \hat{a} \rangle + \sum_l g(\vec{r}_l)\langle \hat{\sigma}_l^- \rangle + \varepsilon \\
\langle \dot{\hat{\sigma}}_l^- \rangle &= -(\gamma_\perp + i\Delta)\langle \hat{\sigma}_l^- \rangle + g(\vec{r}_l)\langle \hat{a} \rangle \langle \hat{\sigma}_l^z \rangle \\
\langle \dot{\hat{\sigma}}_l^z \rangle &= -\gamma_\parallel(\langle \hat{\sigma}_l^z \rangle + 1) - 2g(\vec{r}_l)(\langle \hat{a}^\dagger \rangle \langle \hat{\sigma}_l^- \rangle + \langle \hat{a} \rangle \langle \hat{\sigma}_l^+ \rangle),
\end{aligned} \tag{2.14}$$

where $g(r_i) = g_0|\psi(r_r)| = g_0|\exp(-(x^2+y^2)/w_0^2)\sin(kz)|$.

We begin with a series of "tosses" of atoms into the cavity mode. Each toss consists of choosing randomly the (x_j, y_j, z_j) coordinates of N_s atoms and evaluating the mode function $\psi(\vec{r}_j) \equiv \psi_j$ for each atom. The simulation volume V_s contains, and is much larger than the mode volume V_m. In the experiment an atomic beam propagates along $\hat{x}$ and is collimated in the $\hat{z}$ direction by the cavity substrates and uncollimated along

$\hat{y}$. If a snapshot in time is taken, a distribution of atoms is found throughout the space between the cavity mirror substrates. The simulation consists of generating random snapshots and averaging the results of, e.g., a transmission measurement, over many such snapshots. V_s is chosen to be $10w_0$ along the Gaussian waist (x-,y-directions) since coupling outside of this is region significantly reduced. Along the cavity axis (z-direction), it is sufficient to distribute the atoms along only $\lambda/4$ since this covers all possible couplings along the standing wave. For each snapshot, or "toss" an effective number of atoms $N_e = \sum_{j=1}^{N_s} |\psi_j(\vec{r}_j)|^2$ is calculated. Typically, to achieve $N_e \sim 1$ in V_s, $N_s \approx 100$. Simulations with a larger V_s and N_s have been run, with little change in the resulting spectra. From N_e a transmission spectrum is generated using Equation 1.8. The modulus-square of the transmission function ($|T|^2$) generated with each toss is then averaged over a large number $N_t \sim$ 2000–40000 of tosses.[1] Thus, finally produced is an averaged spectrum $Q_a(\omega) = 1/N_t \sum_{i=1}^{N_t} |T(N_{e_i}, \omega)|^2$. Q_a is the result of an overall average number of atoms $N_a \equiv \sum_{i=1}^{N_t} N_{e_i}/N_t$. The experimentally determined number of atoms, I will call $\bar{N}$. If the model discussed here is correct for the experiment, then $\bar{N} \leftrightarrow N_a$.

For linear simulations, Eq. 1.8 is used to generate the appropriate transmission function which is then averaged over a large number of tosses to produce $Q_a(\omega)$. It is clear that $Q_a(\omega)$ will not be identical to a spectrum generated by directly inserting N_a into Eq. 1.8 (and then taking the modulus-square), especially in the case $N_a \sim 1$ when Poissonian fluctuations are relatively large. It could be, however, possible from the definition of N_e and N_a that a given averaged transmission spectrum could be equivalently generated either from a few atoms strongly coupled to the cavity mode or from many atoms weakly coupled to the cavity mode, which is certainly the case for $g_0 \to 0, N_e \to \infty$ with $g_0^2 N_e$ constant. However, for $N_e \sim 1$ this is actually not true, simply because the number fluctuations in the two cases leave observably different signatures on the resultant spectrum. Still, it is worthwhile to pursue this issue in

[1] In principle, it depends on the *measurement type* whether one chooses $|T|^2$ or $|T|$ for averaging. The results can be different. We find that $\langle |T|^2 \rangle$ fits the data better than $\langle |T| \rangle^2$. This will be discussed at greater length in Part II. This point is not found to be very important in our 1-D atom experiment.

more detail, that is, we would like to know the distribution of atoms which contributes to a given experimental or simulated spectrum. Particularly, we would like to know the role of a single nearly optimally coupled atom in a spectrum with $N_a \sim 1$. The impact of a single atom in a cavity with the parameters of this experiment is large. For example, the cavity transmission on resonance changes by a factor $1/(1+2C)^2 \sim 10^{-1}$ when a single optimally coupled atom traverses the cavity mode, so one optimally coupled atom is expected to play a significant role in a given spectrum.

Let us continue this pursuit. We define a region in the space between the two mirrors of volume V_g in which an atom will have a coupling greater than a certain fraction of the optimal coupling, $g(r) > \epsilon_g g_0$ for $r \in V_g$ (in which case the "coupling" volume $V_g = \epsilon_s V_s = \epsilon_m V_m$). Now for each toss of atoms (N_s is chosen to give $N_e \sim 1$) we count the number of atoms N_g in V_g and keep track of those cases in which exactly 1 atom appears in V_g ($N_g = 1$), when no atoms at all appear in V_g ($N_g = 0$) and when two or more atoms are present in V_g ($N_g \geq 2$). For most of the simulations, we choose V_g such that $|g(r_i)|^2 > (0.56)^2$ which corresponds to $V_g = V_m \equiv (1/4)\pi w^2 l$. The result of such a tracking is histogrammed in Fig. 2.12 and shown along with the sum of all contributions. We show the distributions for $N_a \approx 1.0$ (top) and $N_a \approx 0.5$ (bottom) for parameters of cavity #3. In Fig. 2.13 we show the corresponding averaged spectra, with the contributions to the overall spectra shown for the same breakdown as in Fig. 2.12. Contrast the averaged spectrum with a spectrum due to a single atom optimally coupled to the cavity mode with $C = N_a C_1$ in Figure 2.14.

Several comments are in order at this point.

1) For $N_a = 1$, the breakdown in numbers is: $N_g = 0$ occurs in 38% of the tosses, $N_g = 1$ occurs in 35% of the tosses and $N_g = 2$ occurs in 28% of the tosses. For $N_a = 0.5$, the breakdown in numbers is: $N_g = 0$ occurs in 62% of the tosses, $N_g = 1$ occurs in 29% of the tosses and $N_g = 2$ occurs in 10% of the tosses. This is just the way it works out for our choice of V_g. I think the most important aspect here is the contribution to the spectrum from those tosses in which there are two or more atoms in V_g. For $N_a = 1$, this occurs with a frequency comparable to that of the $V_g = 1$ case and the contribution to the spectrum is non-negligible. For $N_a = 0.5$ it occurs quite

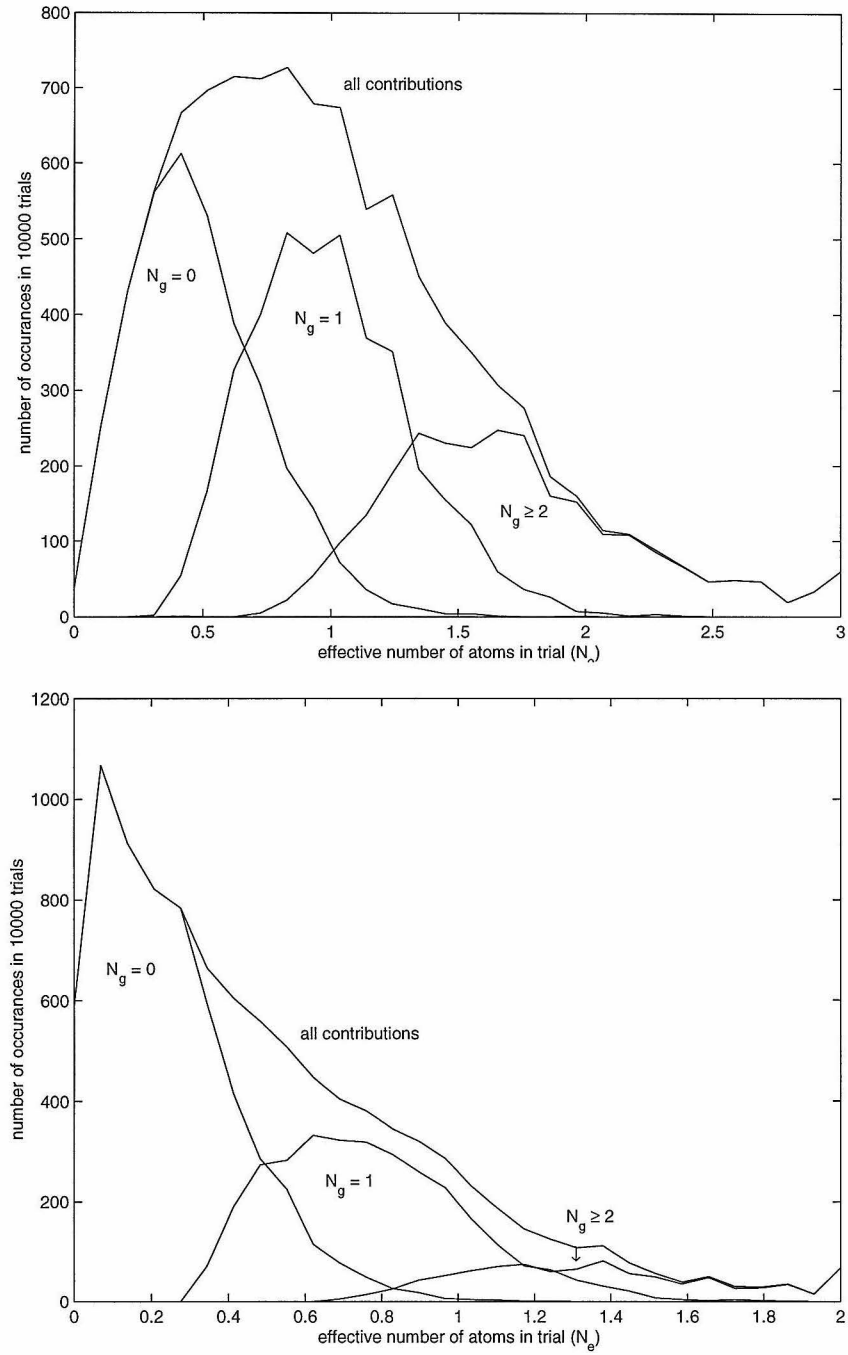

Figure 2.12: Occurrences of mode volume (V_g) occupation N_g (as discussed in the text) for typical 10000 trial simulation of $N_a \approx 1.0$ (top) and $N_a \approx 0.5$ (bottom).

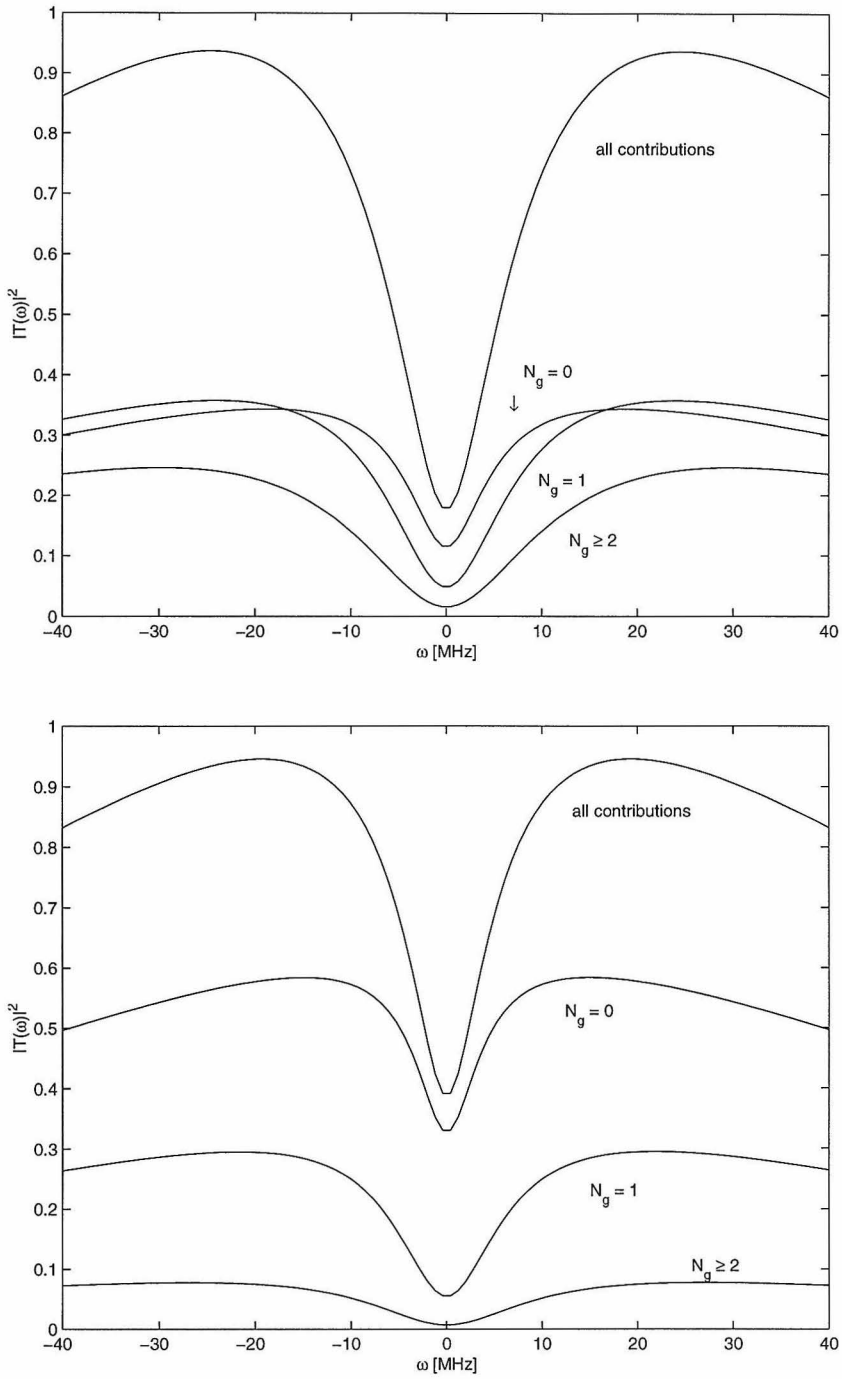

Figure 2.13: Breakdown of the contributions of various numbers of atoms in the cavity mode volume (as discussed in the text) for two different average intracavity atom numbers. In each graph is shown the full simulation (sum of all contributions), the contribution with exactly one atom in the mode volume, the contribution with no atoms in the mode volume, and the contribution with 2 or more atoms in the mode volume. Graph (top) has $N_a \approx 1$ atom and graph (bottom) has $N_a \approx 0.5$ atoms. The atom-cavity parameters are those of cavity # 3 from Table 2.1.

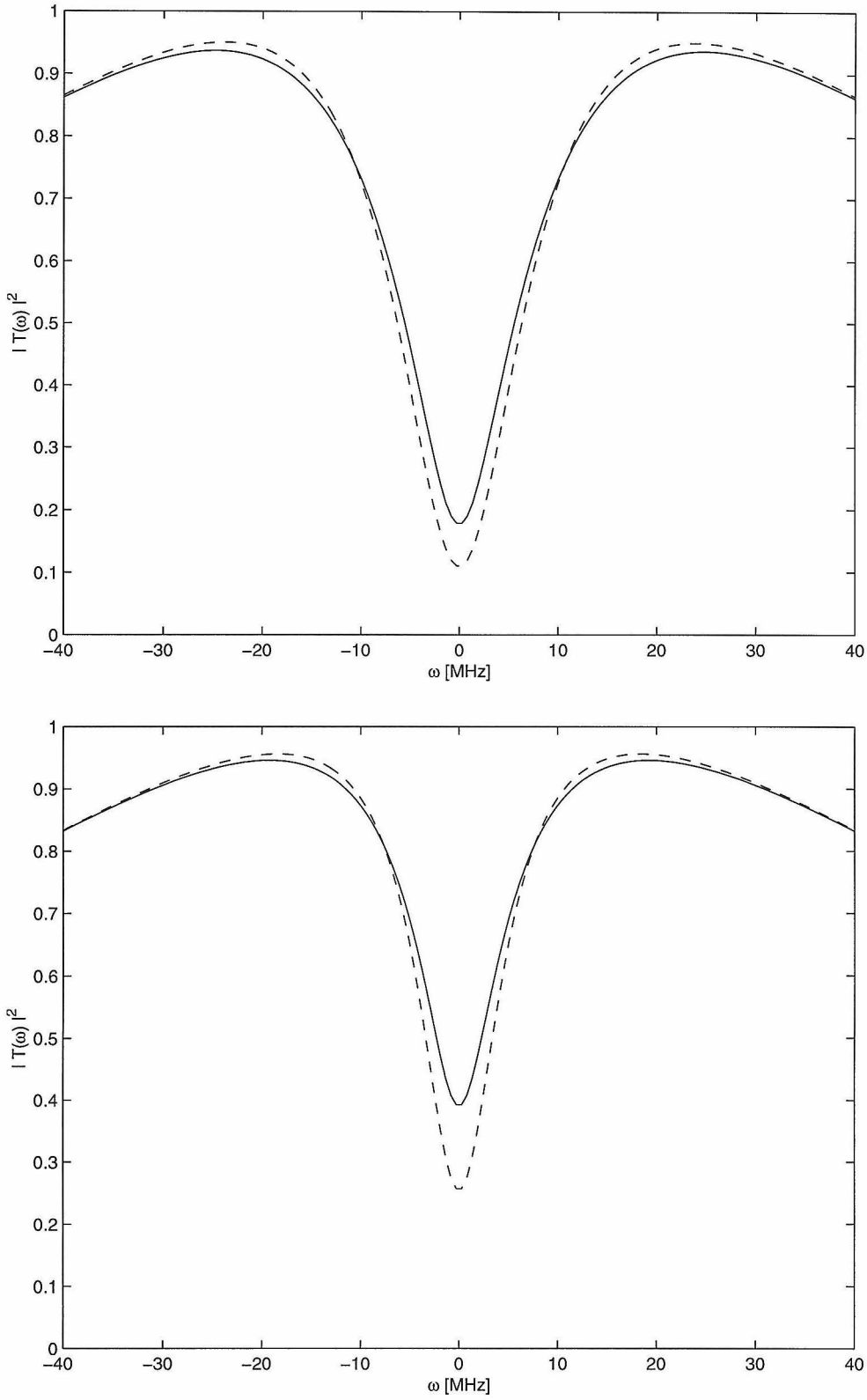

Figure 2.14: Comparison of the averaged spectrum for N_a atoms the and optimal spectrum with $C = N_a C_1$. The solid curves are the averaged spectra and the dashed curves are the optimal spectra. The top graph has $N_a = 1$ and the bottom graph has $N_a = 0.5$. Atom-cavity parameters as in Figure 2.13.

infrequently and correspondingly its contribution to the overall spectrum is small.

2) It can be seen in Fig. 2.13 that there is a significant contribution from the case in which there are no atoms in V_g. During the times when there are no atoms in V_g, there are still $N_s \sim 100$ atoms in the simulation. These spectator atoms play a critical role in keeping the empty cavity from dominating the transmission spectrum. That is, even when there are no atoms in V_g, there is still a spectrum whose dip implies an effective average number of atoms only slightly less than N_a.

3) I alluded to an important question above: to what extent does a spectrum generated by averaging over tosses, such as $Q_a(\omega)$ represent an optimal coupling case such as $|T(\omega)|^2$? To answer this question I have performed a least-squares fit to $|T(\omega)|^2$ on the simulated "data" of $Q_a(\omega)$. The free parameter of the fit is the number of atoms inferred from the "data" N_i. The relative accuracy with which the fit predicts N_a depends on atom number with $N_i \to N_a$ as $N_a \to \infty$. The fit converges to within 15% at $N_a = 1$ atom, with $N_i/N_a = 0.87$ at $N_a = 1.05$. For the record: $N_i/N_a = 0.79$ with $N_a = 0.48$ and $N_i/N_a = 0.65$ with $N_a = 0.10$. In what follows, I use exclusively the *unaveraged* transmission function $|T(\omega)|^2$ to determine $\bar{N}$ from the experimental data. This means that I may be systematically underestimating the number of atoms by 15% at $\bar{N} \sim 1$. I believe that other uncertainties dominate this systematic offset. Also, there is no guarantee that the simulations correctly model the experiment at the 15% level. All in all, I do not consider this to be a significant problem, but I mention it for the record.

2.1.4 Probe beam generation

In order to probe the cavity over a wide range of frequencies, a probe beam tunable independently of the lock beam, other auxiliary beams and the heterodyne local oscillator is needed. Additionally, it must be a clean beam, free of contamination at frequencies other than the one of interest, and it must be scannable over a wide frequency range without beam steering. We achieve this by detuning a beam directly from the laser with AO's and generating a sideband in a a travelling-wave electro-optic

modulator (TWM). It is the sideband, tunable by rf drive at the desired frequency that is used as the probe beam. Figure 2.15 shows the optical set-up. Since sidebands are typically 10% of the carrier power, it is essential to keep the carrier very far detuned from resonance in order that it not affect the atom-cavity physics. This is especially true at high probe powers, where the nonlinear coupling between photons of different frequencies can be quite strong.[2] If both carrier and probe are well in the weak field, then the presence of the carrier should not affect the probe measurement, as this is essentially the definition of the weak-field (linear) regime.

The exact choice of detunings, AO's and laser lock frequency was mainly driven by availability of AO's and rf drivers, so it should not be assumed that this is an optimal arrangement. Originally, the TWM input beam was upshifted by a single double-passed 200 MHz AO, with the upper sideband placed on resonance by a 260 MHz drive on the TWM (recall that the laser is already 140 MHz below resonance). This proved to be inadequate for strong-field measurements, so two double-passed AO's were set to detune by $\nu_{\text{probe carrier}} = \nu_{\text{LO}} + 800$ MHz as shown in Figure 2.15. Thus, a resonant probe was generated with an rf drive of $\nu_{\text{TWM}} = 640$ MHz into the TWM. The double polarizing-beam-splitter (PBS) configuration shown in Figure 2.15 was used to avoid contamination of the probe beam from the unshifted input laser beam. The polarizations are explained in the figure caption.

The polarization of the probe beam must be good circular in order that the two-state atom be realized (a contaminating component of orthogonal polarization will drive the atom out of the cycling transition). The probe originates s-polarized through its polarizer (labelled 'pol.' in Fig. 2.15) and then propagates through a quarter-wave plate. Fidelity of circular polarization is measured by backreflecting the probe beam through its quarter-wave plate and polarizer and compensating the waveplate for maximum extinction. Typical extinction was 100:1. On the output side, the original input linear polarization must be reconstructed. A polarizing beam splitter on the output side (not shown) is aligned to reflect s-pol, and the reflection is maximized by rotating the output waveplate.

[2] A well-controlled photon-photon "coupling" is the basis of the experiment of Chapter 4.

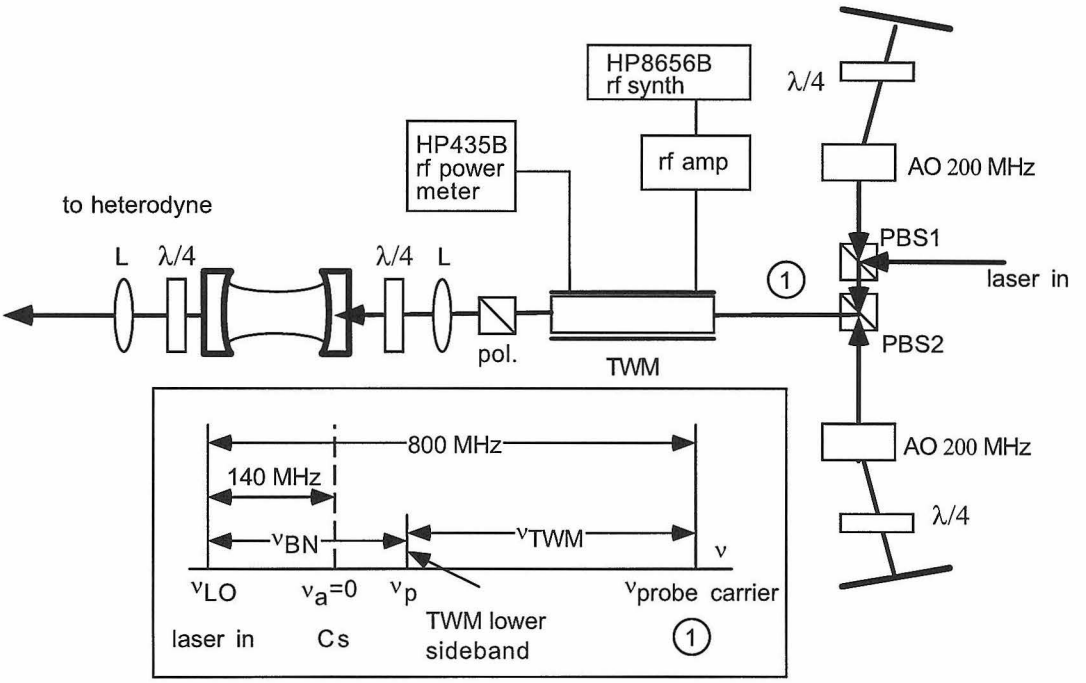

Figure 2.15: Probe field generation schematic. The 'laser in' is s-polarized (s-pol), reflects from PBS1 is upshifted by the AO, on the return path through the AO the beam is rotated to p-pol via two passes through the quarter-wave plate ($\lambda/4$). This p-pol is transmitted through PBS1 and 2, double-passed and rotated so that the resulting $\nu_{\rm LO}+$ 800 MHz beam is s-pol and reflected from PBS2 towards the TWM (at point 1). The tunable sideband frequencies are shown in the inset. The "probe beam" at frequency ν_p is the lower sideband of the TWM and is ultimately detuned from resonance by $\nu_p = 800 - 140 - \nu_{\rm TWM}$ MHz. The probe creates a beatnote on the heterodyne detectors of $\nu_{\rm BN} = 800 - \nu_{\rm TWM} = 140 + \nu_p$ MHz.

2.1.5 Detection

The essential job in spectroscopy of the atom-cavity system is to detect the light which has built up in the cavity and leaks out the output coupler (mirror M_2). We detect either the outgoing *field amplitude* via a balanced super-heterodyne detector, or count the outgoing photons on an avalanche photo-diode photon-counting module. The only difficulties in this procedure are attaining high quantum efficiency η_q and detecting the rather low levels of light in the cavity output beam. To get an idea of the light powers involved, I will consider a typical experiment. It is rare that we desire to have more than about one intracavity photon, and in fact in order to probe in the weak field, we operate several orders of magnitude below m_0, often at $\bar{n} \sim 10^{-4}$. (We drive the system so that the steady-state intracavity photon number is $\bar{n} \equiv \langle a^\dagger a \rangle = 10^{-4}$, leading to a steady rate of output photons.) The output photon flux associated with this intracavity photon number is essentially the average number of intracavity photons times the rate at which the photon hits the output mirror times the transmission of the output mirror: $\bar{n}\nu_{\rm FSR}\delta_2 \sim 10^{-4} \times 3 \times 10^{12} \times 3.5 \times 10^{-4} \sim 10^5$ photons/sec. This corresponds to an output power at 852 nm (photon energy $E_{\rm phot} = 1.455$ eV) of P_{sig} ~25 fW.

2.1.5.1 Photon counting

I used photon counting only rarely, once in the early phases of the nonlinear spectroscopy (see Part II) and then later to verify calibration of the heterodyne detectors (see Section 2.1.5.3). 10^5 photons/sec is nearly to the point of saturation of our modules, so the low light levels pose no problem. Measured quantum efficiency was $\eta_q \sim 23\%$.

2.1.5.2 Heterodyne detection

The basic idea of heterodyne detection is to amplify a low-level signal beam by multiplying it against a strong (typically a few mW) local oscillator (LO) beam. In the case of heterodyne detection, the two beams are detuned from each other by a ra-

dio frequency offset, overlapped on a beam splitter and sent to a fast photo-diode. Written into the photo-current is a signal at the offset frequency, known as the beat-note, which represents the field amplitude of the signal beam. We use a balanced heterodyne scheme as depicted in Figure 2.16 for two reasons: first, in the difference photo-current I_- it cancels technical noise on the LO (in the absence of a signal beam), and second, it collects all of the signal beam while avoiding the need to use a very strong LO behind a $R = 99\%$ beam-mixing optic.

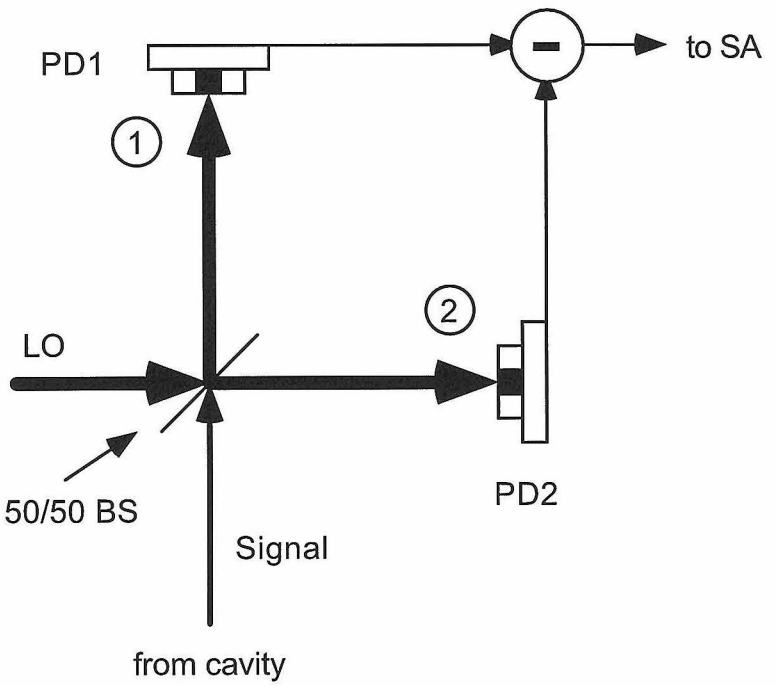

Figure 2.16: A balanced heterodyne detector.

The naive mathematics of heterodyne detection is simple, but has been a source of confusion in terms of exactly what noise immunity the balanced setup provides.[3] Following the numbering of Figure 2.16, we start with the local oscillator (LO) field at the optical carrier frequency ω: $\mathcal{E}_{\rm LO} \equiv (\mathcal{A}_{\rm LO} + \mathcal{N}_{\rm LO}(t))e^{-i\omega t}$ where $\mathcal{A}_{\rm LO}$ is a noiseless

[3]H. Mabuchi first pointed this out to me.

steady amplitude and $\mathcal{N}_{\rm LO}(t)$ is the noise on the LO. The signal field is similarly represented as $\mathcal{E}_{\rm s} \equiv (\mathcal{A}_{\rm s}(t) + \mathcal{N}_{\rm s}(t))e^{-i(\omega+\Delta)t}$, where $\mathcal{A}_{\rm s}(t)$ is the envelope of the (steady-state) signal field detuned from ω by rf frequency Δ and the noise on the signal is not necessarily correlated with that of the LO. The beam-splitter imparts a phase shift of π *between* the outputs of the signal, but not the LO, (or vice-versa, as this choice would an irrelevant overall phase). The output field of port 1 of the beamsplitter is $\sqrt{2}\mathcal{E}_1 = \mathcal{E}_{\rm LO} + \mathcal{E}_{\rm s}$ while out port 2 comes $\sqrt{2}\mathcal{E}_2 = \mathcal{E}_{\rm LO} - \mathcal{E}_{\rm s}$. The photo-diode is a square-law detector, and we take the difference of the two photo-diode outputs to get the difference photocurrent $I_- \propto \mathcal{E}_1^\dagger\mathcal{E}_1 - \mathcal{E}_2^\dagger\mathcal{E}_2$. Skipping the algebra, we find

$$\begin{aligned} I_- \propto\ & \mathcal{A}_{\rm LO}^\dagger\mathcal{A}_{\rm s}(t)e^{-i\Delta t} \\ & + \mathcal{A}_{\rm LO}^\dagger\mathcal{N}_{\rm s}(t)e^{-i\Delta t} \\ & + \mathcal{N}_{\rm LO}^\dagger(t)\mathcal{A}_{\rm s}(t)e^{-i\Delta t} \\ & + \mathcal{N}_{\rm LO}^\dagger(t)\mathcal{N}_{\rm s}(t)e^{-i\Delta t} + \text{H.c.} \end{aligned} \tag{2.15}$$

Now, in the traditional treatment, it is assumed that $\mathcal{A}_{\rm LO} \gg \mathcal{A}_{\rm s}, \mathcal{N}_{\rm s}$ which is certainly true, and also that $\mathcal{N}_{\rm LO} \ll \mathcal{A}_{\rm LO}$, which is not necessarily true. If these limits hold then the only term left from Eq. 2.15 is the first (and its Hermitian conjugate). This term is the traditional beatnote between the LO and the signal which oscillates at the rf-frequency Δ. Technical noise from the local oscillator is ignored, since it multiplies the very small signal amplitude. However, in the case where the noise on the local oscillator is some non-negligible fraction of its amplitude, then the noise of the LO is *not* cancelled in the balanced heterodyne, since it beats with the amplitude of the signal (producing a contribution to the total beat-note given by the third term). In most of the experiments here, this is a small contribution which is ignored, as the noise on the LO tends to be less than 10% of its amplitude, localized to frequencies below 400 Hz. Noise on the signal, on the other hand, (from various sources) is a noticeable effect (it contributes to the beat-note via the second term of Eq. 2.15), and will be discussed where necessary.

Of course, the heterodyne detector has non-unit detection efficiency, and is not exactly balanced, which leads to some degradation in performance. There is a complete discussion of the faithfulness of the shot-noise in a slightly imperfect balanced homodyne setup in Ref. [52]. The balancing can be disrupted by an imperfect beamsplitter, different photo-response in the diodes and different subsequent photo-current amplification, and phase mismatch in the rf photo-current at the subtraction junction. By making detectors as similar as possible and choosing equal cable lengths, phase turns out to be a minor problem at the relatively long wavelengths of our typical 140 MHz beat-note. To test the balancing, AM modulation is directly applied to the LO. Blocking one of the arms of the heterodyne unbalances the detection, so the AM beat-note appears in the photocurrent. The suppression for the balanced detector ranged from 20–40 dB over several measurements at the central beat-note frequency. (Remember, this has nothing to do with the heterodyne response, only its immunity to technical noise on the LO. There are many other sources of noise which tend to dominate over this contribution anyway.) The upshot is that the unbalances in our heterodyne do not degrade significantly the types of measurements that we make, in which we are simply measuring the optical power of the cavity output. The circuit diagram of the heterodyne detectors is shown in Fig. 2.17.

It is crucial to know the overall quantum efficiency of the balanced heterodyne detection so that we can infer accurately the intracavity photon number from measurements of the beat-note size. There are two numbers that contribute to the overall heterodyne efficiency: the quantum efficiency of the diodes themselves η_q, and the overlap of the output probe beam and the local oscillator ϵ^2. The photodiode quantum efficiency is the ratio of the number of photo-electrons produced to the number of photons incident on the photo-diode; for $\eta_q = 1$ every incident photon produces a measurable photo-electron (our diodes have typically $\eta_q = 0.85$). The overlap efficiency is given by an integral over the modes of the signal and LO beams at the detector $\epsilon^2 = |\int_{\text{det.}} d^2r\, u_{\text{LO}}(r) u_{\text{sig}}(r)|^2$. The signal beam and local oscillator must be made to occupy the same spatial mode; they must match in size and curvature. The output of the cavity is a clean, single-mode Gaussian beam collimated by the output

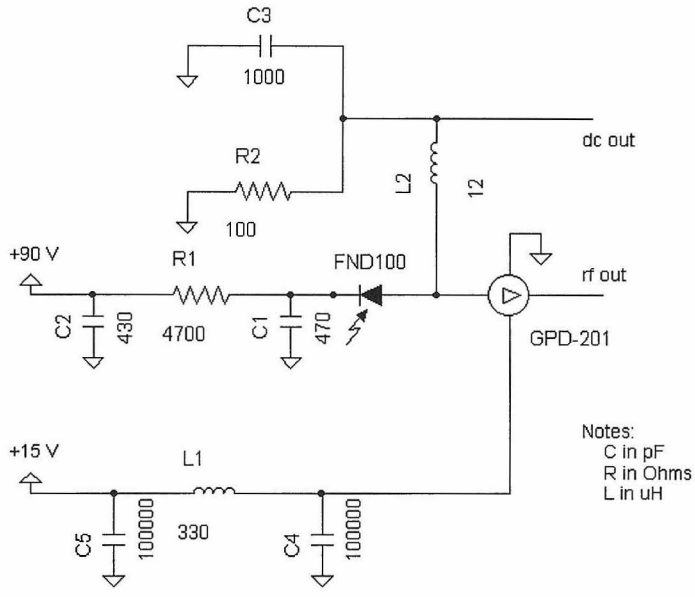

Figure 2.17: Heterodyne detector schematic.

lens. However, the LO propagates through many optical elements on its way to the heterodyne. Care must be taken to keep the LO beam spatially clean and to match its size and shape to the cavity output. In later experiments, we built a cleaning cavity into the LO, but this is not essential for decent (80%) overlap.

The overall detection efficiency is measured in both a heterodyne configuration and in a homodyne arrangement to confirm the accuracy of the heterodyne measurement. From day to day, the heterodyne efficiency is determined by the heterodyne method, since it requires relatively less complication. The essential idea of the detection efficiency measurement is to measure the response of the detector to a known input power. The method is as follows: the power in the cavity-lock beam is set so that the output power through the cavity is $P_l \sim 50$ nW. This choice is a good one, since it is large enough to measure the power on a good power meter, but not so large that it saturates the detector rf amplifiers for a typical LO power of 5 mW into the beam-splitter (2.5 mW on each detector). The LO is set at the 5 mW level so that the detectors are not near saturation (this occurs at 5 mW per detector) yet

so that the shot noise actually comes up above the electronic noise of the detectors. At this LO power, the shot noise is not much more than 5 dB above the electronic noise. Since this tends to underestimate the size of the shot noise, a correction must be applied to derive the true shot-noise level. In addition, due to the nature of the measurement made by the spectrum analyzer, a 2 dB correction to measurements of noise powers must be made.[4] The shot noise level is recorded, and the size of the coherent beat-note from the 50 nW locking beam is recorded. The efficiency is given by:

$$\eta_q \epsilon^2 = D^2 \frac{E_{\text{phot}}}{P_l} B \tag{2.16}$$

where D^2 is the *power* ratio for the photo current between the rms beat note power in the calibrating beam and the rms power in the shot noise (corrected for electronic noise and the 2 dB SA noise measurement correction), and B is the detection bandwidth in Hz. The efficiency measurement was usually performed at 1 or 10 kHz resolution bandwidth (RB). In practice, the measurement procedure is: measure the power of the locking beam as transmitted through the cavity P_l (on the UDT power meter); block all light to the detectors, measure the noise level on the spectrum analyzer, this is the so-called electronic-noise P_{EN}; unblock the LO, the noise level registered by the SA rises above P_{EN}, record this level as well, this is the shot-noise P_{SN}; unblock all paths to the detector and measure the power in the coherent beat-note on the SA, this is P_{BN}. On a typical day, the numbers for this are: $P_l = 8.5/0.8$ mW, $P_{\text{BN}} = -11.8$ dBm, $P_{\text{SN}} = -85.5$ dBm, $P_{\text{EN}} = -91$ dBm, RB = 1 kHz, which gives $\eta_q \epsilon^2 = 0.45$ (see Appendix B.2). This efficiency is typical, though measurements were made with efficiencies from 25% up to 70%. Once the efficiency is known, a beat note power in dB above the shot-noise can be converted to a photon flux incident on the balanced detector assembly which can then be converted to an inferred intracavity photon number (see Appendix B.3). In this way, intracavity photon numbers as low as 10^{-6} are easily resolved in reasonable integration time. (Of course one of the niceties of

[4]This is described in the HP spectrum analysis technical note: *Spectrum Analysis Basics*, AN-150, 1989. Note that the 2.0 dB correction is only for log scale measurements, there is a different correction in linear scale. See also Ref. [53].

shot-noise limited detection is that in principle *any* flux of photons can be measured with sufficient patience.)

The heterodyne efficiency measurement is subject to inaccuracy, due mainly to one's ability to measure the actual noise power in the shot-noise on the spectrum analyzer. A consistent and correct procedure must be strictly followed. To confirm that this efficiency measurement procedure was indeed correct, it proved imperative to compare it to one that is more direct. This comes in the form of the homodyne measurement, which amounts to measuring a fringe visibility in an optical interferometer. In homodyne detection, the frequencies of the signal beam and the LO are degenerate (and of equal power), thus perfectly overlapping beams will interfere depending on the relative phase at the beamsplitter. By deliberately scanning the phase of the LO by translating a mirror on a PZT, interference fringes are observed. The visibility of the fringes then gives a measure of ϵ^2, so that knowledge of the quantum efficiency of the diode (86% at 852 nm for the FND-100) gives the overall detection efficiency. Measurements of the efficiency (nearly) simultaneously via the heterodyne and homodyne methods gives agreement to within 5–10%. The heterodyne method gives a systematically slight underestimate relative to the homodyne method.

Of course, the calibration via heterodyne relies on absolute knowledge of the power. Thus one must have a reliable power meter. I began to suspect our UDT power meter (the lab workhorse at the time) of inaccuracies. We also have a thermopile meter (EPPLY) with a relatively recent NIST calibration, so I did a comparison of the two power meters. The results are shown in Figure 2.18. The Epply meter cannot be used directly in the heterodyne calibration since it is fairly difficult to read anything below 100 μW. The net result was that the UDT was reading around 20% low. This correction was applied to all subsequent efficiency measurements (that is, virtually everything in this thesis).

The hassles involved in heterodyne measurement are far outweighed by its merits. Primarily, these are insensitivity to background light and frequency selectivity. In order for the heterodyne to respond to incoming light, that light must be well matched to the LO and share the same polarization as the LO. This effectively removes any

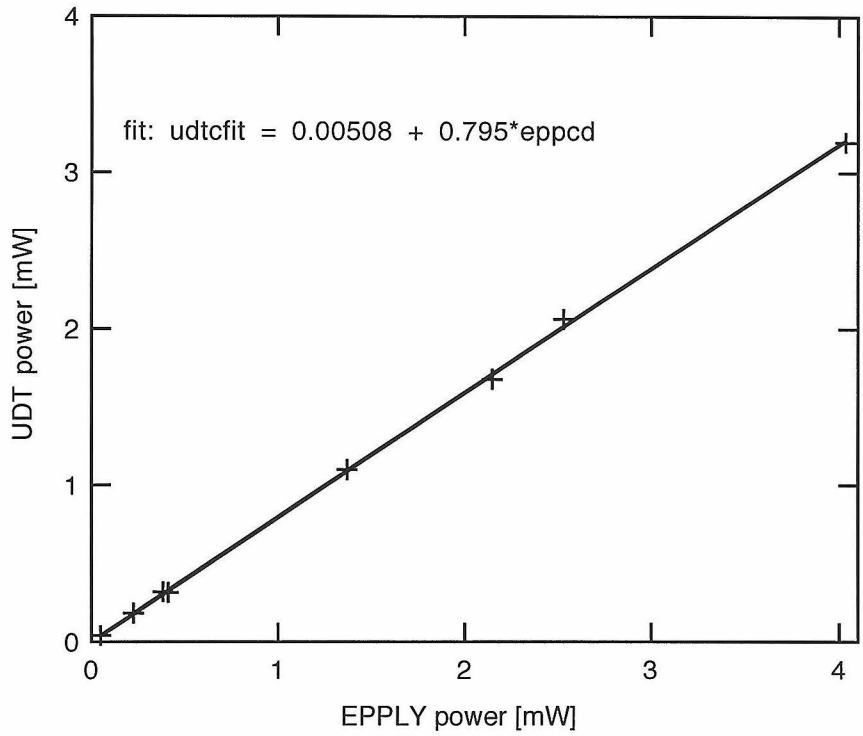

Figure 2.18: Calibration of the UDT power meter against the EPPLY thermopile. The '+' are the data, the solid line is a least-squares fit with slope 0.80.

problems with stray light. A photon counter on the other hand, is very sensitive to stray light and heroic measures must be made to eliminate background sources. The heterodyne detector has nearly arbitrary frequency selectivity. If the measurement is one of a steady-state property, which nearly all of ours are, then the bandwidth of detection can be centered on the signal and narrowed until limited by noise in the offset-frequency (probe) generation.

For our probe beam, the beat-note was, rather surprisingly (given the quoted specifications of what I believe to be the limiting element in the probe generation chain, the AO driver), found to be stable at 100 Hz resolution bandwidth (RB). (The RB is the frequency bandpass filter applied by the SA to the input signal.) Here, stable is defined by the following measurement: The beatnote is observed by scanning the spectrum analyzer across the appropriate frequency and monitoring the peak height. The RB is made smaller and smaller and the peak height is observed not to change, as is expected for a coherent rf signal whose inherent bandwidth is

narrower than the RB. Eventually, the peak height does drop as the RB and the excursions of the source become comparable. This does not happen until the RB is at or even below 100 Hz. This is entirely adequate for our purposes.

With narrow-band detection such as we use, it is critical that the detection frequency (of the SA) and the actual frequency of the probe be chosen compatibly. Nominally speaking, the SA should be set to a center frequency $\nu_{\mathrm{SA}} = \nu_{\mathrm{BN}} = 800 - \nu_{\mathrm{TWM}}$ MHz (see Section 2.1.4 and especially Figure 2.15 as well as Section 2.1.6). Clearly, this is not a sufficiently accurate specification of the offsets for 1 kHz RB detection, as the nominal 800 MHz could really be 800.01 MHz. In other words, the exact detuning between the LO and the probe must be known, as well as any offsets in the SA. This is accomplished by fine (as small as 10 Hz) adjustment of the TWM frequency. The technique is to fix the SA center frequency and simply to observe the beatnote at a narrow rf bandwidth (1 kHz) and to adjust the TWM frequency to maximize the detected signal. It is important not to confuse the real maximum with a local maximum due to sidebands at the lock dither frequency. Typically, this offset ($\sim$ 6 kHz) is constant over the course of a night's run, but must be adjusted from day to day.

Finally, I mentioned in Section 2.1.1.2.5 that we chop the cavity locking beam on and off and take data only during the lock "off" cycle. This is accomplished by synchronously chopping the rf photocurrent from the heterodyne detectors before it gets to the SA. If the signal is not chopped, then (1) the output from the cavity lock beam will be averaged into data during the lock "on"/data "off" periods if we are near resonance with the probe, and (2) we will average contributions from the probe beam during the lock "on" cycle, which is probing the atom-cavity under undesirable circumstances. There is no way to "hold" the SA, it averages continuously, so chopping the signal rf is the only option. By chopping the signal, we average the probe field with the shot-noise. This could make the conversion from SA beat-note size to intracavity photon number problematic. However, we have a direct empirical method for extracting the proper quantity. After measuring the heterodyne efficiency as outlined above, we chop the rf signal (in this case the lock beam beat-note) without

actually chopping the light itself. We know the flux incident on the heterodyne from the measurement of $P_l \sim 50$ nW, and we now have a new, *averaged* (over the data/lock chop cycle) beat-note with which to calibrate the intracavity photon number. Thus when it is the probe that the heterodyne is measuring, we have an intracavity photon number as if the probe were continuously monitoring the correct atom-cavity physics, which is exactly the quantity we need.

2.1.5.3 Direct comparison of heterodyne and photon counting

As a final act of confirmation of the validity of the heterodyne efficiency, we compared the flux inferred from the heterodyne to that measured on an APD photon-counting module. The experimental procedure for the photon-counting data acquisition is somewhat complicated. We followed the procedure from Refs. [7, 48], so I will not go into the details here. The results were quite good, and are shown in Figure 2.19. From the fit, there was an overall error at extrapolated zero flux of 3000 photons/sec. The slope was 0.74, with the heterodyne inference on the low side relative to the photon count inference.

2.1.6 Summary of the probe generation and detection chain

Now that all the pieces are in place, I would like to summarize the myriad beams and frequency offsets of the probe generation and detection chain. The laser is locked such that its direct output can be used as the heterodyne local-oscillator (LO). Its frequency, defined as ν_{LO} is 140 MHz below the $F = 4 \leftrightarrow F' = 5$ transition within the Cs D2 line. Thus, $\nu_{\mathrm{LO}} = \nu_a - 140$ MHz, where ν_a is the atomic transition frequency. The probe beam carrier frequency $\nu_{\text{probe carrier}}$ is shifted 800 MHz above the LO, $\nu_{\text{probe carrier}} = \nu_{\mathrm{LO}} + 800$ MHz. The probe carrier is then given sidebands at frequency ν_{TWM}, the lower of which becomes the probe beam at frequency $\nu_p = \nu_{\mathrm{LO}} + 800 - \nu_{\mathrm{TWM}}$ MHz. The beat-note between the probe beam and the local oscillator is at a frequency $\nu_{\mathrm{BN}} = \nu_p - \nu_{\mathrm{LO}} = \nu_p - (\nu_a - 140)$ MHz. The spectrum analyzer is set to measure the power in this beat note, so $\nu_{\mathrm{SA}} = \nu_{\mathrm{BN}}$. Note that it is possible for the beat-note

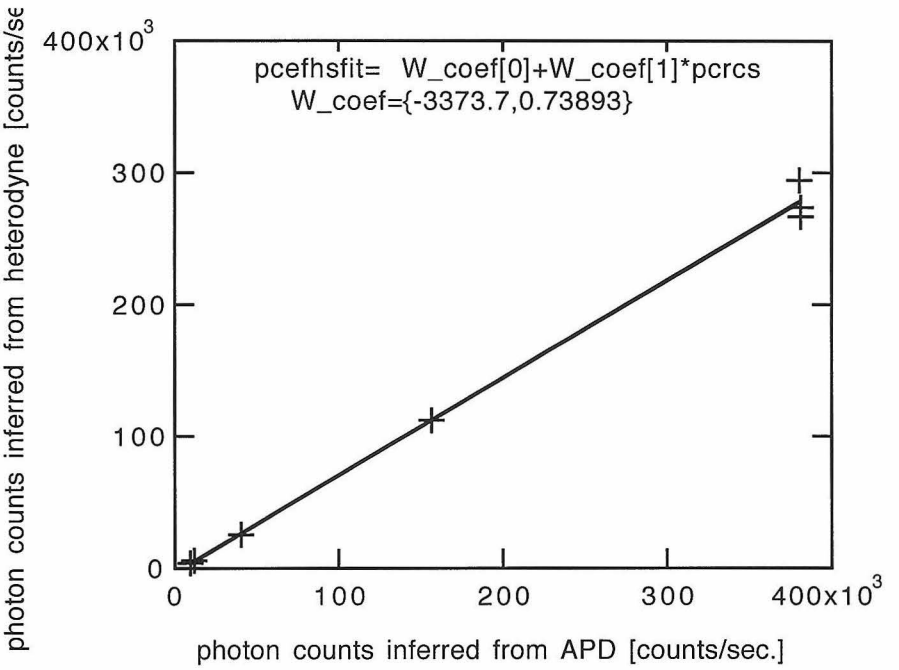

Figure 2.19: Comparison of photon flux as inferred from the heterodyne and from photon counting. The '+' are the data and the line is a least-squares fit, discussed in the text.

frequency to go negative. All this means is that the probe has gone on the other (low frequency) side of the LO. This causes absolutely no problem with the detection on the SA, which cannot distinguish between positive and negative frequencies. For example, consider a probe at frequency $\nu_p = \nu_a - 200$ MHz. This makes a beat-note at $\nu_{\rm BN} = -60$ MHz. The spectrum analyzer set to $\nu_{\rm SA} = -60$ MHz will also respond to any signal that may be present at +60 MHz as well. But signals at +60 MHz are detuned from the atom by −80 MHz, which is certainly unlikely to be generated by any nonlinear process involving the original −200 MHz detuned probe.

2.2 Data

2.2.1 Extremely brief recapitulation of experimental strategy

It is probably fairly easy to lose the thread of the overall experimental strategy from the depths of the preceding section, so I will restate the basic idea. In addition, Figure 2.20 summarizes in block format the critical constituent elements of the optical apparatus. An atomic beam continuously traverses the cavity mode at a flux set so that there is $\bar{N} \sim 1$ atom in the mode volume at any given time. We now perform spectroscopy on this system. For this, we bring a probe beam generated as an rf sideband of a far detuned carrier beam near the cavity resonance. We observe the transmission of this probe beam through the atom cavity system on a balanced heterodyne detector. The power in the photocurrent from the detector at the beat-note frequency is measured on a spectrum analyzer. The signal from the experiment is ultimately a voltage on the spectrum analyzer recorded for various settings of the probe detuning from the atomic resonance and the probe power.

2.2.2 Linear transmission spectrum

I will start with the linear spectrum measurements. Figure 2.21 shows the transmission spectrum for $\bar{N} = 1.5$. The atom and cavity detunings are nominally set to zero

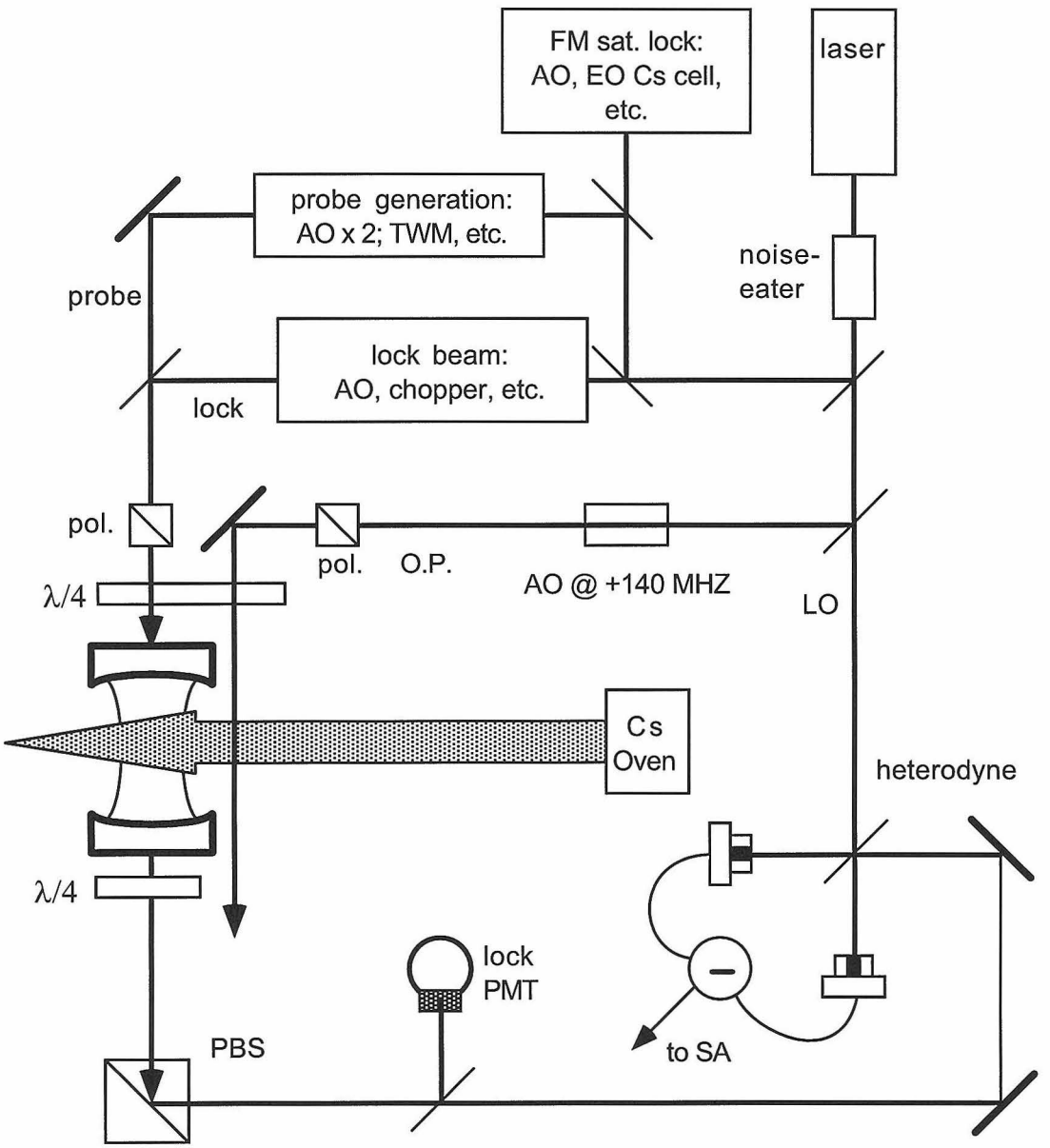

Figure 2.20: Summary of the experimental optical apparatus. Details of the constituent components are found in the following places: Noise-eater, Figure 2.8; Hetrodyne detector, Figure 2.16; Cavity lock, Figure 2.6; FM laser lock, Figure 2.7; Optical pumping and atomic beam, Figure 2.11; Probe generation, Figure 2.15.

($\Delta \simeq \Theta \simeq 0$) and the coincident atom-cavity resonance is defined as the frequency zero ($\omega_0 = 0$). The atom-cavity is driven with an external probe field incident on mirror M_1 ($\delta_1 \approx 1$ ppm) and the output through mirror M_2 ($\delta_2 \approx 350$ ppm) is measured on the heterodyne detectors. This transmission spectrum is in the weak field as can be seen on the ordinate, which is converted to the average intracavity photon number $\bar{n}$, with $\bar{n} \ll n_0 = 0.02$. The ordinate is converted in this way by measuring the beat-note height on the SA, inferring a flux on the heterodyne detectors and from this inferring the intracavity photon number. The detunings are not exactly right; the cavity is shifted off the atoms by a small amount ($\kappa\Theta/2\pi = 10$ MHz). The raw data are shown in Figure 2.22. These are the actual signals which emerge from the SA and are then normalized by the normalization data of Figure 2.4 to generate Fig. 2.21. The frequency scale for Figure 2.22 is in terms of actual beat-note frequency on the heterodyne ν_{BN}. The LO is detuned from resonance by 140 MHz, so the probe at line center makes a beat-note at 140 MHz, as discussed in Section 2.1.6. A comment on the units of the ordinate of Figure 2.22 is appropriate. A beatnote on the SA read in units of Volts actually represents a field amplitude. This is true because the heterodyne detection is sensitive to the cavity output field (see Eq. 2.15) so the detection photocurrent represents a field, the photocurrent drives some resistance and is converted to a voltage which is still proportional to the field amplitude. The data are squared so that they look "right," that is, so that the empty cavity will be a Lorentzian rather than the square-root of a Lorentzian.

To automate the data taking process, an experimental control/data acquisition program was written for computer control of the relevant experimental parameters, and transfer of data from the SA to the computer. The control had a few features. The probe frequency and power were determined by computer control of the frequency synthesizer creating the TWM sidebands. The appropriate detection center frequency was chosen for the SA. In addition, the computer had control over the video input of the depleter AO (see Fig. 2.11), so that the depleter could be switched full "on" to deplete completely the atomic beam. The data acquisition sequence consisted of: dwell at a frequency and collect the "atoms on" data for 1 sec, deplete the beam,

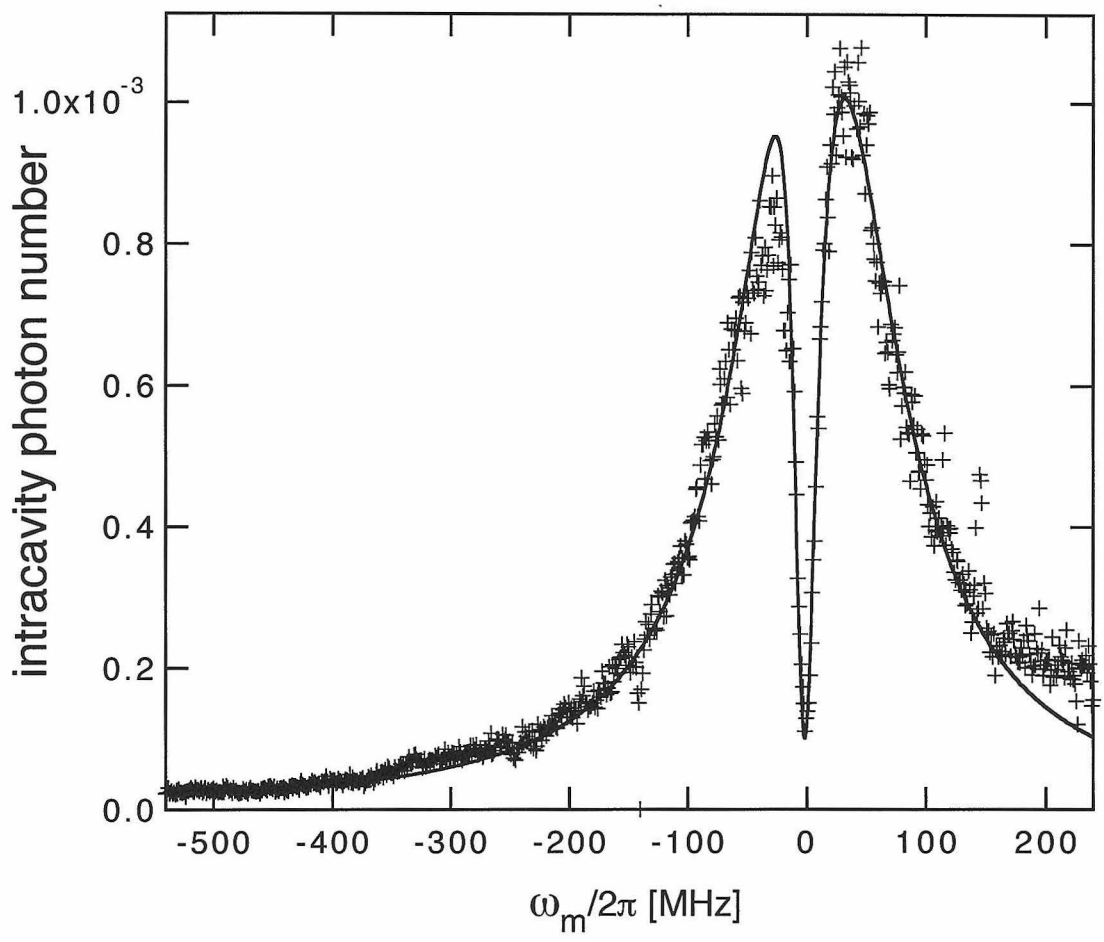

Figure 2.21: Transmission of the atom-cavity for $\bar{N} = 1.5$. $\kappa\Theta/2\pi = 10$ MHz. $\Delta = 0$

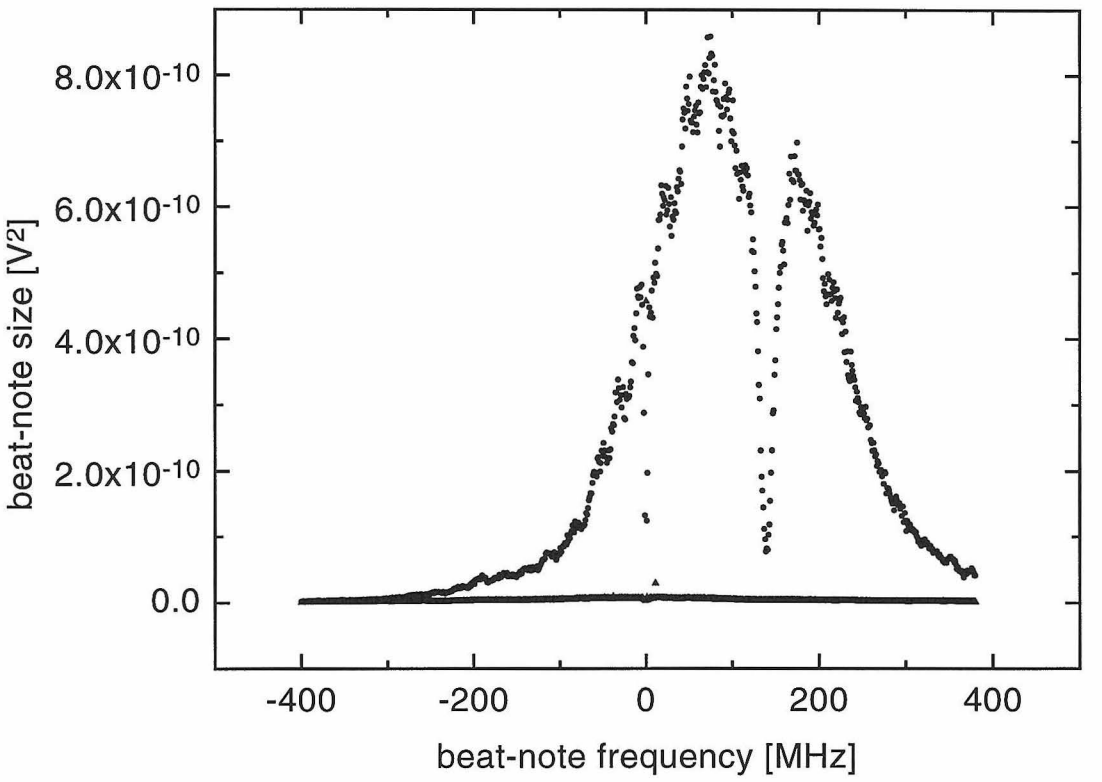

Figure 2.22: Raw data for Figure 2.21. The apparently flat line near 0 V^2 is the background trace. For smaller drive fields, it is important to subtract this from the probe data.

collect the "empty cavity" data for 1 sec, then step the TWM and the SA and repeat with a frequency step of $\Delta\omega/2\pi = 2$ MHz. The interleaving of the atoms on/empty cavity data at each probe frequency point minimizes the effect of probe power drift. After a complete frequency scan, the probe beam would be blocked to collect the background shot-noise which was later subtracted from the probe data (after squaring everything).

To probe across only the "dip" in the atom-cavity transmission shown in Fig. 2.21, we turn to a higher resolution scan ($\Delta\omega/2\pi = 0.5MHz$) with a frequency span $\pm$ 30 MHz. Such a scan for $\bar{N} \simeq 0.95$ average intracavity atoms is shown in Fig. 2.23c, where now the data are normalized to the measured empty cavity response. The resulting normalized transmission is defined as:

$$T_n(\omega_m) \equiv \frac{|T(\omega_m, N = \bar{N})|^2}{|T(\omega_m, N = 0)|^2}, \tag{2.17}$$

where $T(\omega_m, N)$ is given by Eq. 1.8 with Eq. 1.9 and $g_0 \rightarrow g_0\bar{N}^{1/2}$, or $C \rightarrow C_1\bar{N}$. This normalization procedure automatically removes the effects of $R(\omega_m)$ described in Section 2.1.1.2.4 and leaves an almost pure (to the extent dictated by Eq. 2.17) Lorentzian dip of $\Delta\nu_{\mathrm{HWHM}} = \gamma_\perp/2\pi(1 + 2C_1\bar{N})$ on a flat asymptote. The number of atoms $\bar{N}$ is determined by performing a nonlinear least-squares fit to the normalized transmission data using expression 2.17 with $\kappa, \gamma_\parallel, \gamma_\perp$ fixed and $\bar{N}$, $\gamma_\parallel\Delta/2\pi$ and $\kappa\Theta/2\pi$ as fitting parameters. Despite the fact that the height cancels out in Eq. 2.17, the fit still has a free overall scaling to account for variations in probe power between scans with atoms and empty cavity scans (the data was not always interleaved). Of course, $\bar{N}$ is still determined by the fit. Most of the time, detunings were set to zero because (as long as they are small enough as they are here with $|\gamma_\parallel/2\pi\Delta| \lesssim 1$ MHz and $|\kappa/2\pi\Theta| \lesssim 10$ MHz) they have little effect on the value of $\bar{N}$ chosen by the fit.

To illustrate the behavior of the probe spectra as $\bar{N}$ is changed, we also present in Fig 2.23 a series of scans for several values of $\bar{N}$. For each trace, a theoretical $T_n(\omega_m)$ is shown as a fit, from which $\bar{N}$ is determined. In this case, cavity and atom detunings are left free in the fits with the range of detunings found to be:

$-0.7 \lesssim \gamma_{\parallel}/2\pi\Delta \lesssim +0.3$ MHz and $-1 \lesssim \kappa/2\pi\Theta \lesssim 12$ MHz. The range of atomic detunings is insignificant, while the range of cavity detunings is due to drift of the lock point of the cavity between scans and does not affect the resulting $\bar{N}$. As is seen in Fig. 2.23, we can continuously vary $\bar{N}$ over the range from $0.09 \lesssim \bar{N} \lesssim 1.2$ atoms. We do this by changing the power of the depleter beam from Fig. 2.11.

2.2.3 On the determination of $\bar{N}$

Absolute knowledge of the intracavity atomic number $\bar{N}$ is important. It can be seen from Eqs. 1.8–1.10 and 2.17 that the interplay of the rates $(g_0, \gamma_\perp, \kappa)$ dictates the details of the transmitted spectra. For example, in the weak field and in the absence of fluctuations in atomic number and position, if $\bar{N}$ changes but $g_0\bar{N}^{1/2}$ does not, the spectrum will not change. (In the case with fluctuations in atomic number and position, as our real experiment has, the situation is more complicated (as discussed in Section 2.1.3.3).) Convincing ourselves that the values for $\bar{N}$ which we obtain from fits to the data are accurate reflections of the number of intracavity atoms is a several step process. It begins with a firm knowledge of $(g_0, \gamma_\perp, \kappa)$. Some of the following has been said, but it probably bears repeating.

First of all, from the definition $g_0 = (\mu^2\omega_A/2\hbar\epsilon_0 V)^{1/2}$, we see that g_0 depends upon geometrical factors such as the radii of curvature of the mirrors (known through the vendor) and the length of the cavity l (through the mode volume V), and atomic terms such as the dipole transition moment μ (known through the lifetime), and the atomic resonance frequency ω_A (known from accurate wavelength measurement). The length of the cavity l can be measured accurately via the method of Section 2.1.1.2.3. The length does however vary over long time intervals on a larger (than $\lambda/2$) scale due to thermal effects, but by not more than $\pm 3\%$. In other words, some days we may lock the cavity with 100 half-wavelengths in it and some days 102 half wavelengths. Also relevant to the determination of g_0 is knowledge of the efficiency of optical pumping into the $m_F = 4$ component of the $F = 4$ ground state and of the excitation of the $[F = 4, m_F = 4 \longrightarrow F' = 5, m'_F = 5]$ transition with circular polarization (σ^+

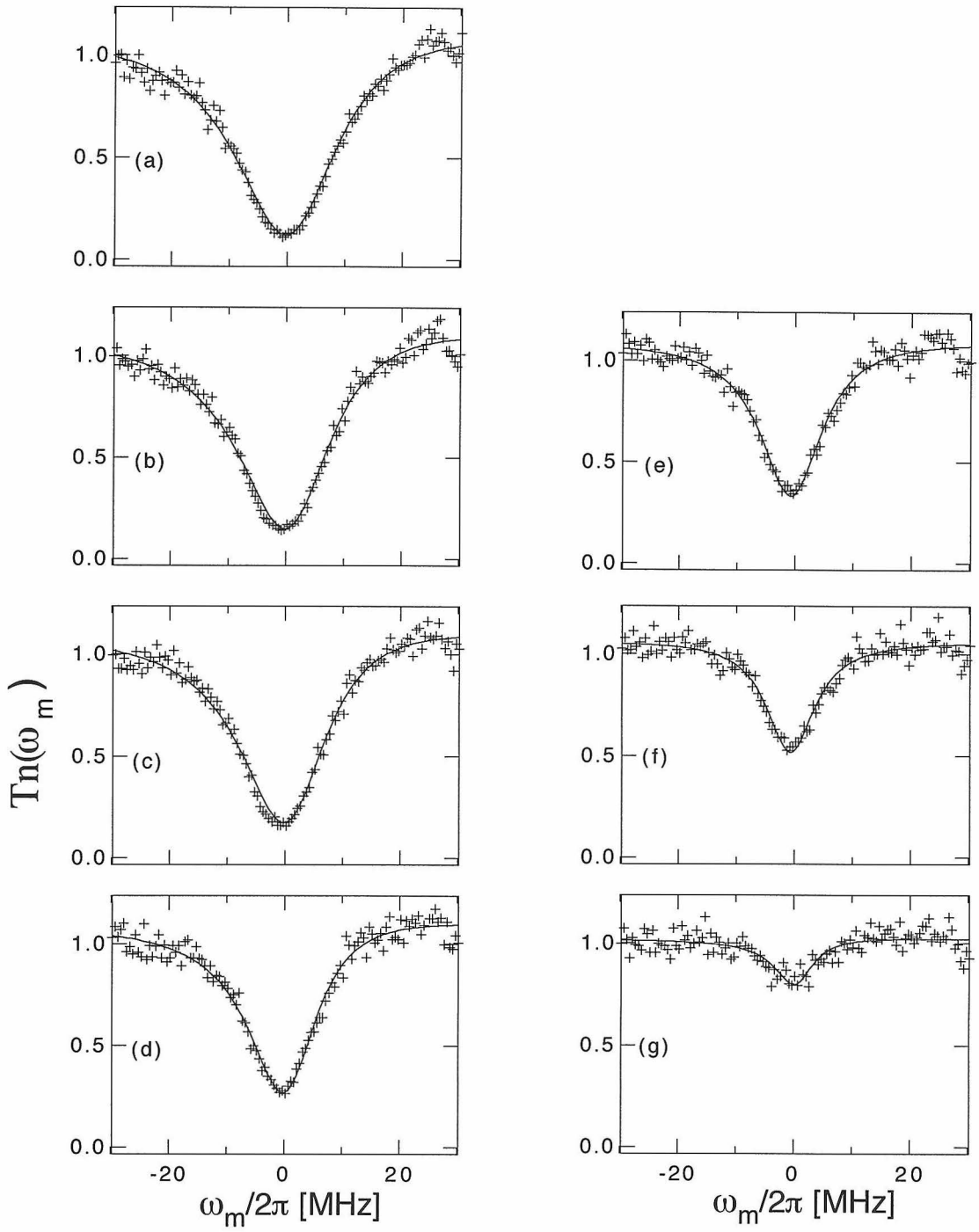

Figure 2.23: Normalized transmission spectra for several values of $\bar{N}$. In order from (a) to (g), $\bar{N} = 1.2, 1.1, 0.95, 0.65, 0.51, 0.27, 0.09$. $\omega_m/2\pi \equiv \nu_p$

transition). Here, we have relied on comparisons of probe transmission spectra with (w) and without (wo) the presence of the optical pumping beam (Fig. 2.11) and the value of $C_{\bar{N}} = \bar{N}C_1$ so determined in the two cases. From the Zeeman structure of the ground and excited states (see Fig. 2.9), the calculated ratio $C_{\rm w}/C_{\rm wo} = 2.45$. This comes from the following: A non-optically pumped Cs atom has equal probability of being in any of the 9 Zeeman sublevels of the $F = 4$ ground state. A beam of such atoms will experience a range of cooperativity values C_i due to the different strengths of the transitions out of the different sublevels of the ground state. This results in an average coupling for a beam of non-optically pumped atoms given by an average over the transition weights $\bar{C} = C_1(1/9)\sum_{i=-4}^{i=+4} P_{i\rightarrow i+1}$ where $P_{i\rightarrow i+1}$ is the transition weight for the transition $F = 4, m_F = i \leftrightarrow F' = 5, m'_F = i + 1$ (the weight of the $m_F = 4 \rightarrow m'_F = 5$ is unity). This transition weight is the square of the transition amplitudes connecting the transitions shown in Figure 2.9. The theoretical ratio is to be compared to our measured ratio $C_{\rm w}/C_{\rm wo}|_{exp} \approx 2.4 \pm 0.2$. Data with and without optical pumping, with associated fits is shown in Fig. 2.24, with measured ratio $C_{\rm w}/C_{\rm wo}|_{exp} = 2.4$. This is a typical example of "typical data"—rarely was the optical pumping this good. In fact over time (years) the efficiency of the OP degraded, resulting in a measured ratio $C_{\rm w}/C_{\rm wo} = 1.9$. The cause of this degradation was likely a drift in the bias magnetic field, since when we reestablished the bias field, the efficiency of the OP improved to almost its best value. There are other possible reasons why the measured value would register low, including, the optical pumping is only partially efficient, the optical pumping beam tends to push the atoms slightly out of their original path thereby reducing the number of atoms which enter the cavity when the beam is present relative to when it is absent, or the fact that a direct comparison of measured C's is not entirely appropriate. Circular polarization of the probe beam is measured to be better than 100:1, so that it is less of a concern than the optical pumping. However there is some cavity birefringence, which acts to mix the incoming polarization states. This was measured to be less than a 20% contribution. Overall, these various measurements and constraints lead us to the conclusion that g_0 is known with an accuracy of $\sim -8/+3\%$, that is, $g_0/2\pi = 20 - 2/+1$ MHz.

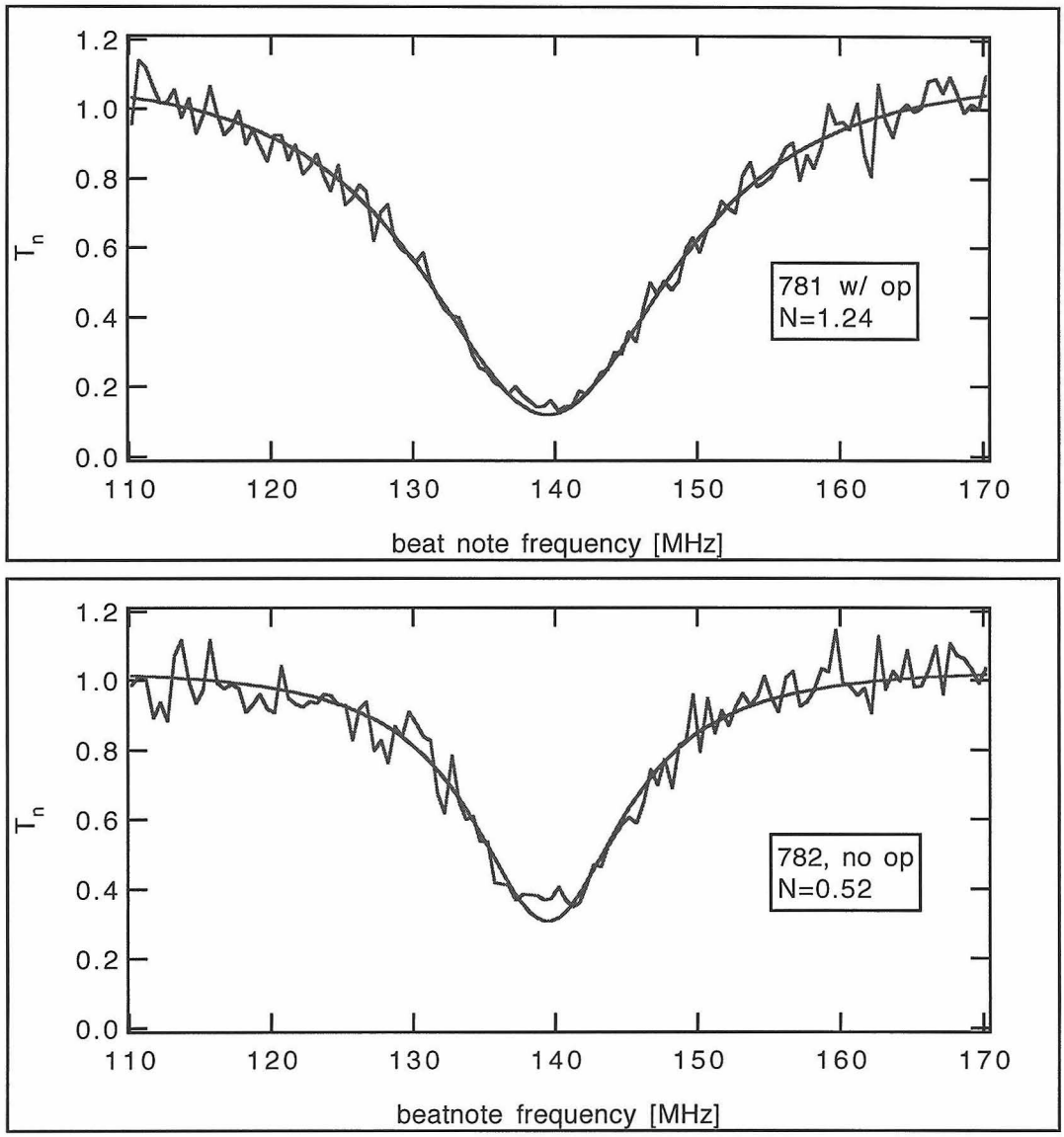

Figure 2.24: Transmission with and without optical pumping. The inferred $\bar{N}$ from the smooth curve fit is shown for each data set (the wiggly curves are the data). The measured ratio $C_{\mathrm{w}}/C_{\mathrm{wo}}|_{exp} = 2.4$.

The next parameter to consider is κ which has already been discussed at length in Section 2.1.1.2.4. Our determination of κ and its variation over the course of a few days' running time is at the 10% level. Given this, we fix $\kappa/2\pi = 75 \pm 8$ MHz.

The last of the parameters is $\gamma_\perp$ which deviates from its radiative value of $\gamma_\parallel/2$ due, at least in an approximate sense, to transit broadening (that is, broadening due to the finite time T_0 that the atoms remain in the cavity) . In our fitting procedure (as in Figs. 2.21 and 2.23) we account for this possibility by way of the parameter $\Gamma \equiv \gamma_\parallel/2\gamma_\perp$, where $\Gamma = 1$ for radiative decay and $\Gamma < 1$ for homogeneous dephasing. We find that in fits where Γ is allowed to vary, the same value of $\bar{N}$ is produced but that the quality of the fit, especially at $\omega_m/2\pi = 0$, improves with decreasing Γ. In this way, we have found that $\Gamma = 0.7$ gives the best fits. This is also the value of Γ found in previous experiments in the strong coupling domain, [7, 44] which had a similar mode waist and should give rise to similar transit effects. Furthermore, an estimate of Γ can be made from a previous numerical integration of the Bloch equations [32] via the parameter $\tau_0 \equiv (\gamma_\parallel w_0)/(2\sqrt{2}u_p)$ where $u_p = \sqrt{2kT/m}$ is the most probable velocity for a beam at temperature T. For our present experiment, $\tau_0 \simeq 1.1$, leading to $\Gamma \simeq 0.75$ which agrees well with the value from the fits to data.

In total then, an aggregate error ΔN in our determination of $\bar{N}$ from fits to the data is brought by uncertainties in $(g_0, \kappa, \gamma_\perp)$. We estimate this experimental uncertainty to be $\Delta\bar{N} \simeq 0.2$ for $\bar{N} \sim 1$ atom.

These comments address the absolute uncertainty in $\bar{N}$ determined from a given trace. On the other hand, some sense of the relative uncertainties as well as of the consistency of our procedure can be obtained by comparing the values of $\bar{N}$ deduced from the individual scans to a proportional monitor of the atomic beam flux. Such a comparison is presented in Fig. 2.25, which plots $\bar{N}$ as derived from fits to data from Fig. 2.23 to the fluorescence of the "monitor beam" (Fig. 2.11). In each case, while the scans were being taken the fluorescence intensity I_F was measured on the "monitor PMT" of Fig. 2.11. The curve of $\bar{N}$ *vs.* I_F should be a straight line passing through the origin. The data fit fairly well to such a line (curve i in Fig. 2.25), but the best fit (curve ii) reveals a residual offset of 0.07 atoms for $I_F = 0$, that is, for

no monitor fluorescence. This is a negligible error when operating at $\bar{N} = 1$ atom (and tolerable even at $\bar{N} = 0.5$) and is in any case, below our estimated $\Delta\bar{N}$. While this fluorescence does not directly yield $\bar{N}$ in absolute terms, it nonetheless helps to validate the consistency of our fitting procedure since the relative roles of $(g_0, \kappa, \gamma_\perp)$ in the fitting function of Eq. 2.17 change with $\bar{N}$. Fig. 2.25 also confirms the absence of gross offsets due to, *e.g.*, a cloud of background atoms in the cavity independent of atomic beam flux.

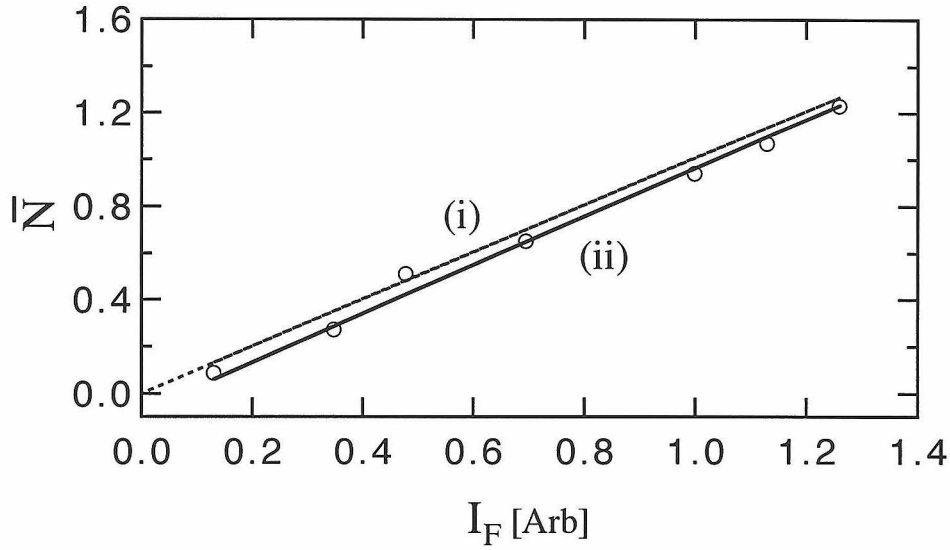

Figure 2.25: Intracavity atom number $\bar{N}$ vs. fluorescence intensity I_F. See text.

The third and final test of the accuracy of $\bar{N}$ comes through the fluctuations in atomic number intrinsic to the thermal beam and fluctuations in coupling through $g(\vec{r})$. This is discussed more fully in Ref. [7] and in Section 2.1.3.3. Basically, the procedure consists of running simulations of the experiment which average over random numbers of atoms tossed into the cavity-mode volume, with number and position distribution governed by the Poissonian statistics of the thermal beam. In this way, the spectra depend in an identifiable fashion on the absolute value of $\bar{N}$ via the fluctuations associated with a given $\bar{N}$. Unfortunately (from this point of view) the effects of fluctuations are not as pronounced as they are in the strong coupling regime, but even still, we are able to put reasonable bounds on $\bar{N}$ which confirm that we are not far afield. Results of simulations agree with our previous fitting procedure

(to the extent discussed in Section 2.1.3.3) and demonstrate that, for example in a data set for which we predict $\bar{N} \simeq 1$ atom from fits of Eq. 2.17, a complete simulation rules out the possibility of $\bar{N} = 1.5$ or $\bar{N} = 0.5$ atoms, for any set of (g, γ, κ) within our expected errors.

2.2.4 Nonlinear measurements

Issues of atom number aside, we have in addition investigated the response of the 1D atom to a "strong" probe, that is, one for which the intracavity photon number approaches and surpasses n_0 (recall that $n_0 \simeq 0.02$ photons). From the semiclassical theory of optical bistability (i.e., the state equation for strong driving fields [31], Eq. 1.19) we anticipate the onset of nonlinear behavior for intracavity photon numbers near n_0. However, a full quantum theory appropriate to our specific experiment of strong-field probe spectra including the influence of fluctuations in atomic number and coupling (via $g(\vec{r})$) is not available. The closest fully quantum result has proved too cumbersome to be of use [54]. However, we certainly do not need a theory to pursue whatever measurements strike our fancy. In Fig. 2.26 we present measurements showing the normalized response $T_n(\omega_m)$ for intracavity photon numbers $\bar{n}$ (at $\omega_m/2\pi) = 0$ ranging from $\bar{n} \sim 4 \times 10^{-6}$ to $\bar{n} \sim 0.11$, for $\bar{N} \simeq 1.6$. Clear evidence for nonlinear behavior is the change in $T_n(\omega_m)$ in moving from curve (i) to (ii), for which the transmission $T_n(\omega_m = 0)$ doubles in a modification brought about by only $\bar{n} \simeq 0.024$ intracavity photons (at $\omega_m/2\pi = 0$). This is in reasonable correspondence to our expectations based on the value of n_0. Thus in moving from free space to the cavity, we move into a new regime for nonlinear spectroscopy where the onset of saturation is characterized by extremely small fields corresponding to small fractions of one quantum.

To flesh out the nonlinear properties, we perform a slightly different measurement. Instead of scanning the frequency for a fixed power probe, we scan the power for a fixed frequency probe. This is the saturation curve described in Section 1.3.2. The data acquisition program was rewritten to scan the power of the rf to the TWM,

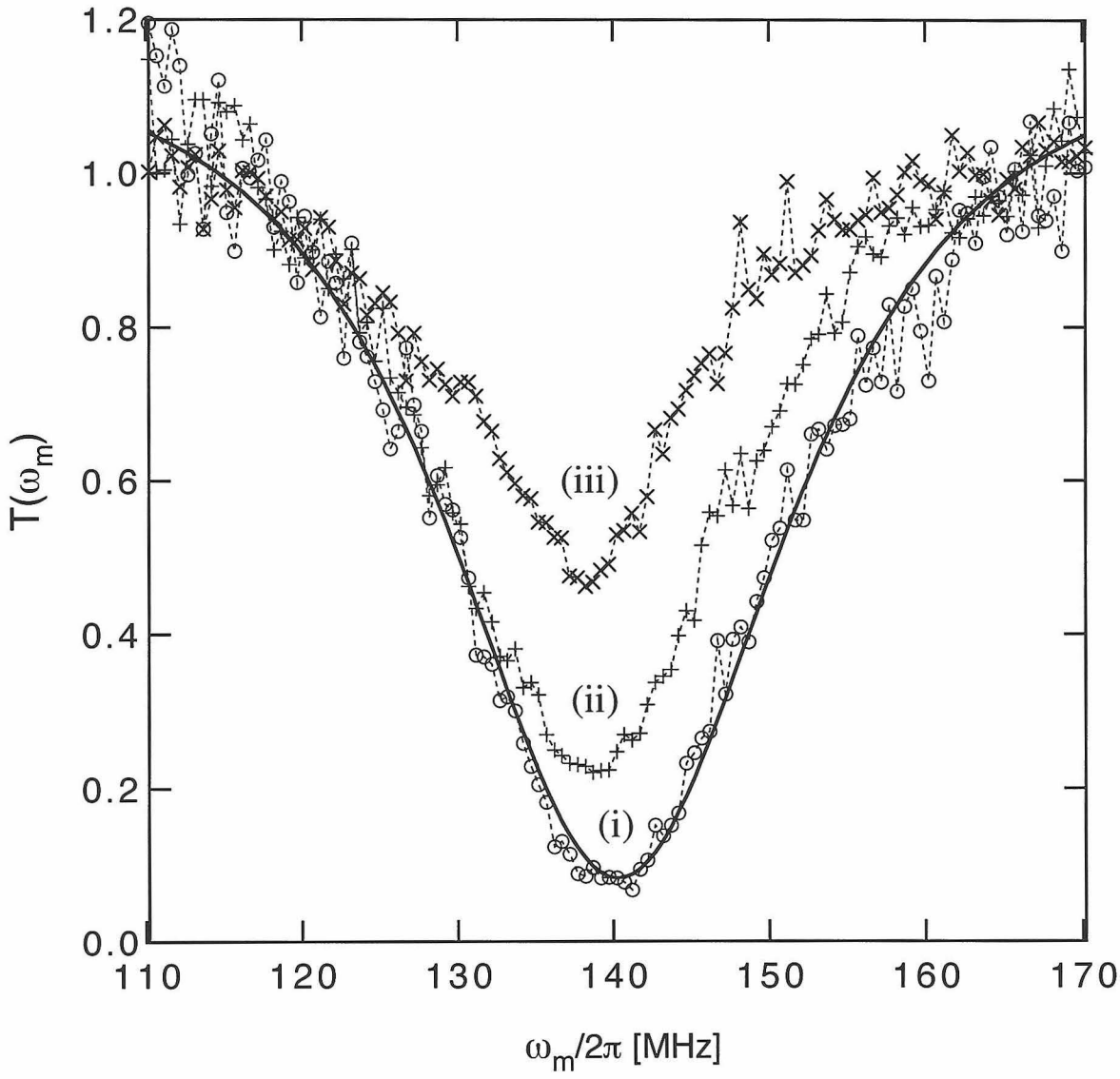

Figure 2.26: Strong-field normalized transmission spectrum. $\bar{N} = 1.6$. (i) $\bar{n} = 4 \times 10^{-6}$; (ii) $\bar{n} = 0.02$; (iii) $\bar{n} = 0.11$. $\bar{n}$ is measured at $\omega_m = 0$.

with again, data with and without atoms interleaved at each point. This is shown for a resonant probe (actually 1 MHz detuned) in Figure 2.27. A few comments are in order. First, the ordinate is the normalized transmission $T_n(\Omega_p/2\pi = 1\text{MHz})$. Second, the abscissa is plotted in terms of intracavity photon number *with atoms*. Thus the quantities plotted against each other are (nonlinear) scaled versions of each other. The curve has the form of a classic saturation curve. The linear response for low drive fields is clearly shown by the flat line with y-intercept at $1/(1+2C)^2$ with $C = \bar{N}C_1$. As the drive is increased, the response of the atom eventually saturates out to the unit normalized transmission characteristic of the empty cavity response.

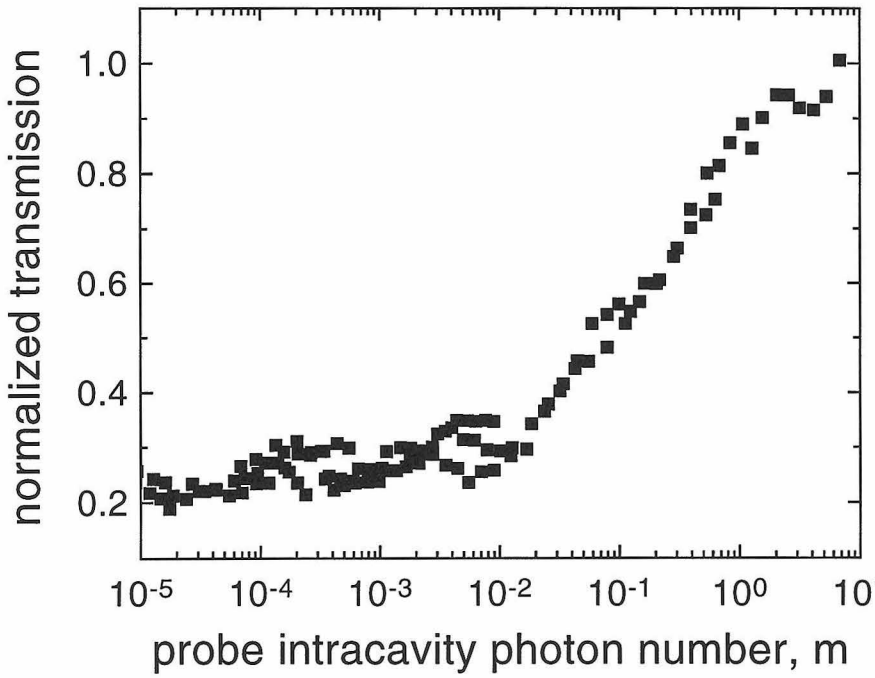

Figure 2.27: Saturation curve, on resonance. $\bar{N} = 0.6$.

Three saturation curves are shown in Figure 2.28, each taken at different probe detuning. Note that the y-intercept moves up, as the off resonance dip is always less deep than that on resonance. The solid lines are the no-free-parameters saturation curves predicted from the optical bistability state equation with $C = \bar{N}C_1$. All the cavity parameters are fixed from the associated linear transmission spectrum

measurement (not shown). The behaviour of the data is qualitatively similar to the theory curves, which is really all we could hope for. It is not, after all a correct theory. Something about the data does stand out, however, which is that the saturation while it is rising, is always much "straighter" than the theory would predict, especially towards large drive fields (clearly seen in the top graph of Fig. 2.28). This may have something to do with the fact that when large fields are used, any stray off-resonant fields become more important. While great care was taken to eliminate such effects (and indeed for the most part they are eliminated) there may still be residual effects at the extremely large drives (intracavity photon numbers approaching 10 photons). Note also that the point of upturn of the curves moves progressively to the right as the absolute detuning is increased. This is to be expected, as it is harder to saturate an atom with off-resonant light.

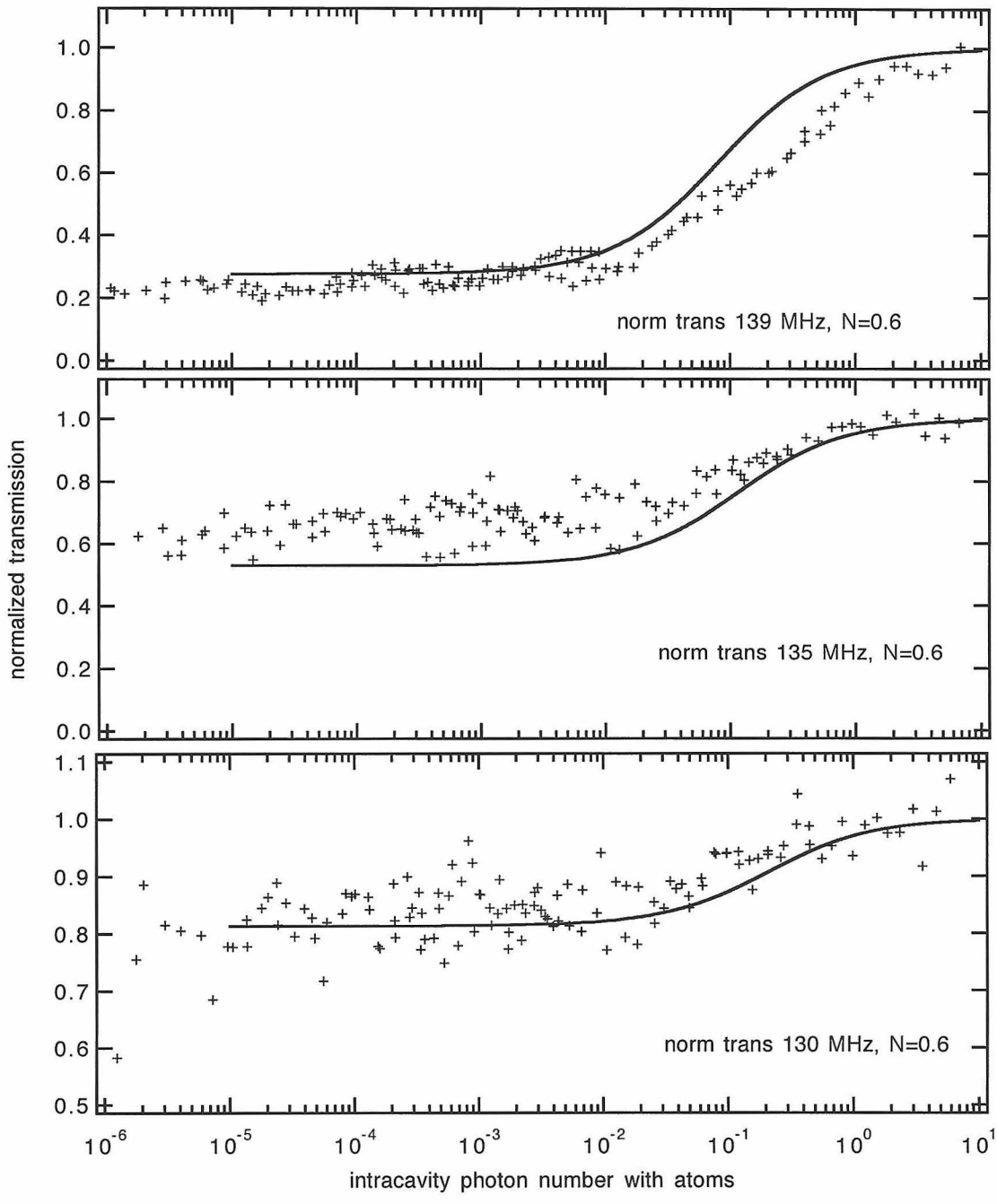

Figure 2.28: Saturation curves for various detunings. $\bar{N} = 0.6$. The top graph has a nearly resonant probe at $\gamma_{\parallel}\Delta/2\pi = -1$ MHz. The middle has a probe detuned by -5 MHz and the bottom graph has a probe detuned by -10 MHz. $\bar{N} = 0.6$. The top graph shows the same data as in Figure 2.27.

Chapter 3 One-D atom with squeezing

One of the canonical questions in Quantum Optics is the nature of the radiative properties of an atom when the normal vacuum state of the electromagnetic field is replaced by a squeezed vacuum. A squeezed vacuum has fluctuations in one quadrature which dip below the "standard quantum limit", or vacuum-state limit (with a corresponding increase in the fluctuations in the other quadrature).

A serious technical obstacle to investigating the interaction of atoms with nonclassical light (and indeed to measuring nonclassical light produced by the atoms themselves) is the efficient coupling of optical "beams" to the dipole radiation pattern of an atom. For the atom-squeezed light interaction, Gardiner [55] has predicted reductions and enhancements in the spontaneous decay of the components of the atomic polarization proportional to the variances $\Delta X_{\mp}^2$ of the "quiet" and "noisy" quadratures of the squeezed vacuum. Unfortunately, in a realistic experiment, the decay rates $\beta_{\pm}$ of an atom in squeezed vacuum can be altered from the free space value $\gamma_{\perp}$ only according to $\beta_{\pm} = \gamma_{\perp}[(1-\eta_f) + \eta_f \Delta X_{\pm}^2]$, where η_f is a measure of the efficiency with which the squeezed field is coupled to the atom. For an atom in free space illuminated by Gaussian beams of squeezed light the overlap of the incident field distribution with the dipole radiation pattern is typically very small so that the coupling ($\eta_f \sim 10^{-4}$) is so weak that any effect of the squeezed field is masked by the "normal" vacuum. In principle, this can be completely different for the 1-D atom, since the problem of efficient coupling of the squeezed light to the atom is reduced to that of effective mode matching of a beam of squeezed light to the cavity containing the atom (see Figure 3.1). Qualitatively, the effect of the squeezed vacuum on the 1-D atom is reflected in an inhibition of the cavity-enhanced spontaneous emission component of the 1-D atom spectrum. Thus in the squeezing/1-D atom case, the radiative rate alterations can be described by $\beta_{\pm} = \gamma_{\perp}[1 + 2C_1 \Delta X_{\pm}]$, where for the case of perfect squeezing, $\beta_{-} \rightarrow \gamma_{\perp}$.

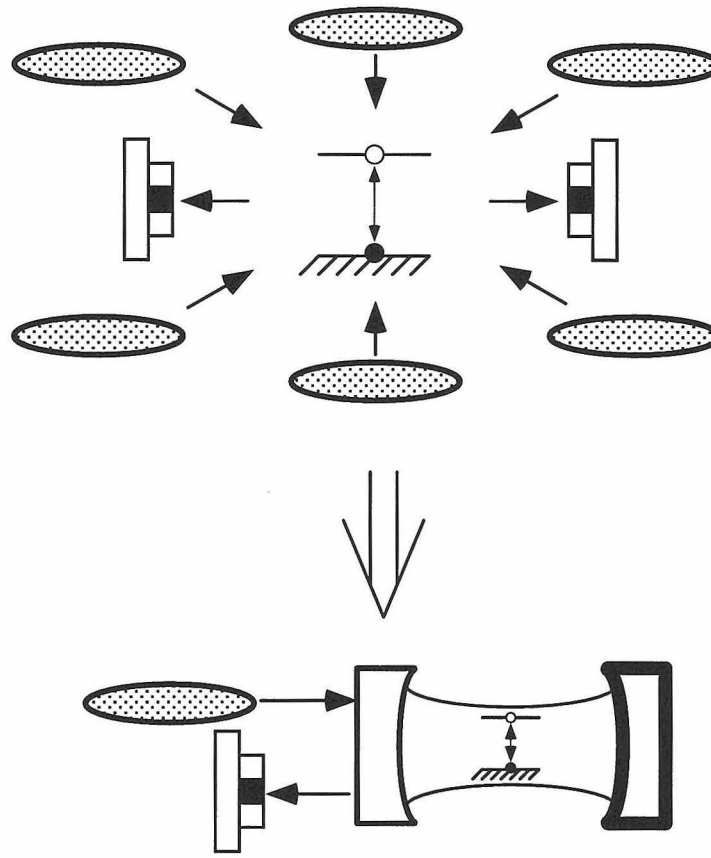

Figure 3.1: It is difficult to excite a free-space atom with 4π of squeezed light, and then to collect all of its fluorescence (top), while it is relatively easy to excite a 1-D atom in a cavity with 1-D squeezed light, and to collect all of its radiation into the cavity mode (bottom).

This experiment was a rather complicated one, involving two labs, each of their associated experimenters, and spanning 3 years of on-again, off-again effort. For the early spectrum measurements, the squeezing lab was run by Eugene Polzik and Nikos Georgiades, and the cavity QED lab by me and Rob Thompson. For the later phase-sensitive transmission measurements, the squeezing lab was taken over by Nikos and the cavity QED lab was largely run by Christina Hood; I would pop in fairly frequently to take data, but most of the tedious set-up work was done by Christina and Nikos. In addition, Nikos has invested much time and effort in the data manipulation and analysis.

3.1 Background and motivation

3.1.1 Why do it?

When I give a talk on the squeezing-on-atom-cavity experiment, I start with a statement such as: "There has been slight theoretical interest in the interaction of squeezed light and atoms over the years..." Then I show a list of about 50 (!) references on the subject that have been generated in the last decade, since the first few "seminal" works on the subject by Gardiner [55] and Milburn [56, 57]. For purposes of completeness, there follows a short compendium of the topics that the theorists have covered.

Extensions of the early work on the basic radiative properties of atoms in ideal squeezed light has continued unabated [58, 59, 60, 61, 62, 55, 63, 64, 65, 66, 67, 68, 69, 70] with some consideration of atoms in finite bandwidth squeezing [71, 72, 73] and much attention to resonance fluorescence of atoms in squeezed vacuum [74, 75, 76, 77, 78, 79, 80, 81, 82, 83, 84, 85, 86]. Optical bistability in squeezed vacuum has been considered [87], as have optical pumping with squeezed light [88] and photon echoes and revivals [89, 90]. There was a spurt of interest in lasers with squeezed pump fields or squeezed reservoirs [91, 92, 93, 94, 95, 96, 97], gain without inversion [98, 99] and electromagnetically induced transparency in squeezed light [100]. Squeezed light

interacting with atoms in cavities has been given significant coverage [101, 102, 103, 104, 105, 106, 107]. Two proposals in the bad cavity limit are particularly relevant to our work [108, 109] and a proposal in the strong-coupling limit has great promise [110]. Opportunities for laser cooling in squeezed vacuum [111, 112, 113, 114] have not been missed. Squeezed light consists of correlated pairs of photons, so three-level atoms and two-photon effects [115, 116, 117, 118, 119, 120, 121, 122, 123, 124, 125, 126] have been of considerable interest. There are at least two papers related to the consequences of the phase of the squeezing [127, 128]. Interesting ideas involving cooperative effects with multiple atoms in squeezed vacuum [129, 130, 131, 132, 133, 134] have been noted, as well as diverse other effects [135, 136, 137, 138].

This theory is well ahead of a restricted body of experimental work in which a squeezed field has interacted with an atomic sample [139, 140, 141]. I will elaborate only on those experiments from our lab. Ref. [139] is really the only work that deals with a fundamental aspect of the atom-squeezed field interaction. They have measured a departure from a quadratic rate of two-photon absorption for excitation with a very weak squeezed field. Normally two-photon absorption is quadratic in the power of the applied field, but since squeezed light comes in pairs of photons, the rate can be altered with an asymptotic linear dependence. The collection efficiency and squeezing/atom overlap were fairly small in this experiment, so that the resulting photon count rate was extremely low, making the experiment a very difficult one. Refs. [140, 141] involve atomic spectroscopy with squeezed light for sensitivity below the vacuum level. An otherwise noise-obscured resonance signal is brought out by the application of squeezed vacuum. There have been many other experiments involved in increased measurement sensitivity via squeezed light, but they are outside the main focus of this chapter.

Of course, an immense bulk of theoretical work is no guarantee that a subject merits experimental investigation. Indeed, for the most part, quantum opticians have latched onto a problem that has an infinitude of subtle variation and cranked out the calculations. As always, the experimentalist sorts through this opus for something striking, or more likely, something that he or she can actually do in the lab.

In a broader context, our particular realization of the squeezed light on atom-cavity is an instance of what is known as a cascaded quantum system (see Fig. 3.2). In such a system, the output field of one quantum system drives, or provides the input field for another quantum system. It is a scenario that offers a simple and elegant theoretical treatment [142, 143], but which has not to any significant extent been realized in the laboratory. It is, after all, hard enough to realize and control one quantum system!

In its most basic sense, our system investigates the consequences of atomic excitation with noise fields (not necessarily nonclassical). This has received some attention from other quantum optics groups. For example, Hamilton et al. have studied the saturation properties of an atom subject to controlled (classical) fluctuations in laser frequency and/or phase [144, 145]. Our experiments provide a complementary study of the effects of *saturation* on the noise response of an atomic transition (although we hope that the nonclassical nature of our noise fluctuations provide the dominant effect).

Despite interest from diverse perspectives, I will focus in this chapter on the canonical problem of demonstrating an effect which is a unique feature of the nonclassical nature of the squeezed light-atom interaction. Unfortunately, our experiments have not been an overwhelming success from this point of view. It is, however, this problem that motivated us from the beginning and still dominates my thoughts on the subject. The experiments are quite difficult, and a null result relative to a somewhat arbitrary criterion (of what constitutes nonclassical behaviour, e.g.) should not be construed as a total condemnation of the accomplishments that we have been able to achieve. To my knowledge, our experiments represent the only realization of the coupling of two distinct, complex quantum systems, and certainly represent the only attempt to excite a cavity QED system with nonclassical light.

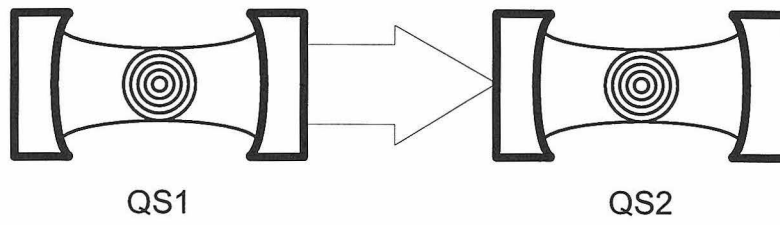

Figure 3.2: A cascaded quantum system.

3.1.2 What is squeezed light?

There are many places where squeezed light (also called "squeezing") is explained in detail [146, 147, 148]. For our purposes, squeezing is the oblong distribution of fluctuations in the quadrature amplitudes of the electromagnetic field shown in Figure 3.3b. Note that the "squeezing ellipse" has two relevant quantities associated with it: ϕ, the angle of the squeezing ellipse with respect to a coherent field $|\alpha\rangle$ (the "stick" extending from the origin) and ΔX_-, the "width" of the minor axis of the ellipse. (ΔX_+ is obtained from ΔX_- in a minimum-uncertainty state.) When the coherent component is absent we have what is called squeezed vacuum, despite the fact that it actually contains real photons. The quadrature field operators are defined as:

$$X_\theta \equiv \hat{a}e^{-i\theta} + \hat{a}^\dagger e^{i\theta} \tag{3.1}$$

where the (single-mode, single polarization) electric field E at frequency ω is quantized as:

$$E = i\sqrt{\frac{\hbar\omega}{2\epsilon_0 V}}\left[\hat{a} - \hat{a}^\dagger\right]. \tag{3.2}$$

The variances in the quadrature phase operators are

$$(\Delta X_\theta)^2 \equiv \langle X_\theta^2\rangle - \langle X_\theta\rangle^2. \tag{3.3}$$

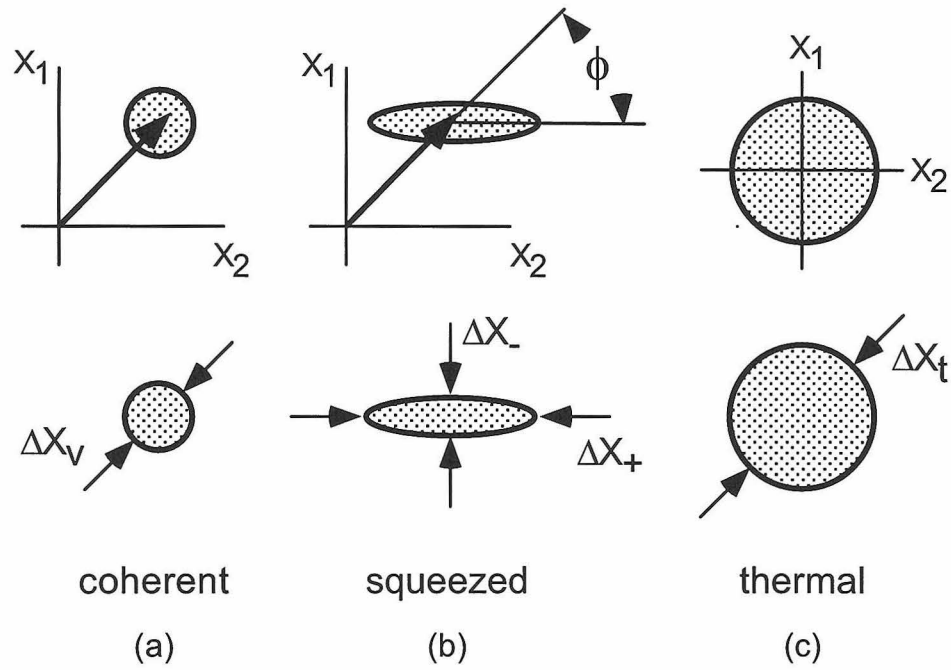

Figure 3.3: Ball and stick diagrams of a) a coherent field, b) a squeezed field and c) a thermal field.

For a minimum-uncertainty state

$$\Delta X_\theta \Delta X_{\theta+\pi/2} = 1, \tag{3.4}$$

for some $\theta = \theta_0$ ($\Delta X_- \Delta X_+ = 1$). The squeezed vacuum is generated by applying the squeezing operator to the vacuum

$$S(r,\theta) = \exp\left(\frac{1}{2} r e^{-2i\theta} \hat{a}^2 - \frac{1}{2} r e^{2i\theta} \hat{a}^{\dagger 2}\right), \tag{3.5}$$

where r is the squeezing parameter. A squeezing ellipse on the end of a coherent "reference" component is generated by displacing the squeezed vacuum with the displacement operator which has the following property

$$D(\alpha)|0\rangle = |\alpha\rangle \tag{3.6}$$

so that the final squeezed field is $D(\alpha)S(r,\theta)|0\rangle$. (The displacement operator can be realized with a beam-splitter and a coherent laser beam.) I introduce these quantities only to quantify what I will refer to as the degree of squeezing which is a way to quantify the property that the fluctuations in one of the quadratures of the squeezed vacuum can dip below the vacuum level. Coherent states satisfy:

$$\Delta X_\theta^{coh} = \Delta X_{\theta+\pi/2}^{coh} = 1 \tag{3.7}$$

which is a result of the "normal" vacuum fluctuations which are independent of phase. On the other hand, the ideal squeezed vacuum satisfies

$$\Delta X_{\theta_0} \equiv \Delta X_- = e^{-r}; \quad \Delta X_{\theta_0+\pi/2} \equiv \Delta X_+ = e^r \tag{3.8}$$

which is qualitatively portrayed the picture. This said, when I refer to the degree of squeezing, I mean some measure of r. Usually, I express this in terms of the noise level of the quiet quadrature of the squeezed vacuum in dB below the shot noise

level. There is a convenient parameterization of squeezed vacuum which I will use extensively, namely,

$$N \equiv \langle a^\dagger a \rangle \tag{3.9}$$

$$M \equiv \langle aa \rangle. \tag{3.10}$$

For a minimum-uncertainty squeezed state

$$|M| = \sqrt{N(N+1)}. \tag{3.11}$$

M and N are a complete specification of the degree of squeezing, as is N alone for a minimum uncertainty state.

3.1.3 The DOPO in brief

One means to generate squeezed light is via parametric downconversion in a sub-threshold degenerate optical parametric oscillator. The ideal DOPO generates the quadrature-squeezed light considered above. Rather than go into detail about the OPO, I will merely introduce the parameters that are relevant.

The ideal OPO below threshold produces light with a spectrum of squeezing $S(\omega)$ which is a Lorentzian dip below the vacuum level with a width similar to the cavity width:

$$S(\omega) = 1 - \frac{4\kappa_s \epsilon}{(\kappa_s + \epsilon)^2 + \omega^2} \tag{3.12}$$

where κ_s is the cold-cavity linewidth (no pump) and ϵ is the scaled pump amplitude, with $\epsilon = \kappa_s$ specifying threshold for second-harmonic generation. The squeezing bandwidth depends on the pumping, and hence on the degree of squeezing. A displaced squeezed field is generated by simply mixing a coherent field with the squeezed field on a beamsplitter (BS). In order to avoid any loss of degree of squeezing 99% of the squeezing is reflected (or transmitted) and 1% of a very strong coherent beam is transmitted (or reflected) through the other port of the BS.

The discussion thus far has focussed on the properties of ideal squeezed light. Needless to say, no laboratory system generates anything ideal, nor do the laboratory measurements necessarily reflect directly the quantities that I have used in my discussion. It is therefore necessary to introduce quantities that are laboratory-relevant and non-ideal. A prime example is the degree of squeezing. I have introduced the parameter r in Eq. 3.5. The measurement of the degree of squeezing is a measurement of noise level compared to the shot noise of a LO in a homodyne measurement. The resulting quantity is the number of dB below the shot-noise level, not r. The bandwidth of the squeezing provides another example. It can be inferred from a readily measurable quantity, the so-called gain of the OPO, G_+, which is measured as the phase-sensitive amplification of a coherent field injected through the OPO. The gain G_+ is given by

$$G_+ = \left(\frac{1+x}{1-x}\right)^2 \tag{3.13}$$

where x is the pump parameter with $x = 1$ representing threshold. There is also a corresponding de-amplification G_-. The $G_\pm$ are related to the N and M of Eq. 3.11 via:

$$1 + 2(N \pm M) = G_\pm. \tag{3.14}$$

We define a measure of the bandwidth of the squeezing as a quantity $b_\pm$ (which depends on the phase of the squeezing),

$$b_\pm = \frac{\kappa_s}{2}(1 \pm x), \tag{3.15}$$

where κ_s is the *fullwidth* of the OPO cavity with no pump.[1] It can be related to the N and M by:

$$\pm\left(\frac{b_+^2 - b_-^2}{2b_\mp^2}\right) \equiv (N \pm M) \tag{3.16}$$

from which

$$\frac{b_\pm^2}{b_\mp^2} = 1 + 2(N \pm M) = G_\pm. \tag{3.17}$$

[1] I apologize for this definition of κ_s as a fullwidth, while all of my other κ's are half-widths, but I am using a convention consistent with that of A. S. Parkins. [149]

The most important functional relationship is between $b_\pm$ and G_+ and is:

$$b_+ = \kappa_s \frac{\sqrt{G_+}}{\sqrt{G_+}+1} \tag{3.18}$$

$$b_- = \kappa_s \frac{1}{\sqrt{G_+}+1}. \tag{3.19}$$

$b_\pm$ will be the parameter of choice for characterization of the degree of squeezing later; it can be found from the measured gain via Eqs. 3.18 and 3.19.

3.2 Theory of squeezing and atoms

3.2.1 Free-space atom and squeezing

An atom decaying to a squeezed-vacuum reservoir of "infinite" bandwidth obeys the following optical Bloch equations (OBE) for the mean dipoles and inversion:

$$\langle \dot{\sigma}_x \rangle = -\gamma(N - M + 1/2)\langle \sigma_x \rangle \tag{3.20}$$

$$\langle \dot{\sigma}_y \rangle = -\gamma(N + M + 1/2)\langle \sigma_y \rangle \tag{3.21}$$

$$\langle \dot{\sigma}_z \rangle = -\gamma(2N + 1)\langle \sigma_z \rangle - \gamma \tag{3.22}$$

where σ_x, σ_y, σ_z are the atomic Pauli operators, related to those of Eq. 1.5 by $\sigma_+ = \sigma_y + i\sigma_y$ and $\sigma_- = \sigma_y - i\sigma_y$ and $\gamma \equiv \gamma_\parallel$. The spectrum of light emitted from the atom illuminated by squeezed vacuum consists of two parts: a flat wide component of width $\gamma(N + M + 1/2)$ associated with ΔX_+, and a tall skinny component of arbitrarily narrow width $\gamma(N - M + 1/2)$ associated with ΔX_-. The narrow component eventually dominates the spectrum and has a width which is below the natural linewidth of the atom. This is a direct result of the reduced fluctuations in the quiet quadrature of the squeezed vacuum and is called inhibition of atomic phase decays [55, 146]. In fact Gardiner considered the atom as a detector of squeezed light, which responds with a narrowed spectrum of fluorescence.

3.2.2 Atom in cavity and squeezing[2]

I will consider the atom-cavity with squeezing system only in the 1-D atom limit. Here, the separation of time scales between the atom (enhanced) decay and the cavity decay is such that the system can be treated as a modified atom, as discussed in Section 1.1.3.1. There are thus Bloch equations and expressions for the transmission of the cavity to a weak probe that are a valid approximation regardless of the type of squeezing. I will introduce these quantities and then specialize to the cases of broadband and narrow-band squeezed light.

Assume to start that the system composed of atom + cavity + squeezing obeys OBE's of the form [103]:

$$\langle \dot{\sigma}_x \rangle = -\gamma_x \langle \sigma_x \rangle \tag{3.23}$$

$$\langle \dot{\sigma}_y \rangle = -\gamma_y \langle \sigma_y \rangle + \Omega_z \langle \sigma_z \rangle \tag{3.24}$$

$$\langle \dot{\sigma}_z \rangle = -\gamma_z \langle \sigma_z \rangle - \frac{\gamma}{2}(1+2C) - \Omega_y \langle \sigma_y \rangle \tag{3.25}$$

where $\gamma_{x,y,z}$ are sensitive to the phase of the squeezing and also depend on other parameters of the squeezing. $\Omega_{y,z}$ represent the effect of a coherent drive field which defines the reference for the phase of the squeezing. We can consider either the case of squeezed vacuum ($\Omega_{y,z} = 0$) or a displaced squeezed field, in which $\Omega_{y,z}$ will be related to the amplitude of the displacing coherent field Ω in some way which depends on the actual buildup of photons in the cavity, which in turn depends on the decay of the atoms, and hence, ultimately on the parameters of the squeezing. For a probe at frequency ν incident on the atom-cavity-squeezing system, the transmitted probe amplitude is given by [149]:

$$A_p(\nu) = \frac{1}{\frac{\kappa}{2} - i\nu} \tag{3.26}$$
$$-\frac{\gamma C}{\kappa}\langle \sigma_z \rangle_{ss} \left[\frac{1}{p^s} \left[\frac{\lambda_+^s + \gamma_y}{\lambda_-^s + i\nu} - \frac{\lambda_-^s + \gamma_y}{\lambda_+^s + i\nu} \right] - \frac{1}{\gamma_x - i\nu} + \frac{\Omega_z^2}{\gamma_y p^s} \left[\frac{-1}{\lambda_+^s + i\nu} + \frac{1}{\lambda_-^s + i\nu} \right] \right]$$

[2]This section borrows heavily from theoretical work done by A. S. Parkins, described in his notes *Modulation of the probe field*, April 1996 [149].

where

$$\langle\sigma_z\rangle_{ss} = -\frac{\gamma(1+2C)\gamma_y}{\gamma_x\gamma_y + \Omega_z\Omega_y} \tag{3.27}$$

and

$$\lambda_{\pm}^{s} = -\frac{1}{2}(\gamma_y+\gamma_z) \pm \frac{1}{2}p^s; \quad p^s = \sqrt{(\gamma_y-\gamma_z)^2 - 4\Omega_y\Omega_z}. \tag{3.28}$$

The transmission on resonance is

$$A_p(\nu=0) = \frac{2}{\kappa}\left\{1 + \frac{\gamma}{2}C\langle\sigma_z\rangle_{ss}\left[\frac{1}{\gamma_x} + \frac{1}{\gamma_y}\left(\frac{\gamma_y\gamma_x - \Omega_z^2}{\gamma_y\gamma_z + \Omega_y\Omega_z}\right)\right]\right\}. \tag{3.29}$$

Note that this is purely real. Parkins [149] has found expressions for $\gamma_{x,y,z}$ and $\Omega_{y,z}$ for arbitrary squeezing parameters, but first I will consider the simple case of broad-band squeezing.

3.2.2.1 Broadband limit

I will start with a discussion of the simple broadband squeezing model. To have broadband squeezing means that the spectrum of squeezing is broader than any of the atom-cavity rates: $\kappa_s \gg g, \kappa, \gamma$ (and possibly $\kappa_s \gg \Omega_{x,y}$ for the case of displaced broad-band squeezing) with $\kappa_s \to \infty$ defining "perfect" squeezing. In the infinite bandwidth squeezed vacuum case, Rice and Pedrotti [108] show that

$$\gamma_x = \frac{\gamma}{2}\left[1 + 2C\left(1 + 2N - 2M\right)\right] \tag{3.30}$$

$$\gamma_y = \frac{\gamma}{2}\left[1 + 2C\left(1 + 2N + 2M\right)\right] \tag{3.31}$$

$$\gamma_z = \gamma\left[1 + 2C + 4CN\right]. \tag{3.32}$$

The phase of the squeezing is taken to line up with one of the quadrature decay channels of the atom. (If we take the opposite phase γ_x and γ_y change roles.) In the limit of strong squeezing, from Eq. 3.11 $M \approx N + 1/2$ and

$$\gamma_x = \frac{\gamma}{2} \tag{3.33}$$

$$\gamma_y = \frac{\gamma}{2}\left[1 + 4C + 8CN\right] \tag{3.34}$$

$$\gamma_z = \gamma\left[1 + 2C + 4CN\right]. \tag{3.35}$$

Thus, there is an inhibition of the cavity-enhanced spontaneous emission (compare Eq. 3.33 with $\gamma_\perp(1+2C)$ from Eq. 1.11). Strictly speaking, this interpretation and derivation are valid only with an infinitely wide cavity, in the sense of the true "bad cavity" limit discussed in Section 1.1.3.1 and infinite bandwidth squeezed light. (Note that in this chapter, $\gamma \equiv \gamma_\parallel$.)

The power transmission of the probe $|A_p(\nu)|^2$ is shown in Fig. 3.4 for several values of N for the broadband case. Note that the "dip" associated with the 1-D atom gets both shallower—the squeezed vacuum carries photons which saturate the atom—and narrower (that the narrowing is not immediately evident is problematic in and of itself).

The question arises if this inhibition of the cavity-enhanced spontaneous emission is the result of the nonclassical character of the squeezed field, or if other types of light will lead to similar behaviour. Fig 3.5 addresses this issue. I have shown the "width" of the spectrum of fluorescence (out the sides of the cavity, Eq. (16) from Ref. [108]) for excitation with light of various statistics. A thermal field (Figure 3.3c) has $M = 0$ while classical squeezing has asymmetric fluctuations in which neither quadrature goes below the vacuum level, with $M = N$. Note that from Fig. 2.26, a strong coherent field also has an effect on the spectrum of transmitted light that is similar (at least superficially) to that shown in Fig. 3.4. I have left coherent excitation off of Fig. 3.5 because alignment of the axis with the other types of light is somewhat problematic. Suffice it to say that a coherent field should have a significantly different behavior than a squeezed field.

3.2.2.2 Narrow-band squeezing

Our source of squeezing does not even come close to satisfying the broadband limit. In fact $\{\kappa, \gamma(1+2C)\} > \kappa_s$, so we are forced to consider a narrowband theory. The expressions for $\gamma_{x,y,z}$ and $\Omega_{y,z}$ are absurdly complicated, and are explicitly written out in Appendix A. I will only state here, that with these expressions, everything

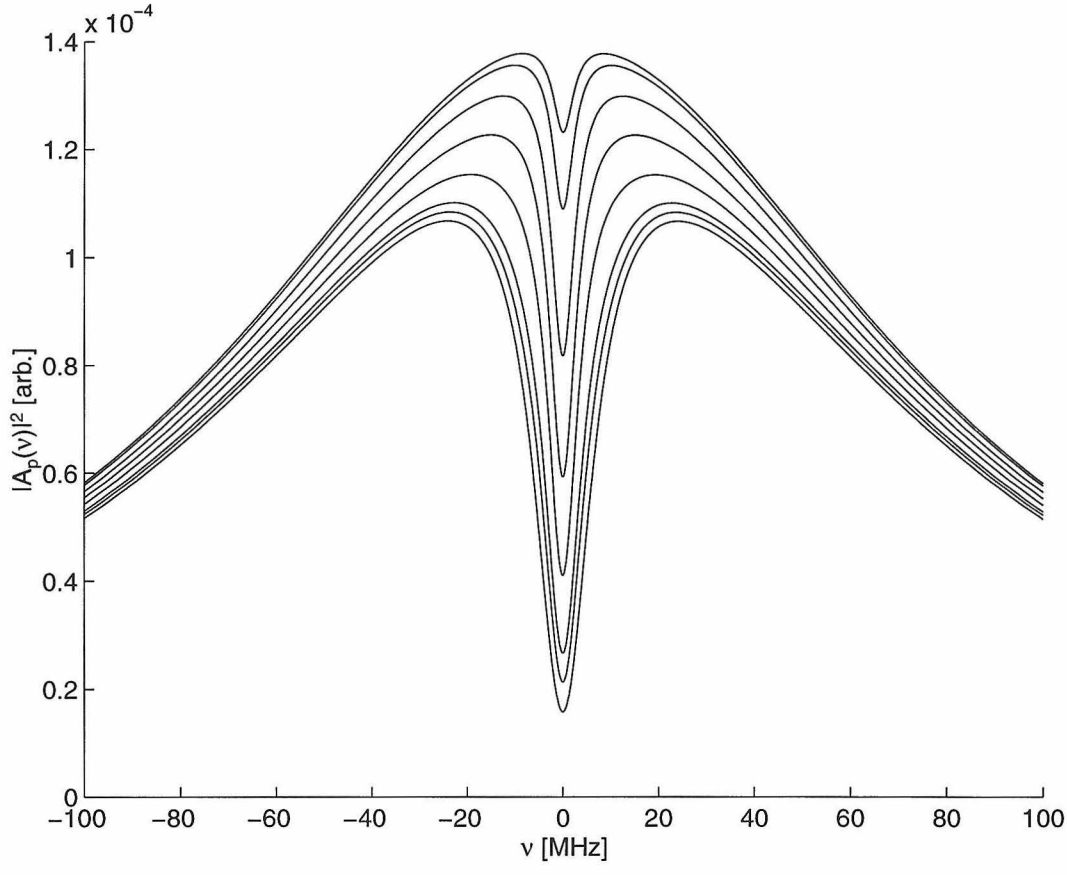

Figure 3.4: The effect of broadband squeezed vacuum on the transmission spectrum of an atom-cavity system, for various degrees of squeezing. From bottom to top, $N = 0, 0.1, 0.2, 0.5, 1, 2, 5, 10$. Note that this calculation is done in the strict bad cavity limit it which there is no atom-enhanced cavity decay. $C = 1$, $(g, \gamma_\perp, \kappa)/2\pi = (20, 2.5, 80)$ MHz.

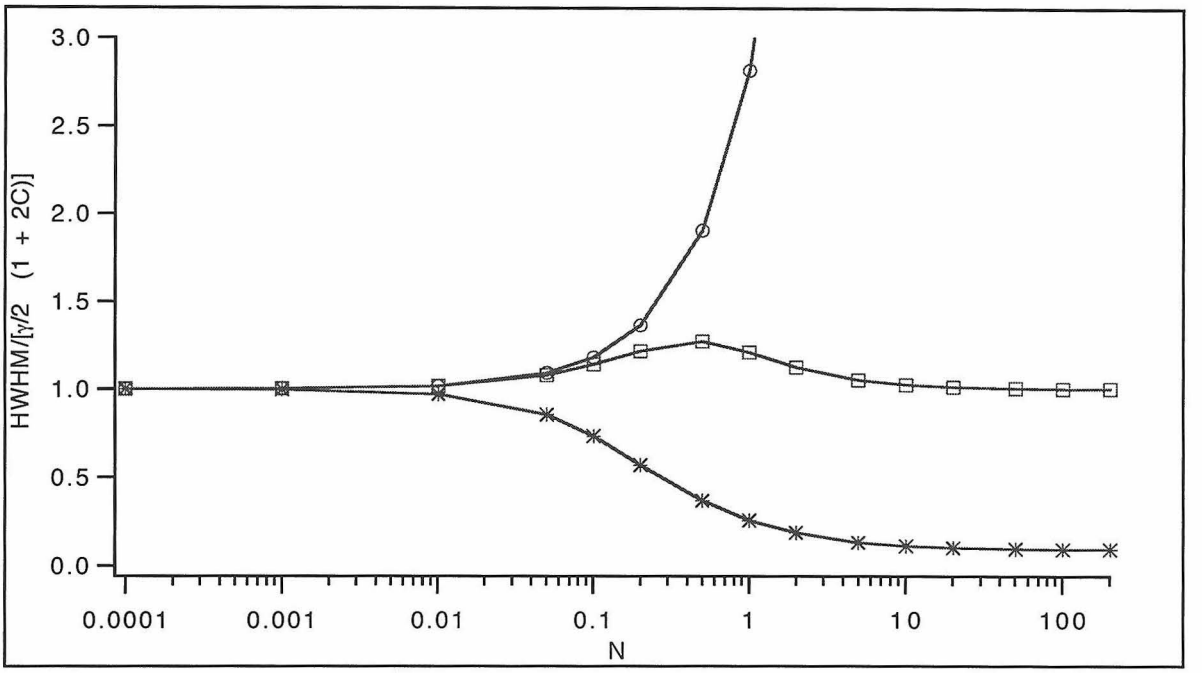

Figure 3.5: Widths for various kinds of light. Quantum squeezing: $*$; Classical squeezing: $\square$; Thermal: $\bigcirc$.

is fixed by C, $b_{\pm}$ (or G_{+} via Eqs. 3.18 3.19), and the strength of the drive field Ω. These are all *measured parameters* of each instance of the experiment, so we should have a complete theory to compare to the experiment (albeit a grossly simplified one in terms of the discussion of Section 2.1.3.3).

Despite the added complication, and perhaps surprisingly, the transition to narrowband squeezing has only a small effect on the transmission spectra shown in Fig. 3.4, even though our squeezing bandwidth does not even cover the full enhanced atomic linewidth. Rather than pursue this point further, I will now turn my attention to a different measurement.

3.2.2.3 Phase-sensitive transmission

The measurement of the transmitted spectrum of the atom-cavity in squeezed vacuum turns out to be a difficult one (more on this below). In pursuing this second measurement strategy, which attacks the problem from a completely different angle, it was hoped that an effect of the squeezing would be more pronounced, or more robust

against complications of the experiment. I will now describe this second measurement scheme.[3]

In this new scheme, there are again two fields incident on the atom-cavity. This time, one is a *displaced* squeezed field. For concreteness, I will call the coherent displacing field the "reference" field. The other incident field is the fixed frequency, weak probe which is resonant and of fixed power. We measure the transmission of the weak probe as we change various parameters of the system. There are three parameters that we can change: the degree of squeezing (via the OPO gain G_+), the amplitude Ω of the reference field, and the orientation ϕ of the squeezing ellipse with respect to the reference field.

Now consider the scenario outlined in Fig. 3.6. We probe the 1D atom as in Chapter 2. First we apply the coherent reference field to saturate the atoms to some desired level (1). The transmitted field will be at some DC level (the dashed line in Fig. 3.6(2)). Next, we apply the squeezed field and monitor the probe transmission as a function of the phase of the squeezed light with respect to the reference field. The transmitted probe field will oscillate at twice the frequency at which the squeezing is rotating around the coherent reference field (solid curve in Fig. 3.6(2)). Let me emphasize that for a weak probe, which we are considering here, the modulation of the probe will be independent of its strength.

The level of the transmitted probe field with squeezing will be different from the level without the squeezed field, which I will suggestively call the "vacuum-only" level (it is the transmission of the probe with only a vacuum field on the end of the coherent reference field "stick," see Fig. 3.3a). Could it be the case that a dip of the transmission below this "vacuum"-only level is one of the elusive indicators of the quantum nature of the squeezed field? In other words, is this level analogous to the "vacuum level" defined by the shot-noise of a local oscillator on a photodiode? The answer is, alas, not so straightforward. Apparently, in some cases yes, in some cases, no. I will now explore the relevant parameter space to find those locations in which the vacuum-only level is an indicator akin to the shot-noise of a homodyne

[3]The idea for this measurement came in discussions with Scott Parkins.

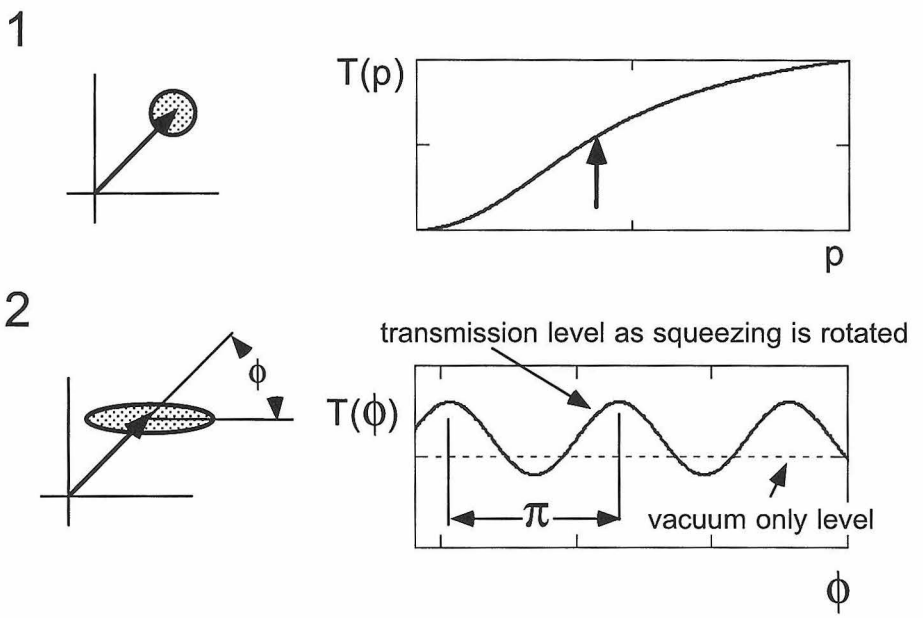

Figure 3.6: The idea of the phase-sensitive transmission measurement.

squeezing measurement. I want to point out here that the measure of a nonclassical effect that we are considering is not identical to a measurement in which the noise spectrum of a squeezed field is directly compared to a shot-noise level of a LO. Here we are considering the *probe transmission* as a measure of the potentially nonclassical interaction of the squeezed vacuum and the 1-D atom: we are using the 1-D atom as a detector.

The quantities to consider are formally the maxima and minima of the phase sensitive transmission amplitude. I define the normalized modulation amplitudes as:

$$\epsilon_{\pm}^{\mathrm{p-p}} \equiv \frac{A_p^{\pm}(\omega=0) - A_p^{\mathrm{nosqz}}(\omega=0)}{A_p^{\mathrm{nosqz}}(\omega=0)} \tag{3.36}$$

in which $A_p^{\mathrm{nosqz}}(\omega=0)$ represents the transmission amplitude with only the coherent reference field and no squeezing and $A_p^{+}(\omega=0)$ is the squeezing-in-phase amplitude transmission and $A_p^{-}(\omega=0)$ is the squeezing-out-of-phase amplitude transmission. What I mean by in- and out-of-phase is that the squeezing ellipse is aligned with the reference field for in-phase ($\phi=0$) and the squeezing ellipse is aligned perpendicular to the reference field for out-of-phase ($\phi=\pi/2$), with reference to the definition of ϕ from Figure 3.6. Eq. 3.36 is a measure of the height above ($\epsilon^{\mathrm{p-p}}>0$) or below ($\epsilon^{\mathrm{p-p}}<0$) the "vacuum-only" level.

Once again, we must determine the behaviour of the probe transmission for inputs other than squeezed light, in order to identify an effect that is unique to squeezed light. Rather than perform an exhaustive search, we will take a classical squeezed field as the test case—as it is a non-quantum field with fluctuations which vary with phase. In Figures 3.7, 3.8 and 3.9 I plot the normalized envelope of the modulation $\epsilon_{\pm}^{\mathrm{p-p}}$, for both quantum squeezed light and classical squeezed light as a function of OPO gain G_+, for three values of the coherent field amplitude. Parameters are chosen to be similar to those of our DOPO and 1D atom: $\gamma_{\parallel}=5$ MHz, $2\kappa=168$ MHz, $C=0.95$, $\eta=1$, $\kappa_a=2.4\gamma_{\parallel}$, where η is the efficiency of coupling of the squeezed field to the cavity. (This will be discussed in more detail later in this chapter.)

This series of figures (3.7–3.9) helps to outline the experimental strategy. The

line at $\epsilon_{\pm}^{\mathrm{p-p}} = 0$ serves to demarcate the "vacuum"-only level. If the envelope of the modulation dips below this level, this could be indicative of a purely nonclassical effect We attempt to determine whether this is so by plotting $\epsilon_{\pm}^{\mathrm{p-p}}$ for both the quantum squeezed case and the classical squeezed case, for several values of the coherent reference field amplitude Ω. In Fig. 3.7, only the quantum squeezed case dips below the "vacuum" level, the classical squeezing goes immediately up from zero gain. For this level of coherent reference field, the dip below zero does seem to be an indicator of a nonclassical effect. However, in Fig. 3.8, the classical squeezing also dips slightly below zero, though not in nearly as pronounced a way as the quantum case. In Fig. 3.9 both fields dip well below the (now-irrelevant) "vacuum"-only level. Thus there does appear to be a regime in which quantum squeezing has a unique effect, but it is a limited regime. Unfortunately, in addition, the regime is defined by the drive field strength, which is not necessarily known to sufficient absolute accuracy, and the relevant region is for low gain, where the overall modulation signal is smallest.

3.3 Experiment

3.3.1 Generating the squeezing

This is a two-lab experiment. Lab 1 contains the 1-D atom apparatus explained in Chapter 2. Lab 2 generates the squeezing. Since I am not a denizen of Lab 2 (that honor goes to Nikos Georgiades), I will only explain the generation of squeezing in passing. It is covered more fully in Refs. [140, 141]. A Ti:Saph laser, locked to Cesium at 852 nm pumps an optical parametric oscillator above threshold to generate frequency doubled blue light at 426 nm. This doubled light pumps an OPO operated below threshold, which downconverts one high energy photon into two correlated low-energy photons (via a non-ideal and more complicated version of the squeezing operator of Eq. 3.5) to serve as the source of squeezed light. The OPO cavity bandwidth (FWHM) is $\kappa_s = 2.4\gamma_{\parallel} = 2\pi \times 12$ MHz, which as stated earlier is less than $\gamma_{\parallel}(1 + 2C)$, the full-width of the cavity-enhanced 1-D atom. The OPO is capable

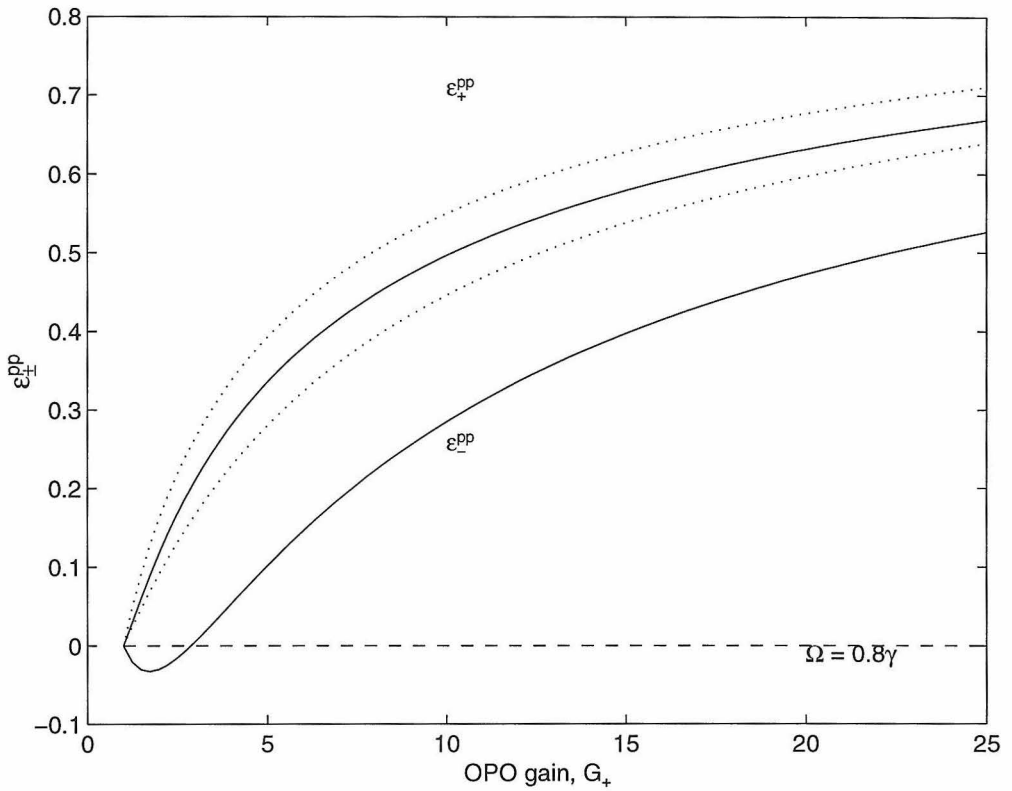

Figure 3.7: Envelope of amplitude modulation $\epsilon_{\pm}^{\mathrm{p-p}}$ as a function of gain G_+ for quantum (solid line) and classical (dotted line) squeezed light. The parameters are: $\gamma_{\|} = 5$ MHz, $2\kappa = 168$ MHz, $C = 0.95$, $\eta = 1$, $\kappa_a = 2.4\gamma_{\|}$, as appropriate for the experiment. The coherent reference field amplitude is $\Omega = 0.8\gamma$.

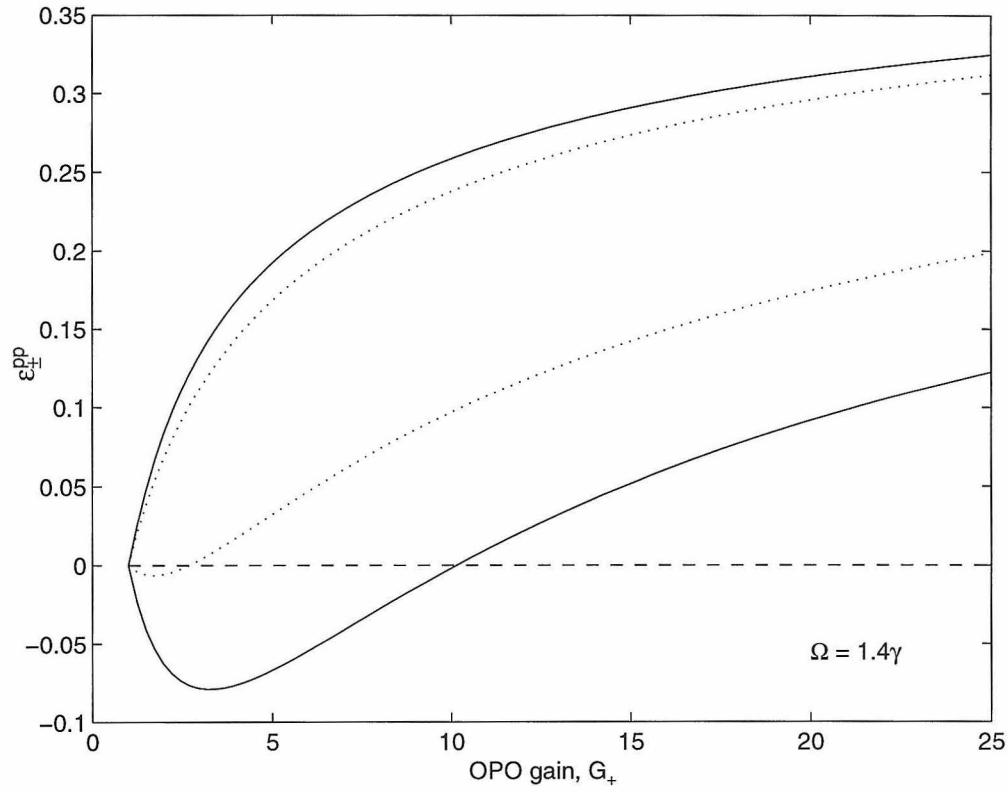

Figure 3.8: As in Fig. 3.7, with larger coherent reference field amplitude $\Omega = 1.4\gamma$.

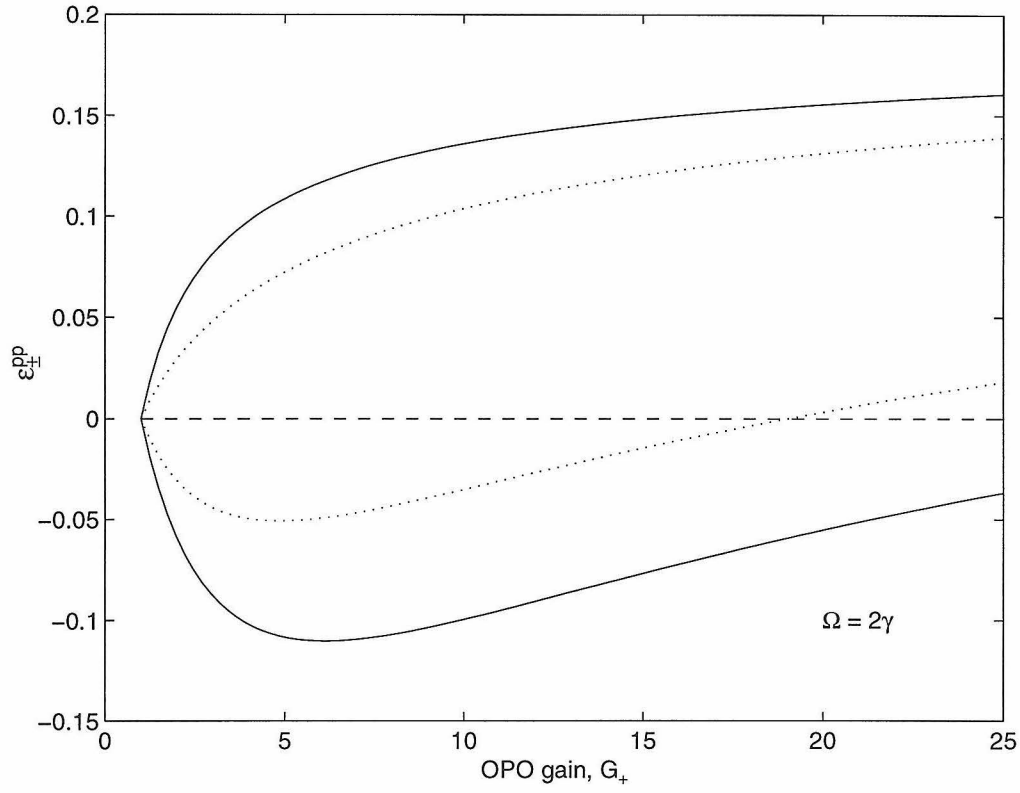

Figure 3.9: As in Fig. 3.7, with yet larger coherent reference field amplitude $\Omega = 2\gamma$.

of producing squeezed light with noise level reduced by 6 dB below the shot-noise level, near the OPO cavity peak. The gains that can be reached in practice range over $0 < G_+ < 20$. The squeezed field typically carries a few pW of optical power. The displacing reference field can have virtually arbitrary power P_{ref} but is typically restricted to $P_{ref} < 200$ pW, since at this point, the 1-D atom is entirely saturated.

3.3.2 Getting the squeezing into the cavity

To my knowledge, a rather important practical issue has been left mostly unconsidered in the literature. This is the issue of getting the squeezed light from an external source into the atom-cavity. In much of the work done on the subject of squeezed light interaction with atoms in cavities, the squeezing is inserted in a rather idealized way directly into the cavity. In this picture, the effects of the squeezed light (whatever they happen to be) are always better the larger the cooperativity parameter C_1 is made. But if we consider the point made in Section 2.1.1.1.3, that the atom can be treated as a lossy intracavity medium with associated loss-parameter

$$\delta_A = 2(\delta_1 + \delta_2)C_1, \tag{3.37}$$

then it is not at all clear that large C_1 is the optimal approach. For large C_1, the associated intracavity losses δ_A are also large, so the squeezed field does not actually build up in the cavity. To emphasize this point, I have plotted in Figure 3.10 the cavity buildup and the cavity reflectivity as C is increased. For these plots, the cavity is one-sided, with the input mirror $\delta_1 = 350$ ppm, the essentially perfect back mirror $\delta_2 = 1$ ppm and $\delta_0 = 0$, as required for Eq. 3.37 to be valid. From Figure 3.10 we clearly see the expected behavior in that the buildup decreases as C is increased. This does not really help us determine an optimal value of C however, as the buildup is largest when there is no atom in the cavity. The cavity reflection does, however, imply an optimal value of $C = 1/2$. At this point, there is no squeezed light reflected from the cavity, so in some sense, the most squeezing possible is building up in the cavity (in the presence of an atom) and interacting with the atom. This idea can

be further quantified in the third and final graph of Fig. 3.10. We have seen that the effect of the squeezing is to modify the cavity-enhanced decay rate of the atom: $\beta_{\pm} = \gamma_{\perp}[1 + 2C_1\Delta X_{\pm}]$. The squeezing varience $\Delta X_{\pm}$ is the one that actually builds up in the cavity. In our experiment, we have an *external* squeezing with varience $\Delta X_{\pm}^{\text{ext}}$, which then builds up in the cavity *in the presence of the atom* to a value $\Delta X_{\pm} = \mathcal{B}\Delta X_{\pm}^{\text{ext}}$ where $\mathcal{B}$ is the cavity buildup. The product $\mathcal{B}C$ thus determines the effect on the 1-D atom from an external squeezed field. This is plotted in the bottom graph of Fig. 3.10; it is also seen to be optimal for $C = 1/2$. The value of $C = 1/2$ is a generic feature of the one-sided cavity driven through the high transmission mirror, as can be seen from Eq. 3.37 in Eq. 2.10. This is, of course, the case of the impedance-matched resonator. That our 1-D atom has $C_1 \approx 1$ is quite fortuitous from this perspective.

As an extension of this line of reasoning, we can immediately get a qualitative understanding of the detrimental effects of fluctuations in the atomic beam density. We have seen in Section 2.1.3.3 that there are some time instances when the average coupling is larger than the nominal value $\bar{N}C_1$. These events, which in the case of $\bar{N} = 1$ occur with non-negligible frequency, will act to prevent the squeezing from building up in the cavity. Additionally, when there is one atom near the maximum of the cavity field, there are still many spectator atoms on the wings of the Gaussian and near the nodes of the standing-wave. These atoms contribute an additional loss mechanism, without being sensitive to the photon statistics of the squeezed field. This is likely to be the single greatest problem with this experiment. In this light, we have attempted to run the experiment with $\bar{N} \approx 0.5$, where the large-coupling events occur less frequently, and the contribution of the spectator atoms may be smaller. Unfortunately, this lowers $C = \bar{N}C_1$, so that the effects of the squeezed light will be less pronounced. We have not found an optimal balance between these competing effects, and indeed, there may not exist any easy work-around, beyond realizing an optimal system in which a single, stationary and localized atom is employed.

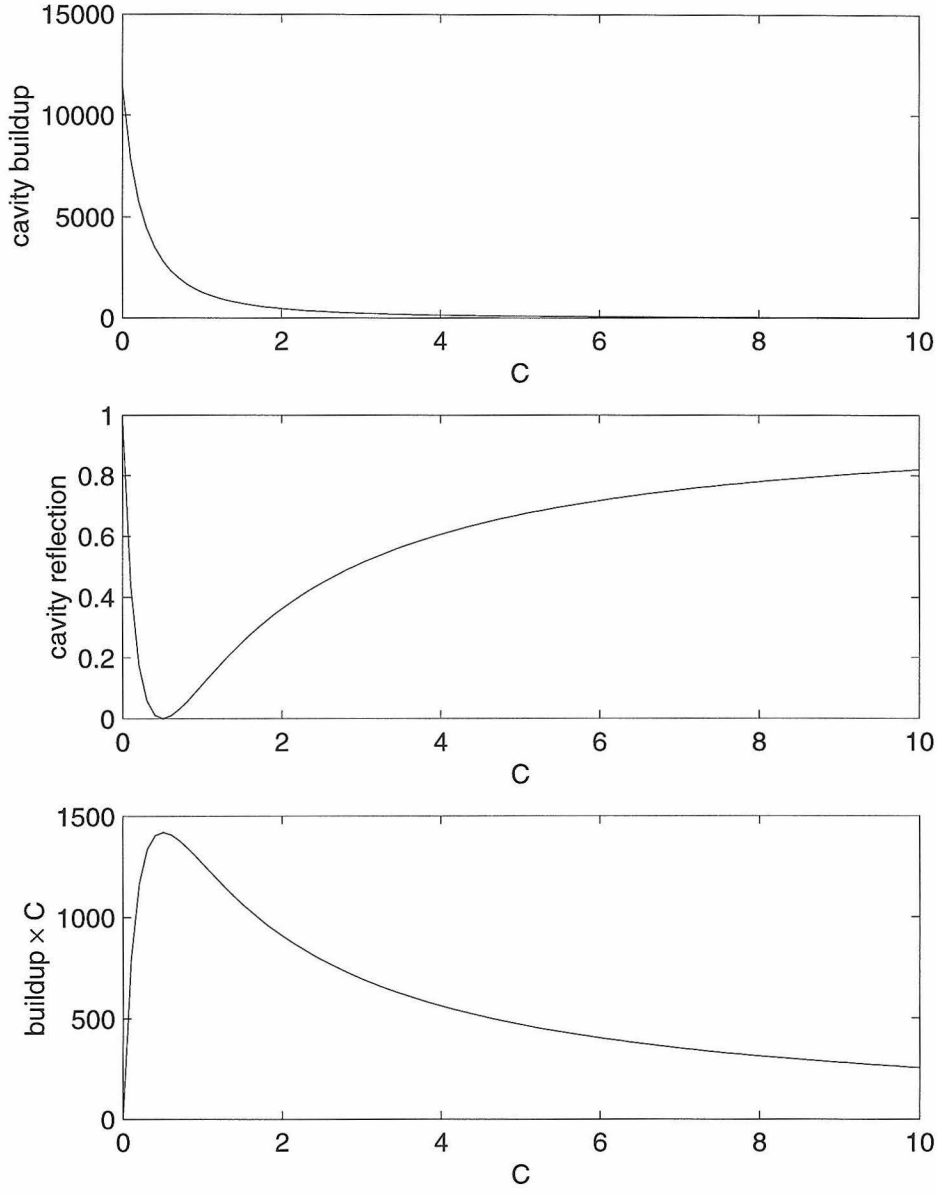

Figure 3.10: The cavity buildup, reflection and buildup-C product vs. C. The buildup is given by Eq. 2.11 with Eq. 3.37, and the reflection is given by Eq. 2.11 with Eq. 3.37 with $\delta_1 = 350$ ppm, $\delta_2 = 1$ ppm and $\delta_0 = 0$. The product buildup $\times$ C is discussed in the text.

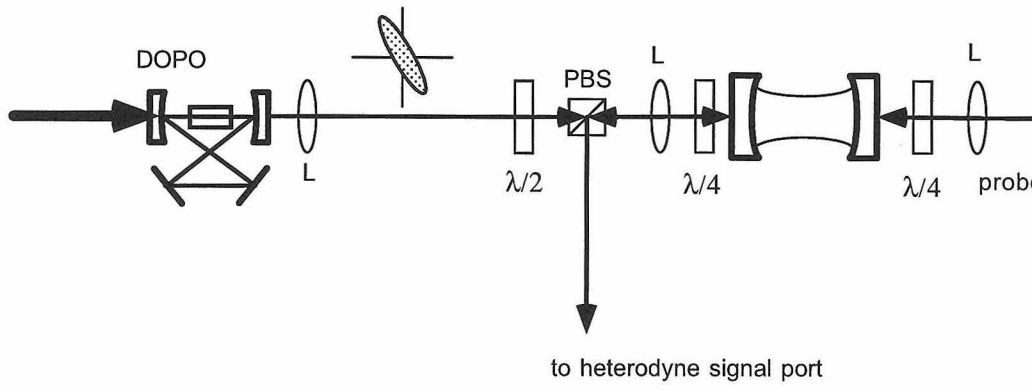

Figure 3.11: The squeezing on atom-cavity experimental schematic.

3.3.3 Measurements of probe transmission spectra with squeezing

The experimental arrangement for the spectrum measurements is shown schematically in Figure 3.11. A weak probe is scanned in frequency across the atom-cavity resonance (coincident as usual). The transmission is measured both with and without the squeezed vacuum input. The squeezed vacuum (no coherent reference piece) enters the cavity through the output coupler ($\delta_2 = 350$ ppm) of the cavity. The polarizations are arranged so that the squeezed field has the same helicity (σ^+-pol) as the probe field. Because of this, the squeezed light bounces off of the cavity and is reflected along the same path as the probe transmission, and will be detected at the heterodyne detector. Because the squeezing beats against the LO, and has power spread over some bandwidth given by κ_s, this gives rise to what amounts to a measurement of the spectrum of output power of the OPO. This "measurement" was used to assure us that there was actually light from the OPO and that the detuning of the squeezed field was near zero. This detuning tended to drift during the experiment so it was important to check it periodically.

The heterodyne detector is sensitive to all the incident fields, in various ways, so an elaborate, but straight-forward procedure of subtracting various quantities was

employed. Consider the following sequence of measurements:

	atoms on	**probe on**	**squeezing on**	**measured quantity**
M_1	NO	NO	NO	$k_d B_g$
M_2	NO	NO	YES	$k_d B_g + k_d S_e$
M_3	YES	YES	NO	$k_d B_g + k_p k_d A_v$
M_4	YES	YES	YES	$k_d B_g + k_p k_d A_s + k_d S_a$
M_5	YES	NO	YES	$k_d B_g + k_d S_a$
M_6	NO	YES	NO	$k_d B_g + k_p k_d R_c$
M_7	NO	YES	YES	$k_d B_g + k_d k_p R_c + k_d S_e$

where I have called k_d the detector efficiency, k_p the efficiency of probe generation, B_g the background spectrum, S_e the squeezing spectrum reflected from an empty cavity, S_a the squeezing spectrum reflected from a cavity with atoms (different from S_e), A_s the probe transmission for atoms in the presence of squeezed vacuum, A_v the probe transmission for atoms in the presence of normal vacuum (squeezing blocked), and R_c the empty cavity probe transmission, which is of course the same with or without squeezing. The measured-quantity column is the incoherent sum of the constituent contributions (all of which are defined as power, not amplitude spectra). Now the quantities

$$S_v \equiv \frac{M_3 - M_1}{M_6 - M_1}, \quad S_s \equiv \frac{M_4 - M_5}{M_7 - M_2} \tag{3.38}$$

are the corrected atom-cavity spectra without and with squeezing, respectively. Note in particular that S_v is the same as the measured normalized transmission T_n of Eq. 2.17. In practice, it turns out that there is negligible contribution to the detected photocurrent from S_a, as the 1-D atom effectively eliminates the squeezed field reflection, as expected from Figure 3.10.

Additionally, we can define the quantity Δ_s

$$\Delta_s \equiv S_s - S_v \tag{3.39}$$

as the difference between the spectra with and without squeezing. The initial motivation for looking at Δ_s was the hope that the spectrum with squeezing would be

an approximate Lorentzian dip with the same depth as the vacuum case, but with a decreased width reflecting the inhibition of the enhanced spontaneous emission, discussed above. The difference of two such lorentzians has a characteristic zero point on resonance and unique shoulders. Alas, this naive guess proved to be inadequate, but Δ_s stayed in place for historical reasons. (To jump ahead, see Figure 3.17 for a look at what the predicted difference curves are.)

In the absence of generic theoretical criteria which provide unequivocal tests of the nonclassical effect of squeezed light on an atom in a cavity (especially for our particular realization of that system) it is essential to find *measurements* which differentiate light of various quantum (or classical) character. We have done this by exciting the atom-cavity with both squeezed vacuum and thermal light from a single mode of the non-degenerate OPO (NOPO). If the OPO is locked off of the Cs transition by one longitudinal mode (650 MHz away) such that the next longitudinal mode is resonant with the Cs transition, then the correlations will be between one photon that is resonant with the Cs transition and one photon that is 650 MHz detuned from the Cs transition. Thus the squeezing will be lost, and the 1-D atom will be illuminated with a purely thermal mode. The key to this technique is that the thermal light from the NOPO is identical in all respects to the squeezed light from the DOPO—except for the classical statistics of the former and the quantum statistics of the latter. For the same phase sensitive gain, the bandwidth of both sources is the same and the number of photons in each source is the same. For purposes of comparison, we define the quantity analogous to Δ_s of Eq. 3.39 for thermal light and call it Δ_t.

The effect of the squeezed (or thermal) light proved to be rather small, making the experiment a particularly difficult, and ultimately, unconvincing one. Of the many transmission spectra we have taken, I show in Figure 3.12 a spectrum with vacuum and squeezed inputs, and in Figure 3.13 a spectrum for (practically) identical conditions with thermal and vacuum inputs. The parameters for these data were: $\bar{N} \approx 1$ and $P \approx 2$ where P is a relative measure of the power in the squeezed field (I forget what it is in absolute terms). It can be stated only to some qualitative level that the conditions are identical, because the procedure to switch from squeezed to thermal

excitation did take some time, over which conditions could drift. It was attempted to attain the same conditions by demanding the same measured OPO gain, and (equivalently) by matching the size and shape of the power spectrum reflected from the empty cavity. Despite these efforts, there is no particularly striking aspect of the data which points to the fundamental difference between thermal and squeezed inputs. Unfortunately, the difference spectra do not help to clarify the matter to any great extent. Fig. 3.14 is Δ_s for squeezed input and Fig. 3.15 is the corresponding Δ_t for an "identical" thermal input. All the difference spectra are averaged without regard for experimental parameters (the OPO gain is the only one anyway) and shown in Fig. 3.16. We have argued [150] that the shape of these curves is different, especially in the wings, where the thermal difference spectrum dips below that of the squeezing, as would be expected (see Fig. 3.17).

Independent of these details, by far the most disappointing aspect of the data is the relative height of the two difference peaks. The prediction[4] based on the theory of Section 3.2.2 is that the height of Δ_s should be approximately half as large as that of Δ_t. (A Lorentzian that narrows without losing height will lead to a difference spectrum which dips to zero at line center.) It is only as the efficiency η of coupling of the squeezed (and thermal) field to the cavity is decreased that the two predictions fall atop one another. This is shown in Figure 3.17. Even with a significant effort to improve the matching of the squeezed field to the cavity and to minimize propagation losses, the overall size of the effects never really improved. For the record, a mode-matching of coherent output of the OPO to the 1D atom cavity of at least 20:1 was attained and the total loss from OPO output to cavity input was no more than 20%. In fact, a homodyne was constructed right in front of the 1D atom cavity and the squeezing was measured to be in agreement with that obtained just outside the OPO cavity. (As well, the correspondence between the OPO gain and the degree of squeezing was experimentally confirmed.) We therefore do not believe that η was actually as small as the theory would require to explain the lack of height difference between the squeezing and thermal difference spectra. Among the

[4]Again, from A. S. Parkins

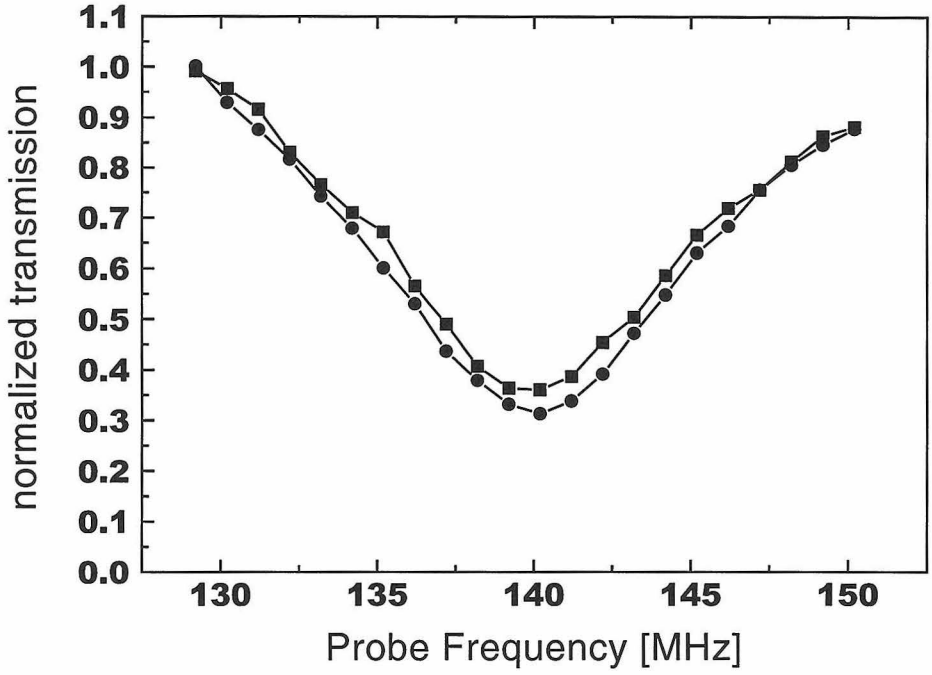

Figure 3.12: The probe spectrum with squeezed light excitation. With squeezing: ■, vacuum-only: •. The coincident atom-cavity resonance is at 140 MHz.

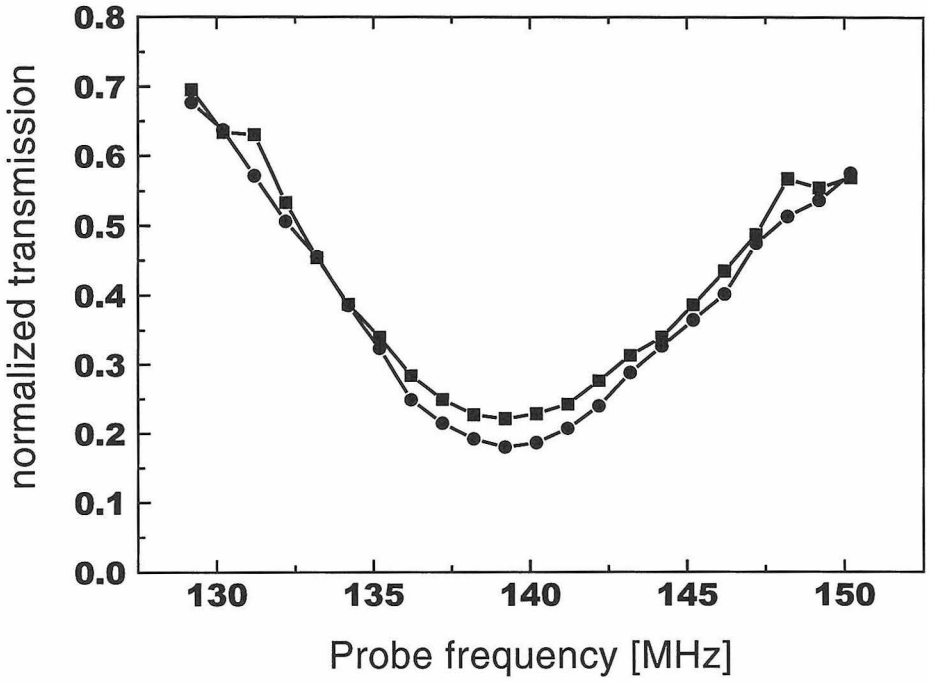

Figure 3.13: The probe transmission spectrum with thermal light excitation. With thermal: ■, vacuum-only: •. The coincident atom-cavity resonance is at 140 MHz.

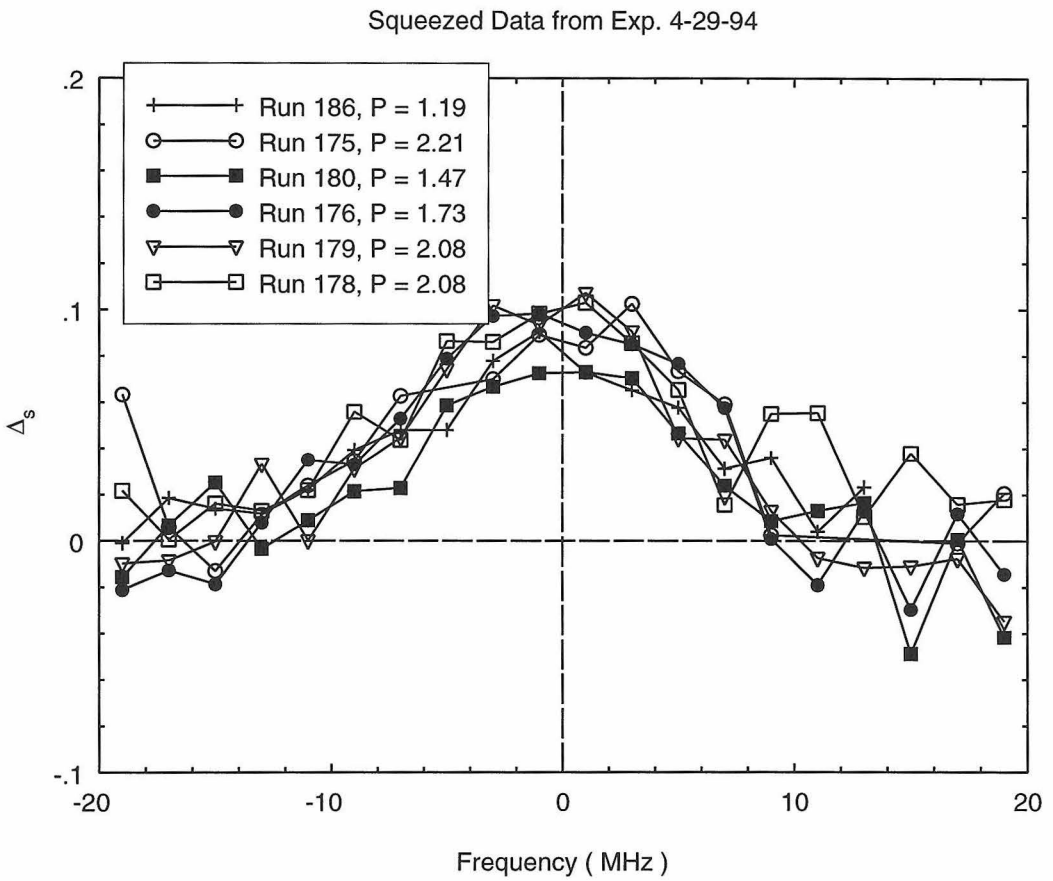

Figure 3.14: The difference spectrum Δ_s with squeezed light excitation.The coincident atom-cavity resonance is at 0 MHz.

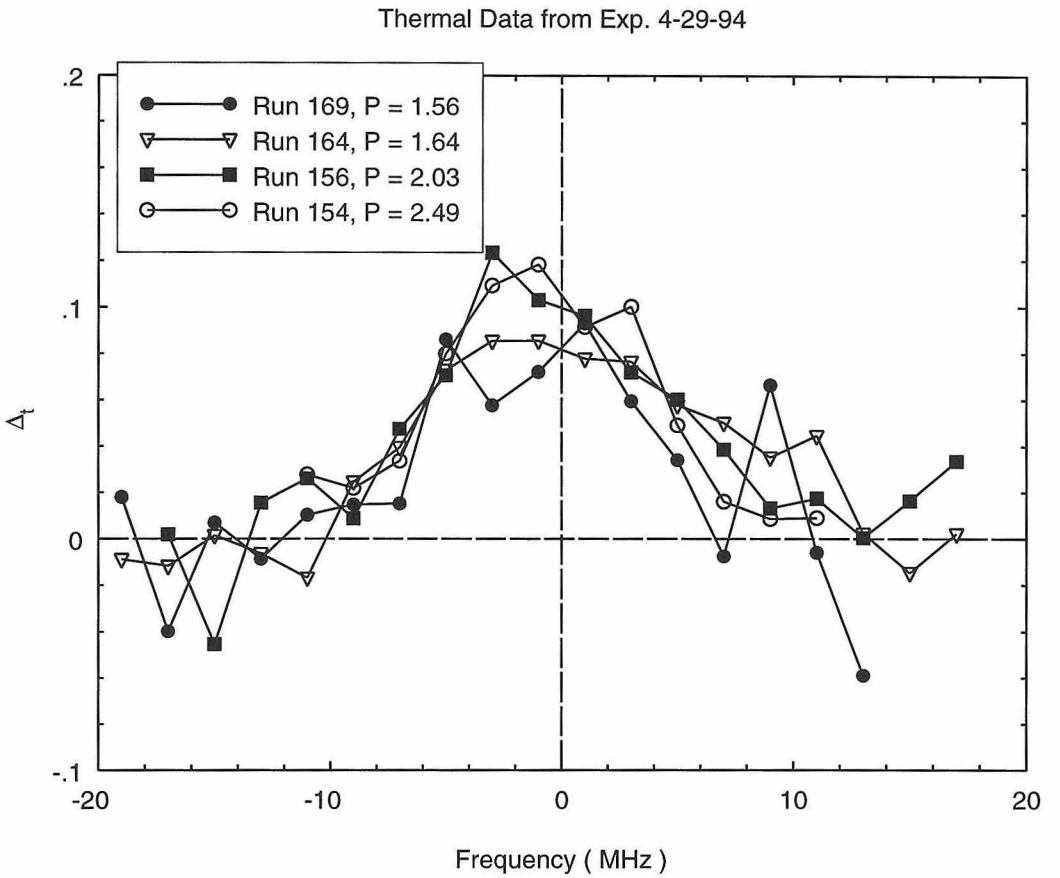

Figure 3.15: The difference spectrum Δ_t with thermal light excitation. The coincident atom-cavity resonance is at 0 MHz

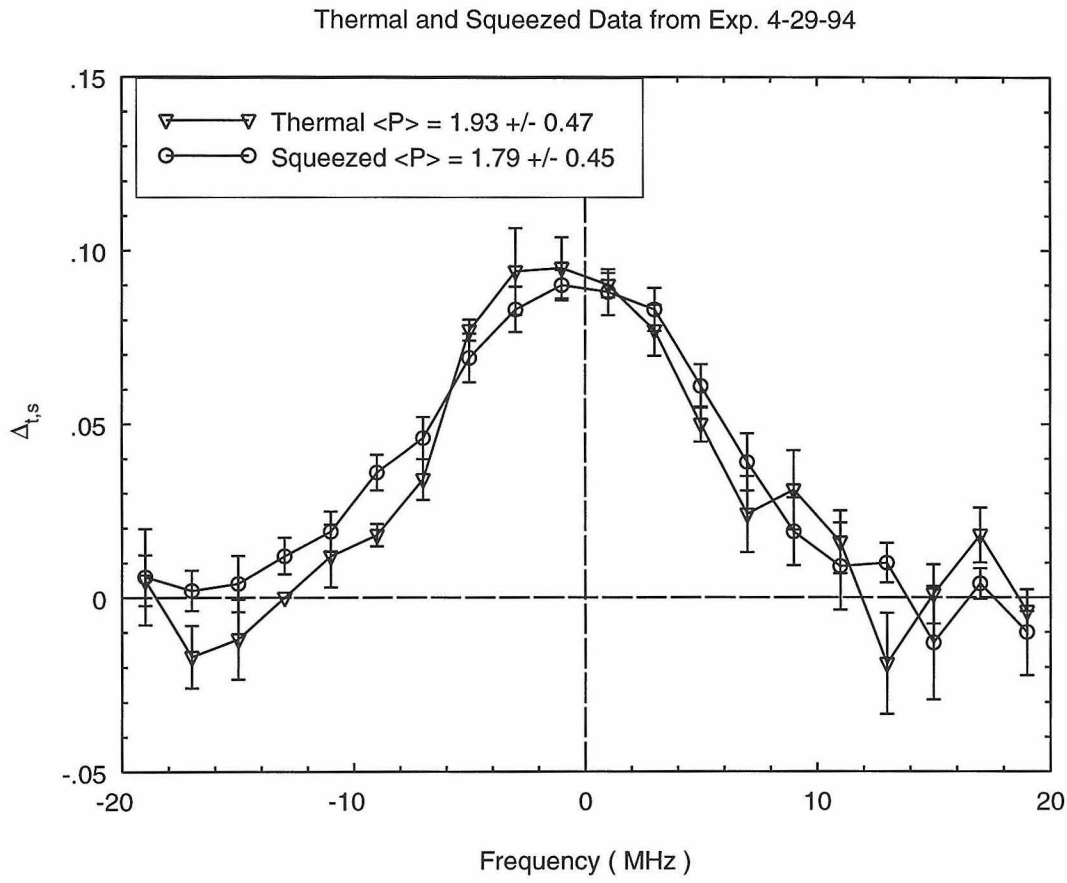

Figure 3.16: Averaged difference spectra, thermal and squeezing. The coincident atom-cavity resonance is at 0 MHz

possible explanations are: effects due to internal losses of the cavity, which were ever-increasing over the 3 years that this cavity was used ($0 < \delta_0 < 50$ ppm), or effects due to the "spectator" atoms on the wings of the Gaussian cavity mode. Simple evidence that multiple atoms in the mode volume is detrimental comes from the observation that in a two atom situation, it is still only C_1 (not C) that can be switched off by the squeezed light, so that the effect of the squeezing becomes relatively smaller in a multi-atom case. As discussed above, in Section 3.3.2 beam fluctuations are the leading candidate. Also, the experiment is performed using two independent optical tables in two separate labs. It is certainly possible, though unlikely, that we have overlooked a mechanism responsible for the degradation of the experimental results.

3.3.4 Measurements of phase-sensitive transmission

Faced with the small signals from the spectra measurements, we decided to pursue the phase-sensitive technique which we had hoped would lead to clearer results. The apparatus is shown in Figure 3.18. The technique is as discussed in Section 3.2.2.3.

Based on the expected size of the modulation signal (up to 25% modulation in Figure 3.8, e.g.), the measurement should have been straight-forward. It turned out not to be. Because of this, the measurement process became convoluted in its dedication to getting quantitative results from rather small modulation signals. The measurement procedure consisted of the following. The SA is as usual set to the center frequency of interest (to measure the probe-LO beatnote), and set in zero span. The phase of the squeezing is rotated with respect to the coherent "reference" field with the PZT of Figure 3.18. This causes a modulation of the probe transmission, which in turn produces a time-oscillating signal in the photocurrent, which is converted to a time-oscillating signal on the SA. The rf-demodulated beat-note signal from the SA video out is directed to the HP3562A dynamic signal analyzer (DSA), which is used essentially as a low-frequency spectrum analyzer. The DSA analyzes the frequency content of the SA video-out signal, with a peak in the power spectrum corresponding to twice the frequency at which the squeezing ellipse is rotated. There is no peak

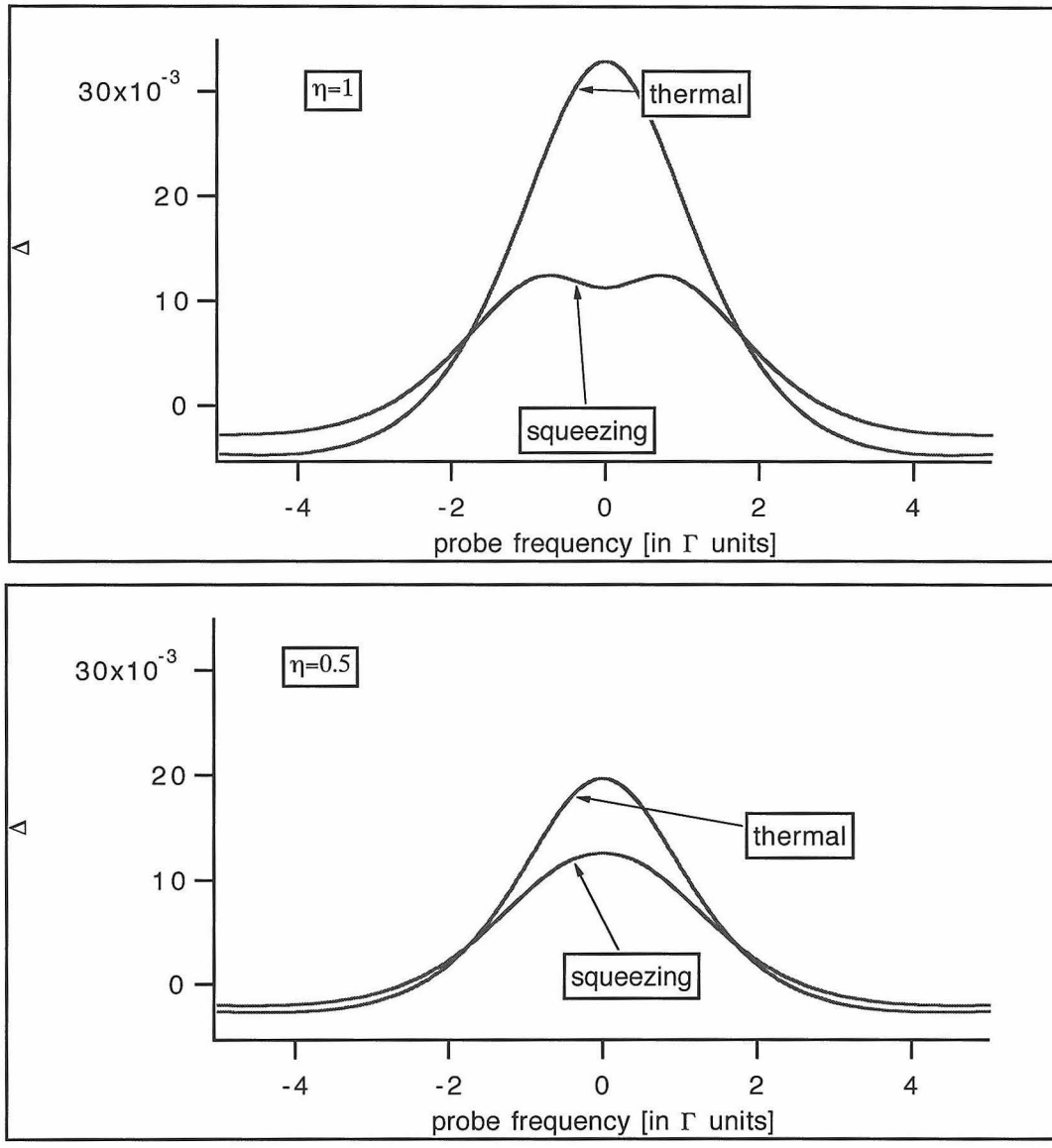

Figure 3.17: The effect of diminishing efficiency η on the difference spectra $\Delta_{s,t}$

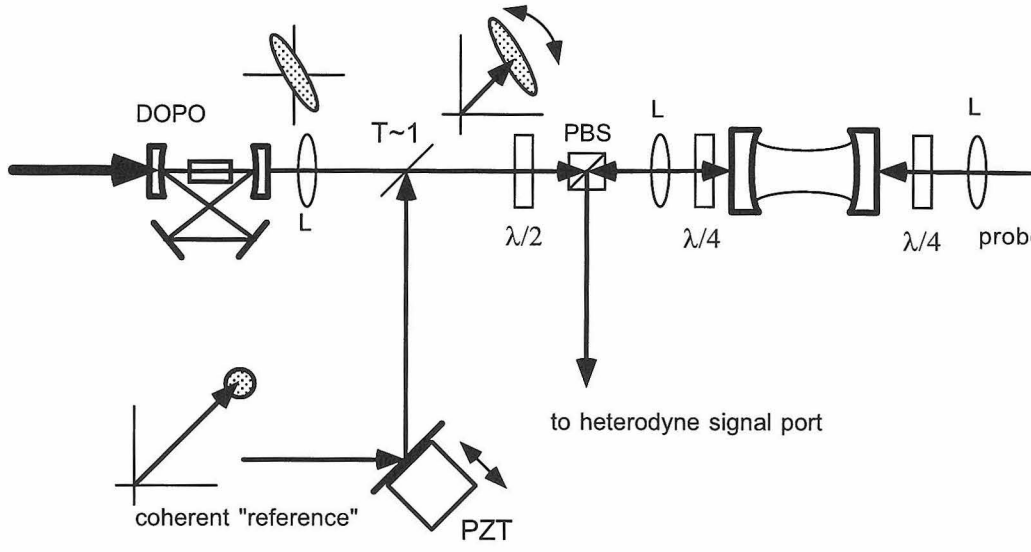

Figure 3.18: The phase-sensitive transmission measurement apparatus.

when the atoms are not present, confirming that the modulation is not merely a result of the squeezing ellipse detected on the heterodyne (there is no simple way for this to be the case anyway). The nominal frequency of squeezing-ellipse rotation is determined by making an interferometer with the coherent reference and an auxiliary coherent beam on the same path as the squeezing. A typical DSA trace is shown in Figure 3.19, showing the peak at the probe modulation frequency. This peak at 300 Hz shows that the probe transmission does indeed have frequency content at twice the frequency of rotation of the squeezing-ellipse, which is independently determined to be 150 Hz.

Note that while the frequency domain S/N is respectable, we were never able to directly resolve the modulation in the time domain. Therefore, due mainly to technical limitations, we are unable to measure the envelope described by Equation 3.36. We can, however, measure the pk-pk magnitude of the modulation. A measure of the magnitude of the pk-pk probe modulation is conveniently given by the "amplitude

fractional modulation," defined as

$$\alpha_{pp} = \frac{|A_P^+(\nu) - A_P^-(\nu)|}{|A_P^{\text{no sqz}}(\nu)|}, \tag{3.40}$$

which is normalized to the "vacuum"-only level $A_P^{\text{no sqz}}(\nu)$. Often, $\nu = 0$ for resonant probe measurements. That Eq. 3.40 is indeed the measured quantity can be determined by a knowledge of the heterodyne detector and by tracing the fate of modulation signals from the photocurrent to peaks in the power spectrum provided by the DSA. First, the heterodyne detector is sensitive to the field amplitude as can be seen from Eq. 2.15. To check the photo-current-SA-DSA chain, an empirical test was performed in which a sinusoidal signal of known pk-pk amplitude and offset is put directly into the SA input. The chain is then traced to the output of the DSA, from which predictions of the *amplitude* of the original sine-wave can be directly inferred. Since we are taking differences of quantities, it could have been the case that we would be sensitive only to a quantity such as $\sqrt{A_P^+(\nu)^2 - A_P^-(\nu)^2}$. This turns out not to be the case, however. Since the photocurrent is sensitive to the field amplitude, it undergoes the same transformation as the test sine-wave, so the measured quantity is indeed given by Eq. 3.40.

Because we could only measure the size and not the sign of the modulation, we were of course unable to observe the modulation as it possibly dipped below the "vacuum-only" level discussed above. Also, unfortunately, in this experiment we have no direct means to compare the quantum system with a classical system as we did in the spectra measurements (Section 3.3.3) with the thermal light and the squeezing (thermal light has symmetric fluctuations, after all). The logical choice would be the classical squeezing as discussed in Section 3.2.2.3, but a source of this type of light was not realized. Nonetheless, we were able to map out the behaviour of the system under variation of many parameters, and the results agree quite well with the *shape* of predictions. The absolute magnitude of the effects, was however significantly below the predictions.

I will now discuss the actual measurements and the data that we have taken

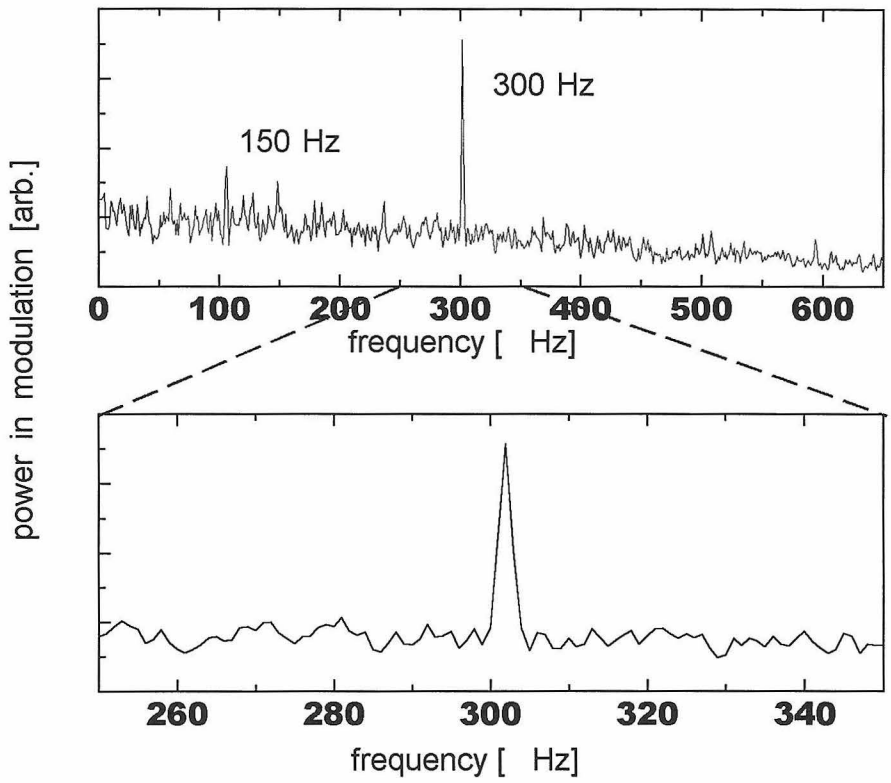

Figure 3.19: The signal from the DSA, after rf demodulation from the SA.

from them. The displaced squeezed field is nominally on resonance. Just as in the spectra measurements for the frequency-dependent probe transmission, the displaced squeezing reflects from the cavity and impinges on the heterodyne detectors. The beat note is very broad and subject to large (several MHz) excursions, since it is between two independent lasers, neither of which is (in absolute terms) stabilized exceptionally well. Thus it is important to get the reference field away from the probe, since subtracting of its beat note is nearly impossible. Actually, the pump did occasionally interfere with the probe, but since our measurement is sensitive only to modulation in the probe transmission, and not the dc level, this proved to be less of a problem than it otherwise could have been. In any event, the reference field and the probe field were separated sufficiently (probe + 2 MHz detuned, reference field −2 MHz detuned from resonance) so that the "vacuum"-only level could be measured without contamination.

We have made measurements of α_{pp} under the following conditions. (1) fixed OPO gain with variable reference field power; (2) fixed reference power with varied OPO gain; and (3) fixed reference power and fixed gain with variable probe frequency (the modulation spectrum). We have also measured α_{pp} as the number of atoms $\bar{N}$ was changed. We attempted to avoid contributions to the signals from the spectator atoms by going to ever smaller mean atom numbers. It was typical for us to work in the regime of $\bar{N} \approx 0.5$ atoms, corresponding to the fluctuations breakdown in the bottom graph of Fig. 2.13. At this operating point the influence of multiple atoms is smaller but of course hand in hand with this is that the empty cavity is a dominant contribution and the overall size of the effect is smaller.

Figure 3.20 shows the amplitude fractional modulation α_{pp} of Eq. 3.40 as a function of the OPO gain G_+ for a fixed coherent reference power of 25 pW. The coherent reference power is measured via its beat-note with the local oscillator on the heterodyne detectors, which is calibrated to account for efficiency of overlap of these beams (which are generated from independent lasers). The fractional modulation eventually saturates, in keeping with the idea that the effect of the squeezing is not limitless, but saturates at the point when the cavity-enhanced spontaneous emission is inhibited.

Even with infinite squeezing, the effect of the squeezing can only be so large. This is certainly also seen in Figures 3.7–3.9.

Figure 3.21(top) shows the amplitude fractional modulation α_{pp} as the reference power is increased for fixed OPO gains of $G = 5$ and 10 (for slightly different numbers of atoms). The modulation amplitude reaches a peak somewhere near the point at which the probe transmission is halfway between its value for an empty cavity and its value for atoms in the cavity with no applied reference field. Again, this is probably not surprising, as the saturation slope is steep at this point and levels off in either direction. The probe saturation curve for the same range of coherent reference power (in the same units) with no squeezed field is shown in Fig. 3.21(bottom) for comparison. (Note that the probe is fixed power in this trace, it is the reference field power that is being varied.)

Figure 3.22 shows the amplitude fractional modulation α_{pp} as the probe detuning is swept for fixed reference power and OPO gain. The squeezing frequency is fixed on resonance. The effect of the squeezing is most noticeable on resonance, not surprisingly.

Just to complete the discussion, I also show the fractional amplitude modulation α_{pp} as the number of atoms is varied in Figure 3.23. This data is for a mish-mash of other parameters, hence the wide variation in α_{pp} at each atom number. We were unable to get the oven to produce any more than $\bar{N} \sim 2$ atoms, unfortunately, as it would have been interesting to mark the point at which the probe modulation disappears (assuming that it does in the many-atom case).

From the theory of Section 3.2.2.2 we have a "no free parameters" prediction for the measurements of Figures 3.20–3.23. Actually, there is one slightly free parameter—η. In fact, by adjusting η the data falls reasonably well onto the predictions. This is shown in Figure 3.24, which has selected data (the $G_+ = 5$ α_{pp} vs. Ω data from Fig. 3.21 and the α_{pp} vs. G_+ data from Fig. 3.20) plotted with the predictions. Unfortunately, the required η is exceptionally small at $\eta = 0.15$, whereas experimentally we estimate $\eta > 0.70$ from measurements of cavity mode-matching and propagation losses. With a theoretical $\eta = 0.30$, the classical squeezing ($M = N$) predictions

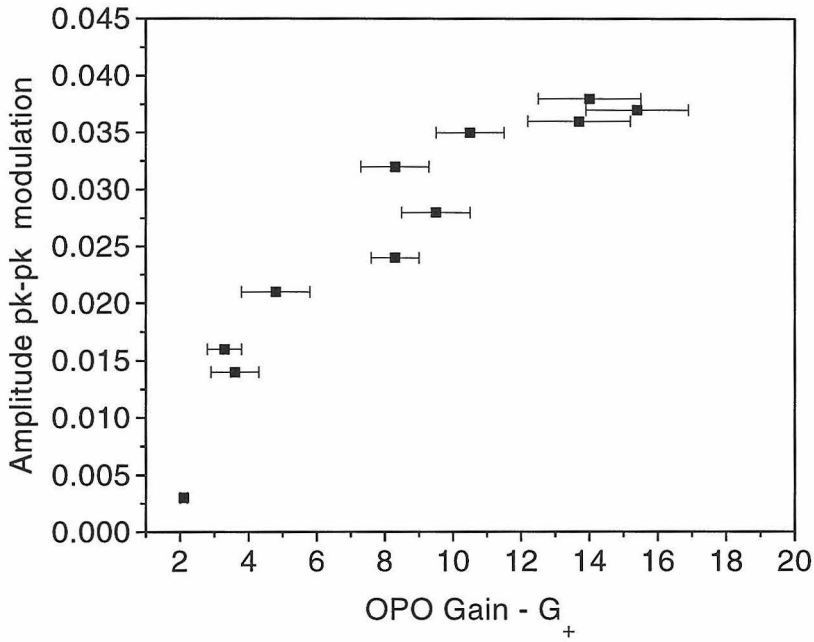

Figure 3.20: Amplitude fractional modulation α_{pp} vs. OPO gain G_+. The reference power is $P_{ref} = 25$ pW, $\bar{N} = 0.7$.

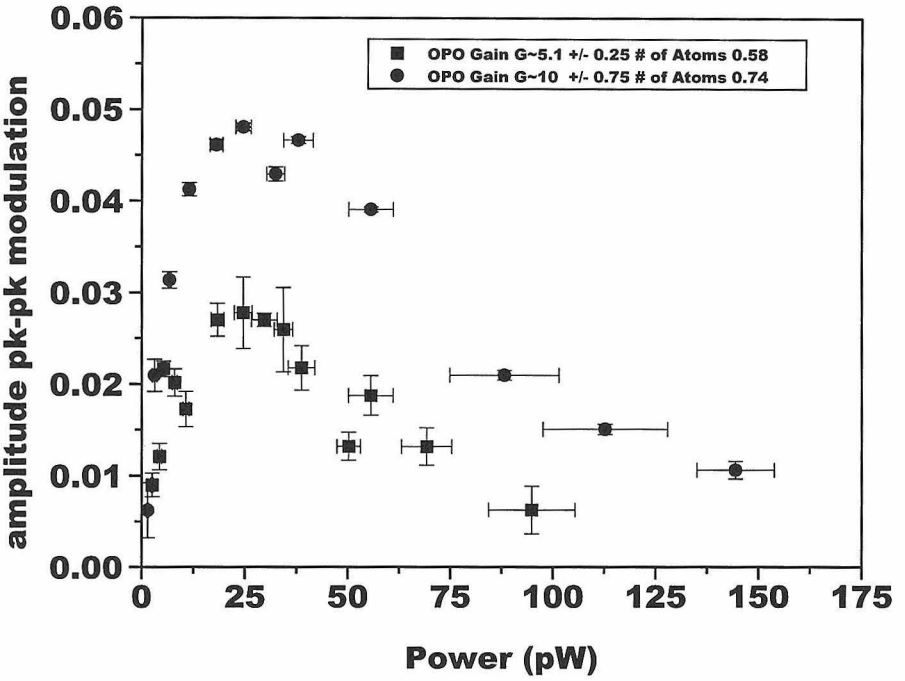

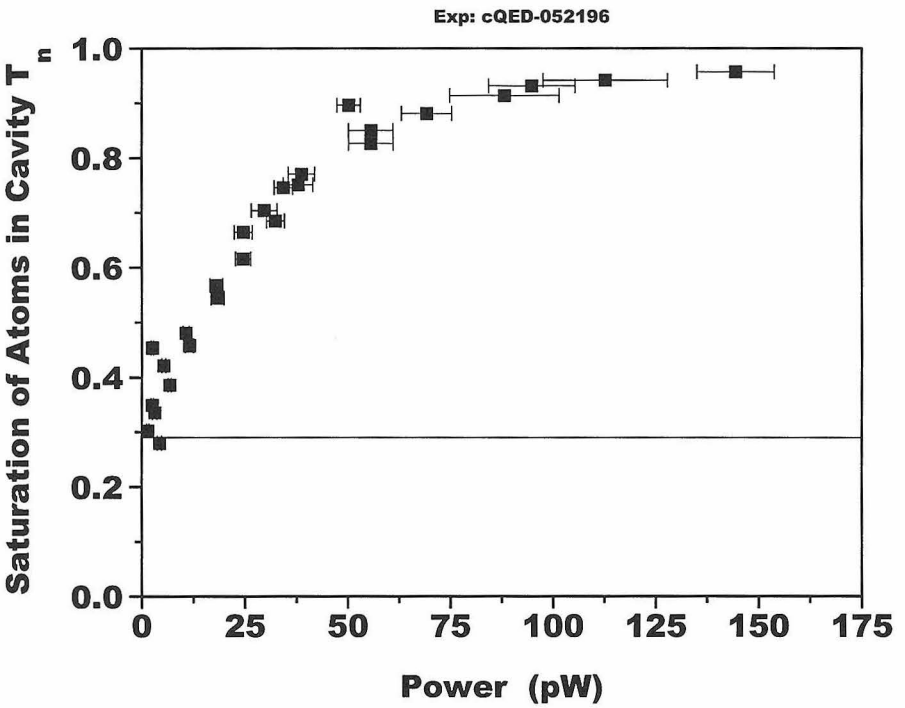

Figure 3.21: Amplitude fractional modulation α_{pp} vs. coherent reference power (top). Saturation of the probe transmission for the same coherent reference input, no squeezing (bottom).

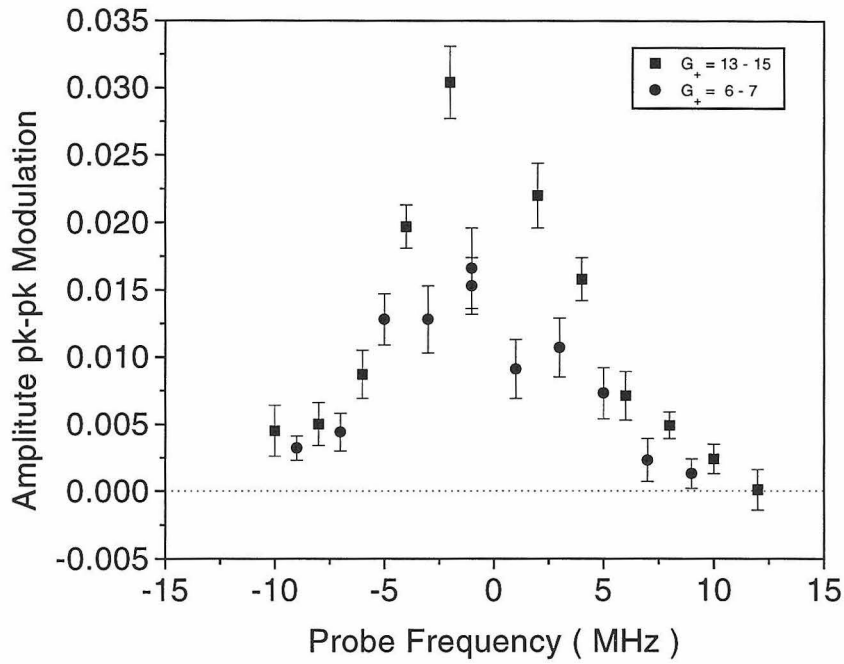

Figure 3.22: Amplitude fractional modulation vs. probe frequency. Reference power P_{ref} =, common atom-cavity center is at 0 MHz.

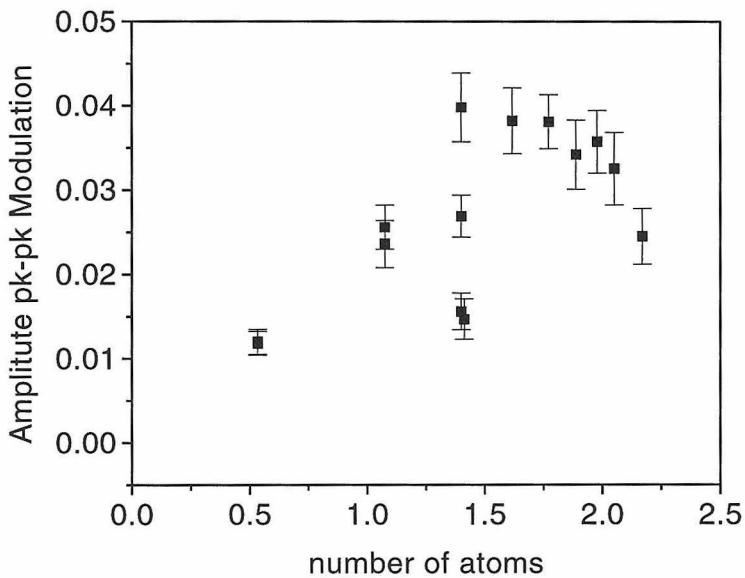

Figure 3.23: Amplitude fractional modulation vs. number of intracavity atoms. $0 < G_+ < 20$, $0 < P_{ref} < 150$ pW.

match the data every bit as well! While we do not have a quantitative explanation for why the data seem to be the result of a drastcally reduced value of η, we can look to the discussion of Section 3.3.2 for a qualitative one. This is the contribution of the spectator atoms as a pure loss mechanism which prevents the squeezing from building up in the cavity, thereby diminishing any observable effects. Presently, we believe this to be the single most likely cause of our reduced signal sizes.

The value of $\Omega = 1.4\gamma_{\parallel}$ for the top graph of Fig. 3.24 gives the best "fit" (χ-by-eye) to the data with all other parameters fixed by the experiment: $\bar{N} = 0.6$, transit broadening $\gamma_{\rm tr} = 0.215\gamma_{\parallel}$ (in keeping with $\Gamma = 0.7$), $2\kappa = 168$ MHz, $\kappa_s = 2.4\gamma_{\parallel}$ (and with $\eta = 0.15$). In order to get the theory and the data on the same x-axis for the graph on the bottom of Fig. 3.24, I must match the measured coherent reference power P_{ref} (measured in pW) with the theoretical quantity Ω^2. I do this by "fitting" (χ-by-eye) the data shown in the bottom graph of Fig. 3.21 to a theoretical prediction. This allows us to make the association from pW of reference power to Ω^2. By doing this, I have found that P_{ref} [pW] $\leftrightarrow S_c[\Omega/(\gamma_{\parallel}(1+2C))]^2$, with $S_c = 125 \pm 50$ pW. (The error completely brackets the data.) (Note that this has been done for only one data set with a fixed value of C.) I then scale the theory by this amount to arrive at the bottom graph of Figure 3.24. This method accounts for factors which would otherwise be difficult to take into account, such as the difference in saturation between one localized atom with cooperativity C and a sample of atoms with $\bar{N} = 1$ and $\bar{N}C_1 = C$. The α_{pp} vs. P_{ref} data itself is used for final adjustment of the conversion from Ω^2 to P_{ref} [pW]. I find that a scaling with $S_c = 75$ "looks" best. Other parameters of the theory are fixed by their measured values: $\bar{N} = 0.58$, $\gamma_{\rm tr} = 0.215\gamma_{\parallel}$, $2\kappa = 168$ MHz, $\kappa_s = 2.4\gamma_{\parallel}$, as before. Given the complexity and difficulty of this experiment, I find it remarkable that the data follow any noticeable trend at all, let alone one that fairly closely follows that of the theoretical predictions. Equally remarkable, is that a simplified (yet still complicated) theory is capable of predicting the trends of the experiment. (It is a matter of perspective.) It is unfortunate that we are not able to make any definitive statement that we are observing manifestations of the nonclassical interaction between atoms and squeezed light. Nonetheless, there

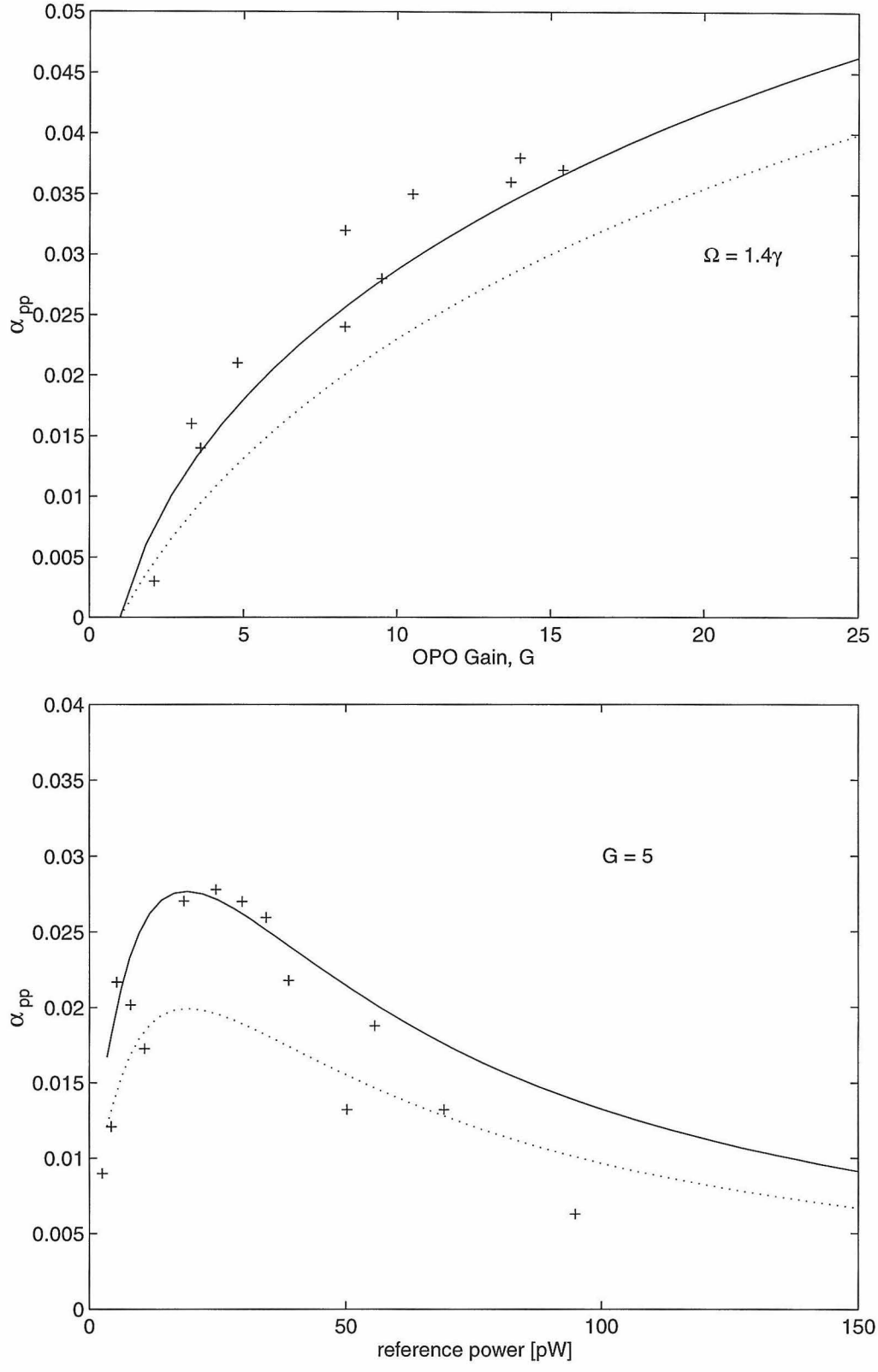

Figure 3.24: Phase-sensitive transmission theory with data. The solid lines are the quantum-squeezing theory and the dashed lines are the classical-squeezing theory, the + are the data. Top graph: data from Figure 3.20. Bottom graph: data from Figure 3.21. See text for a full discussion.

are unquestionably some interesting results from the experiment pertaining to issues that have yet to see the harsh light of the laboratory.

3.3.4.1 Driving through M_1 *vs.* driving through M_2

To end this chapter, I will point out one last item. In the normal saturation measurement, we know only what output flux F_o through mirror M_2 corresponds to a given intracavity field. We do not keep track of or care about the input power at mirror M_1 that lead to this intracavity field. For the squeezing experiment however, we drive (with photon flux F_d) through the output mirror M_2, and want to build up the same intracavity field. What is the relationship between F_o and F_d, both for an empty cavity and a cavity with one atom? It is a somewhat confusing, but trivial task to calculate that in the case of a one-sided cavity with no atoms that $F_d/F_o = 1/4$, so that the drive field should be 4 times smaller than the measured output flux to create the same intracavity intensity. In the case with atoms, the atoms can be treated as a loss mechanism as discussed in Section 2.1.1.1.3 and Eq.3.37, so that in this case, it is found that $F_d/F_o = (1+2C)^2/4$. For $C \sim 1$, the drive field on M_2 must be 9/4 times *larger* than the measured output flux to obtain the same intracavity photon number. We know from Chapter 2 that the 1D atom normalized transmission is approximately doubled for $\bar{n} \approx 0.1$. This corresponds to an output power of $F_o \approx 25$ pW (from Section 2.1.5). The same should occur driving $F_d \approx 50$ pW through M_2. From Fig. 3.21(bottom) this actually appears at more like 25 pW. This is probably due to the fact that my treatment of the atom as a cavity loss mechanism is valid only in the weak-field, and these are both strong fields.

Chapter 4 Quantum Phase Gate

The 1-D atom exhibits a unique single-photon nonlinearity which has been used to demonstrate the principle of a simple quantum logic transformation. In quantum logic, the goal is to control the quantum state of one particle with the quantum state of another particle. When the particles are simple two-state systems, each state can be assigned a truth value; in analogy to a classical bit we can thus define the quantum binary digit, or qubit. Quantum computation exploits the fact that qubits can exist in entangled states, allowing simultaneous exploration of many computational paths at an exponential rate in the number of qubits. The difficulty in realization of laboratory quantum logic comes in the attainment of the strong coupling between qubits necessary for conditional logic, and the preservation of quantum coherence essential to the retention of fidelity over the course of the computation. The 1-D atom provides a medium in which photons can be used as qubits and conditional dynamics between them realized, in a system with minimal dissipation. The efficient and fast input-output channel of the 1-D atom (via κ) allows convenient qubit transfer to and from the gate. The quantum logic gate considered here, the quantum phase gate (QPG), relies on the property that a photon incident on the 1-D atom acquires a phase shift during interaction with the medium. Due to the sub-unity critical parameters of the 1-D atom, a single photon can saturate the atomic response and act as a switch which can turn off the phase shift that another photon would experience. The two states of our photon qubits are polarization states. Due to a circular birefringence of the atomic absorption, one polarization state can control the atom-cavity phase while the orthogonal polarization does not affect the state of the system—this is the conditional logic. A measured conditional phase shift Δ of 16° *per photon* has been achieved and the truth table of the QPG has been constructed.

Once again, I was not alone for this experiment. Most of the daily set-up and data acquisition was done by me and Christina Hood, with some invaluable assistance

by Wolfgang Lange. Hideo Mabuchi provided many key ideas on how to implement quantum computation in cavity QED and put in many hours on the PRL. In addition, we were helped by many fruitful discussions with Seth Lloyd.

4.1 Quantum computation

I will not discuss much of the background of quantum computation here. Many general-interest papers exist on the topic [151, 152, 153, 154, 155], and the popular press has latched onto it quite enthusiastically.[1] The early discussions of quantum mechanical computing by Deutsch [156] and Feynman [157, 158] are also good introductions to the subject. I will merely provide a simple-minded introduction here.

The power of the quantum computer (QC) derives from quantum correlation: that is, coherent superposition and multi-particle entanglement. Consider a register of quantum mechanical bits (qubits) composed of a collection of two-state particles. Whereas a classical bit (cbit) can exist in either the state 1 (true) or state 0 (false), a qubit can be prepared in a coherent superposition of true and false such as $\Psi_{qubit} \propto |1\rangle + |0\rangle$, where I have labelled the qubit states in analogy to the cbit states. A quantum register can thus be prepared in a superposition of all of its possible states: if the classical 3-bit register can store any of the integers 0 through 7, the corresponding 3-qubit quantum register can store all of these integers simultaneously, leading to an exponential gain in storage capacity. This has been referred to as the "inherent massive parallelism" of the QC. Operations on these superpositions lead to entanglements between multiple particles. The Hilbert space occupied by quantum states, including entanglements grows exponentially with the number of qubits. That is basically the whole of the magic of quantum computation.

Just as any operation in a classical computer can be built up from a few fundamental logic gates which operate only on two cbits at a time, so too with the QC. In

[1] QC has been the subject of several articles in *The Economist* (including Jan. 13, 1996, p. 78), one in *The Dallas Morning News* (Feb. 12, 1996, p. D1), one in *Electronics World* (April 1996, p. 273), one in *Signal* (April 1996, p. 47). QC has been in *Byte Magazine* (April 1996) in an article entitled "Three new directions for the future of computing." QC even made the "over-hyped" list in *Wired*! All this before anyone has demonstrated an even slightly practical QC device.

the quantum computer, the logic gate is replaced by virtually any "nontrivial" unitary operation. Nontrivial in this sense means "capable of conditional dynamics between two qubits." The quantum gate is said to be universal if any computation can be built up from that gate alone, augmented with one-qubit operations [159, 160]. For a concrete and simple example, one such "universal" quantum logic gate (when supplemented by simple one-qubit operations) is the quantum controlled-NOT (QCN) gate [161]. In the QCN, the "target" qubit is flipped if and only if the "control" qubit is true. The "truth table" of the QCN gate is described by:

$$\begin{aligned} |0\rangle_a|0\rangle_b &\rightarrow |0\rangle_a|0\rangle_b \\ |0\rangle_a|1\rangle_b &\rightarrow |0\rangle_a|1\rangle_b \\ |1\rangle_a|0\rangle_b &\rightarrow |1\rangle_a|1\rangle_b \\ |1\rangle_a|1\rangle_b &\rightarrow |1\rangle_a|0\rangle_b \end{aligned} \tag{4.1}$$

in which a is the control and b the target qubit.

By tracing the transformation of the QCN gate, it is easy to see that some superposition input states lead to entangled output states; for example, $(|0\rangle_a + |1\rangle_a)|0\rangle_b \xrightarrow{\text{QCN}} |0\rangle_a|0\rangle_b + |1\rangle_a|1\rangle_b$. This output state of the QCN cannot be factored into a direct product of states of the independent qubits; the particles are entangled. The useful information of a QC is processed via the correlations created and manipulated during the course of the computation, since it is the entangled states which lead to the vast size of the multi-particle state-space.

Due to the nature of quantum measurement, extracting the information contained in the composite state of all the qubits comprising the QC is challenging. In general, one must seek global properties of a computational output state since a QC can explore many computational paths simultaneously, but collapses to a single result upon measurement. The outstanding example is Shor's factoring algorithm [162] which exploits the observation that finding the prime factors of a number N can be reduced to the problem of determining the period of the function $F_N(a) = y^a \text{mod} N$ where y is a random coprime of N and $F_N(a)$ is to be evaluated over all integers

a. This utilizes optimally the ability of a QC to extract global properties (in this case the period) of a system. The resulting method has a run-time which scales as a polynomial in the size of the input number, whereas all known classical algorithms scale exponentially. Shor's algorithm has led to an explosion of interest in quantum computation, largely because current crypto-systems rely on the classical difficulty of locating the prime factors of large (presently $\sim$ 130 decimal-digit) numbers.

Because controllable quantum entanglement is difficult to achieve in the laboratory, experimental progress in quantum computation, while substantial, has thus far managed to produce only the most rudimentary 2-qubit quantum logic transformations [163] [164]. Any serious quantum computation (one which exceeds the capabilities of present classical computers) will likely involve entanglements between at least 100 qubits for simple simulations of quantum mechanical systems [165] and up to 10^6 particles to factor a 130-digit number using Shor's algorithm [162, 166]. The huge numbers of time-consuming operations that this implies produced a somewhat skeptical early community [167]. Important advancements in the theory of quantum error correction codes [168] [169] [170] [171], enforcement of coherent dynamics [172], and fault-tolerant quantum computation [173, 174] significantly relax laboratory demands on allowable error rates. Applying some of these results[2] gives an estimate for the reliable factoring of a 130-digit number: the required resources are 10^{14} operations and 10^6 qubits, and error rates (ratio of decoherence rate to coherent processing rate) must be $\varepsilon \lesssim 10^{-6}$. (In fault tolerant computation, the error correction process, though subject to the same rate of error as the computational process, does not itself increase the probability of computational error in the final output state.[3] The cost is an increase in required resources.) These numbers provide a somewhat daunting (present state-of-the-art is 1 operation, 2-particle entanglement, and $\varepsilon \sim 10^{-2}$), but concrete goal which is not necessarily beyond an extrapolation of present technology. That is, the numbers are not disallowed by any known physical principles. Decoherence will determine whether realizable QC systems can maintain the required levels

[2]These estimates come from a fault-tolerant scheme investigated by J. Preskill and colleagues.

[3]This point was missed or overlooked in Ref. [167]

of entanglement for the time demanded by the computation. It is not known whether practical and useful devices will ever be realized.

4.2 The Quantum Phase Gate

A more generic quantum logic transformation than the QCN is the quantum phase gate (QPG). Written in the $\{|0\rangle_{a,b}, |1\rangle_{a,b}\}$ basis as for the QCN, the transformation of the QPG is:

$$\begin{aligned} |0\rangle_a|0\rangle_b &\rightarrow & |0\rangle_a|0\rangle_b, \\ |1\rangle_a|0\rangle_b &\rightarrow e^{i\phi_a} & |1\rangle_a|0\rangle_b, \\ |0\rangle_a|1\rangle_b &\rightarrow e^{i\phi_b} & |0\rangle_a|1\rangle_b, \\ |1\rangle_a|1\rangle_b &\rightarrow e^{i(\phi_a+\phi_b+\Delta)} & |1\rangle_a|1\rangle_b, \end{aligned} \tag{4.2}$$

where $\phi_{a,b}$ are the linear 1-qubit phases, and Δ parameterizes the nonlinear 2-qubit conditional phase. Now we have a concrete idea of nontrivial: if $\Delta \neq 0$ then the QPG is capable of universal quantum computation. The QPG satisfies what we take to be a *necessary* criterion for quantum logic—that it create entanglement between qubits:

$$[|0\rangle_a + |1\rangle_a]\,[|0\rangle_b + |1\rangle_b] \xrightarrow{\text{QPG}} [|0\rangle_a + e^{i\phi_a}|1\rangle_a]\,[|0\rangle_b + e^{i\phi_b}|1\rangle_b] + \left(e^{i\Delta} - 1\right)|1\rangle_a|1\rangle_b. \tag{4.3}$$

For $\Delta \neq 0$ Eq. 4.3 is an entangled output state. For comparison with the QCN, which appears to be a simpler transformation, obviously capable of computation, we consider a limiting case of the QPG. Let $\phi_a = 0 = \phi_b$ and $\Delta = \pi$ and perform a sequence of transformations consisting of: 1) rotate qubit b by $\pi/4$; 2) perform a QPG transformation; 3) rotate qubit b by $-\pi/4$. (When I say rotate qubit b by $\pi/4$, I mean apply the appropriate unitary transformation which has the effect of rotation of the state of qubit b by $\pi/4$.) Under these conditions and sequence of operations, the QPG will perform a QCN (with some minus signs). Since the QCN supplemented by single-qubit operations is universal, the QPG is as well. It may take many QPGs toggled together to perform a useful computation (the same is doubtless true for the QCN as well [175]), but on the other hand, there may be a calculation in which

the quantum-controlled rotation is of interest (e.g. the quantum discrete Fourier transform [151]). It would be useful to have a QPG in which Δ could be varied arbitrarily. It is not at all ridiculous (with an extension of the capabilities discussed in Chapter 7) to consider a QPG whose optimally coupled atom has $\Delta \sim \pi$, so that an atom off to the side of the antinode would have $\pi > \Delta > 0$.

4.3 Experimental QPG

Ultimately, the goal is to make a measurement of the truth table of the QPG, Eq. 4.2. Getting to this point is a roundabout and lengthy procedure, so I will begin immediately with a description of the relevant measurements. Clearly the first step is to demonstrate that the 1-D atom is capable of imparting phase shifts to incoming field states and to demonstrate conditional dynamics between these field states. Then with a (believable, hopefully) model of the underlying physics, the next step is to link the actual measurements with the truth table to infer the parameters ϕ_a, ϕ_b, Δ.

Briefly, we use the nonlinear properties of the 1-D atom demonstrated in Chapter 2 and a circular birefringence of the atoms to realize conditional dynamics between polarization states of incident fields.

4.3.1 The atom-cavity phase

4.3.1.1 The $g_- \to 0$ approximation

Consider the atomic system in Figure 4.1. The strong transition is driven with σ^+ circularly polarized light with coupling strength g_+, while the weak transition is driven with σ^- circularly polarized light with coupling strength g_-. In reality $g_- = g_+/\sqrt{45}$, but for purposes of simplicity (without introducing too much error) I will pretend that σ^--polarization does not couple to the atom at all so that $g_- \to 0$. (Recall that $n_s \propto 1/g^2$ so that $n_s^+/n_s^- = 1/45$ and it takes a field 45 times stronger to saturate the σ^- transition.)

The degree to which the $g_- \to 0$ approximation is valid can be directly tested

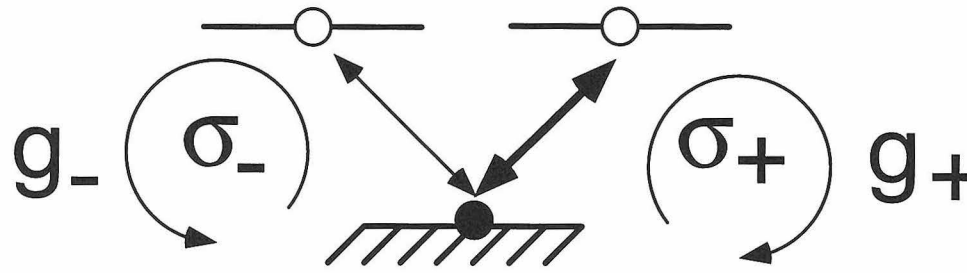

Figure 4.1: The three relevant atomic levels for conditional logic. The $m_F = 4 \rightarrow m'_F = 5$ transition couples to σ_+ circularly polarized light and the $m_F = 4 \rightarrow m'_F = 3$ transition couples to σ_- circularly polarized light. Note that $g_- = g_+/\sqrt{45}$.

experimentally, as we have done in Figure 4.2. These data represent the first of our "pump-probe" type measurements and so I will dwell a moment on the experimental procedure. We measure the normalized transmission (T_n of Eq. 2.17) of a weak probe (labelled a) near resonance (detuned by $\Delta_a\gamma_{\|}/2\pi = -1$ MHz). The atoms in the cavity are saturated with a variable power "pump" field (labelled b), also near resonance (detuned by $\Delta_b\gamma_{\|}/2\pi = +1$ MHz). This slight detuning between pump and probe allows us to monitor either field, by setting the SA center frequency on the frequency of the beat-note between one or the other of the signal fields (a or b) and the heterodyne LO, and setting the bandwidth sufficiently narrow to reject the non-monitored field. Thus the intracavity photon number in each field can be inferred in the usual manner by working back from its associated beat-note size. The weak probe field in this case is polarized σ^+, in order to interact with the closed $m_F = 4 \rightarrow m'_F = 5$ transition. The pump field can be polarized either σ^+ or σ^- and is varied in power from weak to "strong." It can be seen that the saturation curves of the probe transmission for each polarization state of the pump shown in Fig. 4.2 are offset by more than an order of magnitude, it taking that much more power in a σ^- field to saturate the 1D atom. The σ^- situation is muddied by the fact that this polarization does not drive a closed transition, so that when the atom is driven into the excited state, it can ultimately be optically pumped to the $F = 4, m_F = -4$ ground state. This adds significant complication to the interpretation of the measurement. Therefore no attempt has been made to compare an expected theoretical result with the data; they are merely presented as confirmation that the σ^- light does not couple

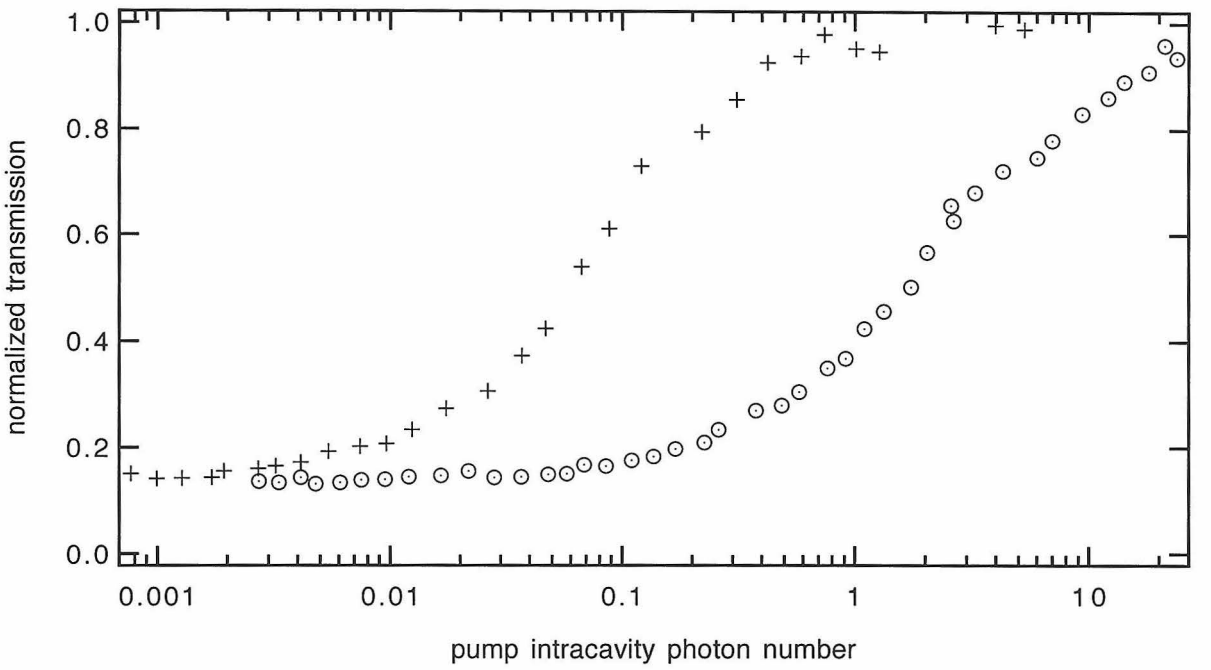

Figure 4.2: Saturation of the atom-cavity transmission for polarized pump beams of opposite helicity. Pump beam σ^+: +, pump beam σ^-: $\odot$. Both pump and probe are near resonance (probe -1 MHz detuned, pump $+1$ MHz detuned. The probe field is weak $n_{probe} < n_0$. The atom and cavity resonances are coincident ($\omega_a = \omega_c$). $\bar{N} = 1.2 \pm 0.2$.

as well to the atom-cavity as does the σ^+. This justifies the approximation $g_- \to 0$. In any event, this approximation can be relaxed and the results of this chapter will not change in any significant way.

4.3.1.2 Converting the intracavity phase to a polarization rotation

To return to the phase measurement, we now consider driving the three-level atom of Figure 4.1 with linearly polarized light (π-polarized), which can be decomposed into counter-rotating circular components as

$$|\uparrow\rangle = \frac{1}{\sqrt{2}}(|\sigma^+\rangle + |\sigma^-\rangle), \tag{4.4}$$

$$|\rightarrow\rangle = \frac{1}{i\sqrt{2}}(|\sigma^+\rangle - |\sigma^-\rangle), \tag{4.5}$$

where $(\uparrow, \rightarrow)$ are linearly polarized beams with polarization vector pointing "up" or "right" (with respect to the optical table, for example). As the light is transmitted through the atom-cavity, the system imparts some phase shift onto the light. That is, the light leaves the 1D atom with a phase that is different from the phase it would have had if the 1-D atom had not been there. Stated another way, the transmission function of the atom-cavity, Equation 1.8, is a complex quantity with associated *modulus* (which has been discussed and measured at length in Chapters 1, 2 and 3) and *phase*. As a linearly-polarized probe passes through the cavity, the constituent circular pieces acquire different phase shifts since they couple to the atom-cavity with different strengths. Thus, the σ^- component acquires a phase shift due to the empty cavity alone (in our $g_- \rightarrow 0$ approximation), while the σ^+ component acquires the atom-cavity phase, which I define as ϕ_a. (For simplicity, I have defined the empty cavity phase as the reference phase and I always consider a phase ϕ_a with respect to the empty cavity phase.) Upon propagation through the atom-cavity, the state of the polarization for an initially linear field, becomes

$$|\uparrow\rangle \xrightarrow{\text{L1D}} \frac{1}{\sqrt{2}}(|\sigma^-\rangle + e^{-i\phi_a}|\sigma^+\rangle), \tag{4.6}$$

where L1D refers to the linear complex transmission associated with the 3-level 1D atom. Transforming back into a linearly polarized basis, it is not difficult to see that Eq. 4.6 corresponds to a linearly polarized beam rotated by an angle $\phi_a/2$. Thus we have converted an intracavity phase to a rotation of polarization of a linearly polarized probe, which is quite straightforward to measure.

4.3.2 One-atom waveplate.

The polarization rotation can be measured by the simple scheme depicted in Figure 4.3. The empty cavity is put between crossed polarizers. Crossed in this case means an adjustment of the half-waveplate between the output of the cavity and the polarizing beam splitter to minimize the field reflected from the PBS to the heterodyne detector for an empty cavity. When there are atoms in the cavity the polarization is rotated

away from this zero reflection state. The half waveplate is rotated again to minimize the reflected field.

The new waveplate angle is one-half of the polarization rotation angle and therefore $\phi_a/4$, since the rotation of linear polarization for a half-wave plate is twice the angle of rotation of the half-waveplate axes. This is somewhat unfortunate, since the actual measured angles then turn out to be fairly small. Nonetheless, by sweeping the angle of the waveplate, and fitting the resulting parabola (we operate very close to the zero), accuracy to $\sim 0.5°$ can be obtained. Raw data from this procedure are shown in Figure 4.4. The data acquisition program was altered to step automatically the angle of a half-waveplate on a stepper-rotator and record the beat-note for each waveplate position, both with atoms and for an empty cavity.[4]

To see how this phase-measurement can be used at different probe detunings, I show a collage of phase data reconstructing the atom-cavity dispersion in Figure 4.5. At each frequency point, the empty cavity phase (different for each frequency) is taken as the reference phase. A more carefully acquired and neatly presented set of phase data along with the corresponding modulus for comparison is shown in Figure 4.6. The solid curve on the phase graph is the difference in angle between $T(\omega)$ (Eq. 1.8) with and without atoms, to account for the empty-cavity reference phase, that is, $\phi_a = \angle T(\Omega, C = \bar{N}C_1) - \angle T(\Omega, C = 0)$. We have called this device a one-atom waveplate, since it is a polarization rotator comprised of one atom (if you do not count all the atoms that make up the mirrors, the vacuum chamber, etc.). Among its many technical limitations, the rotation angle of the one-atom waveplate does not get much larger than 30°.

In general, there is a change in not only the phase but also the modulus of the σ^+ component of the probe beam. For example, near resonance there is very little phase shift, but there is a significant decrease in modulus. When this is true, instead of a purely rotated linear polarization the output is elliptically polarized, with major axis rotated by $\phi_a/2$. Since our measurement projects out the linear part, this does not

[4]W. Lange developed the hardware and software to drive the waveplate rotator, which was integrated with the existing system.

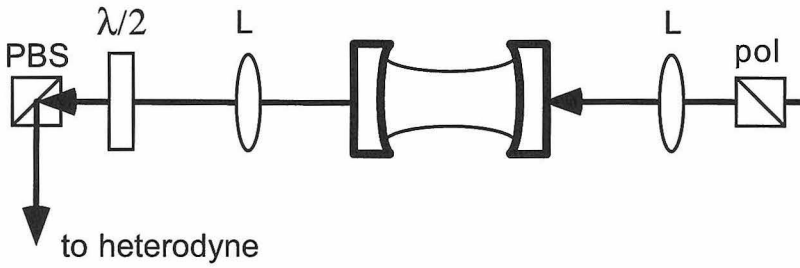

Figure 4.3: Measuring the atom-cavity phase.

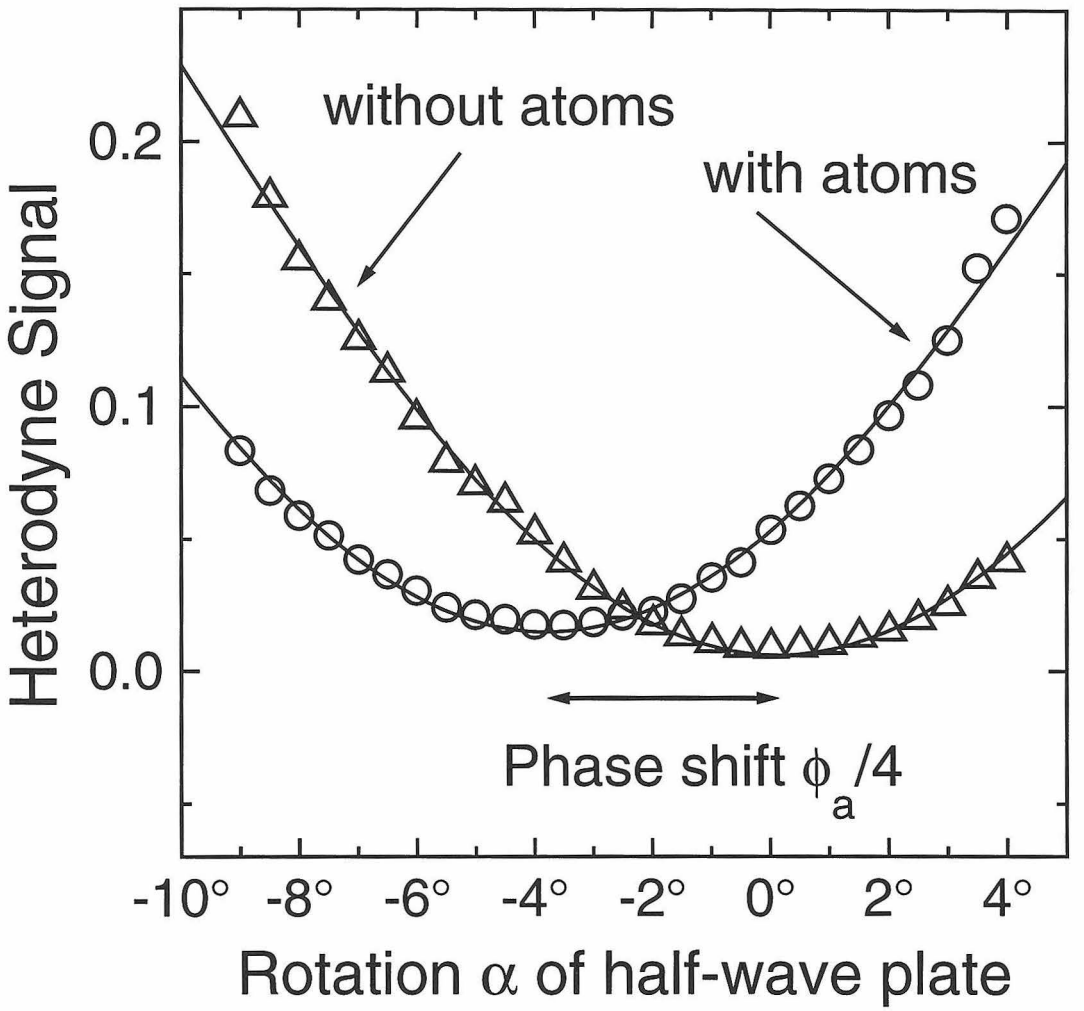

Figure 4.4: Transmission of a weak probe through the phase-measuring apparatus (Figure 4.3) as a function of half-waveplate rotation angle α for the empty cavity and the cavity with atoms. There is no pump field present. $\bar{N} \approx 1$. Probe detuning is -20 MHz from the coincident atom-cavity resonance.

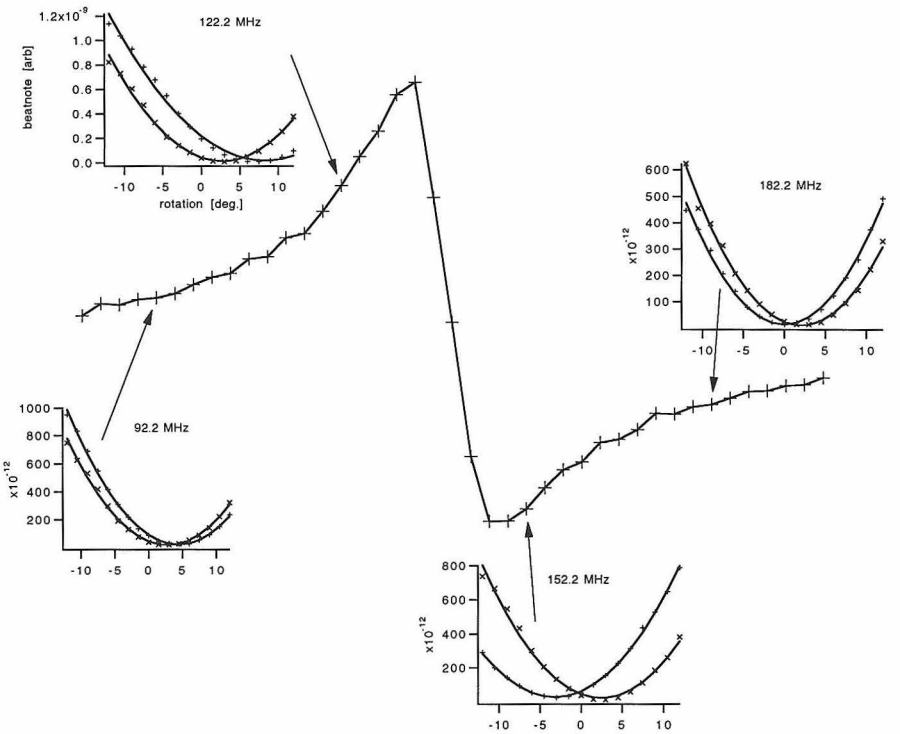

Figure 4.5: Constructing the atom-cavity phase on a weak probe as a function of probe detuning. $\bar{N} \approx 1$. The atom-cavity center is at beatnote frequency 140 MHz: $\omega_a = \omega_c \equiv 140$ MHz.

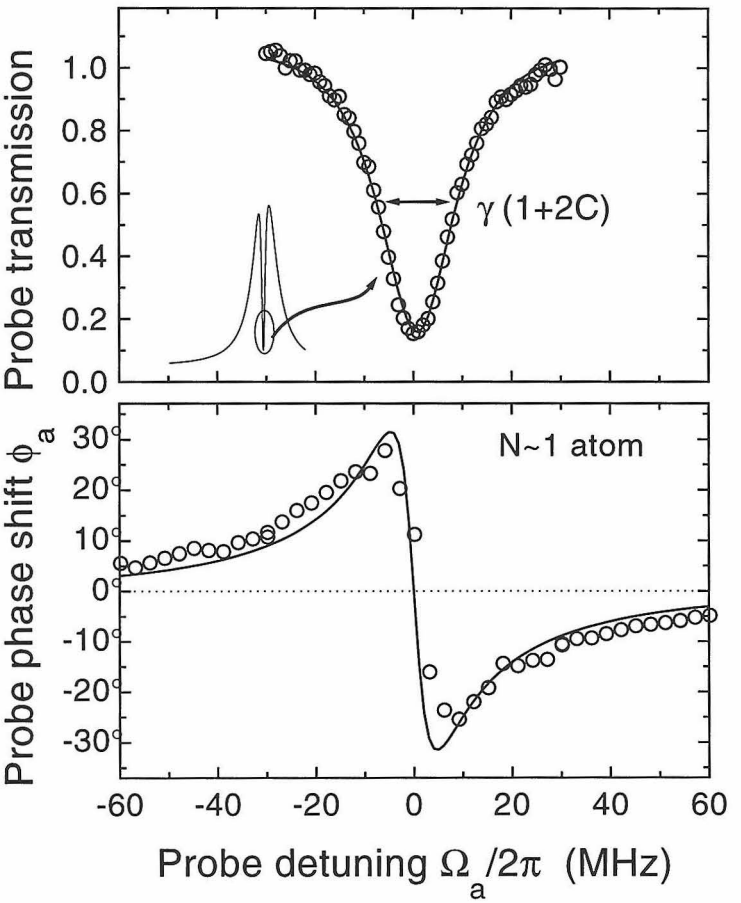

Figure 4.6: Modulus and phase of the atom-cavity transmission spectrum. $\bar{N} = 1$, weak probe field only.

affect the deduction of the polarization-rotation angle or the intracavity phase angle.

4.3.3 Nonlinear conditional phase

Clearly the next thing we must do is demonstrate a nonlinear conditional phase as required for the QPG. The idea of the measurement is shown in Figure 4.7. There are two independent beams, the linearly polarized weak probe beam (labelled a), which is used as described above to measure the atom-cavity phase, and the adjustable polarization, variable power pump beam (labelled b). They are generated independently and so can be frequency, polarization and power tuned in any desired combination. The probe beam path is as before (Figure 2.15 from Chapter 2) with the addition of a quarter-wave plate to compensate the quarter waveplate directly in front of the cavity and produce the required linearly polarized light for the phase measurement. Since the pump and probe beams must overlap into the cavity, there must be a polarization device of some sort behind the beamsplitter which brings the probe and pump together. (See Fig. 4.7.) One beam must hit the BS with linear, the other with circular, polarization. We chose to produce a good circularly polarized pump by reflecting a linear pump beam at the BS which is converted to circular at the quarter-waveplate in front of the cavity. This comes at the expense of transmitting the circular polarization of the probe through the beamsplitter, so that when it nominally reconstructs to linear polarization after the second quarter-waveplate, it will not be perfect. A sacrifice had to be made somewhere. In any event, we measure the respective polarizations to be good to at least 1%, and to be aligned with the optical pumping polarization to this accuracy as well. Indeed, the optical pumping is crucial to this experiment in order to properly realize the 3-level atom of Figure 4.1.

The pump beam is generated from an AO shifted beam which originated from a single-pass shift from one of the AOs of the probe generation (Fig. 2.15). The frequency is tunable over a reasonable range ($\pm$40 MHz), but the beam required realignment for every chosen detuning. The power of the pump was controlled by changing the rf drive power to the AO or by inserting optical attenuators as appro-

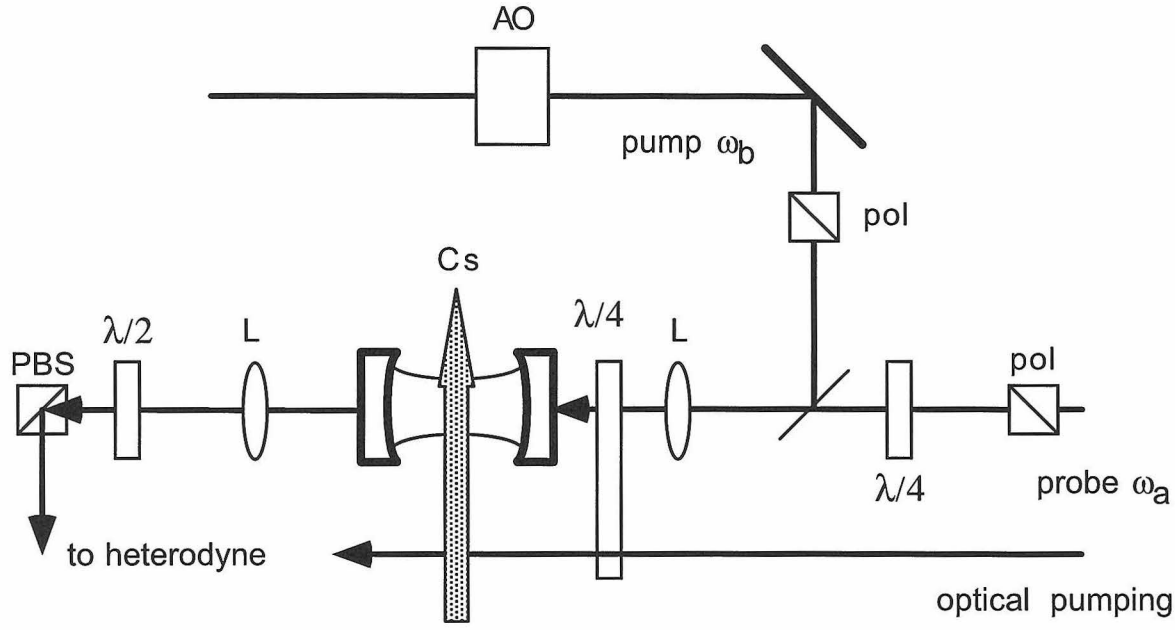

Figure 4.7: The conditional phase measurement setup.

priate.

As a first application of the nonlinear phase measurement procedure, in Figure 4.8 I show the one-atom-waveplate phase shift as the pump power is increased. The pump (σ^+-pol) is at 20 MHz detuning (as shown by the arrow) with power changed for each of the curves as indicated. The decreasing phase as the power of the pump is increased represents a nonlinear effect, since the pump affects the probe phase even when the probe is detuned from the pump. Linear response does not allow one frequency to impact another.

The phase nonlinearity is shown in a form more akin to the transmission saturation curves (of, e.g., Figure 2.27) in Figure 4.9. The pump and probe are fixed in frequency at $\omega_a/2\pi = 30$ MHz and $\omega_b/2\pi = 20$ MHz (0 MHz reference atom-cavity center frequency). The power in the σ^+ pump m_b is scanned, while the phase of the probe

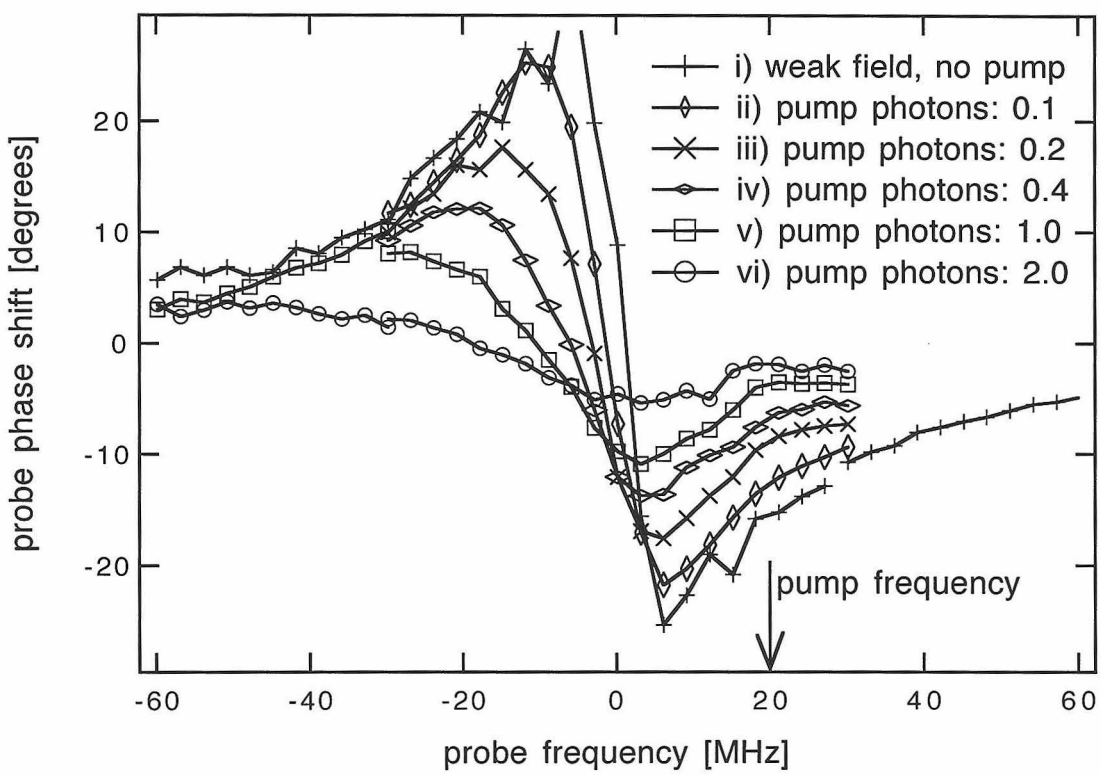

Figure 4.8: Phase of the transmission spectrum as the pump power is varied. $\bar{N} = 1.0 \pm 0.2$.

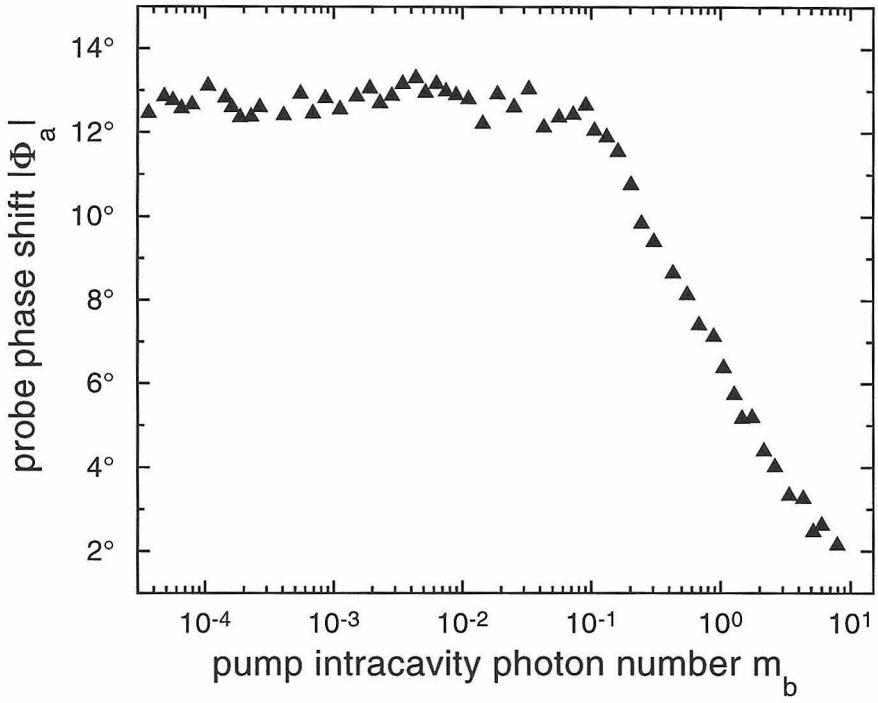

Figure 4.9: Saturation of the phase. $\bar{N} = 0.9$. The σ^+-pol pump is detuned by +20 MHz and the probe by +30 MHz from the common atom-cavity resonance.

Φ_a is measured. It is seen that the phase saturates to a significant degree for a single (average) intracavity pump photon. The probe is of course weak at $\bar{m}_a \sim 10^{-4}$. As $m_b \to 0$, $\Phi_a \to \phi_a$, which is the phase shift for the probe field alone.

4.3.4 Truth table

These measurements represent the realization of a nonlinear optical susceptibility at the single photon level and unambiguously demonstrate the conditional dynamics *necessary* for implementing quantum logic. How is that? It is a rather circuitous and confusing route, so I will spell it out in some detail. We have a transformation Eq. 4.2 that I have called a quantum phase gate. It is written in a Fock basis of $\{|1\rangle_a, |0\rangle_a; |1\rangle_b, |0\rangle_b\}$. This does not seem to relate at all to our nonlinear measurements which are done with *coherent states* of different polarizations, with one weak probe and one (relatively) strong pump. Where are the single photons that must be

the carriers of the quantum information in a quantum logic transformation?

Allow me at this point to introduce some notation which will help to clarify the discussion to come. I will label coherent states in the following form: $|\alpha, p\rangle$ where α is the complex amplitude of the coherent state and p is its state of polarization which can be one of the set $\{+, -, \uparrow, \rightarrow\}$ for circular polarization of positive (σ^+) and negative (σ^-) helicity, and linear polarization pointing "up" or "right," respectively. In addition, in the p slot I may also put an angle θ which represents linear polarization rotated from the vertical by θ. For Fock states, we have $|n, p\rangle$ where n is the number of photons in the Fock state and p is the polarization state as before.

Now, we want our QPG to operate on single photons with the two orthogonal circular polarization states. This is the kind of conditional classical logic that we are able to realize—a σ^+ pump will affect the probe phase, but a σ^- pump will leave the probe phase alone. (To jump ahead a bit, Figure 4.10 clearly demonstrates this.) This is described by the QPG transformation on single photons written in the polarization basis:

$$\begin{aligned}
|1,-\rangle_a|1,-\rangle_b &\rightarrow & |1,-\rangle_a|1,-\rangle_b,\\
|1,+\rangle_a|1,-\rangle_b &\rightarrow e^{i\phi_a} & |1,+\rangle_a|1,-\rangle_b,\\
|1,-\rangle_a|1,+\rangle_b &\rightarrow e^{i\phi_b} & |1,-\rangle_a|1,+\rangle_b,\\
|1,+\rangle_a|1,+\rangle_b &\rightarrow e^{i(\phi_a+\phi_b+\Delta)} & |1,+\rangle_a|1,+\rangle_b.
\end{aligned} \tag{4.7}$$

Note that in Eq. 4.7 + and − have taken the place of 1 and 0 from Eq. 4.2, and that we are now dealing with strictly single-photon states. Why do we insist on single photon states? Let it suffice to say that single photons are somehow more quantum than other states and quantum logic requires quantum states.

For the experiments described in this thesis, we do not use single-photon Fock states as input fields to the cavity. We do not (and cannot at present) drive our atom-cavity system with single-photon Fock states of different polarizations. In principle, we could use single photon states from e.g., parametric downconversion, or some better source (which incidentally would likely come from some cavity QED quantum state synthesizer). It seems reasonable that, if we were to use Fock states (with given polarization and occupied with either 0 or 1 photon) as input states to the atom-cavity

system, they would transform according to the following *ansatz*:

$$\begin{aligned}
|j,+\rangle_a|k,+\rangle_b &\mapsto e^{i\mu_{jk}^{++}}|j,+\rangle_a|k,+\rangle_b, \\
|j,-\rangle_a|k,-\rangle_b &\mapsto e^{i\mu_{jk}^{--}}|j,-\rangle_a|k,-\rangle_b, \\
|j,-\rangle_a|k,+\rangle_b &\mapsto e^{i\mu_{jk}^{-+}}|j,-\rangle_a|k,+\rangle_b, \\
|j,+\rangle_a|k,-\rangle_b &\mapsto e^{i\mu_{jk}^{+-}}|j,+\rangle_a|k,-\rangle_b, \qquad j,k=\{0,1\}. \qquad (4.8)
\end{aligned}$$

This amounts to the physically-motivated assumption that Fock states asymptotically connect to the dressed states of the atom-cavity system and hence are the appropriate eigenstates of the transformation. This is certainly a reasonable *ansatz*, but I am forced to leave it unjustified, since we do not have a two-mode theory (to account for the effect of having the a-mode and the b-mode present simultaneously, each with 1 photon) that is at all adequate.[5]

The content of the *ansatz* must continue. We need to say something about the 16 parameters $\mu_{jk}^{\pm\pm}$. We want to retain the names of the parameters of the polarization QPG of Eq. 4.7. This tells us to call $\mu_{11}^{--}=0$ (just a definition of the reference); $\mu_{11}^{+-}=\phi_a$; $\mu_{11}^{-+}=\phi_b$; and $\mu_{11}^{++}=\phi_a+\phi_b+\Delta$. If our experiment only involved single-photon occupation number states, this would be it, there would be no need to worry about the rest of the $\mu_{jk}^{\pm\pm}$. But the experiment, for reasons to be discussed, does involve other photon states, so we must know how they transform. We expect all of the μ_{jk}^{--} to be zero, since they do not interact with the atom-cavity. Hence $\mu_{00}^{--}=0$; $\mu_{01}^{--}=0$; $\mu_{10}^{--}=0$. It seems clear that the state $|1,+\rangle_a|1,-\rangle_b$ should transform identically to the state $|1,+\rangle_a|0,-\rangle_b$ since (1) the polarization of no photons is irrelevant (I can call it whatever I want); and (2) a photon of polarization σ^- does nothing to and is not affected by the atom-cavity (in the $g_-\to 0$ approximation). Hence $\mu_{10}^{++}=\phi_a$; $\mu_{01}^{++}=\phi_b$; $\mu_{10}^{+-}=\phi_a$; $\mu_{01}^{-+}=\phi_b$. The rest of the $\mu_{jk}^{\pm\pm}$ give zero phase since they involve combinations of σ^+ polarized 0-photon states and/or σ^- polarized 1-photon states: $\mu_{00}^{++}=0$; $\mu_{01}^{+-}=0$; $\mu_{00}^{+-}=0$; $\mu_{10}^{-+}=0$; and $\mu_{00}^{-+}=0$.

One can now see (albeit with some effort, perhaps) with the definitions of the

[5]S. M. Tan has done some numerical calculations which support the ansatz.

$\mu_{jk}^{\pm\pm}$ and the *ansatz* of Eqs. 4.8 that Eqs. 4.8 specify a QPG transformation of the type 4.7. The onus is now on us to determine if the atom-cavity system actually behaves in this way, in particular, we need to measure the parameters of the QPG, especially Δ. If a measured $\Delta \neq 0$ is revealed, then the *ansatz* of Eqs. 4.8 and the $\mu_{jk}^{\pm\pm}$ discussed in its context are equivalent to the QPG transformation with polarization states of Eq. 4.7. I want to stress at this point that we are not making a direct QPG transformation between single photon fields in *any* measurement in this chapter. I will show, however, that the measurements we do make can be interpreted as measurements of the parameters of a QPG via the *ansatz* of Eqs. 4.8 and the well-motivated definitions of the $\mu_{jk}^{\pm\pm}$. If the reader has noticed that I have belabored this point, there is good reason: we wrote a paper on this experiment [164] that few people in the community understand properly (by no fault of their own).

Throughout this thesis, we use weak excitation fields, that is, fields with associated intracavity photon numbers well below unity: $m_a, m_b \ll 1$. Thus our input states (and intracavity fields) are weak coherent states with small amplitudes $|\alpha|^2, |\beta|^2 \ll 1$. (Note that $m_a = |\alpha|^2$ and $m_b = |\beta|^2$.) These weak coherent fields can be written in a truncated Fock basis as

$$|\psi_a^p\rangle \approx e^{-|\alpha|^2/2}\left[|0,p\rangle_a + \alpha|1,p\rangle_a\right], \tag{4.9}$$

$$|\psi_b^p\rangle \approx e^{-|\beta|^2/2}\left[|0,p\rangle_b + \beta|1,p\rangle_b\right]. \tag{4.10}$$

For example an "up" linearly polarized coherent probe state will be written $|\psi_a^{\uparrow}\rangle \approx e^{-|\alpha|^2/2}[|0,\uparrow\rangle_a + \alpha|1,\uparrow\rangle_a]$ and likewise for the rest of the many possibilities. Consider first the composite input state $\psi_{\text{in}} = \psi_a^+ \otimes \psi_b^+$. This state transforms under Eq. 4.8 to the output state

$$|\psi_{\text{ent}}\rangle = |\overline{\alpha},+\rangle_a|\overline{\beta},+\rangle_b + \overline{\alpha}\overline{\beta}\left[e^{i\Delta} - 1\right]|1,+\rangle_a|1,+\rangle_b, \tag{4.11}$$

where $\overline{\alpha} \equiv \alpha e^{i\phi_a}$ and $\overline{\beta} \equiv \beta e^{i\phi_b}$. This state is clearly entangled for $\Delta \neq 0$, reinforcing the importance we assign to Δ. So, without any reference to quantum gates, we see

that if Eq. 4.8 is true, then the atom-cavity system should produce demonstrably entangled states from unentangled coherent state input fields. The problem is that the manifestation of the entanglement is rather difficult to measure.[6]

Now I will consider the states that we actually employ in the pump-probe measurement described in the previous section. This is the state

$$|\psi_{\rm exp}\rangle = |\alpha,\uparrow\rangle_a|\beta,+\rangle_b, \tag{4.12}$$

which is an "up"-linearly polarized probe field a and a σ^+-polarized pump field b. Expanding the coherent states in terms of Eqs. 4.9, 4.10 and the linear polarization in terms of Eq. 4.4 and using Eq. 4.8, we see that (leaving out all normalizations):

$$\begin{aligned} |\psi_{\rm exp}\rangle &\xrightarrow{ansatz} \\ |\psi_{\rm out}\rangle &= |0,+\rangle_b\left[\left(|0,+\rangle_a + \alpha e^{i\phi_a}|1,+\rangle_a\right) + \left(|0,-\rangle_a + \alpha|1,-\rangle_a\right)\right] \\ &+ \beta e^{i\phi_b}|1,+\rangle_b\left[\left(|0,+\rangle_a + \alpha e^{i(\phi_a+\Delta)}|1,+\rangle_a\right) + \left(|0,-\rangle_a + \alpha|1,-\rangle_a\right)\right]. \end{aligned} \tag{4.13}$$

Noticing that the terms in the square brackets ([ ]) are rotated linear polarizations (like those in Eq. 4.6), we can write this as:

$$|\psi_{\rm out}\rangle = |0,+\rangle_b|\alpha,\phi_a/2\rangle_a + \beta e^{i\phi_b}|1,+\rangle_b|\alpha,(\phi_a+\Delta)/2\rangle_a, \tag{4.14}$$

where again, $p = \phi_a/2$ is a linearly polarized field rotated from the vertical by $\phi_a/2$.

Now we must make a measurement of polarization on the probe field alone, as is done in the experiment. The goal is to discover what such a measurement reveals about the parameters of the QPG under the *ansatz* of Eq. 4.8. The output density operator is $\rho^{\rm tot}_{\rm out} = |\psi_{\rm out}\rangle\langle\psi_{\rm out}|$ and from Eq. 4.14, the reduced density operator for the a-mode alone is:

$$\rho^a_{\rm out} = {\rm Tr}_b\rho^{\rm tot}_{\rm out} = |\alpha,\phi_a/2\rangle_a\langle\alpha,\phi_a/2|_a + |\beta|^2|\alpha,(\phi_a+\Delta)/2\rangle_a\langle\alpha,(\phi_a+\Delta)/2|_a. \tag{4.15}$$

[6] A promising scheme is an extension of Ref. [176] investigated by S. M. Tan.

This is a mixed-state density operator, since we are looking at the a-mode alone and it is entangled with the b-mode. It is a weighted sum of a field state of linearly polarized coherent light at angle $\phi_a/2$ with weight factor 1 (I have dropped all normalizations) plus a field state of linearly polarized coherent light at angle $(\phi_a + \Delta)/2$ with weight factor $|\beta|^2$. Recalling the measurement procedure from Section 4.3.2, we rotate a polarizer to minimize the transmission of the a-field (probe) (actually we rotate a half-waveplate, but a polarizer is easier to visualize). The *electric fields* of each component of Eq. 4.15 add and are transmitted through the polarizer (whose *crossed* axis is at an angle θ relative to the vertical). The transmitted intensity is

$$I \propto \left[\sin\left(\frac{\phi_a}{2} - \theta\right) + m_b \sin\left(\frac{\phi_a + \Delta}{2} - \theta\right)\right]^2. \tag{4.16}$$

First, I will change variables to $\theta' \equiv \phi_a/2 - \theta$ so,

$$\begin{aligned} I &\propto \left[\sin\theta' + m_b \sin\left(\frac{\Delta}{2} + \theta'\right)\right]^2 \\ &\approx \sin^2\theta' + 2m_b \sin\left(\frac{\Delta}{2} + \theta'\right)\sin\theta' \end{aligned} \tag{4.17}$$

to first order in m_b. The polarizer is rotated to minimize the transmission. After setting $\partial I/\partial\theta' = 0$ and working the many trig identities, it is found that the minimum angle satisfies:

$$2\theta' = \arctan\left[\frac{-2m_b \sin\Delta/2}{1 + 2m_b\cos\Delta/2}\right] \approx -2m_b \sin\Delta/2 \tag{4.18}$$

for $m_b \ll 1$. Transforming back to the real polarizer angle,

$$\theta \approx \phi_a/2 + m_b \sin\Delta/2, \tag{4.19}$$

or, since the quantity Φ_a is already corrected for factors of 2 in converting polarizer angles to intracavity phases,

$$\Phi_a \approx \phi_a + 2m_b \sin\Delta/2 \qquad \sigma^+ \text{ pump.} \tag{4.20}$$

Therefore, Δ may be determined directly from measurements of the initial slope $\partial\Phi_a/\partial m_b$ in a plot of the phase Φ_a of the probe field versus pump intensity m_b. Note that for a Poisson distribution (appropriate for coherent states) for $m_b = 0.2$, the probability that there is ever more than one photon in the cavity is less than 2%. We therefore will look out to $m_b \approx 0.2$ for the initial linear slope.

Now note that this entire procedure could be repeated with an input state given not by $|\psi_{\rm exp}\rangle$ of Eq. 4.12 but by

$$|\psi'_{\rm exp}\rangle = |\alpha, \uparrow\rangle_a |\beta, -\rangle_b. \tag{4.21}$$

This is a linearly polarized probe beam with a σ^- pump. For this configuration, it is easy to show that the angle of minimum transmission will be $\phi_a/2$ independent of m_b. Therefore,

$$\Phi_a \approx \phi_a \qquad \sigma^- \text{ pump.} \tag{4.22}$$

We expect zero slope with a σ^- pump, since there is no contribution from Δ. If one actually works out all the contributions, $\Phi_a \approx \phi_a$ for a σ^- pump is seen to be a consequence of $\mu_{11}^{+-} = \phi_a$, which we took to be self-evident above, but the validity of which can now be confirmed via a slope measurement with the σ^--pol pump.

Finally, in Fig. 4.10 we show that there is indeed a non-zero initial linear slope for the Φ_a *vs.* m_b data with σ^+ pump, but not for σ^- pump. The one-photon phase shift extracted from the straight-line fits shown in Fig. 4.10 (and others for similar parameters) yield $|\Delta| = (16 \pm 3)^\circ$ and $\mu_{11}^{+-} - \phi_a = (0.3 \pm 2)^\circ \approx 0$ as anticipated. With the roles of the (a,b) modes interchanged, we can likewise find that $\mu_{11}^{-+} \approx \phi_b$ (see Figure 4.12). Hence, subject to the validity of our model (4.8), the experimentally determined parameters for the would-be QPG transformation are $\phi_a \approx (17.5 \pm 1)^\circ$, $\phi_b \approx (12.5 \pm 1)^\circ$, and $\Delta \approx (16 \pm 3)^\circ$ for data as in Fig. 4.10.

The slope and asymptote are of course dependent on the particular choice of parameters, in particular, the detunings of the pump and probe. For the QPG it is important to have pump and probe detuned sufficiently to avoid populating the atomic excited state. They should also be well separated in frequency space. Data

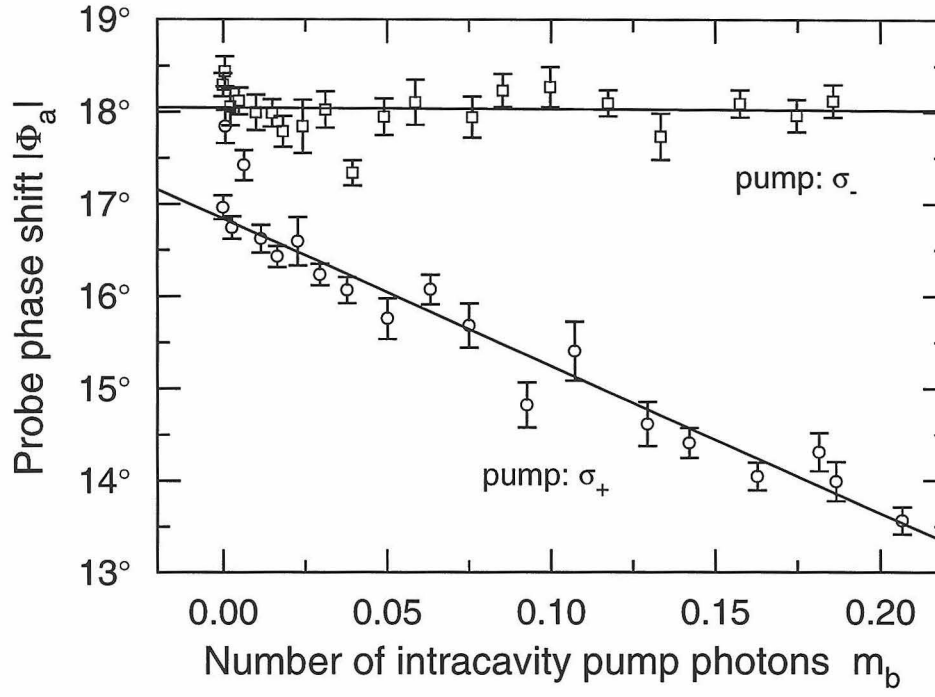

Figure 4.10: The slope reveals the conditional phase term. Pump +30 MHz, probe +20, $\bar{N} = 0.9$. The y-intercepts are different for the σ_+ and σ_- cases because of a slight drift in either cavity detuning or atom number. From these data and others like them, it is deduced that $|\Delta| = 16 \pm 3$ °/photon.

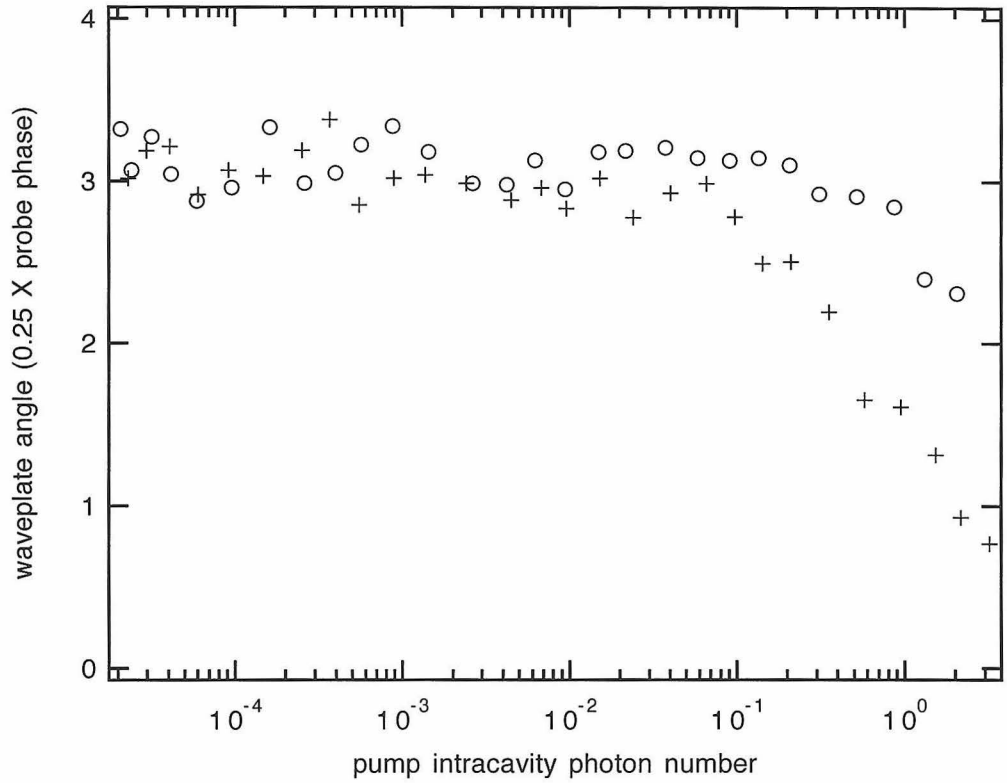

Figure 4.11: Phase saturation for a different set of detunings. The slope from these data are found to be: σ^+ (+): 12°/photon, σ^- (○): 0.3°/photon. The detunings are pump +25 MHz, probe +26 MHz. $\bar{N} \approx 1$

for another set of (arbitrary) detunings is shown if Figure 4.11.

Obviously, the transformation described in Eq. 4.8 knows nothing about what we choose to call pump and probe. One of the consequences of this is that the slope should remain unchanged if we associate the pump with the previous probe frequency and vice versa. Swapping the roles of pump and probe will change the asymptote (ϕ_a, ϕ_b), but should not change the slope (Δ). This is not immediately obvious to me from a semiclassical picture of the system, but it is demanded by the assumptions of Eq. 4.8. This is experimentally confirmed in Figure 4.12. While this measurement surely acts to reinforce Eqs. 4.8, it would be interesting to know if it could be taken as confirmation of this model. If there were a semiclassical model, for example, that predicted that the swapped slopes would not be the same, the *ansatz* could possibly be assigned a larger degree of validity.[7]

[7]Actually, I have run semiclassical simulations using an extension of the pump-probe calculation

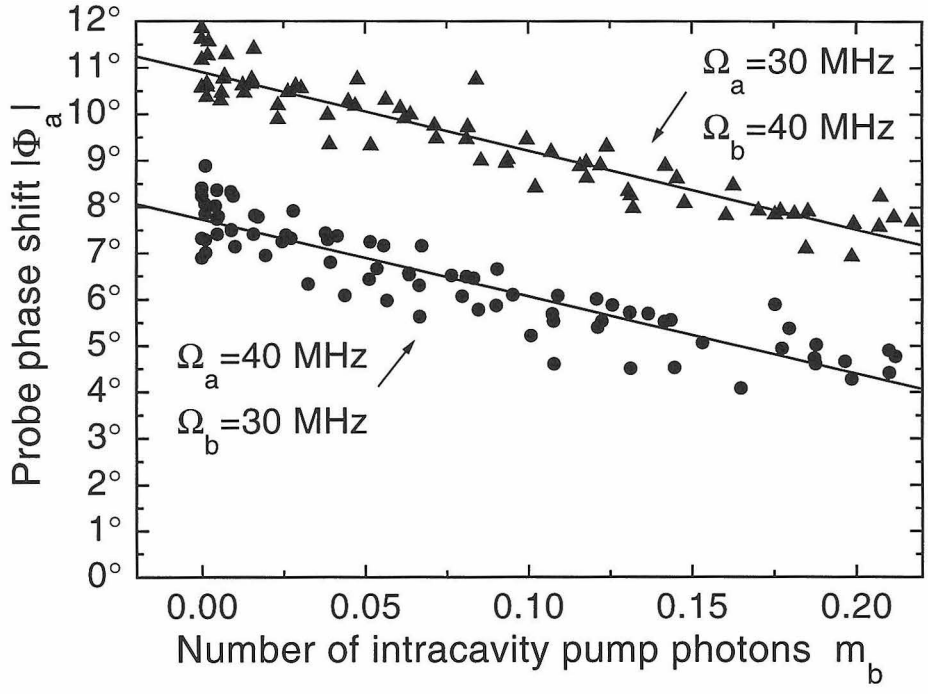

Figure 4.12: Swapping the identities of pump and probe. In the '▲' data, the pump is +40 and the probe +30 MHz detuned. In the '•' data, the pump is +30 and the probe +40 MHz detuned. $\bar{N} = 0.96$.

As an additional curio, the phase shifts for equal detunings on either side of resonance are equal and opposite (see Fig. 4.6). Thus it may be expected that there will be no slope for pump and probe on opposite sides of resonance. (Since Eqs. 4.8 makes no predictions about actual values, it can not help us here.) This seems to be crudely confirmed by the data of Figure 4.13. The pump and probe are $\sim \pm 15$ MHz detuned and the measured slopes are $-4°$/photon and $2°$/photon for σ^+- and σ^--polarized pump respectively. Because this data set was taken with logarithmic point separation, the measured slopes are not very accurate, but are certainly consistent with zero slope.

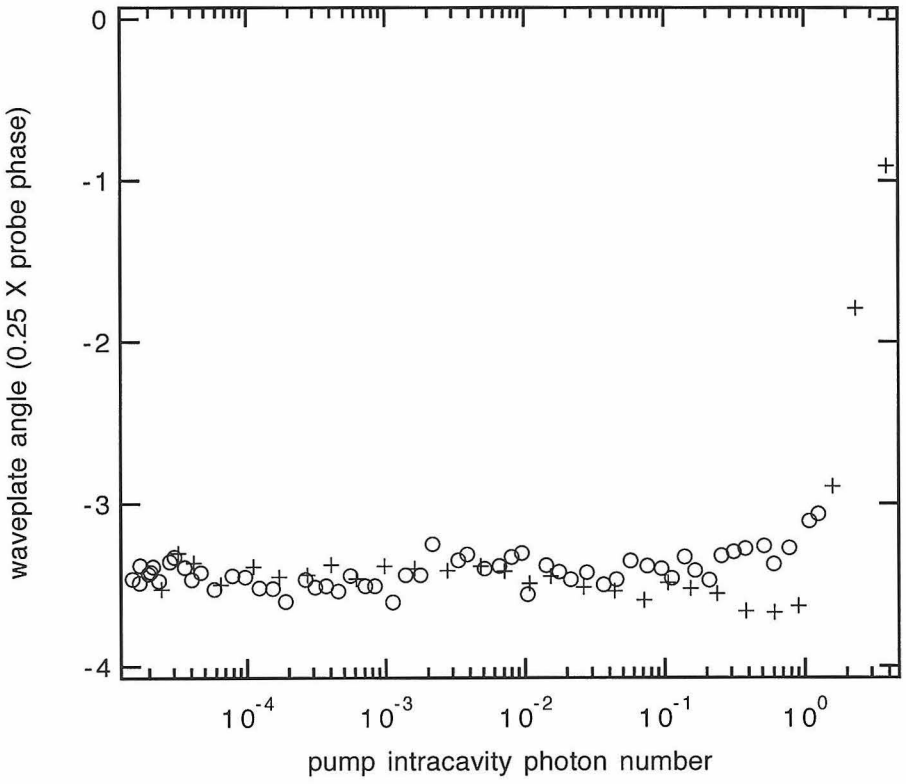

Figure 4.13: Pump and probe on opposite sides of resonance (probe: -16 MHz, pump: $+15$ MHz). $\bar{N} \approx 1.1$.

from Chapter 5 and determined that the slopes are the same when pump and probe are swapped, and furthermore that our measured values are well predicted by the semiclassical calculation. In addition, the role of atomic beam fluctuations is found to have negligible impact on the measured phases.

4.3.5 Issues

We wish to stress that the parameter Δ has model-independent significance as the strength of the dispersive nonlinear interaction between intracavity fields, quoted in degrees per unit of stored energy. Its large measured value represents a unique achievement within the field of nonlinear optics. Our *ansatz* (4.8) on the other hand may be viewed with some skepticism, for although our assumptions seem reasonable we have not explicitly verified the full transformation (4.2).

In particular, we have not addressed the issue of whether the transformation whose parameters we have extracted would actually produce the coherences (entanglements) that we have predicted. There are many forces at work that would prevent our predictions from being realized, one of which is the very fact that Eq. 4.8 may not be a valid model. This is not to say that the nonlinearity that we have demonstrated with single quanta is not useful, it just may not be the exact one predicted from the ansatz. Another potential problem (above and beyond issues of interpretation) is dissipation, which would act to quickly *decohere* any quantum coherences developed. Although the effects of dissipation are neglected in Eqs. 4.8, they could be incorporated via an altered density matrix for $|\psi_{\rm out}\rangle$ (Eq. 4.14). We operate with large detunings from atomic resonance in order to approximate purely dispersive interactions. For example, for the measurements of Figs. 4.9,4.10 the amplitude of the probe beam changes by less than 3% in moving from $N = 0$ to $\overline{N} = 1$ intracavity atom. Nonetheless, let us consider damping of coherences in the output fields by writing their joint density matrix in the generalized form $\rho_{jk}d_{jk}$. Here ρ_{jk} represents a pure-state density matrix in a basis $\{j,k\} = \{0_{a,b}, 1_{a,b}\}$ for Eqs. (4.8,4.11) and $\{j,k\} = \{1^-_{a,b}, 1^+_{a,b}\}$ for Eq. (4.7), and the parameters d_{jk} provide a phenomenological characterization of decoherence. Physical considerations require that $\mathrm{Tr}[\rho_{jk}d_{jk}] = 1$, but dissipative processes could in principle cause complete dephasing of the output density matrix ($d_{j\neq k} \rightarrow 0$). Fortunately, with optical fields there exists a straightforward procedure for establishing that this is not the case – heterodyne detection such as implemented in the current work provides signals which are proportional to off-diagonal matrix

elements $\rho_{jk} d_{jk}$.

Part II

Nonlinear Spectroscopy in the Strong Coupling Domain

Chapter 5 Nonlinear Spectroscopy

We now move into the regime of true strong-coupling with a nonlinear spectroscopic investigation of a strongly-coupled atom-cavity system. A two-field pump-probe experiment is employed to study nonlinear structure as the average number of intracavity atoms is varied from $\bar{N} \approx 4.2$ to $\bar{N} \approx 0.8$. Nonlinear effects are observed for as few as 0.1 intracavity pump photons. A detailed semiclassical simulation of our atom-beam experiment gives reasonable agreement with the data for $\bar{N} \gtrsim 2$ atoms. The simulation procedure accounts for fluctuations in atom-field coupling which have important effects on both the linear and nonlinear probe transmission spectra. We are attempting to use the semiclassical simulations in order to see if our experiment shows any deviations from the predictions of a non-quantum treatment.

The data presented in this chapter was taken during my first couple of years here. Rob Thompson was in charge of the experiment, Olivier Carnal was the postdoc. By the time these two left, we had sorted through most of the data, but there was still a lot of analysis to be done. This chapter is a draft of a paper that we are working on that brings together the analysis and the data with additions and modifications to the way it has been presented thus far [48]. It will eventually appear in Phys. Rev. A.

5.1 Introduction

An exciting development in recent years has been the experimental investigation of open quantum systems in the domain of strong coupling. In this limit the time scale for internal, coherent evolution of a quantum system is much shorter than the time scale for dissipation into an external environment [177]. Increasing the ratio of coherent coupling to dissipation is of primary import in many nascent fields of experimental quantum physics including quantum computation [178] and quantum

state synthesis [179, 180, 181, 182]. Experimental examples of such systems are scarce, with notable exceptions being photon-phonon coupling in trapped ion systems [183], and photon-atom coupling in the field of cavity quantum electrodynamics (cavity QED). Strong-coupling cavity QED experiments have been carried out in both the microwave [184, 4, 5, 185, 186, 187, 188, 10] and optical domains [6, 7, 189, 190, 191, 177, 9, 192].

Thus far, most experiments in strong coupling cavity QED with few atoms which have focussed on structural properties (eigenstructure) of the coupled system have been performed in the linear regime. It has been pointed out numerous times [193, 194, 22, 38, 7, 177, 192] that the linear regime is equally well described by the semi-classical Maxwell-Bloch equations or by a full quantum master equation. As regards *structural* aspects of the coupled system, only (nonlinear) excitations of high-lying dressed states can potentially distinguish between theories [8]. Exceptions to this state of affairs are measurements of *dynamical* processes such as photon antibunching [6] and sub-Poissonian photon statistics [5] for which a manifestly quantum theory of strong coupling in cavity QED is required.

In order to advance spectroscopic investigations in optical cavity QED from the classical (linear) domain to the quantum regime, we have carried out both linear and nonlinear optical spectroscopic measurements of a strongly coupled atom-cavity system with average intracavity atom number ranging from $\bar{N} \approx 4.2$ to $\bar{N} \approx 0.8$. In particular, we have observed with significantly improved resolution over our previous results [7] a weak-field normal-mode (or "vacuum-Rabi") splitting of the transmission spectrum of the coupled system [191, 177]. Moreover, we have recorded modifications of weak-field spectra in the presence of a moderate intensity pump field of fixed frequency. Significant nonlinear effects were observed with as few as 0.1 intracavity photons. This investigation compliments our measurements of nonlinear response in the bad-cavity limit of cavity QED [45], where we have studied a quantum-phase gate for quantum logic with saturation photon number 0.02. [164]

A principle motivation for this research is the identification (in the level structure of the atom-cavity "molecule") of manifestly quantum aspects of the atom-cavity

interaction. In particular we have attempted to observe multiquanta transitions, using a pump-probe technique in which the system is driven to its first excited state using a fixed frequency pump field, with transitions to higher lying states probed by a weak, variable frequency probe field. With on average less than 1 atom in the cavity mode volume, deviations from a semiclassical model are observed, but an unambiguous signature of a multiexcitation resonance of uniquely quantum origin remains elusive to the experiments described here.

It must be noted at the outset that this experiment (along with all optical atomic cavity QED work to date) is performed with an atomic beam which crosses the cavity mode (the exception is Chapter 7). Because of this, the effects of fluctuations in atomic number inherent in the beam, along with spatially variant coupling strength within the cavity, play an extremely important role in the interpretation of observations. While this has been stressed in our previous work [6, 7, 189, 190], which has included detailed quantitative comparisons based on a Monte-Carlo simulation accounting for the effects of these fluctuations, the present nonlinear experiment with larger coupling raises new issues which we likewise address in detailed simulations of this experiment.

The organization of this chapter is as follows. In Section 5.2 we formulate the relevant theory and then in Section 5.3 we discuss methodology and results of our semi-classical simulations. Our measurements are discussed in Section 5.4. We conclude in Section 5.5 with a discussion of future techniques for improving measurements in cavity QED.

5.2 Quantum and semiclassical theory of the atom-cavity system

5.2.1 Preliminaries: Structure of the atom-cavity system

The quantum mechanical structure of a dissipationless, strongly-coupled atom-cavity system (in the absence of number fluctuations) is well known. The single-atom predic-

tion is a spectrum of eigenvalues given by the so-called Jaynes-Cummings ladder [2]; an extension to the multiple atom case is the Tavis-Cummings ladder [195] of dressed states. The formidable task of incorporating small amounts of dissipation in the system (via a master equation or other approach) reveals many interesting quantum mechanical effects (such as photon antibunching in the transmitted light [6, 196]) and indicates that in the strong coupling regime, the overall structure cannot be viewed in the absence of a self-consistent treatment of the nature of the complete interaction *including dissipation* [36]. Semiclassically, the problem has been treated from various perspectives, notably the state equation of optical bistability [31] derived either from the standard Maxwell-Bloch equations [197] or from the full master equation in a system size expansion [198]. Comparisons of the fully quantum and semiclassical approaches indicate that for two limiting cases predictions of the structure of the lowest lying dressed states coincide. These are the limit of vanishing excitation strength and the limit of large numbers of intracavity atoms [199].

Figure 5.1 helps to explain the situation. Figure 5.1a depicts the first two excited states of a single atom optimally coupled to a cavity as derived from a full quantum calculation in which g_0 is the rate of coherent coupling between atom and cavity: $2g_0 \equiv \Omega_{\text{Rabi}}$. Figure 5.1b is the fully quantum extension of the one-atom calculation to the case with M atoms [199]. The exact quantum expression for the first excited state splitting is $g_0\sqrt{M}$ and that of the second excited state is $\pm g_0\sqrt{4M-2}$. For $M \gg 1$ the splitting of the excited state becomes $\pm 2g_0\sqrt{M}$, and transitions from the first to the second manifold occur at frequency $\pm g_0\sqrt{M}$ in agreement with the semiclassical prediction. Note that the semiclassical prediction fails for small M both in terms of level splitting and transition strength. For weak field excitation, the second excited state is never reached, so that the semiclassical and quantum predictions coincide. The quantum character of the second excited state splitting can be expressed in terms of a "quantum anharmonicity" which can be quantitatively defined as the ratio of the second-excited-state splitting for the quantum and semiclassical predictions:

$$q_a \equiv \frac{g_0\sqrt{4M-2}}{2g_0\sqrt{M}}. \tag{5.1}$$

For $M = 1$, $q_a = 0.71$ while for $M \to \infty$, $q_a \to 1$. Of additional note in Fig. 5.1 are the transition rates and spacings from the upper sideband of the first excited state to levels of the second excited state. As explained in the figure caption, the quantum transitions give rise to an additional "anharmonic" resonance at $(\sqrt{2}-1)g_0$, whereas for $M \gg 1$, the allowed large-M transitions lead to no additional resonances other than $\pm g_0\sqrt{M}$.

The simple picture presented thus far becomes significantly more complicated under a typical experimental measurement strategy. For example, in our experiment the number of intracavity atoms fluctuates during the detection time window, the coupling is not constant within the cavity mode (it is an optical standing-wave cavity with a Gaussian transverse profile), the system is driven with an external field, and there is dissipation of both the atoms and the cavity. To see how these conditions impact the observation of the underlying structure, let us introduce each complication separately.

We start by ignoring dissipation, fluctuations in atomic number, and the external drive, while considering the effect of random coupling of many atoms to the cavity field with mode function $\psi(\vec{r}) \equiv \sin(kz)\exp[-(x^2+y^2)/\omega_0^2]$, where w_0 is the Gaussian waist and $k = 2\pi/\lambda$. Consider the case where there are N_s atoms distributed randomly throughout the cavity mode, each with a coupling $g_i = g_0|\psi(r_i)| \equiv g_0|\psi_i|$. The effective number of atoms in the cavity is defined as $N_e \equiv \sum_{i=1}^{N_s}\psi(r_i)$ and the eigenvalues of the first excited state are simply $\pm g_0\sqrt{N_e}$. If we now allow two excitations shared by the atom(s)-cavity system in order to determine the eigenvalues of the second excited state, we find that not only N_e is needed but also the quantity $M_e \equiv \sum|\psi_i|^4$. Diagonalizing the interaction Hamiltonian for a collection of N_s two state atoms coupled to the cavity mode and sharing 2 excitations yields the eigenvalues of the second excited state,

$$0, \quad \pm g_0\sqrt{4N_e - 2\frac{M_e}{N_e}}. \tag{5.2}$$

Note that for all N_s atoms at the same site with optimal coupling, Eq. 5.2 reduces to

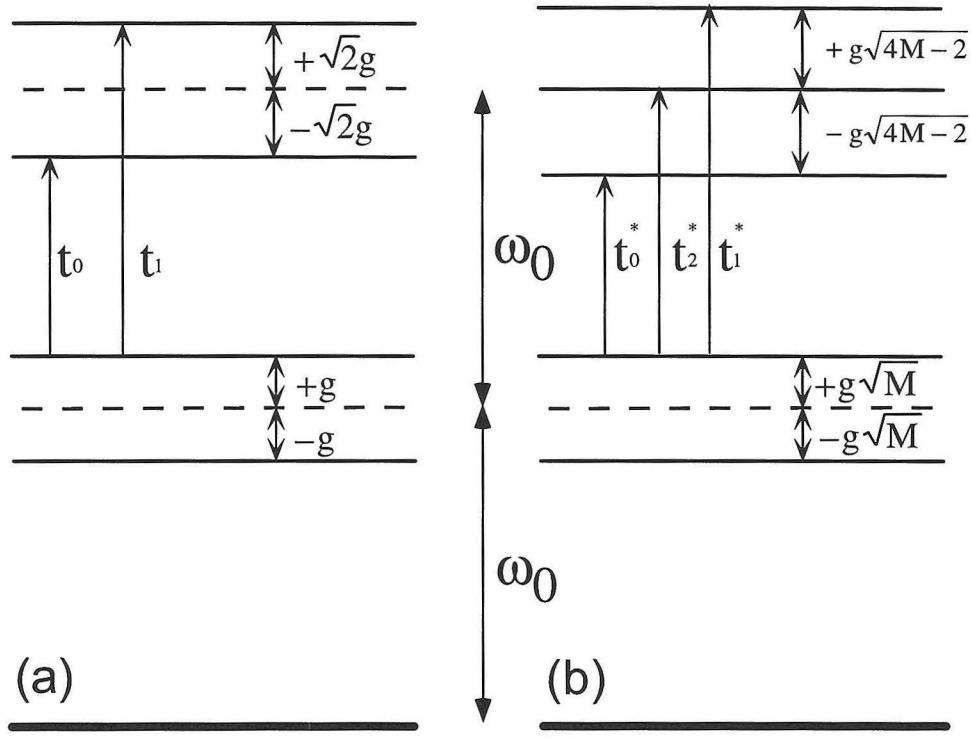

Figure 5.1: Comparison of level structure of the first two excited states of a coupled atom-cavity system for the one atom case (left) and the many atom case ($M \gg 1$) (right). The transitions t_0 and t_1 occur at $-(\sqrt{2}+1)g$ and $+(\sqrt{2}-1)g$ respectively (relative to $\omega_0 \equiv \omega_a = \omega_c$). In the large-$M$ limit transitions t_0^*, t_1^* and t_2^* are at $-3g\sqrt{M}$, $+g\sqrt{M}$ and $-g\sqrt{M}$. For $M \gg 1$, t_0^* is highly suppressed, so that the 1st to 2nd excited state transitions overlap with the ground to excited state transitions, and the quantum anharmonicity is lost. By contrast, for 1 atom, there is a distinct separation between ground to 1st excited state and 1st to 2nd excited state transitions.

$\pm g_0\sqrt{4N_s - 2}$.

If we now allow that the number of atoms and their distribution on the cavity mode fluctuates (on time scales faster than the detection time) then the transmission functions in which these eigenvalues appear must be further averaged. If also the system is driven, the situation gets still more complicated, since in general there are drive-strength dependant level shifts and the intracavity field build-up depends on the exact number and position of the collection of atoms.

A fully quantum treatment of the eigenvalue structure of the atom-cavity system in the presence of continuous excitation and dissipation is a nontrivial theoretical undertaking. However, as has been demonstrated repeatedly over the past 15 years, the utility of a semiclassical model of the coupled atom-cavity system is far-reaching. In addition, the semiclassical equations are more tractable from the perspective of modelling a real experiment in which fluctuations, dissipation and drive must be treated.

We thus begin with the semi-classical treatment. The well-known Maxwell-Bloch equations for the expectation values of the cavity field mode $\langle\hat{a}\rangle$, the atomic polarization $\langle\hat{\sigma}_l^-\rangle$ and inversion $\langle\hat{\sigma}_l^z\rangle$ are given as follows for the l^{th} atom in a sample of N_s atoms:

$$\begin{aligned}
\langle\dot{\hat{a}}\rangle &= -(\kappa + i\Theta)\langle\hat{a}\rangle + \sum_{l=1}^{N_s} g(\vec{r}_l)\langle\hat{\sigma}_l^-\rangle + \varepsilon \\
\langle\dot{\hat{\sigma}}_l^-\rangle &= -(\gamma_\perp + i\Delta)\langle\hat{\sigma}_l^-\rangle + g(\vec{r}_l)\langle\hat{a}\rangle\langle\hat{\sigma}_l^z\rangle \\
\langle\dot{\hat{\sigma}}_l^z\rangle &= -\gamma_\parallel(\langle\hat{\sigma}_l^z\rangle + 1) - 2g(\vec{r}_l)(\langle\hat{a}^\dagger\rangle\langle\hat{\sigma}_l^-\rangle + \langle\hat{a}\rangle\langle\hat{\sigma}_l^+\rangle).
\end{aligned} \tag{5.3}$$

Here ε denotes a coherent driving field at frequency ω_p (which defines the rotating frame for Eqs. 5.3), $\Theta = (\omega_c - \omega_p)/\kappa$ is the cavity detuning, $\Delta = (\omega_a - \omega_p)/\gamma_\parallel$ is the atomic detuning, κ is the cavity field decay rate and $\gamma_\perp$ is the transverse atomic decay. For pure radiative decay $\gamma_\perp = \gamma_\parallel/2$. Note that $\gamma_\parallel$ is in general the decay rate to modes other than the privileged cavity mode. However, for our cavities, $\gamma_\parallel$ is essentially the same as for an atom in free space since we operate in the limit that the solid angle (f)

subtended by the cavity mode is small ($f \approx 10^{-5}$). Finally, the dipole coupling coefficient for an atom with transition moment μ at site $\vec{r}$ within the cavity standing wave is $g(\vec{r}) \equiv g_0\psi(\vec{r})$, where $g_0 \equiv (\mu^2\omega_c/2\hbar\epsilon_0 V)^{1/2}$ is the optimal coupling coefficient and $\psi(\vec{r}) \equiv \sin(kz)\exp[-(x^2+y^2)/\omega_0^2]$ is the cavity mode function for our Gaussian, standing wave mode with mode volume $V_m \equiv \int_{-\infty}^{\infty} dx \int_{-\infty}^{\infty} dy \int_0^l dz\, |\psi(x,y,z)|^2 = \pi\omega_0^2 l/4$. Two useful dimensionless quantities relevant to both the quantum and semiclassical theories which can be derived from the rates $(\kappa, \gamma_\perp, g_0)$ are the saturation photon number, $n_0 \equiv b\gamma_\perp\gamma_\parallel/4g_0^2$, where $b = 8/3$ for a Gaussian standing-wave mode, and the critical atom number $N_0 \equiv 2\gamma_\perp\kappa/g_0^2$. Our task now is to understand the behaviour predicted by Eqs. 5.3 for various drive configurations and strengths.

5.2.2 Weak excitation: linear regime

Under vanishing excitation ($\varepsilon/\kappa \ll 1$), Eqs. 5.3 are readily solved in steady state. The transmission function $T(\omega_p)$ of a weak external probe, operationally defined as the ratio of transmitted to incident field amplitude, is, in the case of coincident cavity and atomic frequencies ($\omega_c = \omega_a$), given by

$$t_{lin}(\omega_p) = \frac{\kappa[\gamma_\perp - i\omega_p]}{(\lambda_+ - i\omega_p)(\lambda_- - i\omega_p)}. \tag{5.4}$$

The eigenvalues $\lambda_\pm$ are given by

$$\lambda_\pm = -\left(\frac{\kappa+\gamma_\perp}{2}\right) \pm \left[\left(\frac{\kappa-\gamma_\perp}{2}\right) - g_0^2 N_e\right]^{1/2}, \tag{5.5}$$

and describe the collective normal modes of the coupled system. Note that in the weak field limit considered here, $\lambda_\pm$ simply contain $g_0\sqrt{N_e}$ to account for the varied couplings of the N_s atoms in Eq. 5.3. Eqs. 5.4 and 5.5 are valid for all N_e in any regime of $(\kappa, \gamma_\perp, g_0)$ as long as the excitation is "weak" (intracavity photon number less than the saturation photon number). That is to say, either the approach we have adopted here or an approach utilizing the full quantum master equation leads to the same prediction of normal mode structure (5.5) and the same transmission function

(5.4).

From Eq. 5.5, a normal-mode splitting is formally expected for $g_0\sqrt{N_e} > (\gamma_\perp - \kappa)/2$ with corresponding $\lambda_\pm \approx -(\kappa+\gamma_\perp)/2 \pm i g_0\sqrt{N_e}$. Only if $g_0\sqrt{N_e} > (\kappa+\gamma_\perp)/2$ will the splitting be observable. Considering the observability of the normal-mode splitting for the case $N_e = 1$ we adopt the criterion $g_0 > (\kappa, \gamma_\perp)$ for the strong coupling regime. The imaginary parts of the resulting eigenvalues give rise to a normal mode splitting, which in the case $N_e = 1$ (in the optimal coupling limit), is known equivalently as the single-atom vacuum-Rabi splitting at $\pm g_0$ or the first excited state of the Jaynes-Cummings ladder, as has been observed in direct spectroscopic measurements [7, 177, 191] in our group.

5.2.3 Strong excitation: nonlinear regime

While the underlying quantum structure of the coupled atom-cavity system in the absence of drive or dissipation is well understood, probing that structure in the laboratory has proved a challenging task. A number of measurement strategies have been theoretically investigated, including single-field coherent excitation [36, 200], and excitation with incoherent light [200, 201]. In response to our experimental investigation, Carmichael and co-workers [202, 203] have explored a pump-probe type measurement and developed both a semiclassical and fully quantum theoretical treatment of the nonlinear response of the coupled atom-cavity system. The semiclassical approach treats a weak external probe in the presence of a strong, fixed frequency pump field in which one finds the steady state solution for the presence of the pump alone, and then treats the probe as a perturbation. We begin from Eq. 5.3, where now the driving field consists of two frequencies such that $\varepsilon \rightarrow \epsilon_{\text{pump}} + \epsilon_{\text{probe}} e^{-i\omega t}$ where ω is the frequency of the weak probe ($\epsilon_{\text{probe}} \ll \epsilon_{\text{pump}}$).

We seek an analytical expression for the transmitted probe amplitude which is valid for a collection of atoms each with arbitrary coupling to the cavity field which can be incorporated into a numerical simulation of our experiment (averaged over many realizations of randomly generated atomic distributions). To do this, we make

an expansion to first order in the probe field ϵ_{probe} and to third order in the pump field ϵ_{pump} which results in the following expression for the transmission spectrum of a weak probe at a frequency ω:

$$t_{\text{nonlin}}(\omega, N_e, M_e) = t_p(\omega, N_e)\left[1 - n_{\text{u}} t_p(\omega, N_e) h_p(\omega, M_e)\right]^{-1} \tag{5.6}$$

where n_{u} is the pump intracavity photon number and

$$h_p(\omega, M_e) = \frac{2g_0^4 M_e}{\kappa(\gamma_\perp - i\omega)}\left[\frac{2\gamma_\perp}{\gamma_\parallel(\gamma_\perp^2 + \Delta_{\text{u}}^2)} + \frac{2\gamma_\perp - i\omega - i\Delta_{\text{u}}}{(\gamma_\parallel - i\omega - i\Delta_{\text{u}})(\gamma_\perp - i\Delta_{\text{u}})(\gamma_\perp - i\omega)}\right] \tag{5.7}$$

with Δ_{u} the detuning between the pump frequency and the uncoupled, coincident atom and cavity frequencies.

The linear transmission part $t_p(\omega, N_e)$ appearing in Eq. 5.6 is given by

$$t_p(\omega, N_e) = \frac{\kappa(\gamma_\perp - i\omega)}{(\kappa - i\omega)(\gamma_\perp - i\omega) + g_0^2 N_e}, \tag{5.8}$$

which is just a rewritten version of Eq. 5.4. We have allowed $2\gamma_\perp/\gamma_\parallel \neq 1$ to account for a slight transit broadening (see Refs. [32] and [45] for a discussion of the validity of this approximation). Eqs. 5.6–5.8 are a complete specification of the transmission of a weak probe in the presence of a pump field with intracavity photon number n_{u} and detuning Δ_{u} for an atom-cavity system with effective atom number N_e and moment M_e.

In a Monte-Carlo numerical simulation of the experiment, we do not know the intracavity pump photon number *a priori* since we drive the atom-cavity with a fixed power, fixed frequency *external* pump field, of strength i_{in}. For each distribution (each instance of N_e, M_e), the pump intracavity photon number n_{u} is found by inverting the the following equation:

$$i_{in} = n_{\text{u}}\left[\left(1 + \frac{2C_1 N_e}{1+d^2} - \frac{2C_1 n_{\text{u}} M_e}{n_0(1+d^2)^2}\right)^2 + \left(\phi - \frac{2C_1 N_e d}{1+d^2} - \frac{2C_1 n_{\text{u}} M_e d}{n_0(1+d^2)^2}\right)^2\right], \tag{5.9}$$

where $d = \Delta_{\text{u}}/\gamma_\perp$ and $\phi = \Delta_{\text{u}}/\kappa$. Eq. 5.9 is an extension of the standard optical

bistability state equation for the case of a randomly distributed atomic sample. So, in total, with Eqs. 5.6–5.9, we now have a complete description of the probe transmission for a fixed external drive which can be related to an experimental measurement.

As implied above, we expect the semiclassical treatment to make incorrect structural predictions as $N_a \rightarrow 1$ (in the strong coupling regime) which is the point at which the quantum anharmonicity should play an important role. For comparison, a full quantum electrodynamical treatment of the coupled system for our particular choice of measurement strategy, including dissipation, but excluding multi-atom couplings and fluctuations has been carried out [204]. In this treatment, the Jaynes Cummings resonances discussed in Section 5.2.1 are clearly evident for an atom-cavity system with sufficiently strong coupling when it is probed using a pump-probe geometry similar to that described in this paper. (It should be noted that even for a single atom without fluctuations in number and position, the observation of distinct multiquanta resonances requires a coupling to dissipation ratio of approximately 20, compared to the ratio $2g_0/(\kappa+\gamma_\perp) \approx 5$ for this work). The essential full quantum treatment which includes the effects of multiple atoms with different coupling strengths, and of fluctuations in both number and coupling, and of transit effects requires a sophisticated approach, and work is currently underway by Carmichael and co-workers[1] to model a system similar to the one described here using the method of quantum trajectories [205]. The computational resources required for such a calculation are large and at present seem too prohibitive to make this a useful technique for detailed quantitative comparison with experimental results.

[1]Personal communication, H. J. Carmichael.

5.3 Semiclassical simulations, or, What exactly is a 1 atom effect?

5.3.1 Description

We turn now to a discussion of modeling our experiment. At the most fundamental level, we have a complex quantum mechanical system consisting of a beam of atoms interacting with a single cavity mode. Ideally, we would like to make predictions of the outcomes of particular measurements on such a system. Quantum mechanically, this is a challenging task. To model our experiment requires keeping track of a phenomenally large amount of information. For example, even when there is on average less than 1 atom in the cavity mode volume V_m, the response of a large number of "spectator" atoms—those atoms which are weakly coupled due to their location on the skirts of the Gaussian beam waist, or those atoms which are near the nodes of the standing wave field—must be taken into account. Indeed, counterintuitively, it is these very atoms which smooth the otherwise much larger fluctuations in cavity transmission and hence allow any sort of useful observation of single atom effects. But these spectator atoms make a full quantum mechanical simulation extremely costly.

Our initial approach has been to develop a semiclassical model based on the results of the preceding section which accounts for fluctuations in number and position of atoms within the cavity mode but which approximates transit time effects by a simple modification of $\gamma_\perp$ (as discussed in the context of Eq. 5.6). The model is equivalent to a full quantum treatment in the weak field linear regime, but is a semiclassical approximation for strong excitation. The semiclassical model starts at Eq. 5.3 and the procedure is as follows:

We begin with a series of "tosses" of atoms into the cavity mode. Each toss consists of choosing randomly the (x_j, y_j, z_j) coordinates of N_s atoms and evaluating the mode function $\psi(\vec{r}_j) \equiv \psi_j$ for each atom. The simulation volume V_s contains, and is much larger than a volume of space equal in size to the mode volume V_m. To model our experiments in which the atomic beam is collimated only by the cavity substrates

(collimation equal to the length of the cavity), V_s is chosen to be $10w_0$ along the Gaussian waist (x-,y-directions) and only $l/4$ along the cavity axis (z-direction) since this accounts for all possible couplings along the standing-wave. For each toss an effective number of atoms $N_e = \sum_{j=1}^{N_s} |\psi_j(\vec{r}_j)|^2$ is calculated. (In addition, $M_e = \sum_{j=1}^{N_s} |\psi_j(\vec{r}_j)|^4$ is computed for the nonlinear simulations.) Typically, to achieve $N_e \sim 1$ in V_s, $N_s \approx 100$. Simulations with a larger V_s and N_s (but with the same N_e) have been run, with little change in the resulting spectra, confirming that atoms further than $10w_0$ from the cavity axis contribute negligibly to the overall probe transmission spectrum. From N_e (and (M_e, n_u) if necessary) a transmission spectrum is generated using either Equation 5.4 or 5.6. The transmission function generated with each toss is then averaged over a large number $N_t \sim 2000$ of tosses. Thus, finally produced is an averaged spectrum $Q_a(\omega) = 1/N_t \sum_{i=1}^{N_t} t_a(N_{e_i}, M_{e_i}, \omega)$ where t_a is either $|t_{lin}|^2$ from Eq. 5.4 or $|t_{nonlin}|^2$ from Eq. 5.6. Q_a results from an average collective atom number $N_a \equiv \sum_{i=1}^{N_t} N_{e_i}/N_t$. More specific details of the simulations depend on the regime (linear or nonlinear) of simulation and the type of probe detection employed.

5.3.2 Linear simulations

We begin with the results of our linear simulations. Eq. 5.4 is used to generate the appropriate transmission function which is then averaged over a large number of tosses to produce Q_{lin}. It is clear that Q_{lin} will not be identical to a spectrum generated by directly inserting N_a into Eq. 5.4, especially in the case $N_a \sim 1$ when Poissonian fluctuations are relatively large. It could be possible, however, from the definition of N_e and N_a that a given averaged splitting could be equivalently generated either from a few atoms strongly coupled to the cavity mode or from many atoms weakly coupled to the cavity mode. This is actually not true, because the number fluctuations in the two cases leave observably different signatures on the resultant spectrum as was first pointed out in Ref. [7]. Indeed, in Ref. [7] a convincing measure of the average intracavity atom number is derived from the effects of fluctuations on the linear probe transmission spectrum. Pursuing this issue in more detail, we

will compute the distribution of atoms which contributes to a given experimental or simulated spectrum. Particularly, we would like to know the role of a single nearly optimally coupled atom in a spectrum with $N_a \sim 1$. The impact of a single atom in a cavity with the parameters of this experiment is tremendous. For example, the cavity transmission on resonance changes by a factor $1/(1+2/N_0)^2 \sim 10^{-3}$ when a single optimally coupled atom traverses the cavity mode, so one optimally coupled atom is expected to play a very important role in a given spectrum.

Let us continue this pursuit. We define a volume in which an atom will have a certain fraction of the optimal coupling, say $g_c = f_c g_0$ (in which case the "coupling" volume $V_g = \epsilon(f_c)V_m$). Now for each toss of atoms (N_s is chosen to give $N_e \sim 1$) we count the number of atoms N_g in V_g and keep track of those cases in which exactly 1 atom appears in V_g ($N_g = 1$), when no atoms at all appear in V_g ($N_g = 0$) and when two or more atoms are present in V_g ($N_g \geq 2$). The result of such a tracking is histogrammed in Fig. 5.2 and shown along with the sum of all contributions. Here we make the choice $\epsilon = 1$, corresponding to $V_g = V_m$ and $f_c = 0.56$. We show the distributions for $N_a \approx 1.0$ (a) and $N_a \approx 0.7$ (b). In Fig. 5.3 we show the corresponding spectra, with the contributions to the overall probe transmission spectra shown for the same breakdown as in Fig. 5.2. Contrast the averaged spectrum with a spectrum due to a single atom optimally coupled to the cavity mode, also shown.

Several comments are in order at this point. 1) For the two values of N_a shown, the $N_g = 1$ case is a major contributor both to the N_e breakdown (35% of the cases had $N_g = 1$) and to the magnitude of the overall splitting. The overall splitting is indeed given by $g_0\sqrt{N_a}$ to good approximation for $N_a = 1$, slightly less so for $N_a = 0.7$. A further study has shown that the absolute error in splitting as determined from the simple prescription of measuring the peak separation and dividing by $2g_0$ to infer $\sqrt{N_a}$ as compared to the result from the simulation remains approximately constant as the number of atoms is lowered, so that the relative error becomes increasingly large. For example for the two values of N_a shown in Fig. 5.3, for the simulation with $N_a = 1$ the splitting is g_0 to within 4%, while for the simulation with $N_a = 0.7$ the splitting is $g_0\sqrt{0.7}$ to 10%. While paradoxically the case for single atom effects may not be as

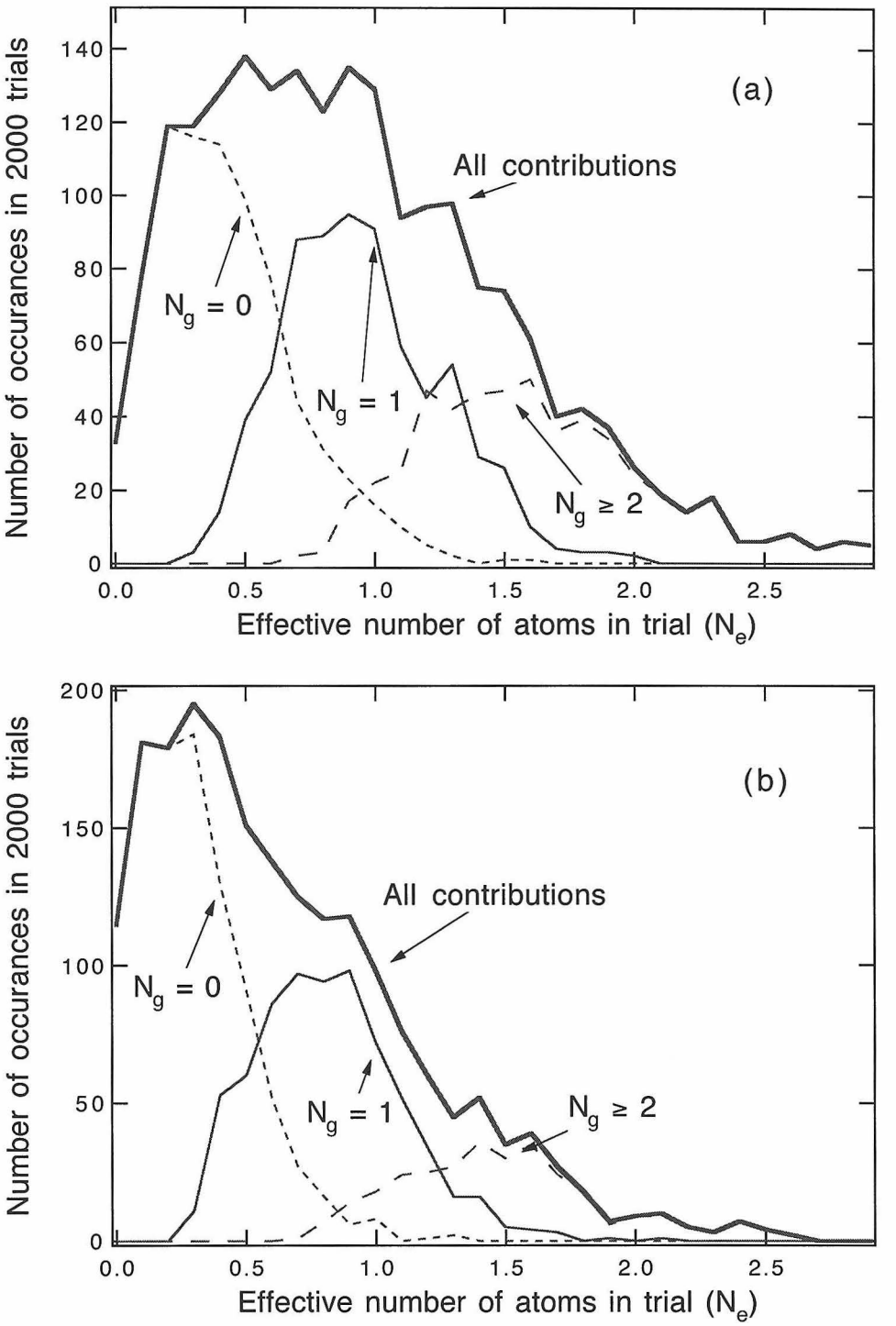

Figure 5.2: Occurrences of occupation number N_g in volume $V_g = V_m$ (as discussed in the text) for typical 2000 trial simulation of $N_a \approx 1.0$ (a) and $N_a \approx 0.7$ (b).

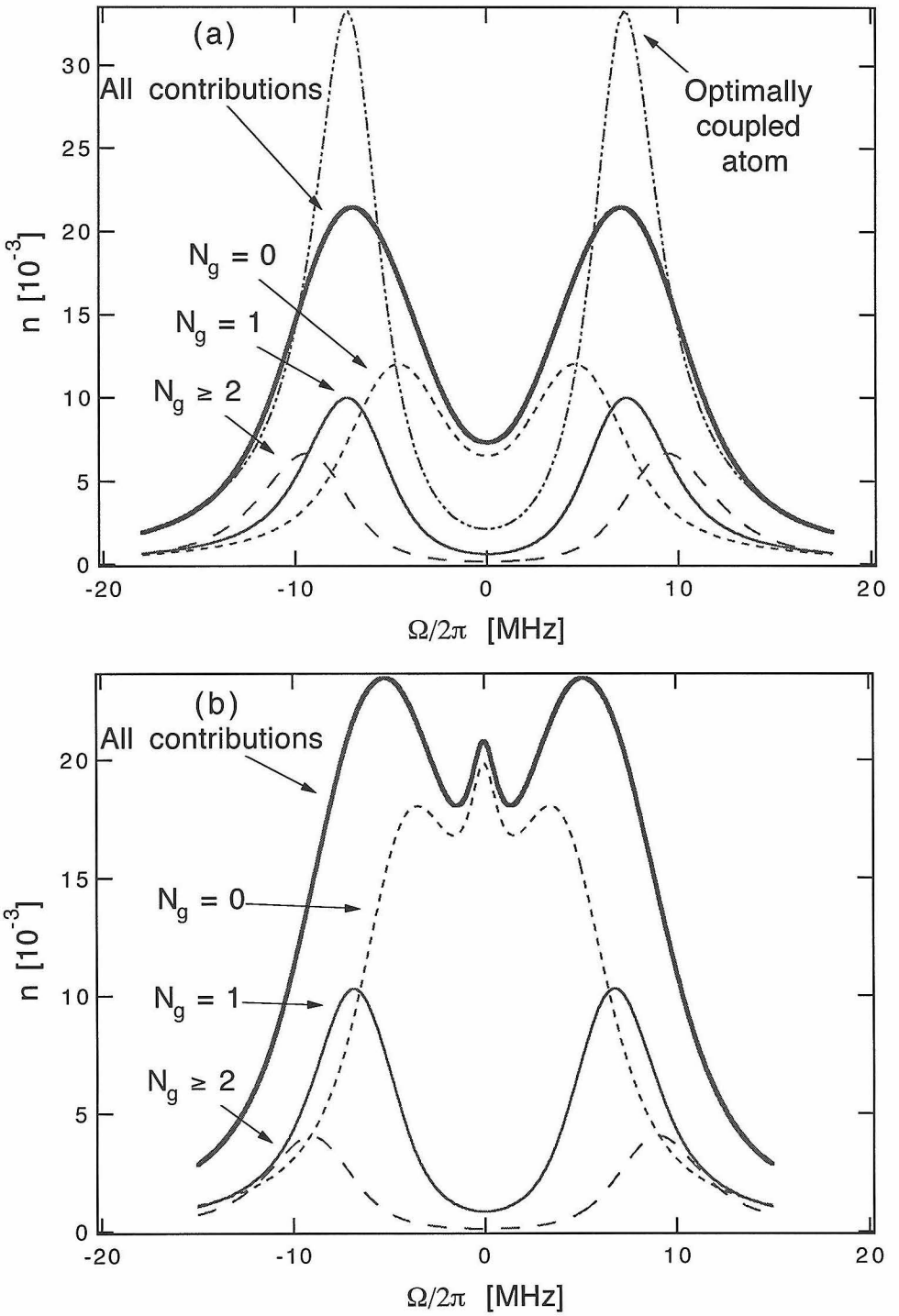

Figure 5.3: Breakdown of the contributions of various numbers of atoms in the cavity mode volume (as discussed in the text) for two different average intracavity atom numbers. Graph (a) has $N_a \approx 1$ atom (with the dash-double-dot curve for one atom optimally coupled for comparison) and graph (b) has $N_a \approx 0.7$ atoms. $(g_0, \kappa, \gamma_\perp)/2\pi = (7.3, 0.6, 2.5)$ MHz.

convincing as for our previous cavity parameters (Ref. [7], with smaller g_0), we are still convinced that what we observe when $N_a \sim 1$ is an effect with unique unambiguous signatures of the strong coupling of single atoms within the mode volume V_m.

2) It can be clearly seen in Fig. 5.3b that there is an auxiliary peak at $\Omega = 0$. The breakdown in terms of the values of N_g shows that this is contributed from those cases in which there are no atoms in V_g—this is simply the transmission function of the (very large) empty cavity peaking through. During the times when there are no atoms in V_g, there are still a large number of spectator atoms giving rise to $N_e \sim 0.4$ from Fig. 5.2b. These spectator atoms play the critical role of keeping the empty cavity from completely dominating the transmission spectrum. The central peak can be made much larger by shrinking V_s and thereby lowering N_s as has been done in Ref. [192]. Our choice of V_s is for an atomic beam whose dimensions are much larger than the cavity waist which has the important effect of diminishing the role of the empty cavity while retaining observability of the essential single-atom effects.

It should be noted at this point that this is not a universally accepted interpretation of the situation. The authors of Ref. [192] have argued that there is no way to observe normal-mode splittings in the "true single-atom regime" with presently realized cavity QED parameters. Their point is as follows: Clearly, the actual cavity volume V_c is much larger than our chosen V_g (formally $V_c \to \infty$), and when $N_e = 1$ there is certainly more than one atom interacting with the whole cavity volume (formally $N_s \to \infty$). If one takes V_g to be much larger than V_m and demands (as a definition of the "true single-atom regime") that at most one atom ever be present in $V_g \gg V_m$, then for an atomic beam experiment in which only the average atomic density can be controlled, most of the time there will be no atoms at all present within V_m. In this case, the single-peaked empty-cavity response will completely dominate the spectrum and no splitting at all will be observeable. As this is simply their choice of a *definition* of the "single-atom regime," it is irrefutable.

Of course the cavity volume V_c is as large in the transverse dimension as the cavity mirror substrates, and where one draws the formal boundary is somewhat arbitrary. Our choice for this boundary is a reasonable definition based on a volume

in space equivalent to the cavity mode volume, in which the coupling is large ($|\psi|^2 > 0.31$ for $V_g = V_m$). In any event, the breakdown of the spectra (especially those of Ref. [7]) clearly show that single atoms contribute significantly to the overall spectra, and that the "spectator" atoms serve the primary function of attenuating the otherwise large empty cavity contribution. To define the "true single-atom regime" by demanding that the empty-cavity peak dominate, as Ref. [192] has in effect done, may be appropriate in some situations (e.g., the cavity transits described in Chapter 7 [46]) but seems to us not to be physically motivated in the current setting of atomic beam cavity QED. The choice $V_g = V_m$ accounts for 70% of the total cooperativity parameter.

Aside from these issues, there are two points which should be set straight regarding claims made in Ref. [192]. That they were "the first to confirm this unique feature," (the unique feature being the central peak due to the empty cavity at low atomic beam flux) is not at all true. Our own observation of this experimental artifact predates their observation by a number of years [206], as do our simulations of the effects of fluctuations in the atomic beam [7]. These are quite well-known effects, and their importance has been amply noted [177]. They also make the claim that they have observed "line-shape splitting without normal-mode oscillations," in an implication that one can be fooled by "line-splitting" observations. This has been done in an experiment in which the atom-cavity parameters are not in the strong-coupling limit (the eigenvalues are purely real), so their observed "line splitting" of course has nothing to do with a normal-mode splitting—in fact it is not a "line-splitting" at all but merely the two maxima in the transmission function on either side of the atom-absorption valley, as we measured and noted well before their result [45].

3) The number of trials in the simulation and the number of spectator atoms N_s are important parameters of the simulation. These must not be chosen too small.

5.3.3 Nonlinear simulations

We first present plots derived directly from Eq. 5.6 via numerical calculation for optimally coupled atoms. For optimally coupled atoms, $N_e = M_e \equiv N$, the actual number of atoms in the cavity. In order to help quantify the nonlinear effect, we derive a difference spectrum simply by subtracting the pump absent case from the pump present case. Fig. 5.4 shows pump on/off transmission spectra along with difference spectra for $N = 4$ and $N = 1$. We expect expression 5.6 to be valid only for pump intracavity photon numbers $n_{\mathrm{u}} < 1$.

The simulation in the nonlinear case is similar, but slightly more complicated than the linear case. We begin by choosing the *desired* number of atoms N_d. Of course, we cannot know N_a until the simulation is complete, but if the calculation parameters are chosen appropriately, then we can get N_a consistently close to N_d. We also choose an approximate desired number of intracavity pump photons n_d from which we can calculate the appropriate, (and approximate) fixed drive by use of the state equation

$$i_{in} = n_d \left[\left(1 + \frac{2N_d C_1}{1 + d^2 + n_d/n_0} \right)^2 + \left(\phi - \frac{2N_d C_1 d}{1 + d^2 + n_d/n_0} \right)^2 \right], \tag{5.10}$$

where d and ϕ are defined in the context of Eq. 5.9. This fixes i_{in} for the entirety of the simulation. As usual, N_e and M_e are computed for each toss. Now, since the the actual pump intracavity photon number n_u builds up depending on the values of N_e and M_e, we must solve Eq. 5.9 in order to have an appropriate n_u associated with the fixed drive i_{in} which can then be used in Eq. 5.6 for each toss. For consistency of notation, I will call this effective pump intracavity photon number η_e in analogy to N_e and M_e and likewise, η_e averaged over the N_t trials will be called η_a in analogy with N_a. In Figures 5.5 and 5.6 we show histograms of N_e, M_e and η_e for $N_a = 3$, $\eta_a = n_0/3$ and $N_a = 1$, $\eta_a = n_0/5$. The corresponding spectra are shown in Fig. 5.7. For these figures, the pump frequency is coincident with the Rabi peak for the desired

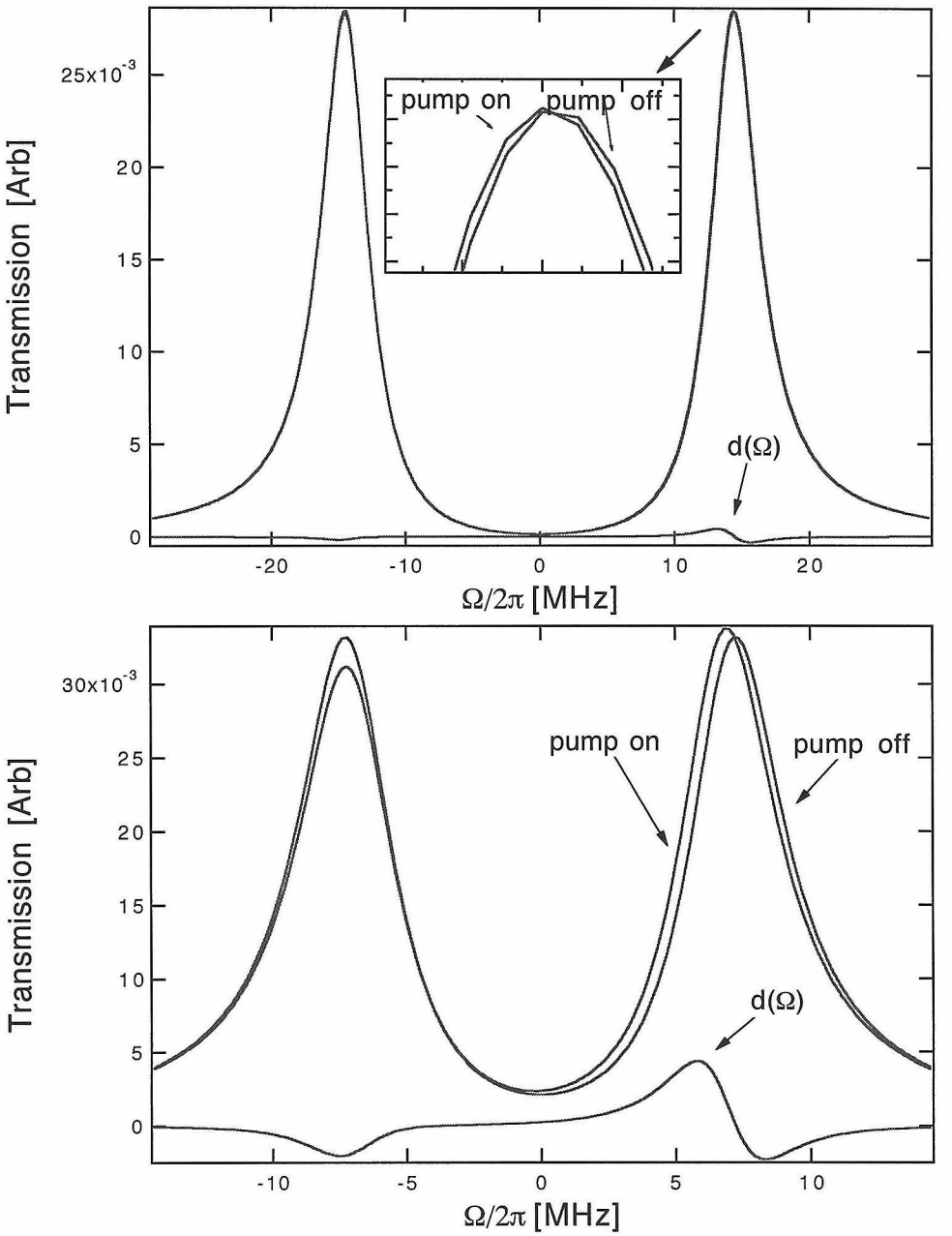

Figure 5.4: Nonlinear spectra (strong pump, weak probe) for optimally coupled atoms. Pump power $n_u = n_0/2$ for (a) $N = 4$ and (b) $N = 1$ optimally coupled atom(s). The frequency of the pump is at $g_0\sqrt{N}$ in both curves. $d(\Omega)$ is the difference spectrum. $(g_0, \kappa, \gamma_\perp)/2\pi = (7.3, 0.6, 2.5)$ MHz.

number of atoms N_d. This is a fixed quantity, the same for every toss with value

$$\Delta_u = -\sqrt{N_d g_0^2 - \frac{(\gamma_\perp - \kappa)^2}{4}}. \tag{5.11}$$

In practice, N_a turns out to be very close to N_d, so indeed Eq. 5.11 does turn out to be a pump at the correct frequency. This procedure is meant to mimic the experimental situation in which there is an estimate of the number of intracavity atoms (based on the linear transmission spectrum) with the pump detuning set accordingly and with an arbitrary external fixed drive power.

5.3.4 Comments on comparison of simulated and experimental data

We are free in the simulations to average over the modulus ($Q_a = \overline{|t(\omega)|}^2$) or the modulus-square ($Q_a = \overline{|t(\omega)|^2}$) of the transmission spectrum. Of course, we can simulate any averaging process, but ultimately we would like to choose one that is actually used in an experiment. Unfortunately, this has proved to be slightly more problematic than it may at first appear. We therefore will discuss carefully in this section how a comparison of simulated and experimental data is made.

All results presented thus far are for averaging over the modulus-square ($Q_a = \overline{|t(\omega)|^2}$). An experiment in which this is the correct choice is one which employs a photon counting detection process. Let us assume that the time scale over which the intracavity atomic distribution evolves is set by the transit time T_0 of atoms crossing the cavity field. Over a time T_0 each atom distribution "snapshot" evolves into the next. Our experimental detection always averages over many snapshots, producing the averaged transmission spectrum Q_a. In the case of photon counting, the detector samples for a time $t_d \gg T_0$ during which the cavity-output photon stream is collected. This performs an average over the *intensity* of the cavity output field so that $Q_{pc} = \overline{|t(\omega)|^2}$ is measured. This was the detection method of our previous work [7] and the simulations fit well with the data. In addition, we have done a

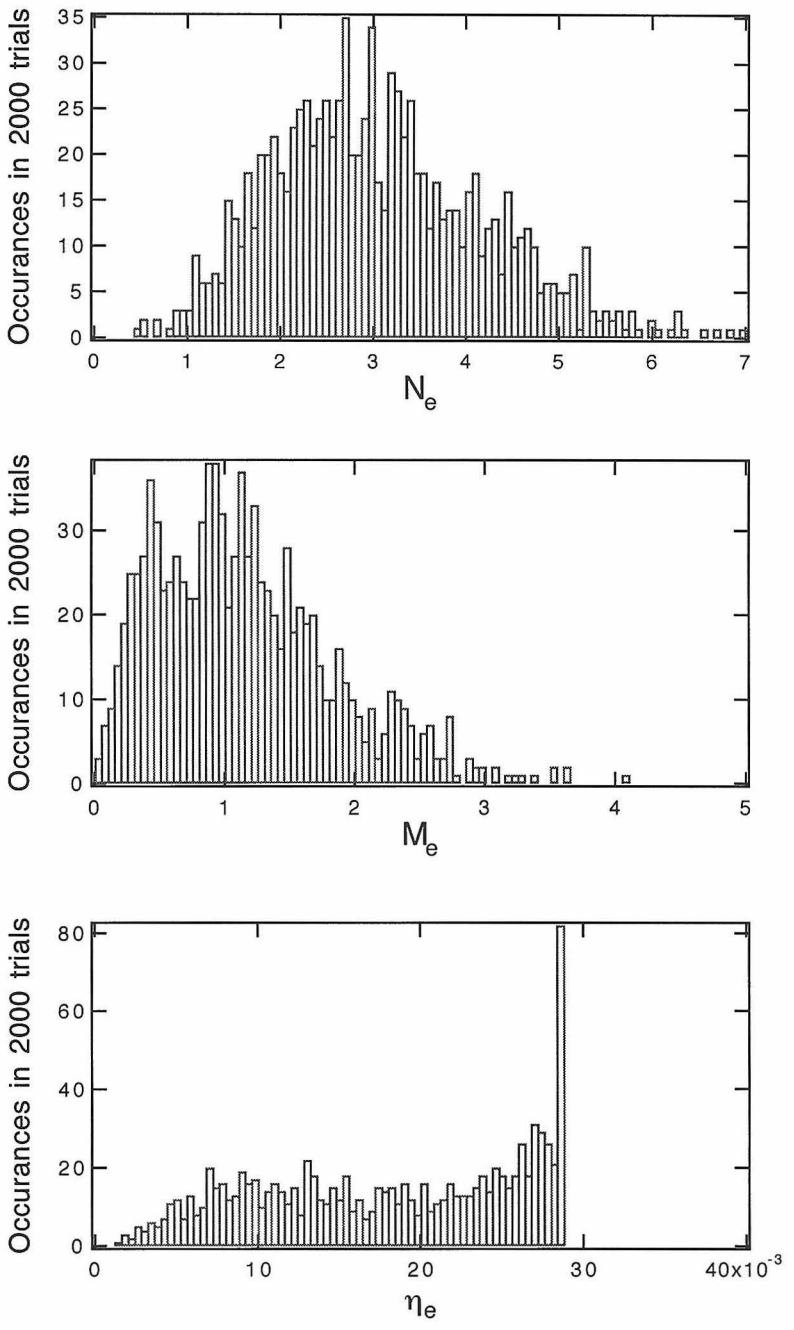

Figure 5.5: Histogram of N_e, M_e and η_e for a full nonlinear simulation ($N_t = 2000$) for $N_a \approx 3$, $\eta_a \approx n_0/3$. The abrupt final point in η_e can be explained by the following. There is a fixed drive strength, so that there is clearly a maximum value of η_e allowed. We are driving with the pump at the Rabi peak, so a fluctuation an atom number in either direction always causes the pump to leave resonance and the build-up to decrease.

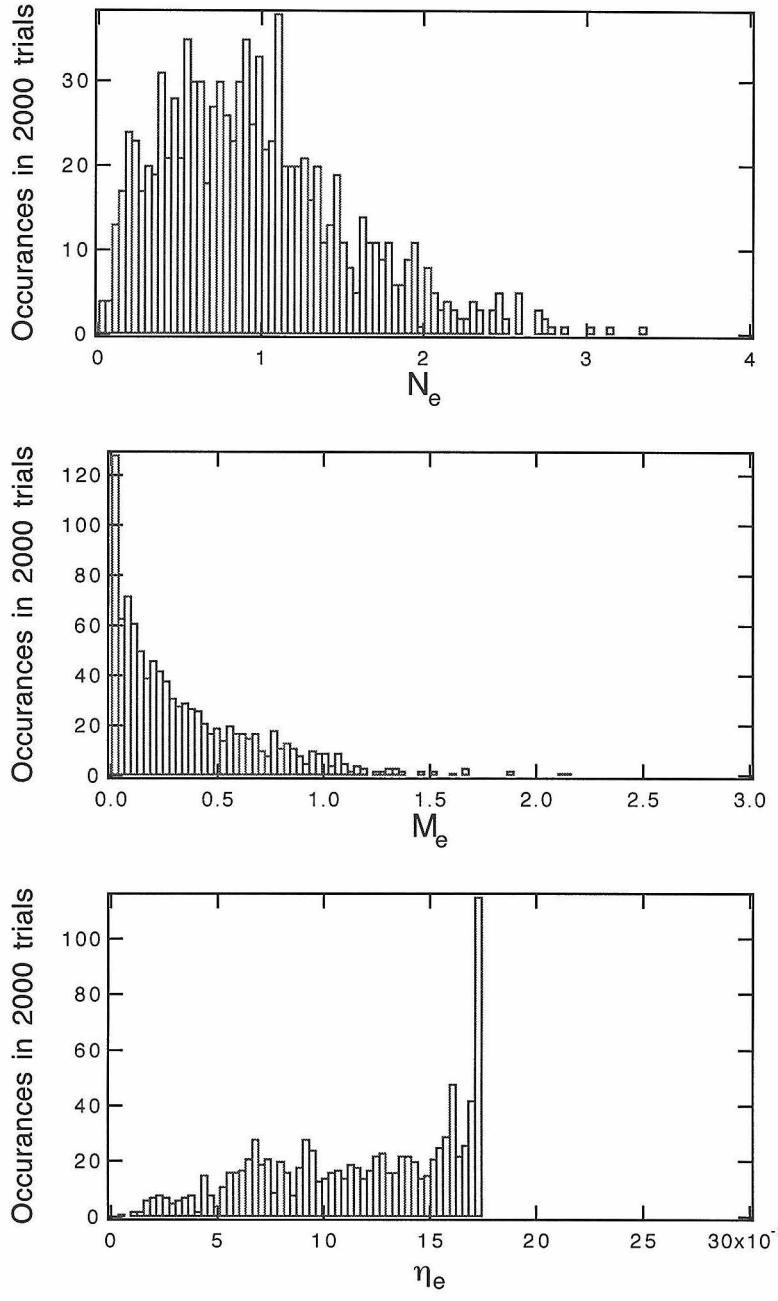

Figure 5.6: Histogram of N_e, M_e and η_e for a full nonlinear simulation ($N_t = 2000$) for $N_a \approx 1$, $\eta_a \approx n_0/5$.

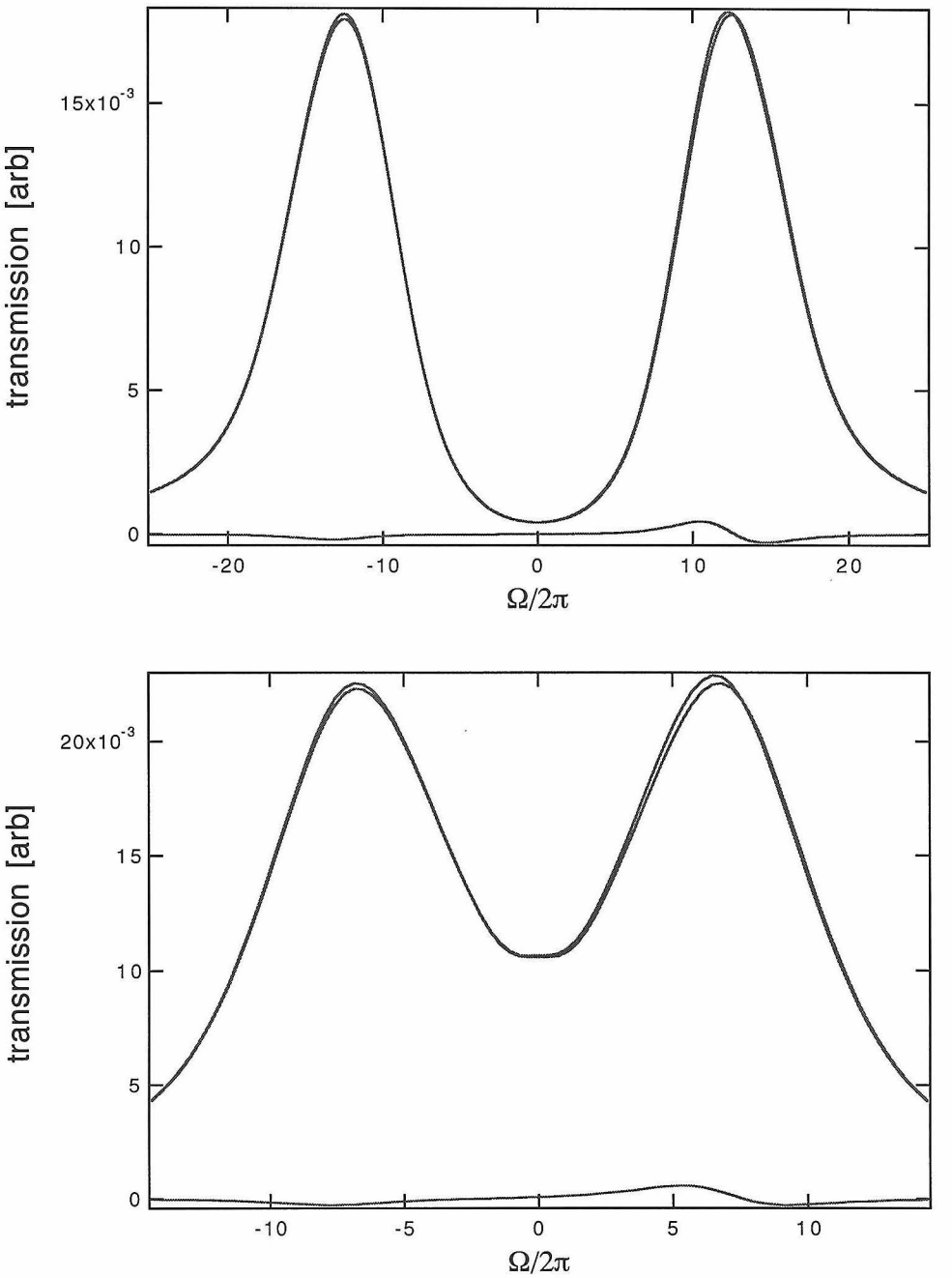

Figure 5.7: Spectra associated with Fig. 5.5 (top graph) and Fig. 5.6 (bottom graph). $(g_0, \kappa, \gamma_\perp)/2\pi = (7.3, 0.6, 2.5)$ MHz.

limited number of photon counting measurements for the cavity parameters of this experiment, and again we have seen good agreement between simulation and data [177]. (To look ahead, refer to Fig. 5.9.)

The photo-detection used in most of the present experiments, however is different. For the measurements of pump and probe fields, there are two different fields with frequency separation ranging from a few to tens of MHz, so good frequency discrimination is required (which is quite difficult with photon counting and frequency selective filtering). Detection via an optical heterodyne was therefore utilized. In this type of detection, the field *amplitude* of the transmission spectrum is written as coherent modulation on an rf photocurrent in combination with (white) shot noise and noise due to atomic fluctuations. The technique by which this photocurrent is then processed determines the appropriate averaging of the data. Any process seeks to extract the coherent signal from the inevitable noise sources. We chose a sensitive (low noise floor) rf spectrum analyzer to mix down the rf and readily view the modulation as a dc signal on the screen of the spectrum analyzer. The critical element is the resolution bandwidth (RB) of the SA which was was chosen small: $2\pi B \ll T_0^{-1}$, so that the spectrum analyzer performs an averaging over many atomic transit times. The spectrum analyzer has an envelope detector and not a true square law detector, so that the averaging performed by the spectrum analyzer is of the $\overline{|t(\omega)|}$ type, which we then square in post processing to produce *in principle* a measurement of $Q_{het} = \overline{|t(\omega)|}^2$.

Spectra simulated with the two different methods of averaging yield qualitatively similar but quantitatively different line-shapes and amplitudes. The differences are by far most pronounced near $\Omega = 0$. This region is also very sensitive in the experiment to uncertainties such as beam alignment. It is an empirical fact, that no matter what we believe the heterodyne detection process to be, that on the whole, the data agree better with a calculation of $Q_a = \overline{|t(\omega)|^2}$ than with $Q_{het} = \overline{|t(\omega)|}^2$. In light of this, we continue to use the $Q_a = \overline{|t(\omega)|^2}$ averaging process in our simulations throughout. While this may seem a brash decision based on our knowledge (both theoretical and for simple empirical test cases) of the inner workings of the heterodyne detection,

it turns out not to be critical for several reasons. The first, as we have stated, is that the most pronounced difference between the two averaging procedures appears in the "valley" between the Rabi peaks, near $\Omega = 0$. This is a notoriously sensitive region. For example, the auxiliary central peak in Fig. 5.3b is exquisitely sensitive to experimental uncertainties, particularly atomic beam alignment, and indeed, to the fluctuations in atom number themselves. Slight changes in N_a (on levels far more sensitive than our control over oven temperature drift, e.g.) produce dramatic changes in the the central peak. Simply put, it is difficult to model the central region of the data successfully. The second saving grace is that the position of the Rabi peaks does not differ to any significant degree for the two methods of averaging as determined from simulations. And finally, the simulated difference spectra are only slightly affected, perhaps indicating that this simple math (subtraction) reveals the true underlying eigenstructure, which surely must be independent of the way the data are averaged. In particular, the position of the difference peak does not change at all under the two averaging types.

5.4 Pump-probe experiment

5.4.1 Apparatus

The experimental setup employed is as depicted in Fig. 5.8. The core of the apparatus is a small ($L = 346$ μm, $w_0 = 38$ μm), high finesse ($\mathcal{F} = 3 \times 10^5$) resonator formed by the two mirrors M_i and M_o with radii of curvature 17 cm and transmission coefficients $\delta_i \approx 1 \times 10^{-6}$ and $\delta_o \approx 1.5 \times 10^{-5}$ (non-transmission, scattering losses in the cavity substrates were on the order of 4×10^{-6}). An optically prepared beam of Cesium atoms intersects the cavity axis at 90°. The transition investigated is the $(6S_{1/2}F = 4, m_F = 4 \rightarrow 6P_{3/2}, F' = 5, m'_F = 5)$ transition at 852 nm. Together with the free-space lifetime of the $6P_{3/2}$ level ($\tau = 32$ ns [207]), these parameters lead to the set of rates $(g_0, \kappa, \gamma_\parallel)/2\pi = (7.3 \pm 0.3, 0.6 \pm 0.1, 5)$ MHz. From the above parameters, $(n_0, N_0) = (0.16, 0.06)$. Transit broadening due to $T_0 \approx 10/\gamma_\parallel$ leads to a modification

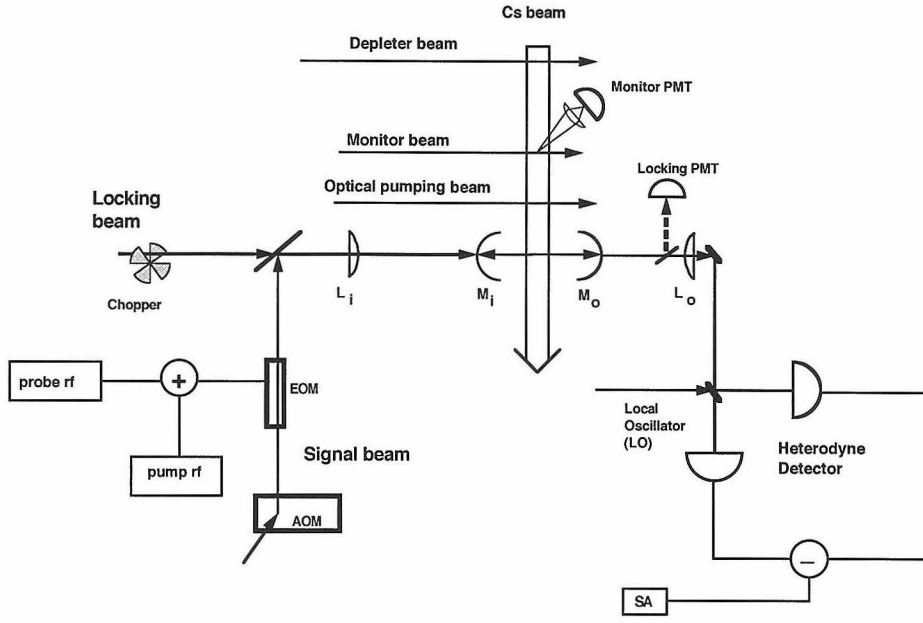

Figure 5.8: Schematic of the experimental apparatus. TWM is an electro-optic travelling wave modulator. The depleter beam controls the atomic flux in the correct (F = 4) ground state, the monitor beam registers this flux. The locking beam is part of the cavity length servo and is chopped at 1.7 kHz. During the "off" cycle of the locking beam, the transmitted probe is measured by the balanced heterodyne detector. L are mode-matching lenses. The reflectivity of the beam-splitter which deflects part of the cavity output to the lock PMT is 15%.

of $\gamma_\perp = \gamma_\parallel/(2 \times 0.7)$. (This is cavity #2 from Table 2.1.)

The linear response of the coupled atom-cavity system is investigated using a frequency tunable probe generated using acousto-optic (AOM) and electro-optic (EOM) modulators from the output of a frequency stabilized titanium-sapphire laser (10-100 kHz rms linewidth). The probe is mode-matched to the TEM_{00} mode of the cavity, whose length is actively servo controlled to within 10% of its full spectral linewidth. The cavity-length servo consists of a large-intensity ($n_{lock} \approx 10^3 n_s$) "lock beam" incident on the cavity; both mirrors are on piezo-electric (PZT) transducers with which the cavity length is dithered very slightly (at 80 kHz); the transmitted lock beam is detected via a lock-in with the error signal fed back to a mirror PZT. The lock beam

is chopped by a mechanical chopper wheel (50% duty cycle at 1.7 kHz) to attain an attenuation of more than 60 dB during the "off" cycle, at which time the probe beam is observed without the interference of the lock beam. The transmission of the weak ($n_p \ll n_s$) probe beam is recorded as a function of its frequency on a radio-frequency (RF) spectrum analyzer (SA) after balanced optical heterodyning with an intense local oscillator frequency detuned -40 MHz from the common uncoupled atom-cavity center. For the nonlinear spectroscopic studies, we employ an additional fixed frequency pump field, which is generated by summing a constant frequency, variable strength, RF signal with the tunable, weak, RF probe signal. The resultant sum of RF signals drives the EOM for pump/probe generation. (Note that this set-up uses a different arrangement of LO/probe frequency generation, but that the basic idea is the same as that of Sections 2.1.4, 2.1.5.)

5.4.2 Linear results

In order to immediately touch base with the simulations we start this section with data taken via a photon counting method, in which the averaging process is unquestionably of the type $Q_a = \overline{|t(\omega)|^2}$. These data for an average intracavity atom number $\bar{N} = 1$ are shown in Figure 5.9. The experimental details are identical with those of Ref. [7], so we will not discuss the details here. Note that we have introduced a new quantity $\bar{N}$. This is the experimentally determined version of N_a from the simulations. As per the discussion above, $\bar{N}$ can be read directly from the measrued splitting between Rabi peaks for $\bar{N} \sim 1$, but should be determined from a fit to simulations with averaging over fluctuations for atom numbers below this. The procedure of fitting averaged transmission spectra $Q_a = \overline{|t(\omega)|^2}$ is seen from Figure 5.9 to work quite well, as expected from our experience with our previous system with smaller g_0. It can be seen already in these data that the data at $\Omega = 0$ are subject to larger variance than those elsewhere in the frequency scan. This does not tend to go away with averaging, but rather just tends to "fill in" the central region. This makes it a problematic region for comparisons with the simulations, as stressed above.

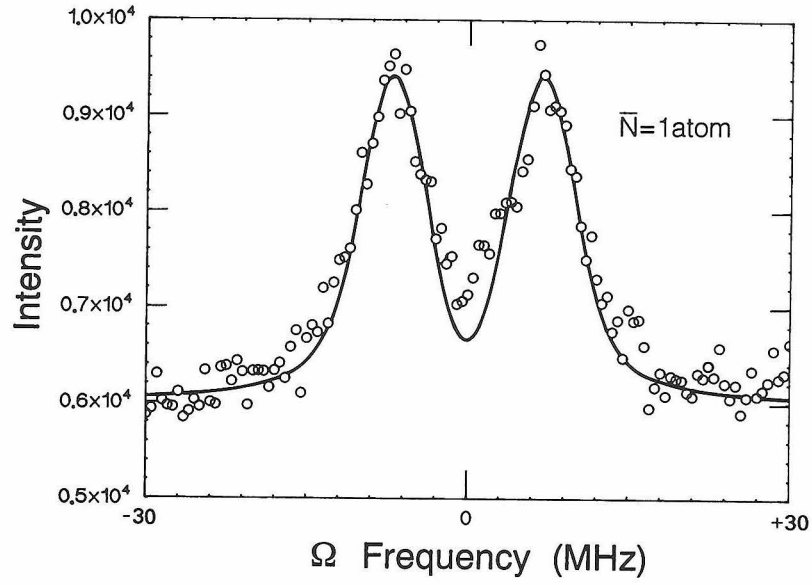

Figure 5.9: Linear spectrum for $\bar{N} \approx 1.0$ atoms measured by photon counting. $\omega_a = \omega_c$. The solid curve is a simulation which includes the effects of atomic number and coupling fluctuations with $g_0/2\pi = 7.3$ MHz and $N_a = 1.0$, $\kappa/2\pi = 0.6$ MHz, $\gamma_\perp = 2.5/0.7$ MHz.

We now move on to the heterodyne measurements, which are imperative for the nonlinear spectroscopy and which are used exclusively onward from this point. We present in Figure 5.10 a typical transmission spectrum of the probe beam for our coupled atom-cavity system, in the weak field limit (with no pump field present). Here $\bar{N} = 1.1$ atom, with $\Omega = 0$ corresponding to the position of the common uncoupled atom-cavity resonance. To facilitate comparison with Eq. 5.4 the data have been processed by squaring the output of the SA, subtracting the background (shot noise) level, and then normalizing to account for the frequency dependence of the probe generation and detection process. Note that the ordinate is normalized in units of the intracavity photon number $n_{\rm probe}$ with $n_{\rm probe} \lesssim 0.02$ over the scan range (compare this to $n_0 = 0.16$). The observed doublet structure with peaks at $\Omega = \pm g_0$ is a direct spectroscopic measurement of the vacuum-Rabi splitting discussed above. (The sharp feature at $\Omega = 0$ is the RF generated during the lock cycle by the lock beam, a small amount of which feeds through electronic RF attenuators which otherwise prevent this signal from reaching the SA. It is **not** present during the data taking cycle.)

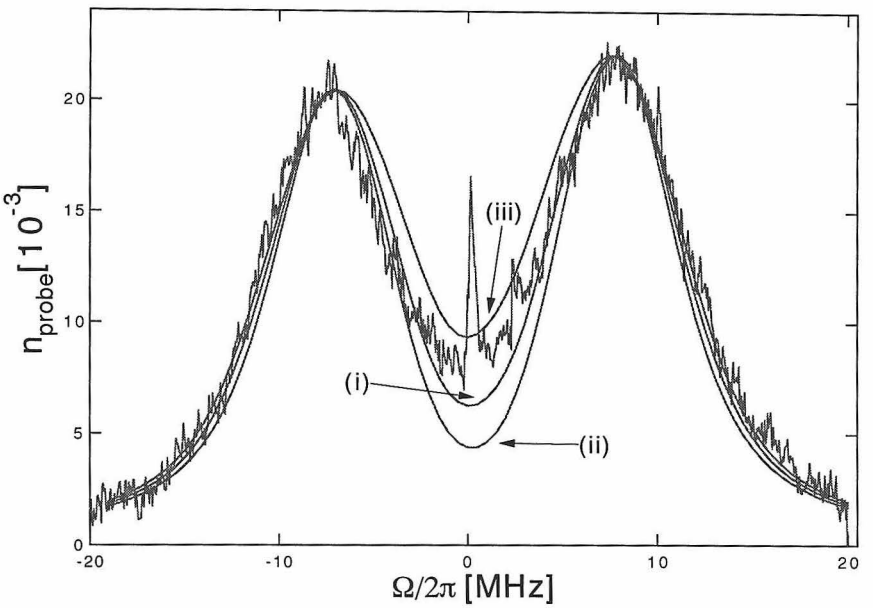

Figure 5.10: Linear spectrum for $\bar{N} \approx 1.1$ atoms measured by heterodyne detection. Nominally $\omega_a = \omega_c$, but there is a slight detuning. The solid curves are simulations which include the effects of atomic number and coupling fluctuations. Curve (i) has $g_0/2\pi = 7.3$ MHz and $N_a = 1.1$; curve (ii) has $g_0/2\pi = 8.0$ MHz and $N_a = 0.95$; curve (iii) has $g_0/2\pi = 6.6$ MHz and $N_a = 1.4$.

Also shown in the figure is a series of simulation plots, using the measured values of g_0 κ and $\gamma_\perp = \gamma_\parallel/2/0.7$. The simulation plots are generated as discussed above in Section 5.3. For the parameters of our system, the magnitude of the splitting even in the presence of fluctuations is $g_0\sqrt{\bar{N}}$ with the principle effect of the fluctuations being a significant increase in the cavity transmission near $\Omega = 0$. Thus, since g_0 is known independently, we can determine the number of atoms to a good approximation simply by measuring the splitting, but we can also calibrate this procedure by studying the sensitivity of our spectra to atomic beam fluctuations in the vicinity of $\Omega = 0$. This is shown with curves (i) - (iii) in which $g_0\sqrt{N_a}$ is kept constant while g_0 and N_a are varied. Curve (i) has $g_0/2\pi = 7.3$ MHz and $N_a = 1.1$, as we would surmise from the data, while (ii) has $g_0/2\pi = 8.0$ MHz and $N_a = 0.95$ (iii) has $g_0/2\pi = 6.6$ MHz and $N_a = 1.4$, neither of which match as well as curve (i). As stated above, we have fixed the simulation averaging procedure at $Q_a = \overline{|t(\omega)|^2}$, which appears to perform quite well. Note that in comparison with our previous measurements [7], the resolution of the splitting for a single atom is significantly improved in our current system, but not by as much as one might naively expect, from the more than two-fold increase in the coupling ($g_0/2\pi = 3.2 \rightarrow 7.3$ MHz) and the more than 8-fold increase in C_1 (see Table 2.1). This disappointing result is due to the even greater role of atomic fluctuations in a system with increased C_1.

5.4.3 Nonlinear results

Armed with this experience in the linear realm, we next move to explore nonlinear spectroscopy of the coupled system. We note immediately that our goal in performing the pump-probe type experiment was to observe multi-photon quantum transitions and to study the evolution of these resonances for large numbers of atoms where the semiclassical equations should correctly predict spectra. If we take Eq. 5.1 as a guide, we conclude that $\bar{N} = 4$ atoms is sufficiently large to be reasonably well described by semi-classical theory, since $q_a = 0.94$ for this atom number. In addition, at this number of atoms, the effects of fluctuations in atom number are less pronounced than

for $\bar{N}$.

In Figure 5.11 we present a sequence of pump-probe spectra, with varying pump intensity, taken for a "large" number of atoms ($\bar{N} = 4.2$ atoms.). The experimentally measured pump intracavity photon number $\bar{\eta}$ ranges from zero intracavity pump photons, to $\bar{\eta} = 0.75 \pm 0.3$ intracavity photons, on average, and its frequency is chosen to coincide with the higher frequency resonance of the un-pumped atom-cavity system at $\Omega/2\pi = +(g_0/2\pi)\sqrt{\bar{N}} = 14.8$ MHz (this is visible as a sharp peak in the data, especially of graph (d)). The data have been processed in the same manner as in Fig. 5.10. For trace (a), taken with no pump, the observed splitting is just that of the weak field normal mode splitting discussed previously. From the fit (solid curve) and the splitting, we find that $\bar{N} = 4.2$, with the only adjustable parameter being the overall vertical scaling. In trace (b) the pump has been turned on, with a pump intensity corresponding to approximately $\bar{\eta} = 0.1 \pm 0.05$ intracavity photons, while in (c) the pump has been increased to $\bar{\eta} = 0.4 \pm 0.2$ photons and finally in (d) the pump is at $\bar{\eta} = 0.75 \pm 0.3$ photons. Clearly evident from the data is a trend towards lower heights for the "unpumped" peak as the pump power is increased. At the same time the pumped peak becomes higher and migrates inward towards the common atom-cavity frequency at $\Omega = 0$. In addition, the width of the "pumped" peak narrows, with the width of the upper peak in graph (d) being 30% reduced compared to that of the peak in graph (a). In each case the pumped peak is higher than the un-pumped peak and no additional resonances are observed. For a linear system, the probe response would be independent of the pump (except of course at $\Omega_{probe} = \Omega_{pump}$), so that the data in Figure 5.11 represent a measurement of the nonlinear "susceptibility" for the atom-cavity system. The solid curve in trace (b) is a theoretical fit from Eq. 5.6 averaged over atomic distributions using the numerical simulation technique described above. Here the average atom number and overall height are parameters of the simulation, having been set from the fit in (a) to $N_a = 4.2$. The pump intensity is then the only free parameter for the fit to the nonlinear case, yielding a value for the intracavity pump intensity of $\eta_a = 0.38$ photons which is high compared to the measured value of $\bar{\eta} = 0.1 \pm 0.05$.

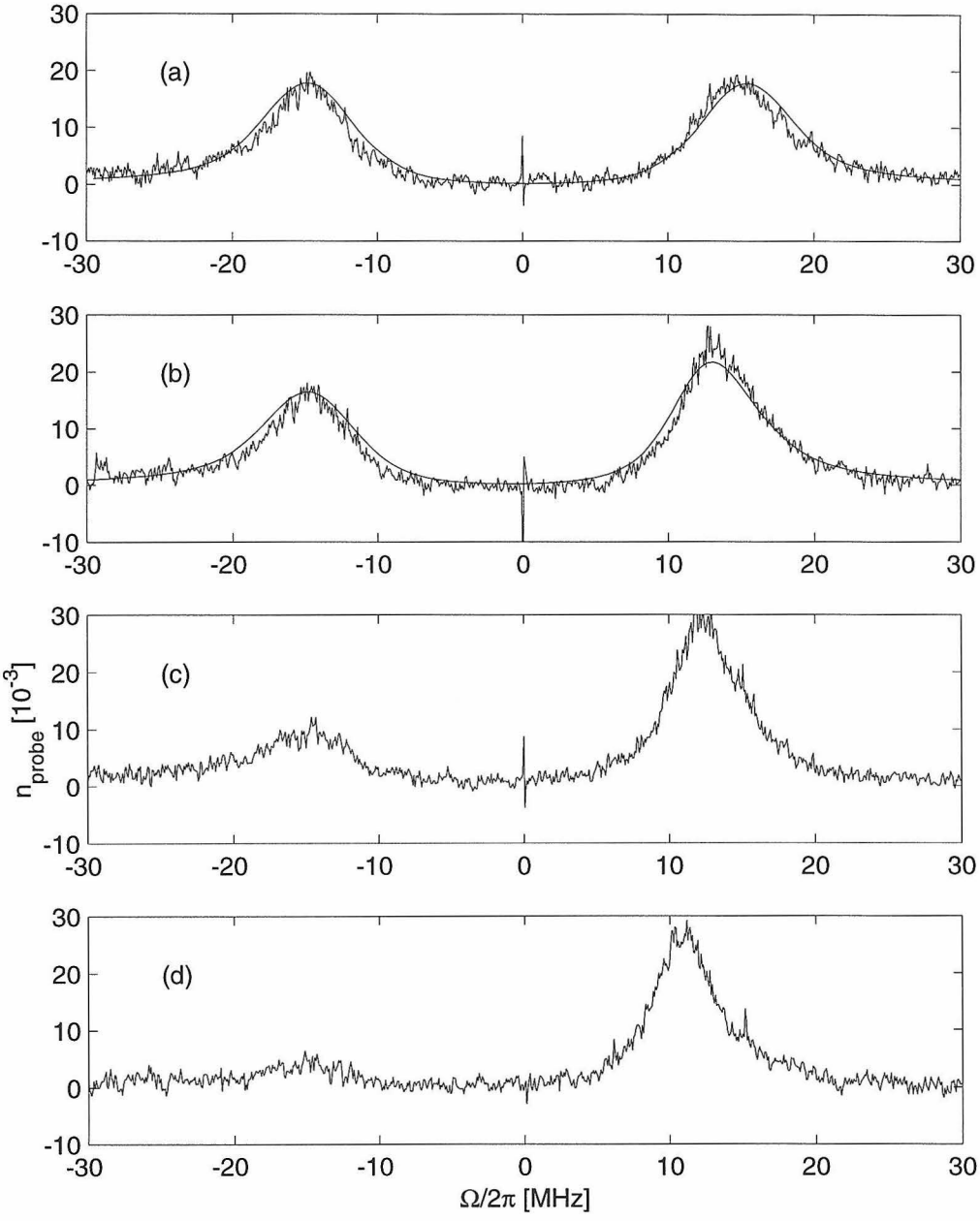

Figure 5.11: Sequence of nonlinear probe spectra for $\bar{N} \approx 4.2$ atoms with $\omega_a = \omega_c$. Here, the frequency Ω of a constant amplitude probe beam is swept and the transmission recorded (in units of probe intracavity photon number $n_{\rm probe}$). Trace (a) has probe field only, with the solid curve a fit to the data including the (minimal) effects of atomic fluctuations. From (b) to (d), the pump powers (again in units of intracavity photon number with atoms present) are $\bar{\eta} \approx 0.1,\ 0.3,\ 0.8$. The pump frequency is $\Omega_{pump}/2\pi = g_0/2\pi\sqrt{\bar{N}} = 14.8$ MHz, as indicated by the sharp feature in trace (d). The solid line in trace (b) is a nonlinear semiclassical simulation including atomic fluctuations and is described in the text. The best fit to the data has $\eta_a = 0.38$.

We next turn to data taken for approximately one intracavity atom. Figure 5.12 shows a sequence similar to Figure 5.11 for $\bar{N} \approx 1.1$ atoms. The solid curves are again simulations, which in this case warrant further discussion. It is seen that the linear simulation in this case is not a good fit, for the following reason. The data are taken under conditions in which the cavity and atomic detunings are nominally zero, but are subject to some drift, as has happened in the case of Figure 5.12. We do not at present model such detunings in our nonlinear simulations. We therefore want to determine an approximate height scaling of the non-detuned linear simulation which can then be applied to the nonlinear simulation. It is clear that this procedure is non-optimal, but it does reproduce the qualitative features of the nonlinear data. The pump powers for Figure 5.12 are similar to those in Figure 5.11. The best fit for pump photon number in Figure 5.12b is $\eta_a = 0.07$ as compared to the measured value $\bar{\eta} = 0.1$. As is obvious from these data, multi- quanta resonances of the sort predicted by Fig. 5.1 are not immediately apparent. As the probe frequency is scanned to investigate the first to second excited state transitions, it of course also probes the ground to first excited state transitions. Thus a means to isolate the nonlinear effect is needed.

In Figure 5.13 we introduce a naive attempt at such a technique by simply subtracting the linear spectrum from the spectrum with the pump field present, thereby deriving a "difference" spectrum from the data, much as the difference spectrum from the nonlinear simulations shown in Figures 5.4 and 5.7. The difference spectrum contains much information. For example, one may look for additional features that arise in a regime where the basic first excited state features change little. This would be indicated by near complete subtraction of the linear features with a new peak appearing at a frequency different from that of the pump frequency. Figure 5.13 shows linear (i), nonlinear (ii) and difference spectra (iii) as $\bar{N}$ is decreased from $\bar{N} \approx 1.6$ to $\bar{N} \approx 1.1$ to $\bar{N} \approx 0.75$. Here we have selected the data based on a level of qualitatively similar magnitude for the nonlinear effects.

The data of Figure 5.13c are data taken with $\bar{N} \approx 0.75$ atoms. Here the pump frequency is at $\Omega/2\pi = g_0/2\pi = 7.2$ MHz. Note that three peaks are evident in both the probe only data and in our linear numerical simulation (curve iv), with the

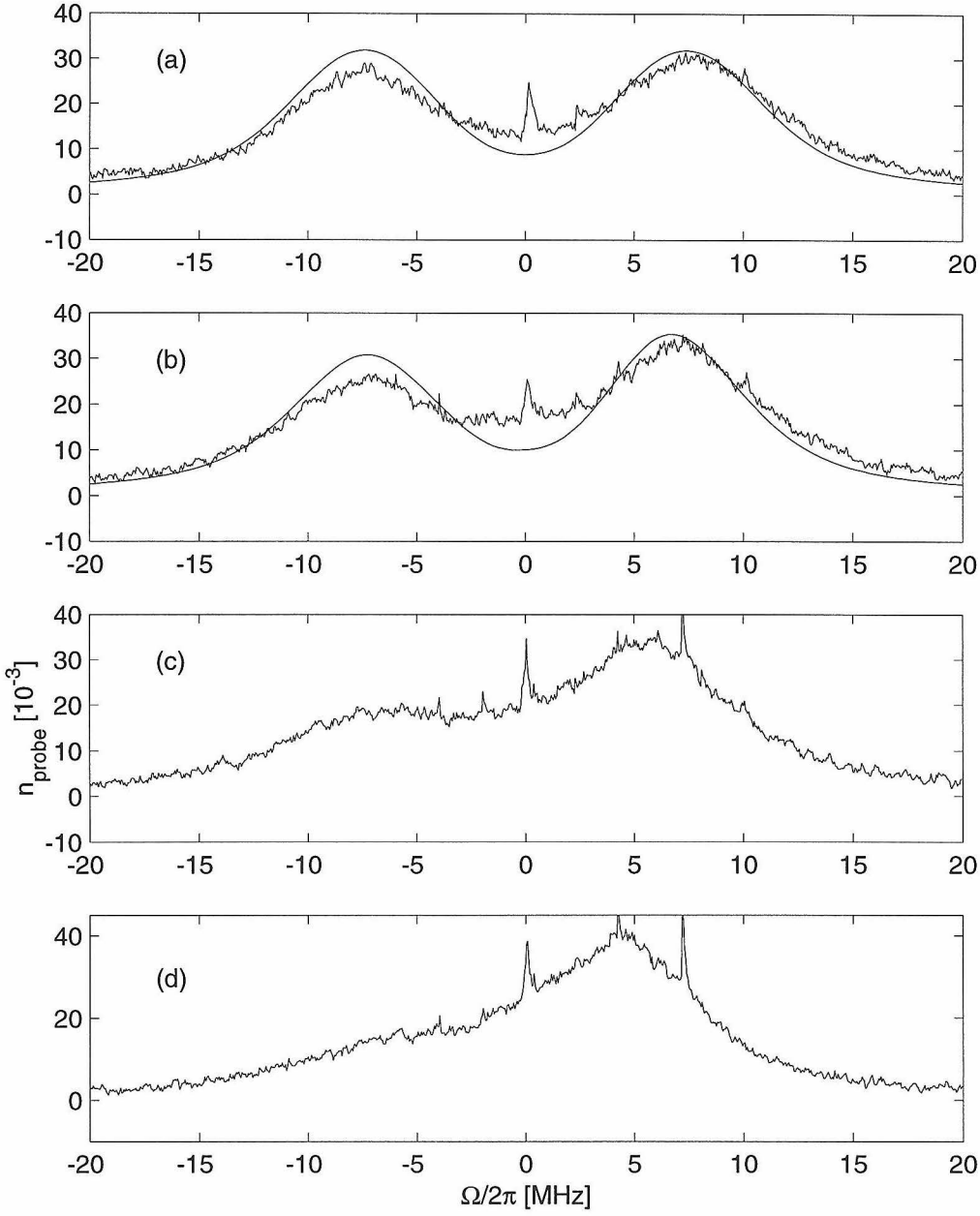

Figure 5.12: Sequence of nonlinear spectra for $\bar{N} \approx 1.1$ atoms with $\omega_a = \omega_c$. The top graph has probe field only. The pump powers are from top to bottom, $\bar{\eta} \approx 0.1,\ 0.4,\ 0.7$ intracavity photons on average. The pump frequency is $\Omega_{pump}/2\pi = g_0/2\pi\sqrt{\bar{N}} = 7.6$ MHz, as indicated by the sharp feature in trace (d). The solid curves are semiclassical simulations with $N_a = 1.1$ and for graph (b) $\eta_a = 0.07$. See the text for a discussion.

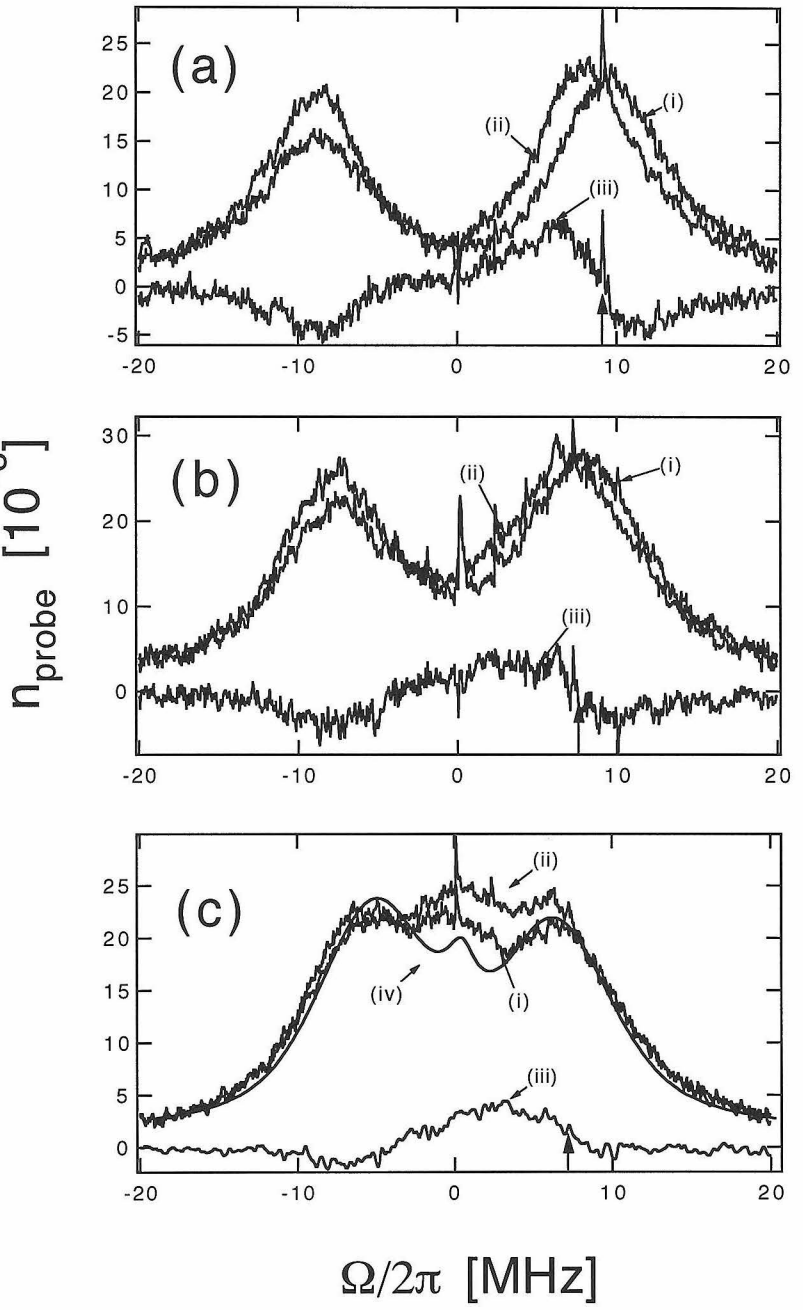

Figure 5.13: Linear and nonlinear spectra as the number of atoms is varied. Each graph contains a linear (no pump) spectrum (curve i), a nonlinear spectrum (curve ii), and a difference spectrum: [(curve ii) − (curve i)] (curve iii). From top to bottom the parameters are: (a). $\bar{N} \approx 1.6$, $\bar{\eta} \approx 0.4$, $\Omega_{pump}/2\pi = 9.1$ MHz; (b). $\bar{N} \approx 1.1$, $\bar{\eta} \approx 0.2$, $\Omega_{pump}/2\pi = 7.5$ MHz; (c). $\bar{N} \approx 0.75$, $\bar{\eta} \approx 0.06$, $\Omega_{pump}/2\pi = 7.2$ MHz. Curve (iv) in graph (c) is a theoretical fit to the linear spectrum, including the extent to which our Monte-Carlo simulations correctly incorporate fluctuations in atom number and position. As stated in the text the region near $\Omega = 0$ is extremely sensitive to imperfections in the apparatus, including atomic beam alignment.

central peak arising from the fact that now there is a significant fraction of the time in which there are no atoms present within the cavity mode volume. This a promising regime, because the contribution from multiple atoms in the cavity mode volume should be small (see Section 5.3), while the response from the zero-atom contribution (i.e., atoms outside the mode volume V_m with coupling $g < \epsilon_c g_0 \approx 0.56 g_0$) should be essentially linear since the saturation intensity is high for these spectator atoms. Thus an observed nonlinear response should be predominately due to contributions from single intracavity atoms within the mode volume. Of course, the trade off is that the peaks have merged to a degree that may drastically obscure the observation of new features. What we observe in the pump-probe spectra is a region of increased probe transmission, again on the inner side of the pumped peak, with very little change in the position or height of the un-pumped peak, or of the outer side of the pumped peak. Clearly evident in the difference spectrum is a broad peak centered roughly at $(g_0/2\pi)(\sqrt{2}-1) = 3$ MHz, which is consistent (but certainly not compellingly so) with what one expects from the QED theory of Section 5.2.3 (not including atomic fluctuations). That there are only small dips below zero at the positions of the pump-off resonances indicate that there has been only minor modification of the single quanta resonances. We emphasize that the peak shown in the figure demonstrates a nonlinear response for a system containing just one atom (on average), and an intracavity photon number of only $\bar{\eta} \approx 0.1$ photons.

While the data shown in Figure 5.13c are suggestive, we should stress that without a QED calculation which models all aspects of our experiment, including atomic transit effects and the critical role played by fluctuations in the atomic number and position it is difficult to determine the extent to which the data of Figure 5.13 can be explained by a semi-classical model (including the proper treatment of transit effects) or whether there are any aspects which have a purely quantum origin.

To further quantify our observations, we present in Figure 5.14 difference spectra with a corresponding set of simulated difference spectra. The pertinent information can be found in the figure caption. Unfortunately, these data and their comparison with simulations does not shed much more light on the issue of multi-quanta reso-

nances. However, they do show that the semiclassical simulations qualitatively agree with the data at "large" numbers of atoms ($\bar{N} = 4.2$) trending towards lesser agreement with the smaller atom numbers, though any quantitative comparison is far from conclusive. Whether this trend is indicative of a fundamental disagreement between a semiclassical theory and the experiment, or due to complications of the experiment such as transit broadening is certainly not easy to determine. It is possible that the features that we seek are to be found in a parameter regime not covered by the simulations. In fact, most of the data that we have taken (e.g., Figures 5.11c,d and 5.12c,d) have pump intracavity numbers that are too large for the analytical approximations that went into the derivation of Eq. 5.6, so that we have no way to compare these data with any theory.

Nonetheless, we continue our pursuit of a quantum feature by focussing in on a particular property of the data: the position of the peak on the high frequency side of the difference spectrum which from Figure 5.1 should coincide with the transitions t_1 and t_1^*. Towards this end, in Figure 5.15 we accumulate some of the nonlinear data that we have taken for this experiment and plot the positions of the measured peaks in the difference spectra ($\Box$) versus the average number of atoms $\bar{N}$, where we have averaged together data for the measured peak position taken over a range of pump powers from $\bar{\eta} = 0.06 - 0.2$ photons. We also show the prediction from our nonlinear semiclassical simulations, represented by a curve that is derived by a fit to many trials of the simulation over a dense collection of atom numbers. (The simulations show that the position of the difference peak is not a strong function of the pump power over the range we consider, even though the height of peaks is.) An interesting feature of the data is a "kink" occurring near $\bar{N} \approx 1.3$, followed by a leveling off of the peak position at a level close to $(\sqrt{2} - 1)g_0$, for $\bar{N} < 1$. The data appear to approach the semiclassical theory at high atom numbers, as we expect, but there are deviations at low atom numbers, with no "kinks" observed in the semiclassical theory. It should be noted that most of the low atom data include the semiclassical result near the limits of the uncertainty of the measurement. The leveling of the difference peak position would certainly be a compelling result from our perspective, but again, it is very

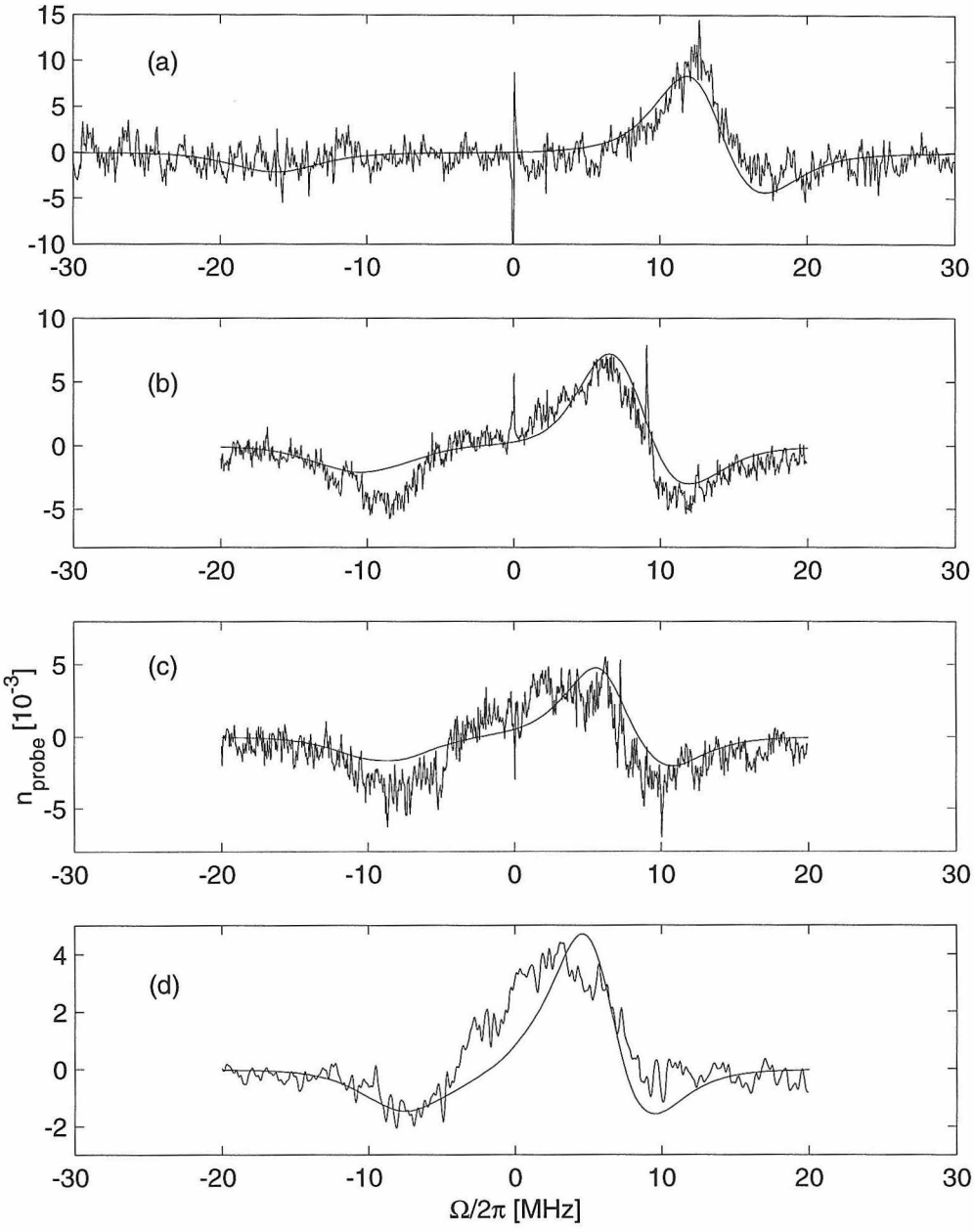

Figure 5.14: Difference spectra with semiclassical theory overlaid. The details are: Trace (a), $\bar{N} = 4.2$, $\bar{\eta} = 0.1$, $N_a = 4.2$, $\eta_a = 0.38$. Trace (b), $\bar{N} = 1.6$, $\bar{\eta} = 0.4$, $N_a = 1.6$, $\eta_a = 0.16$. Trace (c), $\bar{N} = 1.1$, $\bar{\eta} = 0.1$, $N_a = 1.1$, $\eta_a = 0.07$. Trace (d), $\bar{N} = 0.75$, $\bar{\eta} = 0.06$, $N_a = 0.75$, $\eta_a = 0.09$.

difficult to determine whether this represents a true quantum behaviour given the uncertainties in the peak positions and the caveats associated with our semiclassical simulations.

5.5 Conclusions and the future

We have performed extensive measurements of the nonlinear response of a strongly coupled atom-cavity system. While our initial objective was to observe clear multi-photon resonances as a decisive measure of the quantum nature of the system, it appears that our atomic beam system is not optimal for this and allows us to obtain only limited information. In the case of the structural investigation presented here, our strongly-coupled cavity QED system has hidden behind the mask of Poissonian fluctuations in atom number and position. While we have observed a discrepancy between our measurements and the semiclassical predictions, it is not clear whether this is the result of effects omitted from our model (*e.g.*, transit time) or whether it arises from a real quantum underpinning. For small $\bar{N} \lesssim 1.3$, the evidence is suggestive of the underlying quantum anharmonicity, while for large $\bar{N}$, the data asymptotes to the expected semiclassical result. More conclusive data are, no doubt, desirable.

Towards this end we are developing two strategies which we hope will correct the most serious defects of the current atomic-beam system. One involves precisely locating the atoms to the strong parts of $\Psi(\vec{r})$ [208] along with timing information of the atomic transit across the cavity mode. The other involves the use of atom trapping techniques [46]. These are the subjects of Part III.

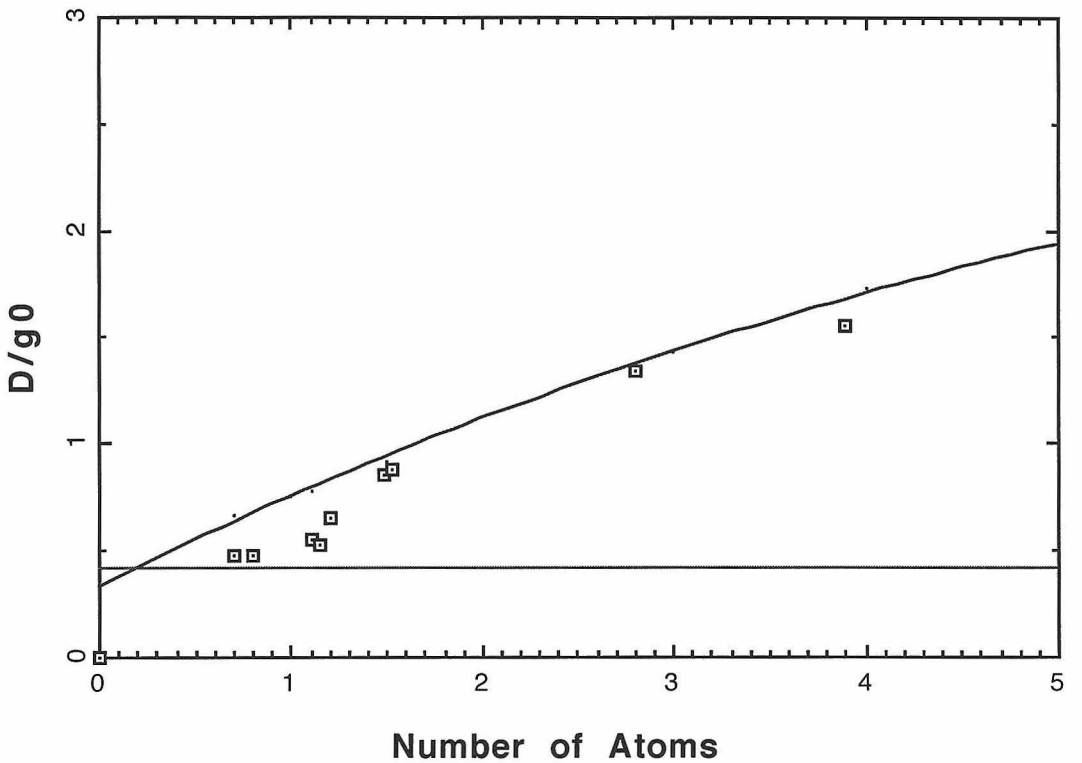

Figure 5.15: Plot of the position of the peak in the difference spectrum D/g_0 *vs.* number of intracavity atoms (N_a for simulations or $\bar{N}$ for the data). The data are shown as the '□' while the simulation results are represented by the solid curve, which is a fit through many runs of the nonlinear simulation to show the trend of the semiclassical prediction. The data are taken with intracavity pump photon numbers in the range $0.06 < \bar{\eta} < 0.2$. Note the suggestive flattening of the data at $(\sqrt{2}-1)$ shown as the straight line perhaps indicative of a quantum anharmonicity. Data are taken with the pump frequency at $\Omega_{pump}/2\pi = g_0\sqrt{\bar{N}}$ for $\bar{N} \geq 1$ and at $\Omega_{pump}/2\pi = g_0$ for $\bar{N} < 1$.

Chapter 6 Other data in the strong coupling regime

6.1 Optical bistability with very few atoms

We have been able to observe optical bistability for a system with only 7 intracavity atoms using the atom-cavity described in the previous chapter. Consider Figure 1.9. The cavity output is not a 1-to-1 function of the drive strength, so the system will exhibit a hysteresis: the part of the input-output curve with negative slope is unstable. As the power of the drive field is increased from zero, the output will follow the lower branch of the input-output curve until it reaches the point at which the slope turns around, at which time the output will jump to the upper branch. Likewise, if we are on the upper branch of the input-output curve and the drive power is decreased, the output will jump to the lower branch when the turning point is reached. This hysteresis can be seen in the data of Figure 6.1.

Although in principle we should see bistability for 1 intracavity atom, since $C_1 = 16$, there are technical reasons why we do not observe bistability until $\bar{N} = 7$. This is attributed (once again) to beam fluctuations, which tend to cause jumps between the upper and lower branches of the bistability curve near the turning points [6]. To see this, consider the following situation. For a given number of intracavity atoms, we are on the lower branch of the input-output hysteresis cycle, just approaching the turning point for transition to the upper branch. If there is an atomic density fluctuation towards a slightly lower number of intracavity atoms, switching will occur irreversibly to the upper branch for that number of atoms. Likewise, fluctuations towards larger $\bar{N}$ cause a truncation of the upper branch as the input intensity is swept down. This happens on fast time scales (set by the inverse transit time) and causes a truncation of the turning points over which our slow (in terms of detection

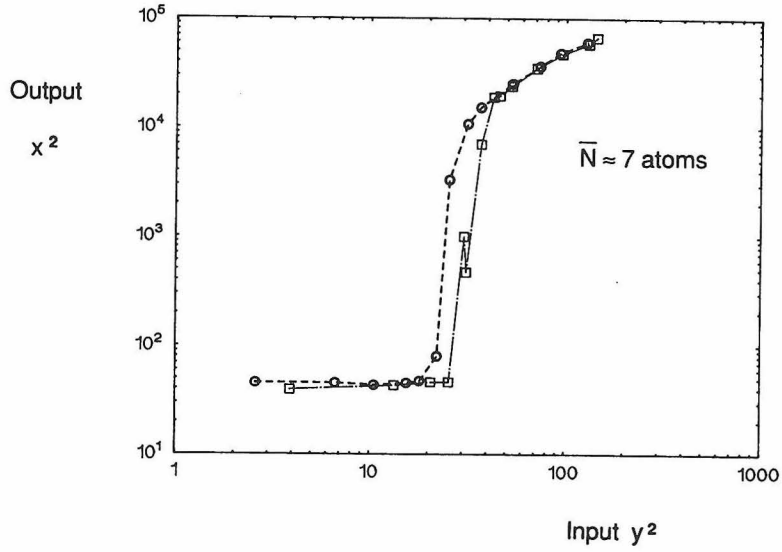

Figure 6.1: Optical bistability for $\bar{N} \approx 7$. The '□' are taken for increasing drive y^2 and the '○' are taken for decreasing drive. $(g_0, \kappa, \gamma_\perp)/2\pi = (7.2, 2.5, 0.6)$ MHz. See Refs. [177, 48].

time) experiment averages. The experiment is explained in Ref [48], so I will not discuss the details here.

Part III

Alternative Atom Sources

Chapter 7 Cavity QED with slow atoms

In our cavity QED experiments with a thermal beam, there are two problems: we do not know *where* the atoms are within the cavity field, and we do not know *when* the atoms will be within the cavity field. Lack of knowledge of *where* means that we are forced to take whatever coupling strength we get at a given instant in time, and ignorance of *when* means that we are forced to average over many such points in time, including the (numerous) instances in which there are actually no atoms in the mode volume. This leads to the averaging effects that we saw in Chapter 2 and Chapter 5: the observed spectrum is composed of an average over instantaneous atomic spatial profiles, with the many "spectator" atoms in the wings of the Gaussian and towards the nodes of the standing-wave cavity field contributing in a significant, and ultimately, deleterious way. It is this experimental complication in a thermal beam that paradoxically allows us to measure single atom effects (see Section 2.1.3.3), but which is also most likely responsible for the sub-par results of the experiments in Chapters 3, 5.

The optimal solution to this problem would be to have a single atom somehow fixed in space and maneuvered so that its center-of-mass is directly on an antinode of the standing wave and at the peak of the Gaussian. A potential realization of this ideal case using rf-trapped ions will be the subject of Chapter 9. Still, we would, for many reasons, prefer to continue to use neutral atoms, and in particular Cesium. A first step towards the goal of localization of neutral Cs is to employ cold (very slow) atoms which can be tracked *in real time* as they enter the cavity, cross the cavity field mode and eventually leave the cavity. In an ideal circumstance, the external kinetic energy of the atoms $H_P = mv^2/2$ can be less than the energy of the atom-cavity interaction $H_I = \hbar g$, so that the atom-field coupling can have a significant mechanical effect. The position-dependent potential energy of an atom in the cavity field can be used to trap and localize an atom—even with the cavity prepared in the

vacuum state [209, 210].

As a replacement to our thermal atomic beam, we have used a source of magneto-optically cooled and trapped atoms, which we let fall under the force of gravity into the cavity. Since an individual atom is strongly coupled to the cavity mode ($C_1 \gg 1$) its passage results in a distinct and appreciably sized feature in the cavity output field, which we then record. In this way, we have been able to monitor the real-time passage of single atoms as they traverse the cavity field. In addition to being a several-order-of-magnitude improvement in *absorption* detection of single atoms [211, 212], and an exceptionally accurate position meter [213], this capability should open the doors to many previously impossible experiments in optical cavity QED. The ultimate goal is not to merely run improved versions of the experiments already presented here, but rather to exploit the unique features of this entirely new system for experiments such as deterministic quantum state preparation of the cavity field [181, 182], real-time monitoring of a single quantum realization (as opposed to ensemble measurements) [214], as well as for next-generation experiments in quantum computation [215], the controlled distribution of quantum information [216], and studies of the interaction between the quantum internal and external degrees of freedom [217, 218, 219, 220].

My collaborators on this experiment were Hideo Mabuchi (who was in charge) and Mike Chapman. The idea was to plug the existing probe generation and detection apparatus described in Part I into an atom trapping apparatus built by Hideo in an adjacent lab.

7.1 Introduction

7.1.1 The new time scales

Before I begin with a description of the experiment and its results, I will point out how dramatic a change this system is over anything previously attained. This is best quantified by Table 7.1. The change is so dramatic in fact, that we have a three-order-of-magnitude improvement in quantities that have not been discussed as yet.

source	$1/2\pi(g_0, \kappa, \gamma_\perp)$ [MHz]	T_0 [μs]	$\Theta = 2g_0T_0$	$I = g_0^2T_0/\kappa$	Ref.
thermal beam	$(20, 75, 2.5/0.7)$	0.3	4π	2	[45]
atom trap	$(11, 3.5, 2.5)$	200	2000π	2000	[46]

Table 7.1: The new world order.

These new quantities reflect the fact that entirely new rates of processing should be relevant in cold-atom cavity QED. We begin with the transit time T_0 which we have already met in Section 2.2.3 in the unfortunate context of transit broadening. I have explicitly written $\gamma_\perp = 2.5/0.7 > \gamma_\perp^{\text{stationary}}$ for the thermal beam experiment to call attention to the fact that there is absolutely no transit broadening for the slow atom source since $T_0 \sim 10^3/\gamma_\parallel$. The transit time is 3000 times longer than it was in the thermal beam, so that the atom is in the cavity for an enormously longer time than any of the dynamical evolution times. This property is likewise captured in the next two parameters. The number of Rabi flops per photon per transit is given by $\Theta = 2g_0T_0$. This tells us how many times we can cycle the transition as an atom crosses the cavity mode. If we were to do a Ramsey-type experiment, this is the accumulated phase as the atom passes through the "interaction region." The optical information per transit is given by $I = g_0^2T_0/\kappa$. It answers the question: how much can we learn about intracavity activity from the stream of photons during each atom transit. From one point of view, it tells us the detectability of single atom transits.

7.1.2 The idea of the experiment

The basic concept behind the experiment is depicted in Figure 7.1 . We monitor the resonant ($\omega_p = \omega_a = \omega_c$) transmission of an empty cavity, with an atom trap formed above the cavity. The atom-cavity parameters are such that the system is in the strong coupling limit as discussed in Section 1.1.3. Hence, when we release the atom trap and an atom eventually enters the cavity, the normal mode structure changes. The resonant properties of the system go from that of the empty cavity, to that of the newly-formed coupled atom-cavity system with associated normal-mode splitting, and what was a resonance of the uncoupled system is no longer a resonance of the

coupled system. In fact, the transmission decreases by an amount $1/(1+2C_1)^2$ (see Equation 1.14), which can be quite substantial. We see a great reduction in output flux when the atom is in the cavity. The output flux reverts to its previous value when the atom leaves the cavity and the system returns to its uncoupled empty-cavity state, once again resonant for the probe. During the time between the extremes, the atom is travelling up (or down) the side of the Gaussian waist of the cavity mode, so there is essentially a time-varying coupling strength $g(t)$ due to the position-dependent coupling $g(s)$ where s labels position transverse to the cavity standing wave. If we detect only on long time scales $\Delta t \gg (1/g_0, 1/\gamma_\parallel, 1/\kappa)$ (but quickly with respect to the transit time $\Delta t \ll T_0$) then at each time step, the atom reaches steady-state with the field and we are able to observe the steady-state response. The transmission of the resonant probe beam under such a scenario is shown in Figure 7.2, ignoring all mechanical effects. The simple normal-mode picture depicted in Figure 7.1 is not quite correct for the stronger drive fields that are used here, but the basic idea is certainly there. The calculation of Figure 7.2 is a quantum calculation with an empty-cavity drive field of $n_s Y = 1$ (1 empty-cavity intracavity photon) so that the optimally coupled transmission is not quite reduced by $1/(1+2C_1)^2$. The spectrum for this drive field Y does not actually have (or just barely has) normal modes as such [221], as can be seen in Figure 7.3.[1]

7.2 The experiment

The experimental setup is a slight modification of that of Part I. The cavity is cavity #4 from Table 2.1. As a reminder, the parameters are $(g_0, \kappa, \gamma_\perp)/2\pi = (11, 3.5, 2.5)$ MHz, which gives $n_s \equiv \gamma_\perp \gamma_\parallel / 4g_0^2 = 0.026$ ($b = 1$ is the appropriate choice here) and $C_1 = 6.9$. See Appendix B.1.2 for more details of the cavity and mechanical parameters. Aside from the atom-cavity parameters, there are two major differences

[1]The quasienergies (akin to the energy eigenvalues of the undriven Jaynes-Cummings model) in the presence of a drive field are given by $\tilde{E}_1 = g[1-(2\varepsilon/g)^2]^{3/4}$ where $\varepsilon^2 = \kappa^2 Y/n_s$ [221]. The threshold for actual normal modes is exceeded when $\varepsilon > g/2$. For the drive fields employed in this particular experiment, this is exceeded by an order of magnitude. Atomic decay is not covered in this treatment, so it is not entirely valid.

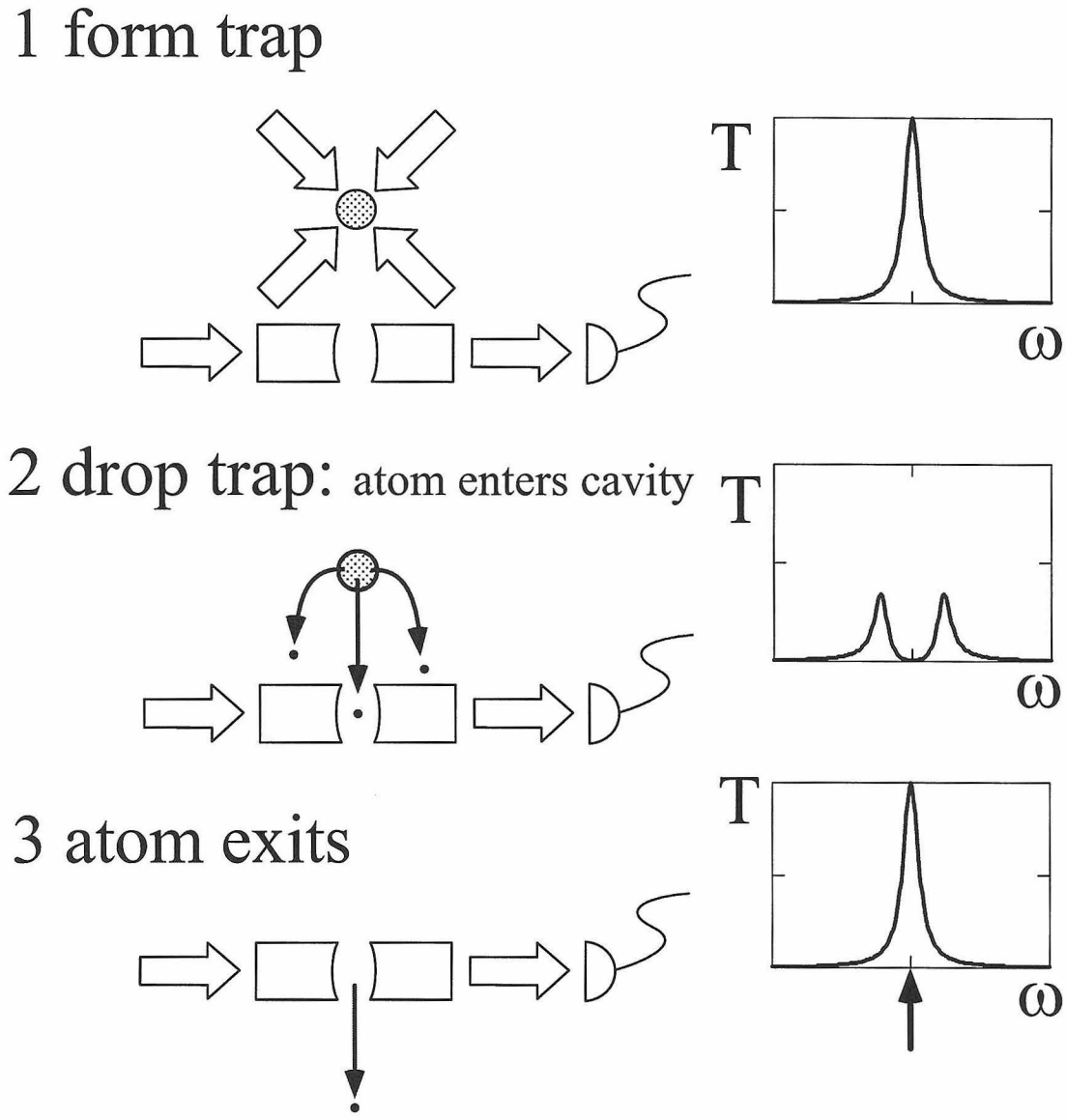

Figure 7.1: Falling atoms. The graphs on the right-hand side show the weak-field transmission spectrum 1) before the atom enters the cavity, 2) while the atom is in the cavity, and 3) after the atom leaves the cavity. A resonant probe (indicated by the arrow) will thus have 1) high transmission, 2) low transmission, and 3) high transmission.

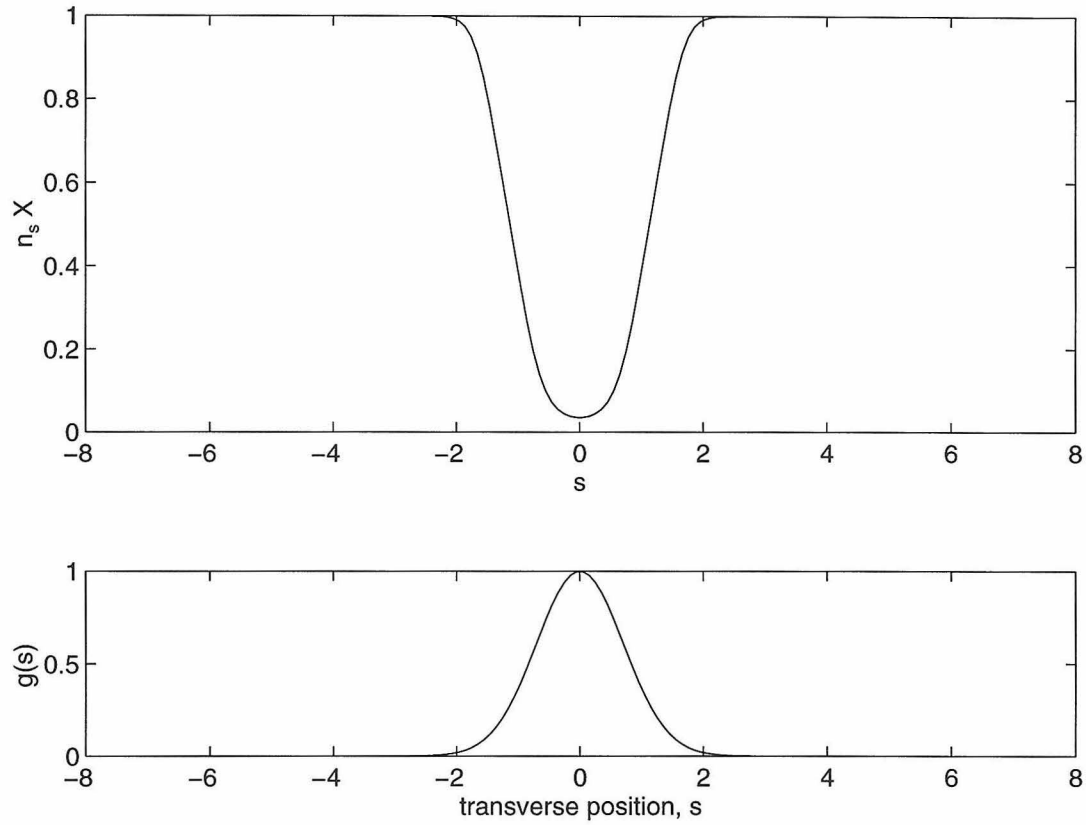

Figure 7.2: Transmission of the resonant probe (quantum calculation of $\langle a^\dagger a \rangle$) as the atom passes through the Gaussian waist, precisely perpendicular to the cavity mode axis and along an antinode of the standing-wave. The calculation does not include mechanical recoil in any direction, so the atom trajectory is not affected by the atom-cavity interaction, as it is in the experiment. Position s is in units of the waist. The top graph shows the probe transmission while the bottom graph shows the waist itself. As can be seen, the drive field is $n_s Y = 1$. The atom-cavity parameters are as appropriate for the cold atoms experiment: $1/2\pi(g_0, \kappa, \gamma_\perp) = (11, 3.5, 2.5)$ MHz.

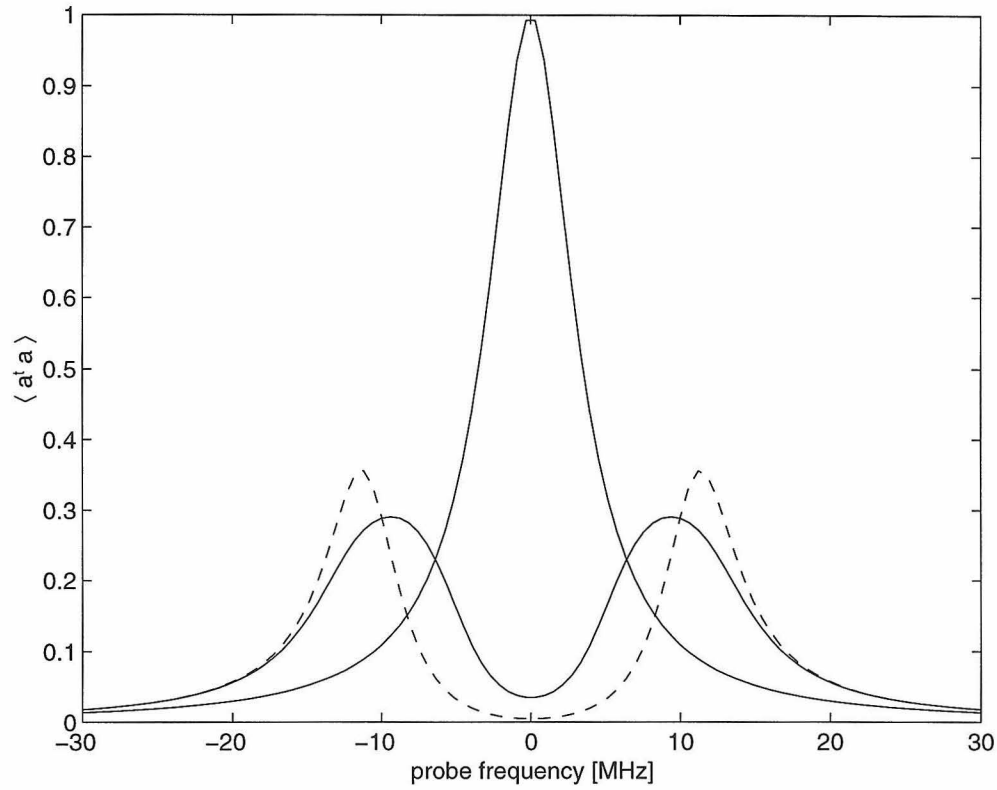

Figure 7.3: The transmission spectrum for fixed drive field corresponding to $n_s Y = 1$ on resonance (solid curves). This is a quantum simulation for both the with atom and empty cavity cases for the same drive. For comparison, the weak field ($n_s Y = 0.001$) spectrum is shown as the dashed line; it has been scaled by a factor of $(0.001)^{-1}$ for comparison with the strong field spectrum (scaled so that the empty cavity transmissions fall atop one another). $1/2\pi(g_0, \kappa, \gamma_\perp) = (11, 3.5, 2.5)$ MHz.

in the experiment. First, the source is replaced by a magneto-optical trap (MOT). I will not describe this in any detail, mainly because I had nothing to do with its construction or implementation, (this was done by Hideo Mabuchi and Mike Chapman) and also because it is fairly standard and can be found any number of places in the literature [222]. Briefly, it is a six-beam trap with pairs of counter-propagating beams along each of three axes. The light is slightly red detuned (10 MHz) so that an atom preferentially absorbs light from beams propagating against its velocity vector. The atom absorbs the photon momentum, causing it to recoil against its direction of motion. Spontaneous emission of the absorbed photon is isotropic, so that a net cooling of the motion is achieved. In order to trap the cooled atoms in a region of space, a magnetic quadrupole along $\hat{z}$ with a zero at the center of intersection of the six beams is applied. The gradient produces a position-dependent potential which grows larger as an atom moves away from the center point in any direction. In our implementation, 10^5 or so atoms are trapped in a 1 mm ball 7 mm above the cavity. The $\hat{z}$-beam is along and just above the cavity axis, with the other beams propagating up the sides of the cavity mount (see Figure 7.8), intersecting at acute angles just above the opening between the cavity mirrors.

The second important difference in the atom-transit experiment is that we are now trying to resolve signals in time. This is fundamentally different from the prior experiments, which took advantage of narrow-band (0.1–1 kHz) detection and extreme averaging to improve S/N. No such luxury is available in this experiment. The transit time is about 200μs, so our detection needs to be at least this fast. The empty cavity with $\bar{n} = 1$ intracavity photons has an output flux of $\kappa\bar{n} \approx 2\pi \times 3 \times 10^6$ photons/sec (double-sided cavity), so within time bins of duration set by the transit time, only 3600 photons are output. We detect a deficit of photons from this steady flux when the atom is present. The contrast in the detection can be written $V = (X_{wa} - X_{na})/X_{na}$ where $n_s X_{na} = n_s Y$ is the intracavity photon number in an empty cavity and $n_s X_{wa} \equiv n_s X$ is the instantaneous photon number in a cavity with an atom (see Section 1.3.1). The contrast is shown in Figure 7.4 for both a quantum calculation of the intracavity intensity (I use $\langle a^\dagger a \rangle$ even though it is not really appropriate for

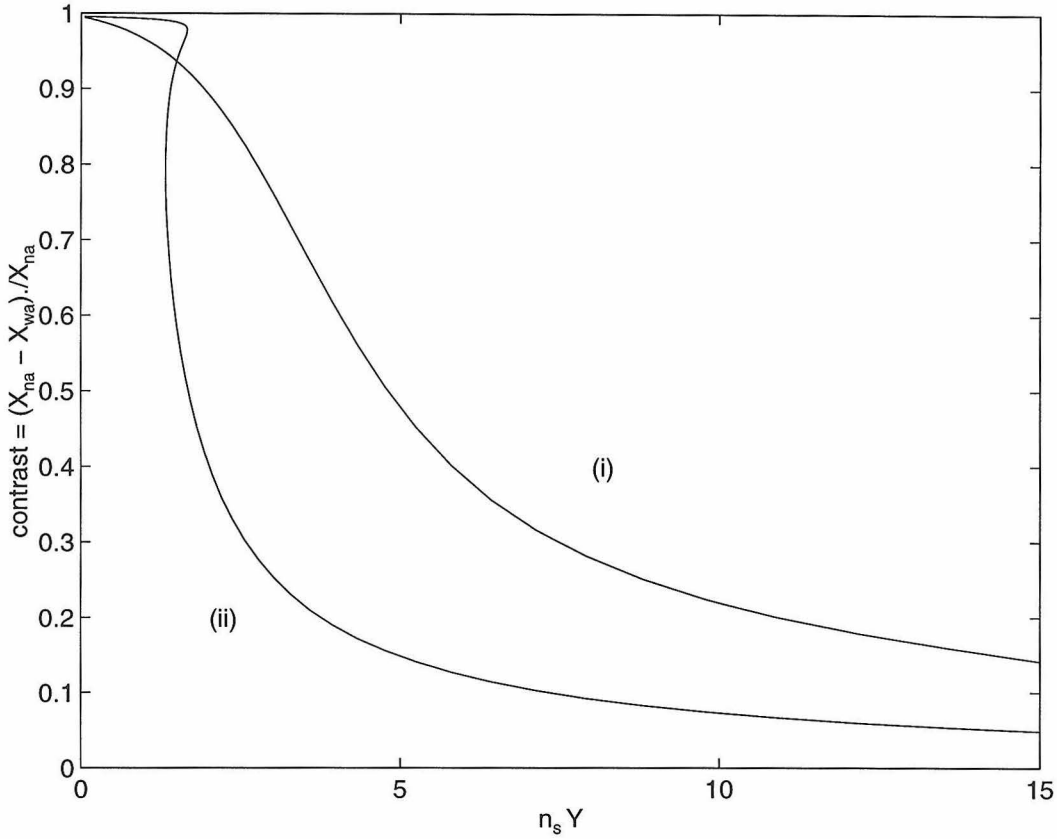

Figure 7.4: The transit contrast as a function of empty cavity drive. The curves are: (i) quantum and (ii) semiclassical. $1/2\pi(g_0, \kappa, \gamma_\perp) = (11, 3.5, 2.5)$ MHz.

the heterodyne measurement which detects $|\langle a \rangle|^2$, it nonetheless gives the basic idea) and for the semiclassical optical bistability state equation (1.24) from Section 1.3.1. In order that there be sufficient contrast in the transit signal, the atom should not enter an empty cavity with too many photons, since atomic saturation leads to a loss of contrast. (For a weak field the transmission is reduced by $1/(1+2C_1)^2 = 4 \times 10^{-3}$, but for a strong field, this attenuation is less due to atom saturation.) On the other hand, too few photons leads to a signal which is too small to begin with. These competing effects lead to an ideal operating point of $n_s Y \sim$ 1–3.

Transit detection warrants further discussion. The detection proceeds as follows. With no probe beam on at all, there is a "signal level" due to the shot noise of the local oscillator on the heterodyne detectors for shot-noise limited detection such as we use (see Section 2.1.5). The shot-noise level increases linearly with the detection

bandwidth B. One can treat the shot noise as due to an equivalent signal of 1 photon per second per unit bandwidth (1 photon/sec/Hz)[2] incident on an otherwise noiseless detector, causing the background level that we call the shot-noise level. For a given bandwidth, this provides a bound on the smallest detectable signal level. (To detect smaller fluxes, one narrows B so that the shot-noise decreases, while the coherent signal remains a fixed size, as long as the signal bandwidth is smaller than B.) When we apply the probe field, a stronger signal field is present so the level out of the heterodyne detectors increases by some amount above the shot-noise depending on the size of the probe field and B (B determines the shot-noise level). The output flux of photons for the empty cavity[3] is $\kappa n_s Y$ and the number of detected photons in bandwidth $B \equiv \Delta\Omega/2\pi$ is $\kappa n_s Y/\Delta\Omega$. As long as $1/\Delta\Omega < T_0$, then the number of photons detected when the atom is present is $\kappa n_s X/\Delta\Omega$. The instantaneous flux is $\kappa n_s X$ photons/sec. The flux due to the shot noise is simply B photons/sec, as discussed above. It is possible that the best signal-to-noise of detection is reached when the cavity output flux with an atom present is just forced into the shot-noise. A stronger drive field will only decrease the contrast as can be seen in Figure 7.4. Stated in symbols, this occurs when $n_s X \kappa = B$. This output field X has a corresponding drive field Y which can be found trivially from the state equation 1.24 or from a full quantum simulation.[4] From the state equation an interesting result arises:

$$\begin{aligned} n_s Y &= \frac{B}{\kappa}\left[1+\frac{2C_1}{1+\frac{B}{n_s\kappa}}\right]^2 \\ &\approx \frac{B}{\kappa}\left[1+\frac{\gamma_\parallel}{4B}\right]^2 \quad \text{for} \quad \frac{B}{n_s\kappa} \gg 1 \\ &\propto \frac{\gamma_\parallel}{\kappa B} \quad \text{for} \quad \frac{\gamma_\parallel}{4B} \gg 1. \end{aligned} \tag{7.1}$$

Note that g_0 has dropped out of the equation which now depends only on the rate at which the atom can scatter photons. The drive field satisfying the "into-the-shot-

[2]Upon further consideration, I believe this should be 2 photons/sec/Hz. This carries through the results in a straightforward fashion.

[3]The cavity is double-sided with $\kappa = \kappa_1 + \kappa_2$ where $\kappa_{1,2} = \kappa/2$ are the partial decay rates for each output channel.

[4]The quantum simulation will give $\langle a^\dagger a\rangle$ for a given drive. From this it can be determined which drive field leads to the condition $\langle a^\dagger a\rangle\kappa = B$ by back-interpolation.

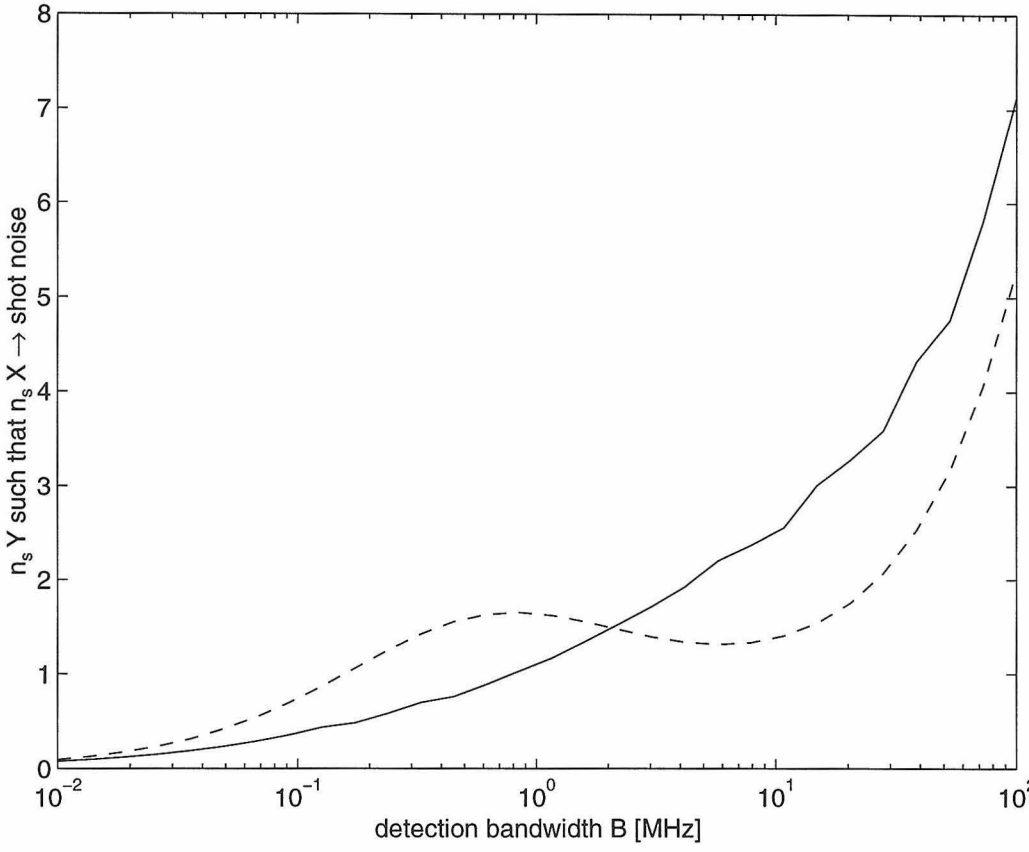

Figure 7.5: The drive field which will just send the with-atom output into the shot noise. The dashed curve is the semiclassical curve. The quantum curve (solid) is jumpy because I have only coarsely interpolated the original quantum simulated data from, e.g. Figure 7.4. For this graph to be of any use, the detection time must be shorter than the transit time, $(2\pi B)^{-1} < T_0$.

noise" criterion is shown in Figure 7.5 both for the semiclassical state equation and a quantum simulation.

This criterion may, however be largely irrelevant. It certainly delimits the weakest drive worth using (a smaller drive will only send the transit signal below the shot-noise level which then cannot be detected any better than if it were just at the shot-noise level), but it may not be the strongest drive field worth using. It may turn out that instead of driving the with-atom signal into the shot-noise, it would be better to drive harder and then not to dip into the shot-noise. This is true because I have thus far left one detail out of the consideration thus far: the empty-cavity signal has noise associated with it. The larger the detection bandwidth, the worse this noise becomes.

This can be significant for a weak probe. (All else equal, the S/N-ratio is $n/\sqrt{n}$ where n is the number of photons in each detection bin.) If we drive hard, the variance of the probe within a time set by the inverse bandwidth will be small and a transit signal can be detected in the presence of this noise. The point-to-point variance in detection bins of time $1/\Delta\Omega$ is given by $\sqrt{\kappa n_s Y/\Delta\Omega}$ for the empty cavity. Thus the signal-to-noise ratio (for $1/\Delta\Omega \ll T_0$) is

$$S/N = \frac{\kappa n_s Y/\Delta\Omega - \kappa n_s X/\Delta\Omega}{\sqrt{\kappa n_s Y/\Delta\Omega}}. \tag{7.2}$$

(Of course, if $1/\Delta\Omega \gg T_0$ then we integrate over the empty cavity for a long time, during which the atom transit is only a short blip, which disappears altogether.) I plot the S/N ratio as given in Eq. 7.2 as a function of drive power in Figure 7.6 for both the quantum and semiclassical cases. The optimum point does turn out to be a bit larger than the "into-the-shot-noise" criterion for a given bandwidth.

The apparatus for combining cold atoms with cavity QED is shown in Figure 7.7. The cavity lock beam of our previous measurements (Parts I and II) is eliminated. Instead, we lock directly to the probe beam signal on the heterodyne. The SA is placed in zero span and the steady transmission of the empty cavity is read through the video out port of the SA. The video out is a logarithmic copy of the demodulated beat note. This signal replaces the PMT signal from the previous setup (see Figure 2.6). This allows us to lock the cavity to output fluxes corresponding to as few as 1 intracavity photon. The probe/lock is nominally resonant $\omega_p = \omega_c = \omega_a$. The transits last only 200 μs, which is well outside of the cavity lock servo bandwidth, so as long as atoms arrive infrequently enough, they do not interfere appreciably with the cavity lock. The actual transit signals are recorded from the same video-out signal. When the atom trap is shut off, we wait 10 ms or so, until the atoms fall through the cavity mode, then we digitize the video-out signal at a 500 kHz sample rate for 50 ms, and look in this record for the atom transits.

The cavity mount is different in construction than those previously described (see Figure 7.8). In order to accommodate the atom trap, we needed an open structure to

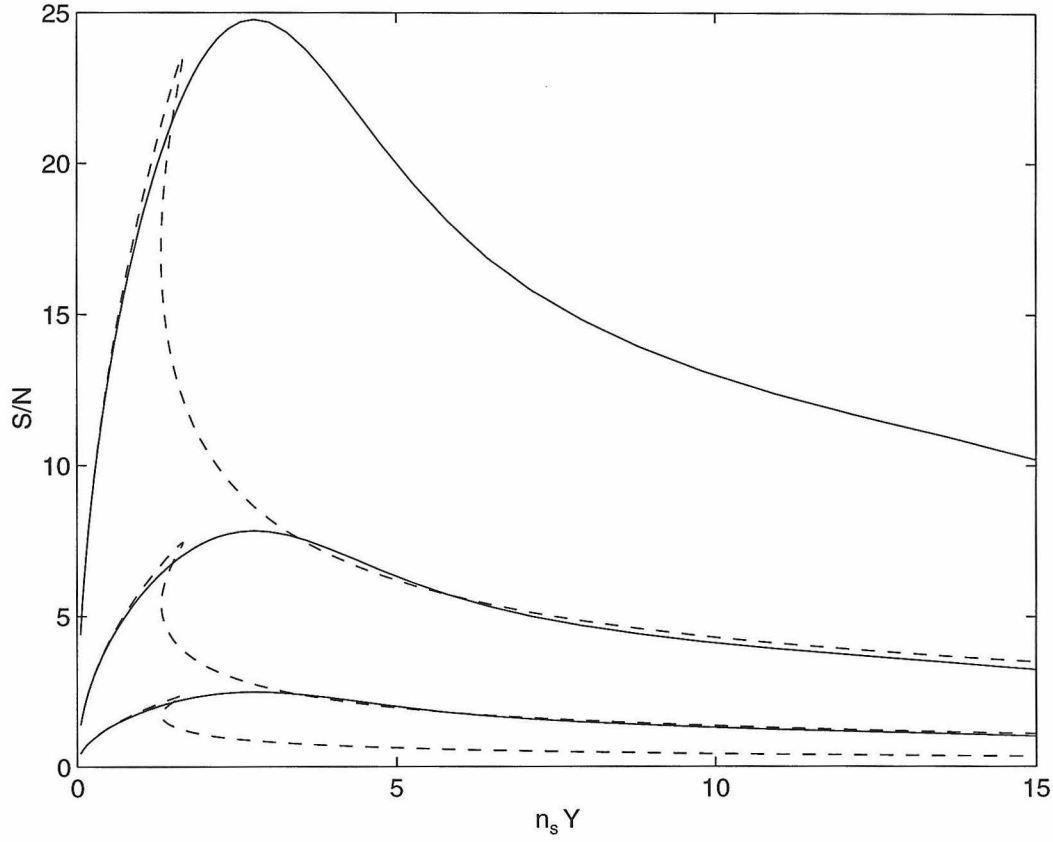

Figure 7.6: S/N in various bandwidths (Eq. 7.2). The solid curves are quantum simulation and the dashed curves are semiclassical. From top to bottom, $B = 10, 30, 100$ kHz. $B = 10$ kHz is the absolute slowest detection for which this treatment (Eq. 7.2) is valid, as the corresponding integration time is approaching the inverse transit time. $1/2\pi(g_0, \kappa, \gamma_\perp) = (11, 3.5, 2.5)$ MHz.

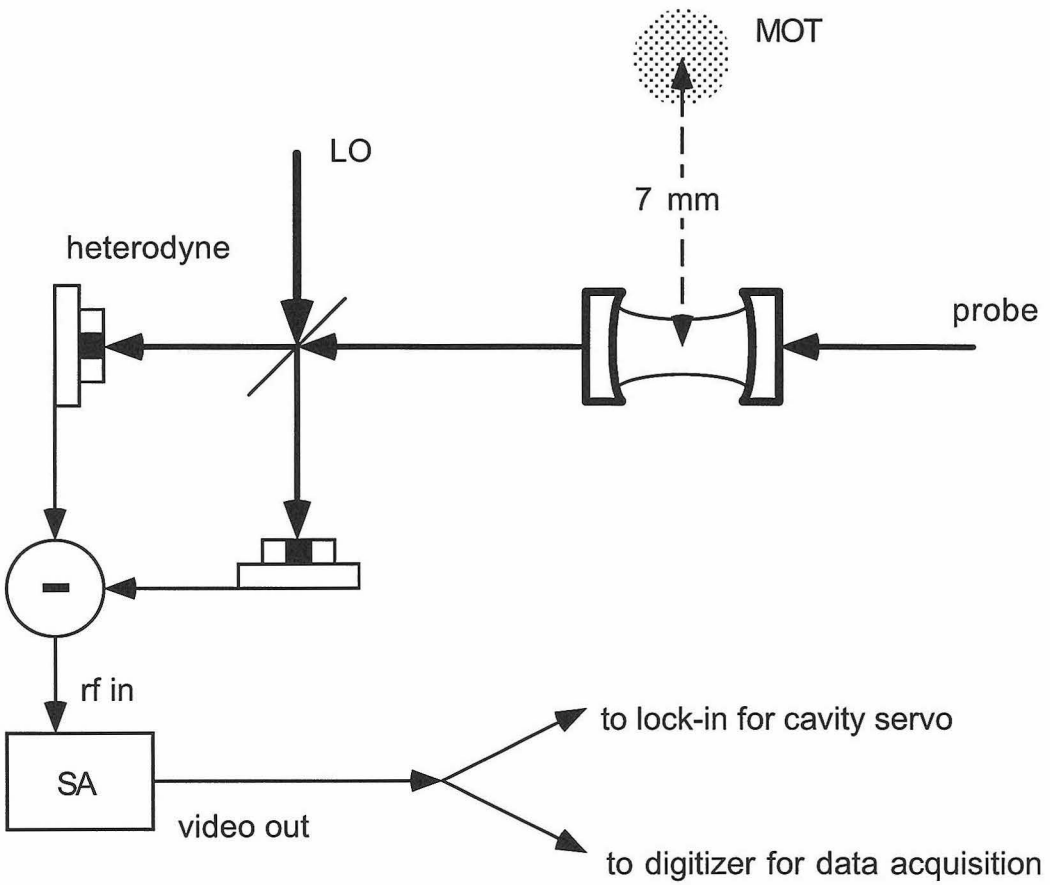

Figure 7.7: Monitoring the falling atoms. MOT: magneto-optical trap.

get the trap as close to the cavity mode as possible. Towards this end, we eliminated the invar tube (of Fig. 2.2) since it is too bulky and not particularly conducive to the much better level of vacuum required for an acceptable trap (acceptable means dense enough so that a few atoms fall into the cavity mode for each trap drop; we operated below 10^{-7} torr). We also had the mirror substrates machined down to a 3 mm diameter (from their nominal 7.75 mm diameter) to get the $\hat{z}$ trapping beams close to the cavity mode without clipping on the mirror substrates. The mirrors sit in two separate V-grooves (into which they are glued) which are connected to each other by a PZT, so that the length can be fine-tuned (see Figure 7.8).[5] The cavity mount structure is placed in the vacuum chamber on a series of alternating copper disks and viton o-rings for vibration isolation, and the optical table was floated for additional isolation. Vibration isolation proved to be critical, and even still, the cavity lock was always just barely adequate. The cavity-lock servo was functional but not optimal. The addition of an integration path in the cavity servo helped to offset cavity length drift which was more of a problem than in the previous experiments since the magnetic field coils and oven would heat the vacuum chamber and cause the cavity mount to thermally expand and contract.

7.3 Atom transits

A typical data set is shown in Figure 7.9. The inset shows a histogram of the arrival times of individual transits for 450 drop sequences. The time scales are as follows. The atoms in the MOT are cooled to the Doppler limit, giving them a temperature $T_{\text{trap}} \approx 120\mu\text{K}$ and an rms speed of 10 cm/sec. The 7 mm distance to the cavity mode gives the atoms a 35 ms drop time with a dispersion of 10 ms from the rms velocity in the trap. These numbers agree reasonably well with the measurements as shown in the inset to Figure 7.9. The different sizes of the individual transit signals are due to the more or less random coupling (due both to random position along the standing-wave and random Zeeman substate occupation) that the atom has as

[5] M. Chapman designed and built the new cavity mount.

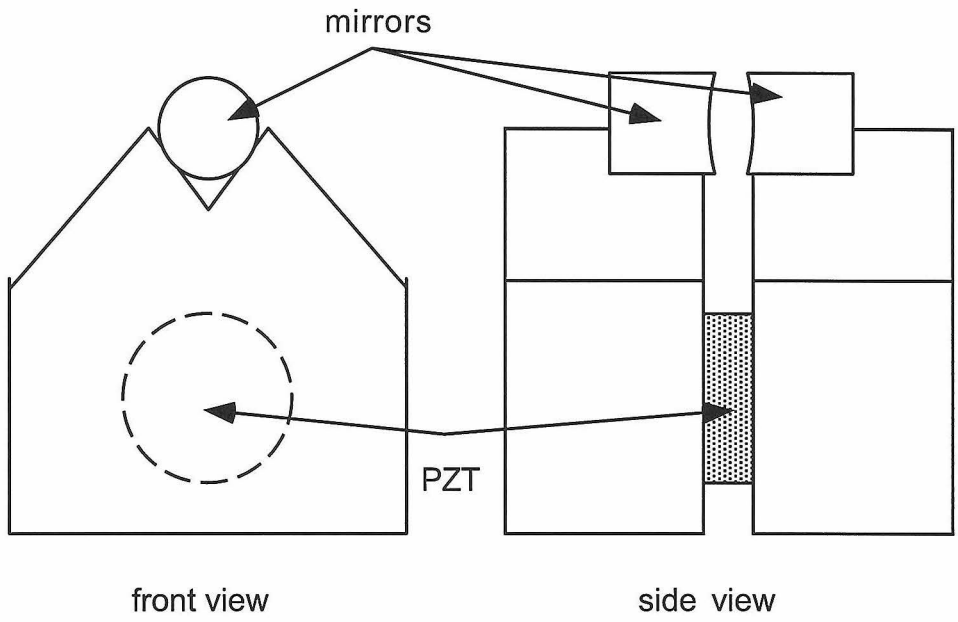

Figure 7.8: The cold atoms cavity mount. Not to scale. The mirror substrates are 3 mm in diameter and 4 mm long. The total height of the cavity mount is ~ 1.5 in.

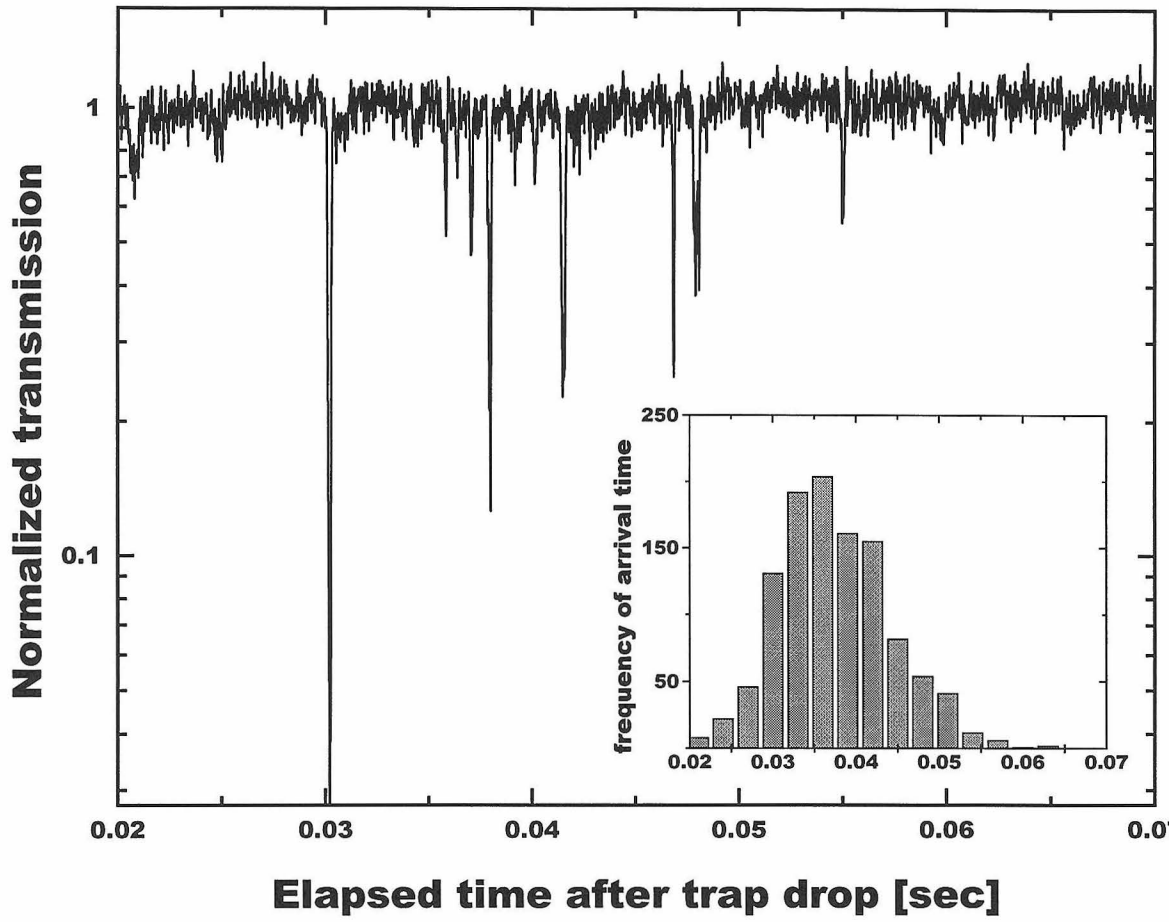

Figure 7.9: Atom transits. Each downgoing spike is an individual atom crossing the cavity field. The probe is set to have $n_s Y \approx 1$. The data are directly out of the apparatus with the only post-processing to filter out high frequency noise. SA RB is 10 kHz. The inset shows a histogram of atom arrival times for 450 sequences like the one in the main graph. This figure comes directly from Ref. [46]

it comes into the cavity. The situation is compounded by the fact that the level of saturation is coupling-dependant

The final velocity of the atoms in the vertical ($\hat{y}$) direction when they reach the cavity mode is $v_f \simeq 40$ cm/sec. This puts their kinetic energy at around twice the energy of the $\hbar g$ interaction, so that mechanical effects in this direction are not profound, that is, the atoms should pass through the Gaussian waist in the expected (uncoupled) transit time $2w_0/v_f = 200\mu$s. The situation is quite different in the $\hat{z}$ direction, along the cavity axis. There is an effective slit formed by the cavity mirrors that has a height given by the diameter of the mirror substrates (3 mm) and

a width given by the cavity length (100 μm). This forms a fairly stringent cavity-axis velocity selector. An atom with $\hat{z}$-velocity larger than about 3 cm/s will hit one of the mirror surfaces on its way through the cavity and will not register as a transit. Thus the atoms that we see are initially travelling relatively slowly along the cavity axis, so that the variation of $\hbar g$ with position can have a large mechanical effect on the atomic motion in this dimension. Since we are probing with resonant light, the net effect is to heat the atom and increase its velocity along the cavity axis in a random, uncontrolled way. This is confirmed by a calculation performed by A. Doherty and S. Parkins [223].

For the sake of completeness, I show another trap drop sequence and some close-ups of the individual transits in Figures 7.10, 7.11. The shot-noise signal is shown in Figure 7.10. I will refrain from making any additional comments on the data for the following reasons. The effects of the atom heating described above mean that there is no well-defined velocity along the cavity axis. Thus extreme care should be taken in associating any of the undulating behaviour seen in Figure 7.11 with atomic motion over the standing wave. For a fixed and unchanging atom velocity, we expect the transmission to go up and down as the atom moves over the nodes and antinodes of the standing wave, respectively. Some of the transmission oscillations we see are tantalizingly suggestive of a 3 cm/sec atom bouncing along a 425 nm standing wave. Alas, due to appreciable heating, it is more likely that we are seeing the effects of a randomly moving atom which can acquire fairly large velocities along the standing-wave as it executes a random walk driven by fluctuations in optical forces. Only on those instances where the atom is slow (in terms of the detection time $1/\Delta\Omega$) would we see anything really having to do with the standing wave. Since we have no independent measure of the velocity of the atom, we really cannot draw conclusions about motion in the standing-wave. In addition, there is no optical pumping present, so the atoms enter the cavity in any one of their magnetic sublevels (see Figure 2.9). It is likely that the atom would very quickly be pumped into the $m_F = 4$ ground state by the cavity field (remember Θ from Table 7.1) *if* the cavity supported a circular polarization relative to a quantization axis along the cavity, as we have for

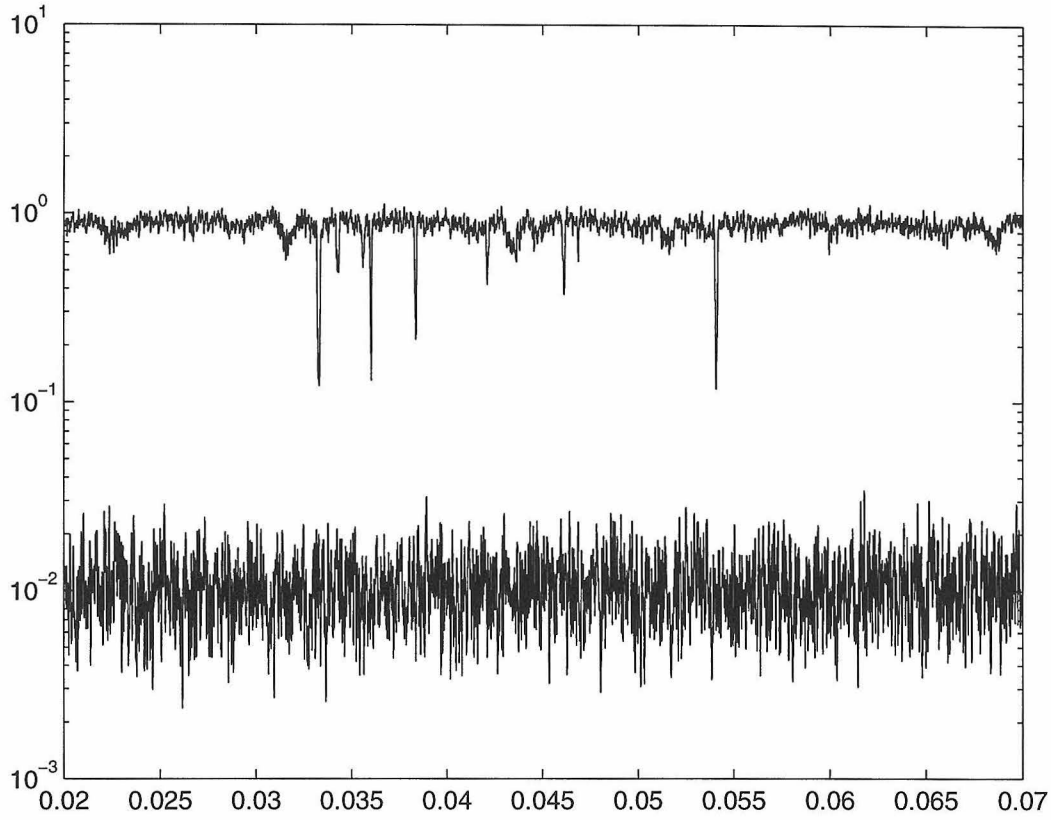

Figure 7.10: Another trap drop, this time shown with the shot-noise. Conditions are the same as those of Figure 7.9, as are the axes.

the experiments of Parts I and II. However, we have no holding quantization-axis-defining magnetic field and the cavity used in these measurements is birefringent and does not support circularly polarized modes. (The birefringent splitting is larger than κ for this cavity, for reasons unknown. Of course, κ is significantly smaller here than it was for the experiments in Part I.) Also, there can be losses due to off-resonant drive to the $F' = 4$ excited state, which will then decay to the $F = 3$ ground state, forever lost to the probe. This may account for the steep drop-off that we observe in the trailing edge of many transit signals.

The initial demonstration has been very important, but more work is needed to make any quantitative statement about the data. Work in this area is underway, with

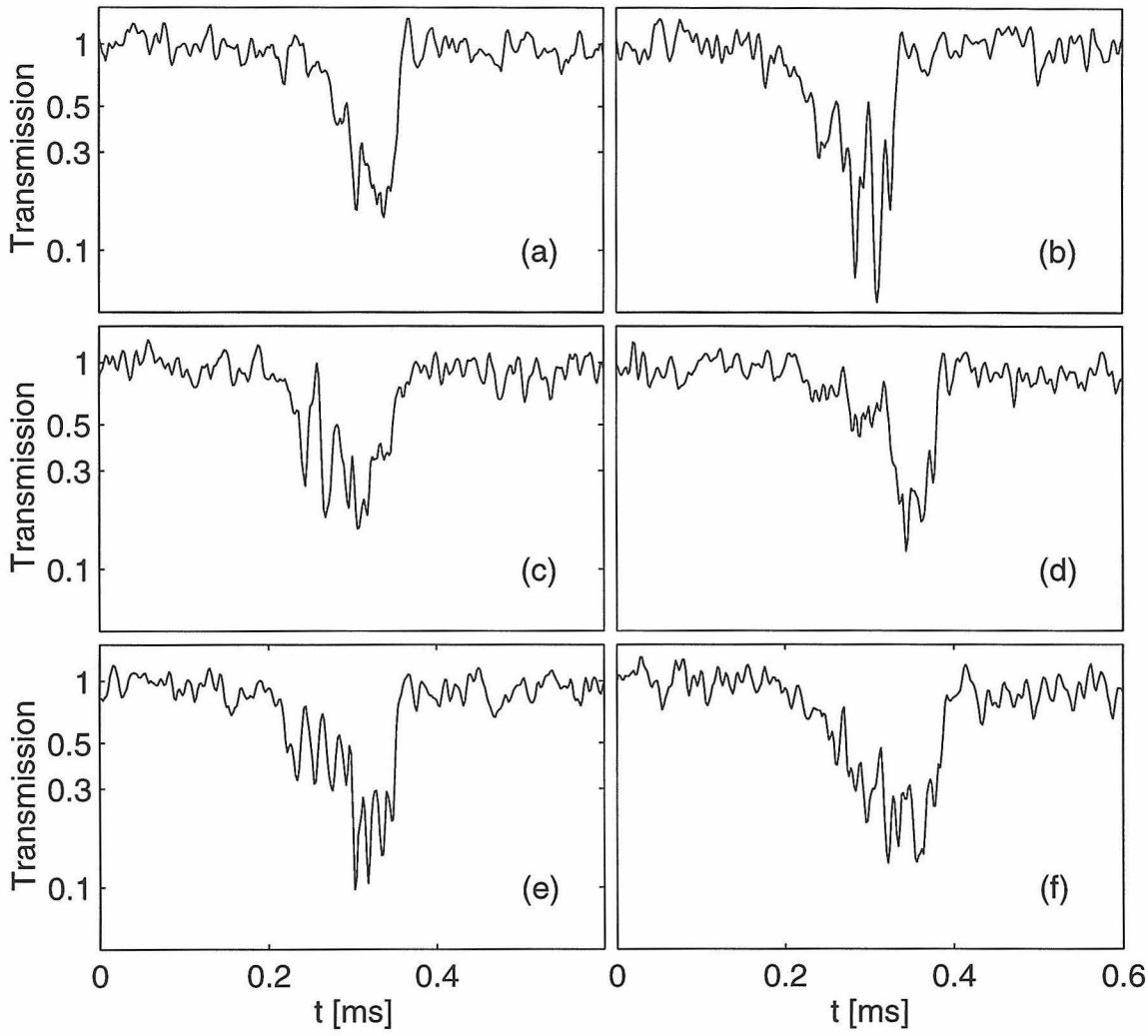

Figure 7.11: Individual transits, time axis expanded relative to those of Figures 7.9, 7.10. Data taken under the same conditions as those figures.

one lab, run by Hideo Mabuchi, dedicated to unambiguous observations of the standing wave structure in the transmission signal and making measurements pertinent to the standard quantum limit for the position measurement of a free mass [224] under continuous observation. Another lab, run by Mike Chapman, Christina Hood and Theresa Lynn is dedicated to trapping an atom in the cavity field itself. In a third "falling atoms" lab, David Vernooy and Akira Furusawa are replacing the traditional Fabry-Perot cavities with microsphere resonators, which have the potential to reach extremely high quality-factors and correspondingly long photon-storage times.

Chapter 8 Would-be cavity QED with fast atoms

While with the cold atom source we have demonstrated that we know exactly when the atoms are in the cavity, they are still free to traverse the mode volume anywhere within the standing-wave. With such a long transit time, we could discriminate against those atoms that are not sufficiently well-coupled and wait for a "good one" to come along. Depending on what coupling strength is considered sufficient, this could happen only infrequently. Ultimately, because of the long transit times, we will be able to use the mechanical forces associated with the atom-cavity interaction to guide the atoms onto the antinodes of the field. However, for some experiments, a very short interaction time is required with atomic localization to the antinodes, so slow atoms do not constitute a viable method. An alternative method is to use fast atoms for a short interaction time and a mechanical mask to force the atoms to traverse the cavity field along the antinodes. The atom source will be a fast, low-velocity-dispersion supersonic atomic beam. The mask (grating) will be nothing more than a series of transparent (to atoms) slits in an opaque (to atoms) substrate, separated by the standing-wave light wavelength $\lambda/2$. How such gratings could be used will be the subject of this chapter. It is a chapter entirely dedicated to atom optics rather than quantum optics.

Many people have worked on the beam apparatus itself, principally Olivier Carnal and Hauke Hansen, then me, and subsequently Wolfgang Lange and Jae Park. I constructed the gratings at Cornell's National Nanofabrication Facility in a collaboration with Dave Pritchard's group at MIT.[1] Olivier Carnal developed the analytical theory for the two-grating localization scheme and I performed the numerical simulations.

[1]There is a complete lab notebook which documents the gratings.

8.1 Why fast atoms?

Before I continue, I will outline briefly the experiment that we had in mind when we decided to pursue the fast-atoms/mechanical grating setup. At the present time, the beam apparatus and atom-optics approach have been abandoned in favor of the slow-atom techniques described in the previous chapter. But with some unforeseen application, such as cavity QED with metastable atoms, the apparatus and idea could certainly see the light of day again. The experiment is "transfer of Zeeman coherence via adiabatic fast passage," in which states of the Zeeman substructure of the atom can be mapped onto states of the cavity field [179, 180]. The idea is most easily explained in the context of preparation of a single-photon cavity Fock state $|1\rangle_c$. Consider the arrangement of optical fields shown in Figure 8.1. A fast atom (already localized to the antinode of the standing-wave via the method to be described) traverses a linearly-polarized cavity field and then an overlapping circularly-polarized classical field (pointing into the page in Figure 8.1). Because of the (Gaussian) variation in field strength as the atom traverses each field, the classical Rabi frequency can be written as $\Omega(t)$ and the cavity-field coupling frequency as $g(t)\sqrt{n+1}$ where n is the number of photons in the cavity. The classical field couples the atomic transition $|g_1\rangle_a \leftrightarrow |e\rangle_a$ and the cavity field couples $|g_2\rangle_a \leftrightarrow |e\rangle_a$ where $|g_i\rangle_a$ are two atomic ground states and $|e\rangle_a$ is the excited atomic state. If conditions are "right," an atom entering an empty cavity in the state $|g_1\rangle_a|0\rangle_c$ will take a photon from the classical field and deposit it in the cavity mode, leaving the system in the state $|g_2\rangle_a|1\rangle_c$. The process occurs via a "dark state" which does not contain any contribution from the excited state, so that the atom never finds itself in the excited state and is therefore not susceptible to spontaneous decay. Thus with near unit probability, an atom can transfer its state to a single-photon cavity Fock state. If an atom enters the system in $|g_1\rangle_a$ and leaves in $|g_2\rangle_a$, it is guaranteed that the cavity has been prepared in a Fock state. The principle can easily be extended to atoms with more sublevels, so that atomic states of the form $\sum_i C_i|g_i\rangle_a$ are mapped to cavity fields $\sum_n C_n|n\rangle_c$. Thus for multilevel atoms a phenomenal array of "arbitrary states" may be synthesized.

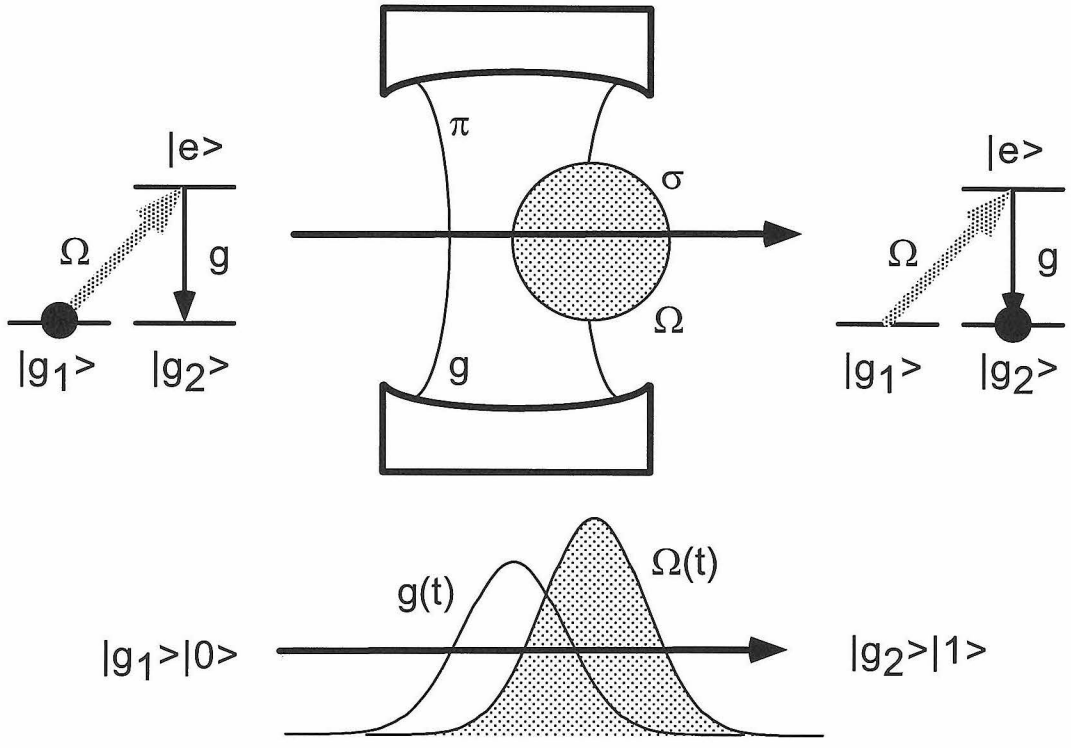

Figure 8.1: The adiabatic fast passage scheme for preparation of cavity field states.

The process is remarkably robust. To force the transition to proceed via the dark state, $\Omega T_0 \gg 1$ and $g_0 T_0 \gg 1$, where T_0 is the transit time. These are not particularly difficult criteria to achieve. However, in terms of the synthesized *intracavity* field (but not necessarily the field that is emitted by the cavity [225]) it is imperative to avoid cavity decay during state preparation so that $\kappa T_0 \ll 1$. This is where the fast comes in. The conditions can be satisfied with $(g_0, \kappa)/2\pi = (20, 1)$ MHz and an 800 m/s beam, all readily attainable parameters. The quantum state synthesizer has a wide range of possible applications, including preparation of controlled Fock states to drive, e.g., the quantum phase gate, as discussed in Section 4.3.4.

8.2 Getting the atoms where we want them

In order to make useful arbitrary cavity field states the atoms must follow well prescribed trajectories through the cavity field. The timing part is difficult with fast atoms, but in principle a single atom detector such as described in Chapter 7 could be employed. It would require comparable S/N in a 10000 times shorter detection time which is no easy task even for much more favorable atom-cavity parameters. The atomic localization should be more straightforward. Consider Figure 8.9a. We put a mask very close to the cavity mode, with open sections only in front of the antinodes to make a shadow of the grating at the location of the cavity field. This would be a clean and comparatively simple solution, except that atoms are waves and eventually will protest to being so well localized, by diffracting away from the perfect shadow. This happens more quickly than might be guessed from the diffraction angle $\theta = \lambda_{dB}/d$ where d is the grating period. To demonstrate this, the spatial distribution of atoms with deBroglie wavelength $\lambda_{dB} = 0.1$ Å at progressively larger distances behind a single grating ($d = 426$ nm) is shown in Figures 8.2, 8.3, 8.4. The simulations are performed with an incident plane wave, that is, the wavelets at each grating slit radiate in phase with each other. Note that the pattern starts out as a perfect shadow of the grating and then degrades very quickly. With the older generation 7.75 mm diameter mirror substrates this rapid degradation of the contrast

poses a real problem, since it is virtually impossible to get the grating sufficiently close to the position of the cavity mode axis. With the new small-diameter cavities, it is entirely possible that a grating could get close enough to the cavity mode to use a direct shadow. (the lower limit on mirror diameter may be 1 mm in order to avoid optical diffraction losses at the cavity edges.) The shadow probably degrades faster with a plane wave than it would with an incoherent source, but I have not confirmed this in a simulation. Also, this simulation uses a slightly larger deBroglie wavelength than our beam apparatus (to be described below) actually has. These features make the grating-shadow a promising candidate for localization.

Notice in Figure 8.4 that the spatial distribution magically reproduces the original grating at a distance $L_T = d^2/\lambda_{dB} \approx 18$ mm. This is a grating self-imaging phenomenon known as the Talbot effect [226]. It could in principle be used to localize our atoms [227], but it requires a spatially coherent source. Because Talbot images from each point in an extended source are shifted in space, the Talbot effect is lost with a spatially incoherent source. Atomic plane waves require severe aperturing which causes a serious loss of flux and also require that the source (or defining aperture) be rigidly attached to the grating. Any relative motion between source and grating will smear out the Talbot pattern and cause a loss of contrast. It may be this latter consideration that ultimately denies us plane waves, since supersonic fluxes are getting very large these days (see Ref. [228]), but the cavity will always need to be mechanically isolated from the rest of the beam apparatus. The rest of this chapter will be dedicated to a description of a 2-grating localization scheme closely related to the Talbot effect which employs incoherent illumination. The incoherent illumination obviates the problems of reduced beam flux for plane waves and allows the source to be mechanically decoupled from the gratings (at the cost of introducing an added level of complexity.)

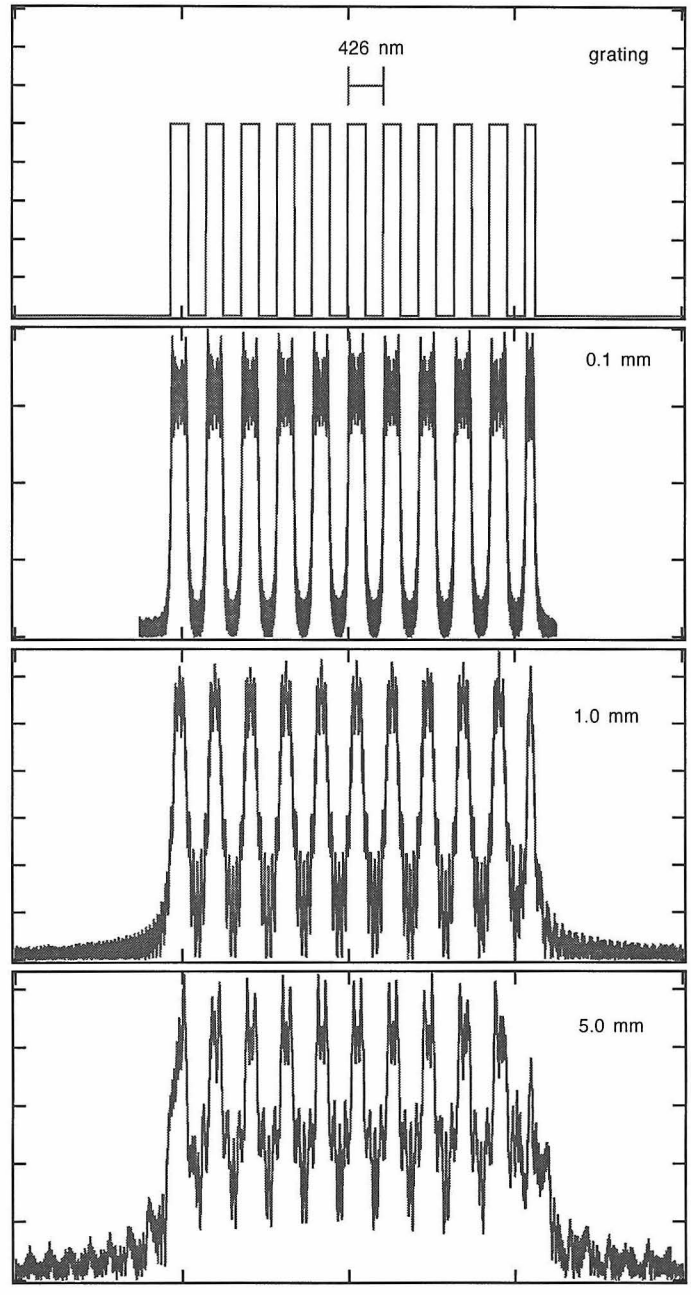

Figure 8.2: Plane wave single-grating simulations showing the atomic density at planes beyond the grating as a function of position. The vertical axes of each graph are different. The top graph shows the grating function used in the subsequent simulations. The atomic wavelength is $\lambda_{dB} = 0.1$ Å.

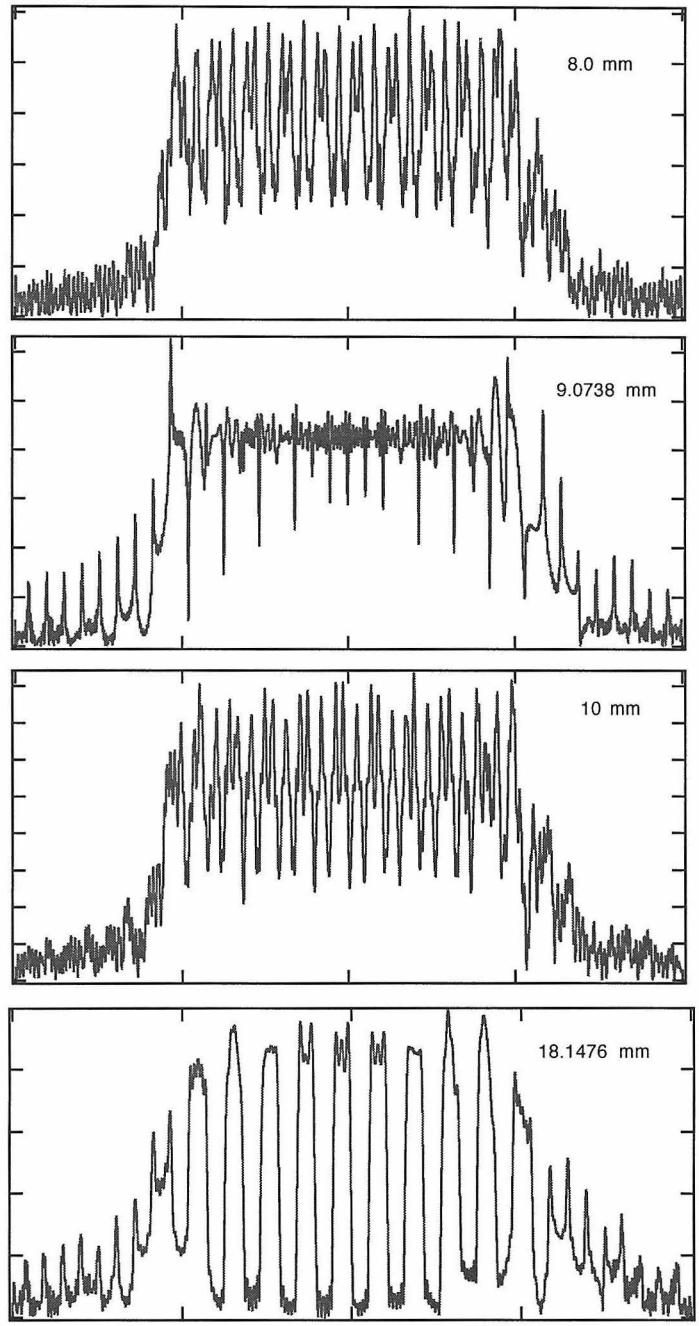

Figure 8.3: Plane wave single-grating simulations, further behind the grating. It is difficult to tell from this figure, but note that the Talbot image (at 18 mm) is shifted by one-half grating period relative to the grating in the top graph of Figure 8.2.

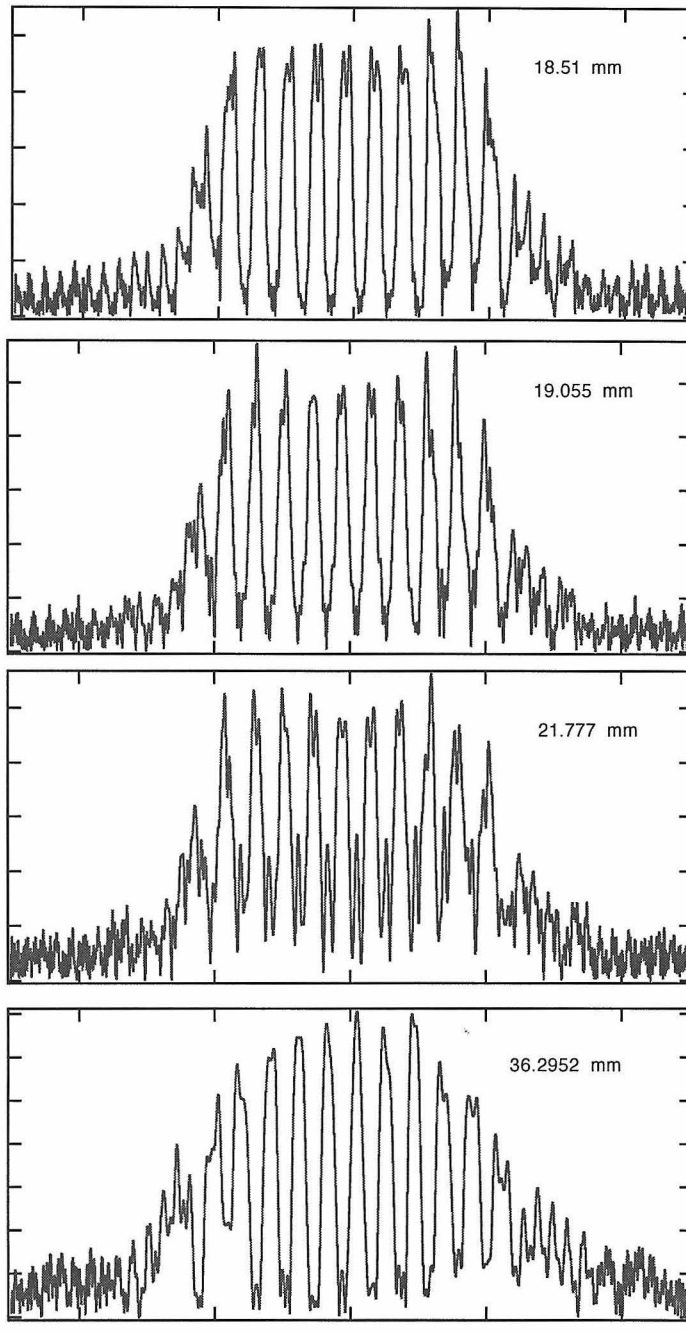

Figure 8.4: Plane wave single-grating simulations, even further behind the grating. Note the second Talbot image at 36 mm.

8.3 The gratings and the OLGA

Before I continue with the description of the localization scheme, I will describe the makeup and manufacture of the gratings and the beam machine in which the localization would be realized. The gratings are formed in a thin (100 nm) free-standing layer of silicon nitride sitting on a frame of silicon. I made a wide variety of grating periods, open fractions and heights. The manufacturing process is described in Figure 8.5 and is based on the process developed in Ref. [229]. Two scanning-electron micrographs of completed gratings are shown in Figures 8.6, 8.7

There is one last issue. We need a large atomic flux and a fast, low-velocity-dispersion beam. This has been accomplished with a supersonic noble-gas-seeded Cs source. A reservoir of Cs is heated and backed with high-pressure noble gas. The gas expands through a nozzle and the shock-front is skimmed off with an appropriately shaped "skimmer." The Cs is carried along for the ride. The expansion and skimming helps to cool the beam in the transverse direction and to narrow the velocity profile in the longitudinal direction, creating a low-divergence, narrow-velocity-dispersion, intense beam of fast atoms [230, 231]. OLGA[2] is shown in Figure 8.8. The numbers are as follows. The velocity is measured to be 800 m/s by shining light simultaneously perpendicular to and counter-propagating to the beam, scanning a laser through the Doppler-free and Doppler shifted resonances. The resonance width in the longitudinal direction gives the velocity profile, which is: $v/\Delta v = 13$. This should allow a two-cavity time-of-flight technique wherein a detection cavity informs the experimenter that an atom is in a cavity and the experimenter waits the flight time for it to appear in the next cavity. The brightness is measured by observing the current of a standard hot-wire detector, and is 3×10^{16} atoms/sec/sr. For a source-to-cavity distance of 1 m, a cavity volume $50 \times 50 \times 50$ μm^3 and a beam velocity of 800 m/s, this gives an average atom number of just over 1, which is not an over-abundance of atoms. Nothing worth mentioning was ever accomplished with the gratings in the machine, though there were several efforts.[3]

[2]Olivier's Latest Great Apparatus. Named by Olivier Carnal, creator and master of OLGA.

[3]The OLGA team consisted originally of Olivier Carnal and Hauke Hansen, later I took over and

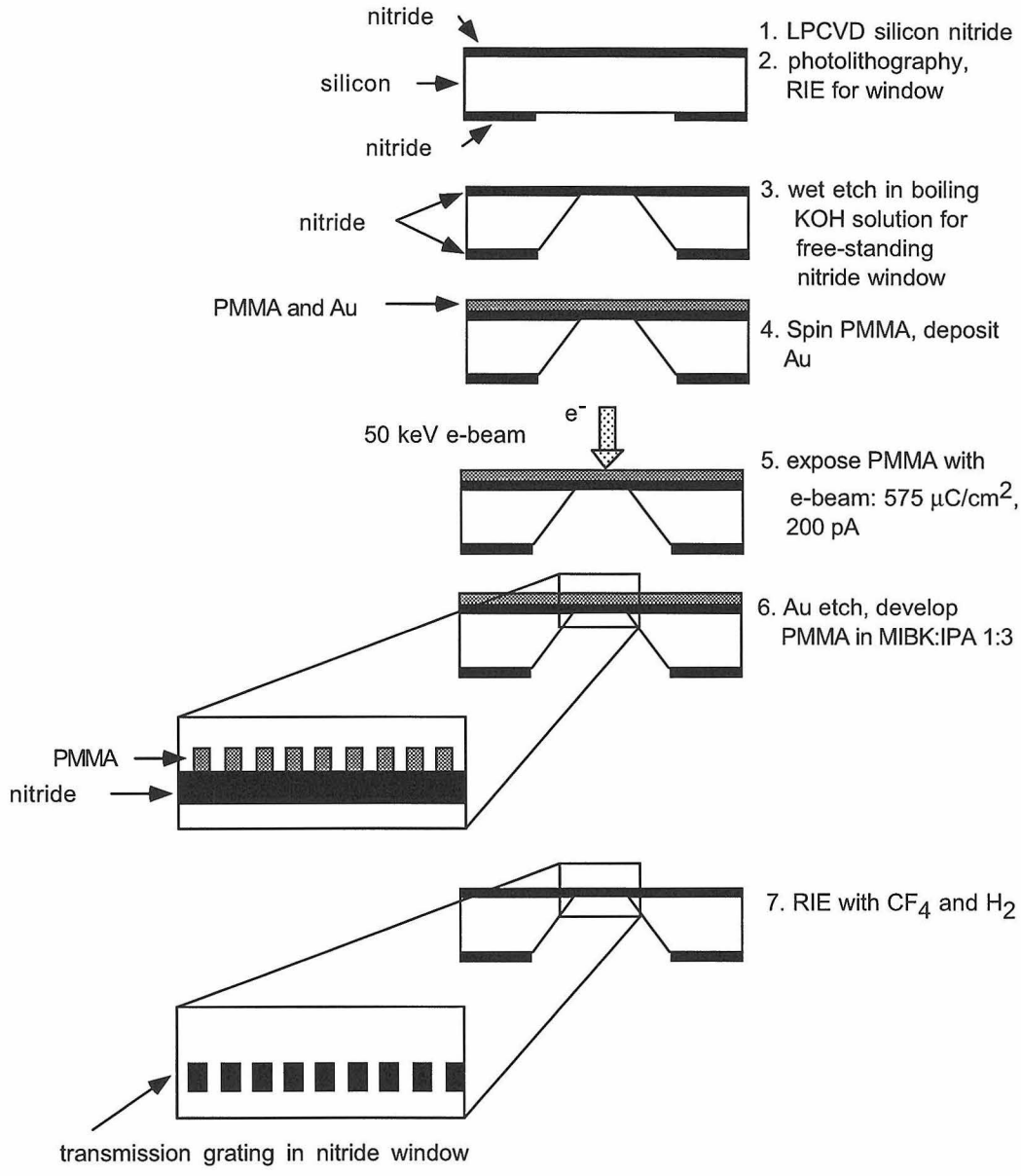

Figure 8.5: Making the gratings. After Ref. [229].

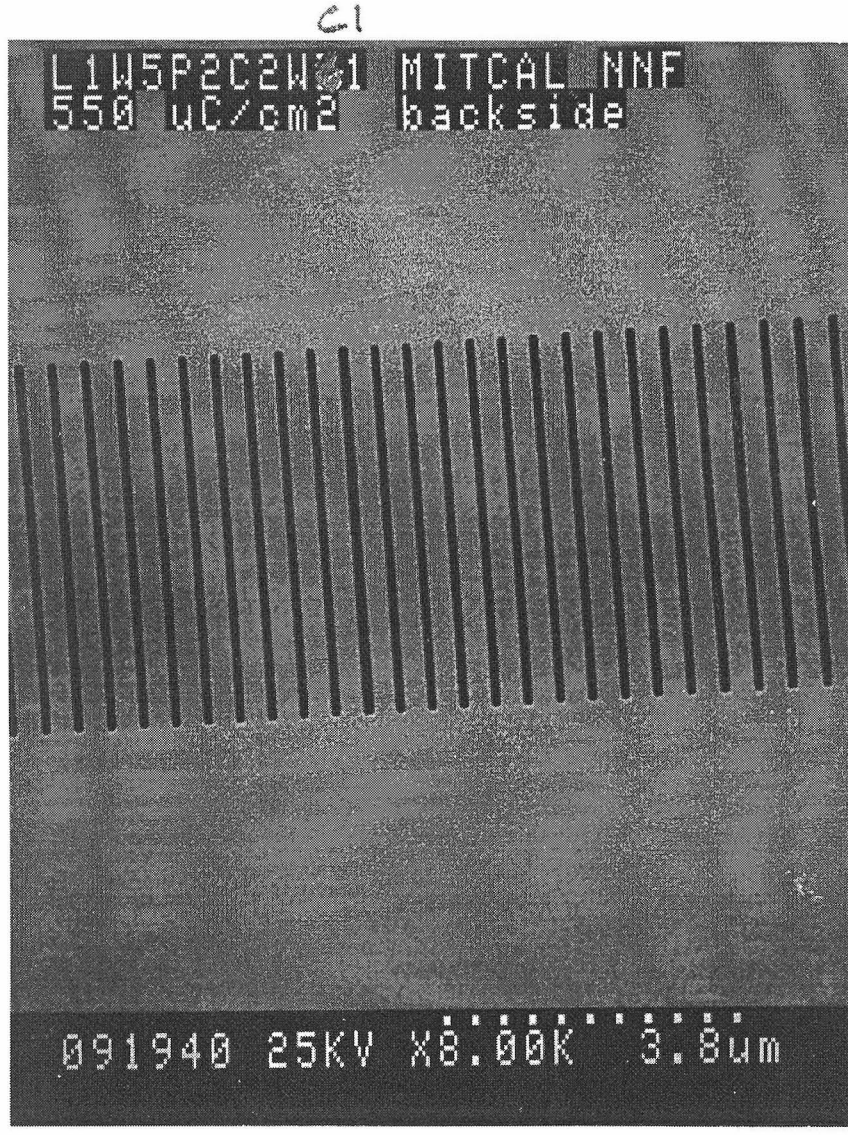

Figure 8.6: SEM photo of a grating.

Figure 8.7: SEM close-up of a grating.

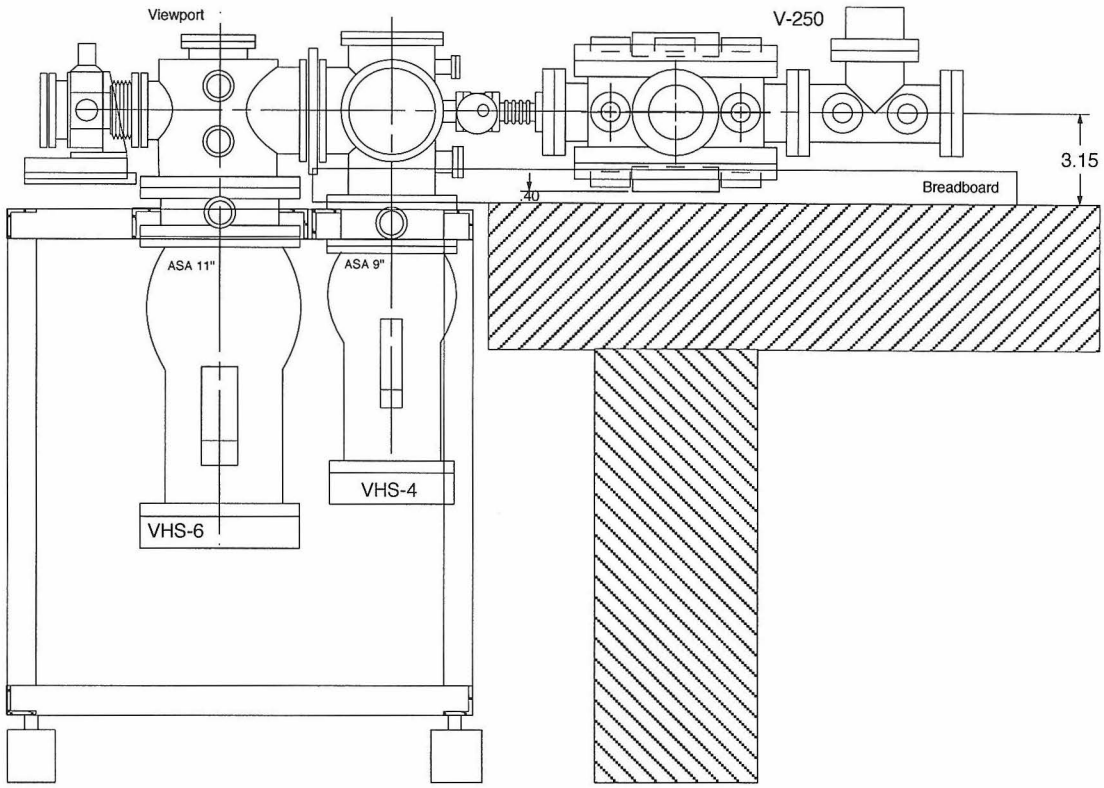

Figure 8.8: OLGA, the seeded supersonic cesium wonder, in profile.

8.4 Near-field imaging with two transmission gratings for submicrometer localization of atoms

8.4.1 Abstract

We now show theoretically that an atomic pattern with period d can be obtained with 100% visibility even for an infinitely extended source by sending atoms through two transmission gratings with periods d and $d/2$, respectively, and separated by half the Talbot length $L_T/2 = d^2/2\lambda_{dB}$, where λ_{dB} is the atomic wavelength, and the source is infinitely far away. For a finite source distance, as would be attainable in any real experiment, a small correction to the grating periods and separations restores the period-d pattern. This effect is closely related to the Talbot and Lau effects in classical

then Wolfgang Lange and Jae Park took the reins and made significant progress but were never able to confirm an atomic localization. Much of the problem likely lies in the unfortunate fact that I only ever made gratings that were 50μm tall. Should the idea of grating-localization be revived, it would be wise to start with some taller gratings in order to get more transmitted beam flux.

optics and can be used to localize atoms to a sub-micron scale without a compromise in atomic flux. We first derive compact analytical formulas for the idealized case of a monochromatic source and large gratings and then verify numerically that finite grating size and velocity dispersion in the beam do not decrease the fringe visibility considerably. Finally, we briefly present an experiment in preparation to exhibit this localization.[4]

8.4.2 Introduction

Self-imaging of gratings has been investigated extensively in light optics, with well-known examples being the Talbot [226] and Lau [232] effects. In the former case, a grating with period d is illuminated by monochromatic and parallel light (wavelength λ) to create an interference pattern similar to the original grating at distances which are multiples of the Talbot length $L_T = d^2/\lambda$ behind the grating. In the latter example, a grating illuminated by spatially incoherent light is imaged by a second identical grating when the gratings are separated by half the Talbot length and the observation plane is at infinity. Both effects can be explained by classical diffraction and coherence theory [233]. Closely related phenomena with partially coherent light are discussed by Liu [234]. A comprehensive review of the theory and application of self-imaging in optics has been written by Patorskii [235]. In addition, self-imaging phenomena have been considered in the context of matter waves in a series of papers by Cowley and Moodie [236].

Recently, these effects have been further investigated and applied to atom optics with de Broglie wavelengths in the 0.1–1 Å range [237]. For example, with a cold beam of Potassium atoms Clauser and Li demonstrated an atom interferometer based on a two-grating setup operated in near-field [238] and Chapman et al. observed first and higher order Talbot images behind a single grating with a beam of Sodium atoms [227]. However, although certain near-field diffractive imaging techniques have been discussed, it seems not to be generally appreciated that, in theory, a two-grating

[4]This article first appeared as Ref. [208]. I have modified it slightly where appropriate. It can safely be skipped in a first reading of the thesis.

arrangement allows *localization* of atoms with 100% contrast *even with an extended source at a finite distance.* The benefits of imaging with the spatially incoherent illumination of an extended source are twofold: a large atomic flux is attainable, and one has the option of mechanically isolating the potentially noisy source from any sensitive experiment downstream. In realizable experiments with finite source velocity spread and finite grating extent, contrast of over 90% is achievable on sub-micrometer scales. This possibility could be of broad importance, including improving experiments in cavity Q.E.D. which probe the energy spectrum and dynamics of coupled atom-cavity systems [7] and which attempt to create arbitrary quantum states of the electromagnetic field [179, 180]. Potential applications may also be found in the field of atom lithography [239].

The purpose of this paper is to extend existing theoretical work by deriving analytical expressions for two-grating near-field imaging from the Fresnel-Kirchhoff diffraction integral. We find an analytical solution for a coherent, point source. Patterns obtained from sources of finite transverse coherence and especially from infinitely extended sources can then be directly derived by incoherent summation of the point source patterns. We give an intuitive picture of the effect for the simplest case of a large source at infinity. The section is organized as follows. In Section 8.4.3 we formulate the problem and describe the suggested experimental setup. The theoretical framework underlying the effect is outlined in Sect. 8.4.4, and this work is then used in Sect. 8.4.5 to calculate patterns resulting from diffractive imaging and the corresponding visibilities behind two gratings. Results of numerical simulations are presented in Sect. 8.4.6 to assess the effects of finite grating width and of non-zero widths in the velocity distribution on the ideal-case results. Finally, in Sect. 8.4.7 we summarize our results and describe possible avenues for implementation.

8.4.3 Outline of the problem

For many applications in optics or atomic physics it is important to localize atoms on scales smaller than 1 μm as, for example, in cavity Q.E.D. where it is desirable to

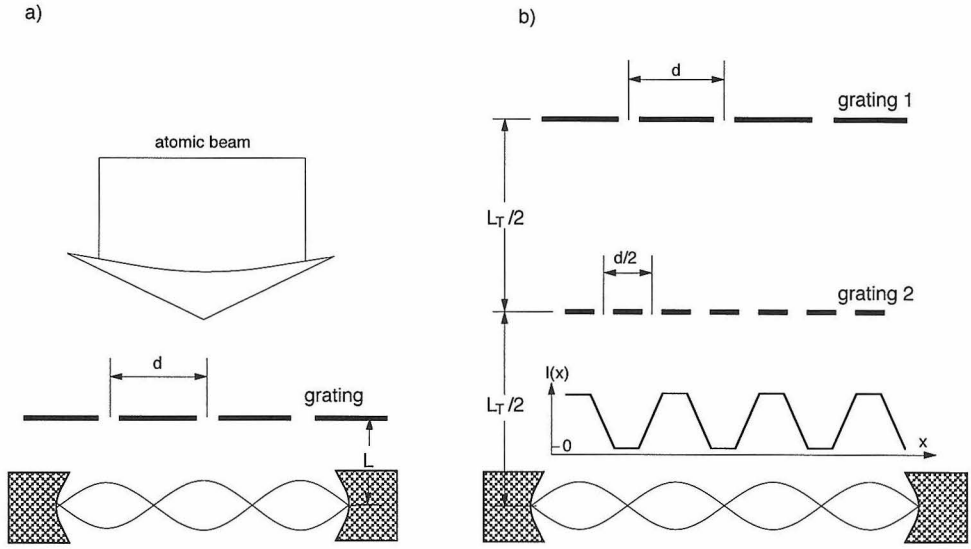

Figure 8.9: Two possible setups to localize atoms from a source at infinity to the antinodes of a standing light field. a) Straightforward approach with one grating very close to the cavity ($L \ll d_2/\lambda_{dB}$), and b) setup including two gratings separated by half the Talbot length $L_T/2 = d_2/2\lambda_{dB}$. The inset shows the theoretical atomic intensity distribution in the plane of the cavity mode.

confine atoms to the antinodes of an optical standing wave. The straightforward solution is to pass atoms through one grating with a period $d \leq 1\mu m$ close to the plane of localization (see Fig. 8.9(a)). The problems with this setup are that diffraction from the grating leads to fast washing out of the originally perfect contrast pattern[5] and that the need for a very small beam divergence and consequently a small source aperture leads to a drastically reduced atomic flux. As we shall show, these drawbacks can be eliminated by moving the first grating back and introducing a second grating with grating period $d/2$ for infinite source-grating distance (Fig. 8.9(b)). Quite remarkably, for a specific grating separation, this arrangement produces an interference pattern with period d and with 100% visibility, even for a large source size. In a realistic experiment with finite source-grating separations the grating periods and separations must be modified slightly (see Eqs. 8.12–8.14).

The general setup that we wish to consider is shown in Fig. 8.10, where an atomic beam is sent through two gratings G_1 and G_2, with grating periods d_1 and d_2. L_1

[5]Numerical calculations show that the visibility drops to 80% within a distance of $0.1d^2/\lambda_{dB}$ behind the grating.

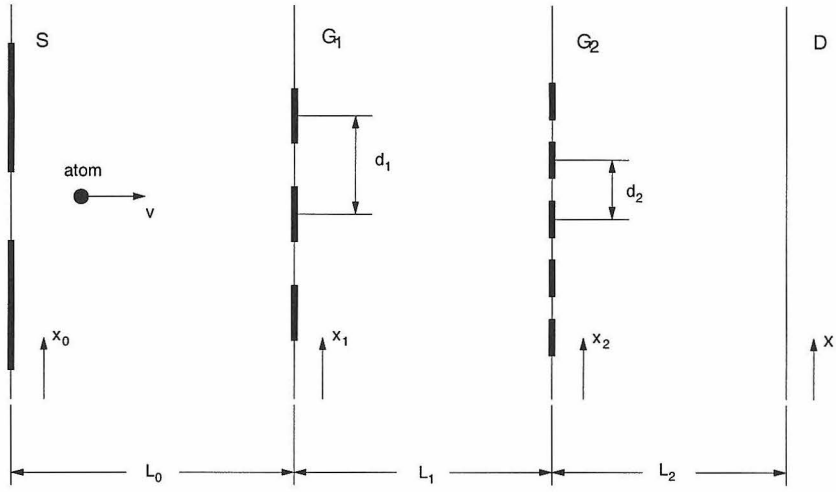

Figure 8.10: General two-grating setup. S: source, G_1: first grating with period d_1, G_2: second grating with period d_2, D: detector plane. The corresponding distances between the parallel planes are L_0, L_1 and L_2. The coordinate of a point in one of these planes is given by x_0,x_1, x_2 and x, correspondingly.

denotes the distance between grating 1 and 2, L_2 is the distance from grating 2 to the observation plane D, and L_0 is the distance from the source to the first grating. All gratings are assumed to be parallel to each other, to be of zero thickness and to extend infinitely[6] perpendicular to the plane of Fig. 8.10, so that the problem can be reduced to two dimensions.

The atomic wavelength λ_{dB} depends on the atomic velocity v and mass m: $\lambda_{dB} = h/mv$, where h is Planck's constant, as was first shown by de Broglie. In all subsequent analytical calculations (but not for our numerical results), the gratings are assumed to have an infinite number of slits and the velocity distribution in the beam is taken to be a delta-function centered at v. In order to investigate the effects of finite gratings and of non-zero dispersion of atomic velocities in the beam, numerical simulations have been carried out.

[6]If taken rigorously, the assumption of an infinite grating is not compatible with the Fresnel approximation as given below. Infinity in our case means that the number of slits in a grating $N \gg 1$. For the experimental parameters given in Sect. 8.4.6 even $N = 1000$ leads to grating dimensions small enough to neglect fourth order terms in $\Delta x_i/L$, $\Delta x_i = x_i - x_1$, in the expansion of the exponential in Eq. 8.4.

8.4.4 Theoretical framework

Due to the wave character of the atomic center-of-mass motion, the problem of atomic diffraction can be formulated completely analogously to classical diffraction problems in light optics. More precisely, the time-independent Schrödinger equation for one non-relativistic particle has the form of a Helmholtz wave equation [240] and if internal degrees of freedom of the particles are not of importance, atomic diffraction from small objects can be described by Kirchhoff's scalar theory of diffraction [241]. On the other hand, all effects described below for atoms can also be readily applied to physical optics, and indeed to waves in general.

With this preamble and with reference to Fig. 8.10, let us begin by calculating the probability distribution $I_2(x_2, L_1)$ of finding an atom at transverse position x_2 in the plane of the second grating G_2. We treat the source as an ensemble of incoherent and monochromatic point sources[7] of equal intensity, with the partial amplitude $d\Phi_1^-(x_0, x_1, L_0)$ just to the left of G_1 due to a point source at position x_0 given by $d\Phi_1^-(x_0, x_1, L_0) \propto e^{ik\sqrt{L_0^2+(x_1-x_0)^2}}$. Here, x_1 is the coordinate of a point in the plane of the first grating and $k = 2\pi/\lambda_{dB}$ is the absolute value of the atomic wave-vector. We introduce the complex amplitude transmission function $t_i(x_i)$, $i = 1, 2$, which connects the amplitude $d\Phi_i^-(x_i)$ immediately to the left of (before) the grating G_i and the amplitude $d\Phi_i^+(x_i)$ just to the right of (after) the same grating:

$$d\Phi_i^+(x_i) = d\Phi_i^-(x_i)t_i(x_i). \tag{8.1}$$

For the gratings used below, the transmission function is real and takes the values 1 (open slit) and 0 (solid bar). The partial amplitude $d\Phi_2^-$ in the plane of the second grating G_2 is calculated by using the Fresnel-Kirchhoff diffraction integral (see, e.g., Ref. [241]) for distances large compared to the grating periods and by making the

[7]The two conditions of spatial incoherence and monochromaticity are incompatible if taken rigorously but they can be justified in most cases. See Ref. [241], Ch. X and especially the footnote on p. 509 for a discussion of this.

paraxial approximation [242]:

$$d\Phi_2^-(x_0, x_2, L_1) \propto \int_{x_1} d\Phi_1^+(x_0, x_1, L_0) \exp\left[ik\sqrt{L_1^2 + (x_2 - x_1)^2}\right] dx_1. \tag{8.2}$$

The total intensity distribution at G_1 and subsequent observation planes is found from an incoherent sum over all source point contributions of the form $I_i(x_i) \propto \int_{x_0} \left|d\Phi_i^-(x_i)\right|^2 dx_0$. Hence, the total intensity distribution just to the left of the second grating G_2 is given by:

$$I_2(x_2, L_1) \propto \int_{x_0} \left|d\Phi_2^-(x_0, x_2, L_1)\right|^2 \, dx_0, \tag{8.3}$$

with the point source amplitude

$$d\Phi_2^-(x_0, x_2, L_1) \propto \int_{x_1} t_1(x_1) \exp\left[ik\sqrt{L_0^2 + (x_1 - x_0)^2}\right] \exp\left[ik\sqrt{L_1^2 + (x_2 - x_1)^2}\right] dx_1. \tag{8.4}$$

Since we are interested in effects occurring in the near-field, we retain all terms up to second order in x_i/L_j, $i, j = 0, 1, 2$, in the diffraction integral.[8] In addition, we assume that both gratings are infinitely wide (see prior footnote on this subject) and can therefore develop the transmission function of G1 as a Fourier series:

$$t_1(x_1) = \sum_{n=-\infty}^{\infty} A_n \exp\left[i2\pi\, n\frac{x_1}{d_1}\right], \tag{8.5}$$

with A_n the nth Fourier coefficient. Throughout this paper we will limit our discussion to gratings with infinitely sharp slit edges and a real transmission function [243]. The corresponding model transmission function and its Fourier components are shown in Fig. 8.11 for a grating with open fraction $f_1 = 3/8$. With the approximation $\sqrt{L_0^2 + (x_1 - x_0)^2} \cong L_0 + (1/2L_0)(x_1^2 + x_0^2 - 2x_1x_0)$ (and accordingly for the exponent in the third term of Eq. 8.4) we obtain the following equation for the amplitude distribution at G_2 arising from a point source at position x_0 (unimportant phase

[8]This approximation is the Fresnel approximation, see Ref. [241], Chapter VIII.7., p. 428.

factors have been removed):

$$d\Phi_2^-\left(\alpha, \tilde{x}_2, \tilde{L}_1\right) = C_1 \sum_{n=-\infty}^{\infty} A_n \exp\left[-i\pi \cdot \tilde{L}_1(\alpha+n)^2\right] \exp\left[i2\pi \cdot \tilde{x}_2(\alpha+n)\right] \quad (8.6)$$

with the dimensionless variables

$$\tilde{L}_1 = L_1 \frac{\lambda_{dB}}{d_1^2}\left(1+\frac{L_1}{L_0}\right)^{-1}, \quad (8.7)$$

$$\tilde{x}_2 = \frac{x_2}{d_1}\left(1+\frac{L_1}{L_0}\right)^{-1}, \quad (8.8)$$

and

$$\alpha = -\frac{d_1}{\lambda_{dB}}\frac{x_0}{L_0}, \quad (8.9)$$

and the proportionality factor $C_1 = \sqrt{dI_0}\left(1+\frac{L_1}{L_0}\right)^{-1}$, where dI_0 is the beam intensity of the point source right before the first grating. Note that for large source-grating distances, $\tilde{L}_1$ is the grating separation in units of the Talbot length and $\tilde{x}_2$ is the coordinate in units of the grating period d_1. α is defined as the angle under which the point source is viewed from the first grating in units of the far-field first order diffraction angle λ_{dB}/d_1. The source will be spatially coherent across d_1 if the source aperture extends to a maximum $\alpha_{max} \ll 1$ and incoherent if $\alpha_{max} \gg 1$.

The advantage of developing the transmission function in terms of Fourier components is obvious: in this case the intensity distribution is given simply by a sum and can be easily analyzed for special distances like, e.g., $\tilde{L}_1 = 1$. If one is not interested in small-scale features (i.e. high diffraction orders) one could truncate the Fourier expansion and limit the discussion to the first few diffraction orders. Here we retain all orders.

The diffraction pattern in the detector plane D arising from the two gratings G_1 and G_2 is calculated in two steps: first, the amplitude $d\Phi_2^+(x_0, x_2, L_1)$ just to the right of the second grating is calculated via Eqs. 8.1 and 8.6, where the second grating

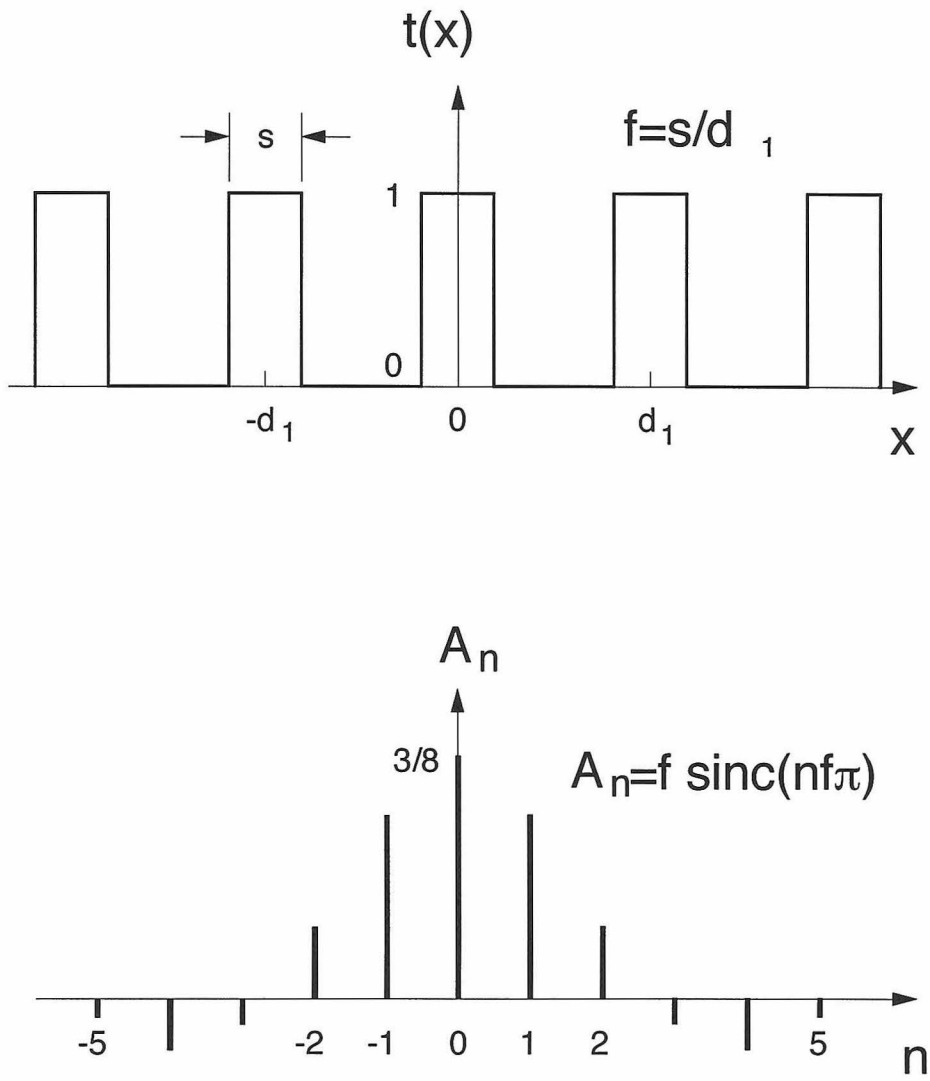

Figure 8.11: Transmission function $t(x)$ for an idealized grating with infinitely sharp edges and open fraction $f = 3/8$. The corresponding Fourier components $A_n = f\text{sinc}(nf\pi)$ up to $n = \pm 5$ are shown below.

transmission function is given by

$$t_2(x_2) = \sum_{m=-\infty}^{\infty} B_m \exp\left[i2\pi\, m\frac{x_2}{d_2}\right]. \tag{8.10}$$

Second, this amplitude $d\Phi_2^+(x_0, x_2, L_1)$ is combined with the Fresnel-Kirchhoff diffraction integral (see Eq. 8.2) for propagation to the detection plane D. The calculation is carried out analogously to the one-grating case. The algebra, however, is tedious and only the final result is given here for the partial amplitude $d\Phi_D(x)$ in the plane D due to a point source at position x_0:

$$\begin{aligned} d\Phi_0(\alpha, \tilde{x}, \tilde{L}_1, \tilde{L}_2, p) \;&=\; C_2 \sum_{n=-\infty}^{\infty}\sum_{m=-\infty}^{\infty} A_n B_m \exp\left[-i\pi\tilde{L}_1(\alpha+n)^2\right] \times \\ &\quad \exp\left[-i\pi\tilde{L}_2(\alpha+n+pm)^2\right] \exp\left[i2\pi\tilde{x}(\alpha+n+pm)\right], \end{aligned} \tag{8.11}$$

where x is the coordinate in the observation plane (see Fig. 8.10), $C_2 = \sqrt{dI_0}\left(1+\frac{L_1+L_2}{L_0}\right)^{-1}$, and the dimensionless variables are defined as:

$$\tilde{L}_2 = L_2\frac{\lambda_{dB}}{d_1^2}\left(1+\frac{L_1}{L_0}\right)^{-1}\left(1+\frac{L_1+L_2}{L_0}\right)^{-1}, \tag{8.12}$$

$$\tilde{x} = \frac{x}{d_1}\left(1+\frac{L_1+L_2}{L_0}\right)^{-1} \tag{8.13}$$

and

$$p = \frac{d_1}{d_2}\left(1+\frac{L_1}{L_0}\right). \tag{8.14}$$

These expressions are greatly simplified for an infinite source distance $L_0/L_i \to \infty$. In this case, p is simply the ratio of the two grating periods and $\tilde{L}_{1,2}$ are the distances $L_{1,2}$ given in units of the first grating Talbot length. Note that Eq. 8.11 was found in [244] for the special case $L_0 \to \infty$. The purpose of this paper is to show that for $p = 2$ and $\tilde{L}_1 = \tilde{L}_2 = \frac{1}{2}$ the atoms can be localized with 100% contrast, even for $L_0/L_i \neq \infty$.

The intensity distribution in the plane D due to an extended source is finally given by:

$$I_{ext}(\tilde{x}, \tilde{L}_1, \tilde{L}_2, p) \propto \int_{\alpha} \left| d\Phi_D(\alpha, \tilde{x}, \tilde{L}_1, \tilde{L}_2, p) \right|^2 d\alpha. \tag{8.15}$$

Eqs.8.5 to 8.15 provide the basis upon which we will now derive a specific two-grating configuration to localize atoms in space.

8.4.5 Patterns and their visibilities behind two gratings

Before discussing patterns associated with two gratings, let us first point out two special cases for the one-grating setup. The starting point for this analysis is Eq. 8.6, from which we compute multiple images of a point source at $x_0 = 0$; ($\alpha = 0$). At odd multiples of the Talbot distance $\tilde{L}_1 = 2k - 1,\ k \in N$, the exponential with the quadratic term in Eq. 8.6 can only take two values: 1 for n even and -1 for n odd. Thus, all even terms in the sum are unchanged, whereas odd terms change sign. This corresponds to a downstream image of the original grating shifted by half a period and magnified by a factor $(1 + L_1/L_0)^{-1}$. On the other hand, the grating image is unshifted at even multiples of the Talbot length. This self-imaging phenomenon is called the Talbot effect and was first observed more than 150 years ago. This effect could be used to localize atoms at the Talbot distance behind one grating [227], but requires a point source since the images are shifted proportional to α.

Another interesting amplitude distribution is obtained for $\tilde{L}_1 = \frac{1}{2}$ and a perfectly rectangular transmission grating with open fraction $f_1 = 50\%$, again with $alpha = 0$ for a point source. The Fourier coefficients for this grating are $A_n = 1/2\mathrm{sinc}(\pi n/2)$. Since coefficients with even $n > 0$ vanish for this grating, the quadratic term in the exponential in Eq. 8.6 is either 1 for $n = 0$ or $-i$ for n odd (which is proved via $n^2 = 4k\,(k-1) + 1,\ k \in N$, for n odd). The resulting probability amplitude is therefore given by: $d\Phi_2^-(\tilde{x}_2) \propto \frac{1}{2}\,(1+i) - it(\tilde{x}_2)$, a function which takes only the two values $\frac{1}{\sqrt{2}} \cdot e^{\pm i\pi/4}$. The intensity is constant, whereas the phase jumps between $\pi/4$ and $-\pi/4$ over one grating period. This somewhat amazing field distribution may be useful in connection with phase sensitive techniques in atom interferometry.

These examples show that in the near-field, gratings can behave in unfamiliar ways and that the characteristic distances for self-imaging are given by $L_T \approx d^2/\lambda_{dB}$ ($\tilde{L}_1 \approx 1$). These simple observations drive the search for similar effects with two gratings. In particular, Chang et al. [244] observed that under special conditions two gratings with periods $d_1 = 2d_2$ can self-image without requiring either a point source (in contrast to the one-grating examples given above) or a monochromatic beam. Additionally, Clauser and Li [238] have used this grating configuration for atom interferometry but a quantitative analysis of high-contrast localization with an incoherent source was not given. For this specific two-grating setup we now derive a remarkably simple analytical expression for the case of perfectly rectangular transmission functions.

In Eq. 8.12 we choose $p = 2$ (which is the generalization of the condition $d_1 = 2d_2$ for infinite source-grating distances), $\tilde{L}_1 = \tilde{L}_2 = 1/2$, and rewrite Eq. 8.11 as follows by omitting unimportant phase factors and by regrouping terms:

$$\begin{aligned} d\Phi_D(\alpha, \tilde{x}, \tilde{L}_1 = \tilde{L}_2 = 1/2, p = 2) \quad &\equiv \quad d\Phi 0(\alpha, \tilde{x}) = C_2 \sum_{n=-\infty}^{\infty} \sum_{m=-\infty}^{\infty} A_n B_m \\ &\times \exp\left[-i\pi/2\left(n^2 + (n+2m)^2\right)\right] \\ &\times \exp\left[-i2\pi(n+m)\alpha\right] \exp\left[i2\pi(n+2m)\tilde{x}\right]. \end{aligned} \tag{8.16}$$

This expression can be readily simplified by using the following identity:

$$\exp\left[-i\frac{\pi}{2}\left\{n^2 + (n+2m)^2\right\}\right] = \begin{cases} 1, \text{ for } n \text{ even} \\ -1, \text{for } n \text{ odd} \end{cases}, \tag{8.17}$$

independent of m. As a result, the two summations over n and m can be factorized:

$$\begin{aligned} d\Phi_D(\alpha, \tilde{x}) \quad \propto \quad &\left\{\sum_n A_n \exp\left[i2\pi\, n\,(\tilde{x} - \alpha)\right] \exp\left[-i\pi\, n\right]\right\} \times \\ &\left\{\sum_m B_m \exp\left[i2\pi\, m\,(2\tilde{x} - \alpha)\right]\right\}. \end{aligned} \tag{8.18}$$

This can now be written in terms of the transmission functions t_1 and t_2 of the first and second gratings (as given in Eqs. 8.5 and 8.10):

$$d\Phi_D(\alpha, \tilde{x}) = C_2 t_1 \left[\left(\tilde{x} - \alpha - \frac{1}{2} \right) d_1 \right] \cdot t_2 \left[(2\tilde{x} - \alpha) d_2 \right]. \tag{8.19}$$

The final probability amplitude arising from a point source at the origin ($\alpha = 0$) is therefore simply given by the product of the transmission function of the first grating, shifted by half a period, and the transmission function of the second grating. Equation 8.19 is the central result of this paper. It describes how the intensity pattern in the detector plane can be obtained when illuminating the two-grating setup coherently with a point source. Any partially coherent source distribution and its pattern can be derived from this equation.

With the point source at infinity, Eq. 8.19 can be readily expressed in real space coordinate x because in this special case $d_1/d_2 = 2$, and $x = \tilde{x} d_1$, and hence

$$I_D(x, \alpha = 0) = dI_0 t_1 \left(x - \frac{d_1}{2} \right) t_2(x). \tag{8.20}$$

The corresponding intensity distributions for the two cases of perfectly rectangular gratings and open fractions $f_1 = 25\%$ and 50% for the first grating and $f_2 = 50\%$ for the second grating are shown in. 8.12(a) and (b). The point source patterns for $f_1 = 25\%$ and 50% are identical and consist of a perfectly rectangular pattern with open fraction 25%, which is shifted with respect to the origin by $d_1/2$Note that the intensity maxima are given by dI_0 , although the total overall transmission of the two gratings is different in the two cases. For sources at finite distances, the result is the same with the exception that the period is $d_1 \left(1 + \frac{L_1+L_2}{L_0}\right)$ and the intensity is reduced by a factor $\left(1 + \frac{L_1+L_2}{L_0}\right)^{-2}$.

Given the result of Eq. 8.19 for a point source the principal question remaining is What happens if we take an extended source for which a runs from $-\alpha_{\max}$ to $+\alpha_{\max}$? Does the fringe visibility persist or is it washed out completely as soon

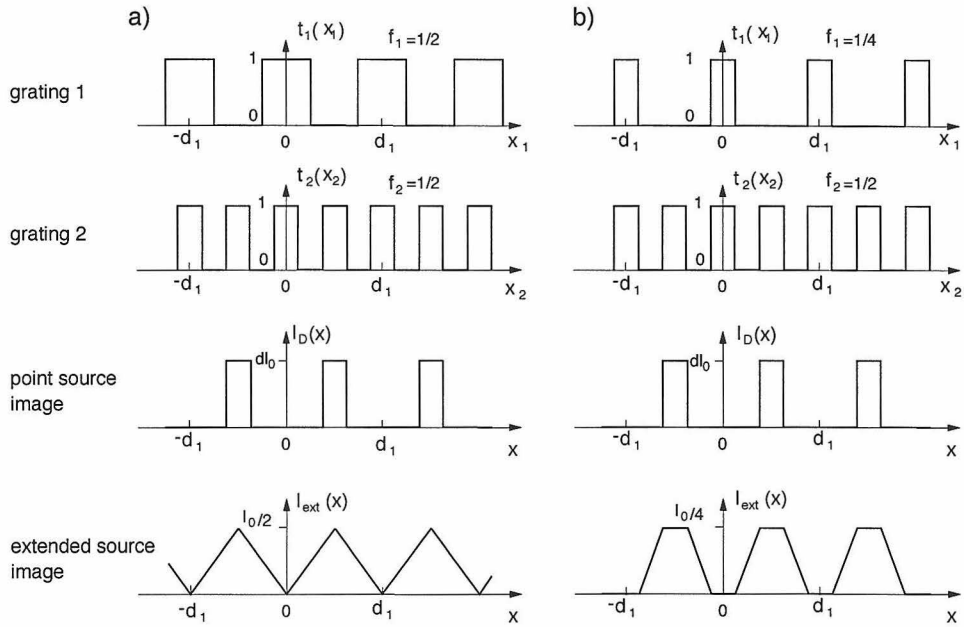

Figure 8.12: Self-images behind two gratings for a point source and for an extended source, both with $L_0 \rightarrow \infty$. The distances are $L_1 = L_2 = L_T/2$ and the open fraction of the second grating is $f_2 = 50\%$. The transmission functions of the two gratings ti(xi) and the resulting intensity distributions for a point source at $x_0 = 0$ (I_D) and an extended source (I_{ext}) are shown for a) an open fraction of grating 1 f_1 =50%, and b) $f_1 = 25\%$.

as $\alpha_{\max} >> 1$,[9] as is the case for a diverging beam from an extended source? This question is answered by applying Eq. 8.15 to Eq. 8.19 and by using the identity $|t_{1,2}(\tilde{x})|^2 = t_{1,2}(\tilde{x})$ for perfectly rectangular transmission gratings to find that

$$\begin{aligned} I_{ext}\left(\tilde{x}, \tilde{L}_1 = \tilde{L}_2 = \frac{1}{2}, p = 2\right) &\equiv I_{ext}(\tilde{x}) \qquad (8.21) \\ &\propto \frac{1}{2\alpha_{\max}} \int_{-\alpha_{\max}}^{\alpha_{\max}} t_1\left(\left(\tilde{x} - \alpha - \frac{1}{2}\right) d_1\right) t_2\left(\left(2\tilde{x} - \alpha\right) d_2\right) d\alpha \\ &= \frac{1}{2\alpha_{\max}} \int_{-\alpha_{\max}}^{\alpha_{\max}} t_1\left(\left(\alpha + \tilde{x} + \frac{1}{2}\right) d_1\right) t_2\left(\alpha \cdot d_2\right) d\alpha \quad , \end{aligned}$$

which is a convolution of grating 2 with the shifted grating 1. The factor $1/2\alpha_{\max}$ was added to ensure convergence of the integral for $\alpha_{\max} \to \infty$. If the source dimension is much larger than $L_0\lambda_{dB}/d$, then $\alpha_{\max} \gg 1$ and the integral is to a good approximation independent of the upper/lower limits and $\alpha_{\max}$ can be set to infinity. Due to the periodicity of the expression under the integral, it is therefore sufficient to evaluate the integral within one period $0 < \alpha < 1$. For two rectangular gratings (G_1, G_2) with open fractions (f_1, f_2) $(f_i \leq 0.5)$, respectively, the result is (with $f_{min} \equiv \min(f_1, f_2)$):

$$I_{ext}(\tilde{x}) = \begin{cases} 0, \text{ for } \mathrm{n} - \frac{1-\mathrm{f}_1-\mathrm{f}_2}{2} \leq \tilde{\mathrm{x}} \leq \mathrm{n} + \frac{1-\mathrm{f}_1-\mathrm{f}_2}{2} \\ I_0 f_{\min}, \text{for } \mathrm{n} + \frac{1-|\mathrm{f}_1-\mathrm{f}_2|}{2} \leq \tilde{\mathrm{x}} \leq \mathrm{n} + \frac{1+|\mathrm{f}_1-\mathrm{f}_2|}{2} \end{cases} , \qquad (8.22)$$

where n is an integer and $I_{ext}(\tilde{x})$ is linearly increasing or decreasing in between. I_0 is the total beam intensity to the left of grating 1.

For illustration of this final result, we take again the above examples of $f_1 = 25\%$ and 50% and f_2 =50% for the two gratings. The intensity distributions $I_{ext}(x)$ for illumination by an infinitely extended source are shown in Figs. 8.12(a) and (b) at the bottom. Although the point-source images are identical, the large-source images differ considerably. For $f_1 = 50\%$ (Fig. 8.12(a)) the resulting image is a perfect triangular sawtooth with a maximum intensity equal to half the incoming intensity. The main problem with this setup is the fact that the intensity drops to zero only

[9]This is possible without violating the paraxial approximation.

at the singular points $\tilde{x} = n$, n integer. This situation is clearly not ideal for an experiment with usually finite position resolution.

By contrast, for $f_1 = 25\%$ (Fig. 8.12(b)) the intensity drops to zero not only at singular observation points but for all $\tilde{x}$ in the intervals $n - \frac{1}{8} \leq \tilde{x} \leq n + \frac{1}{8}$, $n \in Z$, and the contrast is therefore 100% even with a non-ideal detector. The price to be paid for this improved localization is that the maximum intensity drops to I0/4. However, this case offers a reasonable compromise between high atomic flux and good localization.

The origin of this unexpected result of high contrast even for an extended source is somewhat obscured by the lengthy equations. To conclude this section, we will give two somewhat more intuitive pictures of the effect for the simplest case of a large extended source located far from the gratings ($\alpha_{\max} \gg 1$ and $L_0/L_{1,2} \gg 1$). The first explanation of the effect is found by considering G_1 itself as the (structured) source and reducing the problem to imaging with a single grating G_2. The pattern due to a point source in the plane of G_1 is given by Eq. 8.6 and by replacing L_0 by L_1 , L_1 by L_2, and d_1 by d_2 in Eq. 8.7. As a consequence, $\tilde{L}_1 = 1$, and we end up with the simple Talbot effect described at the beginning of Sect. 8.4.5. The resulting pattern I_2^- , however, has a period of d_1 (and not d_2) due to the factor $(1+L_2/L_1)^{-1}$ in Eq.8.8. This point-source image must now be convolved with the transmission function of G_1 to obtain the final intensity distribution. Since both t_1 and I_2^- have the same period d_1, the self-imaging pattern survives. In this picture we also see that analogous to the Talbot effect, localization with period d_1 occurs not only for one specific distance, but for all distances $L_1 = L_2 = nL_T/2$, $n \in N$.

Our second explanation is based on the complex coherence function μ_{12}, as defined in [241]. This approach has already been used by other authors to explain the Lau effect [245]. The coherence function is the time-averaged product of the field amplitude at position x with the amplitude at position $x + \Delta x$ and indicates the degree of spatial coherence for the amplitude from an extended source. If one knows the intensity distribution of an incoherent source in the plane σ, then μ_{12} in a plane

parallel to σ at distance L is given by

$$\mu_{12}(q) = e^{i\psi} \cdot \frac{\int_\sigma I(\xi) e^{-ikq\xi} d\xi}{\int_\sigma I(\xi) d\xi}, \quad \psi = \frac{k}{2L}\left[(x+\Delta x)^2 - x^2\right], \tag{8.23}$$

where $q \equiv \Delta x/L$ and ξ is the transverse position in the source plane σ. Let us now just consider the simplest case of a large extended source located far from the gratings corresponding to a completely incoherent irradiation of grating 1. In this case, grating 1 (with period d_1 and N slits) can itself be considered as an incoherent source. For a first grating G_1 with 50% open fraction, we find from Eq. 8.23 that μ_{12} takes the following form in the plane of the second grating G_2:

$$\mu_{12}(q_2) \propto \operatorname{sinc}\left(\frac{kq_2 d_1}{4}\right) \frac{\operatorname{sinc}\left(N\frac{kq_2 d_1}{2}\right)}{\operatorname{sinc}\left(\frac{kq_2 d_1}{2}\right)}, \; q_2 = \Delta x_2/L_1. \tag{8.24}$$

For $N \to \infty$ the second term in Eq. 8.24 can be approximated by a sum of Dirac delta functions: $\sum_n (-1)^n \delta\left(kq_2 d_1 - n2\pi\right)$. Hence, for $L_1 = L_T/2 = d_1^2/2\lambda_{dB}$ any two points x_2' and x_2'' in this plane are highly correlated if they are separated by a multiple of $d_1/2$. By introducing now a grating with period $d_2 = d_1/2$ into this plane, only correlated points (oscillating perfectly in-phase or out-of-phase) are transmitted. Grating G_2 thus acts as a secondary phased source, which produces a simple interference pattern in a plane $L_T/2$ behind this second grating, as can be seen from the following formula relating the coherence function in the plane of the second grating to the intensity in the observation plane D (located $L_T/2$ away from G_2) [10]:

$$I(x) \propto \int_{x_2'} dx_2' \int_{x_2''} dx_2'' \, \mu_{12}\left(\frac{x_2'' - x_2'}{L_T/2}\right) t_2(x_2'') t_2(x_2') \exp\left[ik\left(s'' - s'\right)\right], \tag{8.25}$$

with s' and s'' the distances from a point x in the observation plane to points x_2' and x_2'' in the plane G_2 , respectively. In the Fresnel approximation this integral can be readily evaluated by inserting the coherence function from Eq. 8.24 and by assuming

[10] See, e.g., Ref. [241], p. 517.

a second grating with infinitely narrow slits ($f_2 \to 0$). In this case the coordinates in the grating 2 can be replaced by $x_2' = md_1/2$ and $x_2'' = (m+n)\,d_1/2$, where m, n are integers; each integral is then transformed into a sum over n or m. With $t_2(x_2' + nd_1/2)t_2(x_2') = t_2(x_2')$, $n \in Z$, and $k\,(s'' - s') \cong -\frac{2\pi}{d_1}nx + \psi$, $\psi = n^2\frac{\pi}{2} + \pi\, mn$, $I(x)$ takes the form:

$$I(x) \propto \sum_n \mathrm{sinc}\left(n\frac{\pi}{2}\right) \exp\left(in\frac{2\pi}{d_1}x\right) \exp\left(in^2\pi\right) = \; t_1\left(x - \frac{d_1}{2}\right), \tag{8.26}$$

which is simply the transmission function of the first grating shifted by half a period. This result also follows directly from Eq. 8.22 with $f_1 = 1/2$ and $f_2 \to 0$.

We can now give an intuitive picture of the effect as follows. A periodic incoherent source (grating 1) with period d_1 produces strong correlations between points separated by $d_1/2$ in a plane $L = L_T/2$ away from the source G_1. By transmitting with G_2 only those parts of the wavefunction which have a high correlation in this plane we obtain a pattern with high contrast in a subsequent plane, located at $L = L_T$ away from the source grating G_1.

8.4.6 Numerical simulations for a realistic experimental setup

All of our preceding analytical calculations were carried out under the idealized assumptions of infinite gratings (along x_i) and monochromatic illumination. If instead the gratings are finite, then from the coherence-function picture just presented one might expect that the error would be small as long as the first grating consists of more than $N_1 \approx 10$ slits. To verify this statement, we have performed a rigorous numerical calculation of the diffraction pattern with finite grating sizes as well as with finite-width velocity distributions in the atomic beam. The calculations are based on a model described in [242] which minimizes computer time by converting the diffraction integrals into convolutions thereby exploiting Fast Fourier Transform techniques. The calculations were performed on a Macintosh Quadra 700 whose memory is sufficient for storing the vectors used in these time-consuming calculations.

For the numerical simulations, we used two sets of parameters, listed in Table 1.

parameter	numerical value I	numerical value II
λ_{dB} (m)	3.7×10^{-12}	3.7×10^{-12}
L_0 (m)	0.65	0.65
L_1 (mm)	22.13	21.9
L_2(mm)	23.69	23.4
d_1 (nm)	398	396
d_2 (nm)	206	204
localization period (nm)	426	426

Table 8.1: The two sets of parameter values used for the numerical calculations. Set I is the test set, and is used for Figure 8.13. Set II is based on values for a proposed experiment and is used in Figures 8.14 and 8.15.

The first set of parameters (set I) forms a numerical "test" set which satisfies Eq. 8.12 with a localization period of 426 nm (equal to the optical standing wave period $\lambda_{light}/2$ in our cavity QED experiments [7]). The second set of parameters (set II) for the gratings and the source was chosen according to an experiment planned with a seeded supersonic beam of Cesium in combination with micro-fabricated Silicon Nitride gratings.[11] Note that, due to the finite source distance the period of the first grating is not exactly twice the period of the second one and is smaller than the period of 426 nm obtained in the detector plane. Because of limited computer memory, the source size in our calculations is only 10 μm, which corresponds to $\alpha_{\max} \approx 1$ which obviously does not meet the requirement of $\alpha_{\max} \gg 1$, but is sufficient to smear out the point source image over one grating period. In the planned experiment we will use a source about 0.5 mm in diameter to obtain a grating-like intensity pattern in the atomic beam allowing localization of atoms to the antinodes of a standing-wave field in an optical cavity.

In a first numerical evaluation run (using numerical value set I) we have confirmed that the image visibility, with $f_1 = 25\%$, remains high even for finite sized gratings. We determined the visibility V by measuring the average maximum and minimum intensity values I_{max} and I_{min} in the calculated fringe pattern and by using

[11]The Silicon Nitride gratings were fabricated at the National Nanofabrication Facility (NNF) at Cornell University. The fabrication procedure is described in Ref. [229].

the following definition:

$$V = \frac{I_{\max} - I_{\min}}{I_{\max} + I_{\min}}. \tag{8.27}$$

By going from $N_1 = N_2/2 = 20$ (same widths for the two gratings) down to $N_1 = 5$ we have found that the visibility remains roughly constant (this is confirmed in Fig. 8.15). For example, the intensity distribution for $N_1 = 20$ is shown in Fig. 8.13 as a function of transverse position x in the detector plane, where we note that due to the finite grating size, no sharp corners appear as in the theory. For a comparison with Fig. 8.12, we have plotted the results of numerical simulations for f_1 =50% and$f_2 = 50\%$ in Fig. 8.13(a) (compare Fig. 8.12(a)) and forf_1 =25% and f_2 =50% in Fig. 8.13(b) (compare Fig. 8.12(b)). In Fig. 8.13(a), the expected singular minima are smeared out due to the diffraction from the grating edges, and as a consequence, the visibility drops to about 86%. By contrast, in Fig. 8.13(b) with $f_1 = 25\%$, the intensity stays low for about a quarter of a period as in the analytical result. The minima do not, however, go all the way to zero, but still the contrast remains high at 97%. The advantage of using a first grating with lower open fraction is evident.

Due to the fact that the two-grating localization depends on the wavelength of the particles through Eq.8.12, a velocity spread in the beam will deteriorate the effect. The role of non-zero velocity dispersion is investigated by calculating the intensity patterns for different de Broglie wavelengths and weighting each result incoherently by a function $N(\lambda)$ corresponding to a Gaussian velocity profile for the beam[12]:

$$N(\lambda)d\lambda = N_0 \exp\left[-\left(\frac{\lambda - \lambda_0}{\Delta\lambda}\right)^2\right] d\lambda. \tag{8.28}$$

The numerical result for numerical values set II with a finite wavelength width $\lambda_0/\Delta\lambda = 20$ ($\lambda_0 = 3.7 \times 10^{-12}$ m), as we have measured in our seeded Cesium beam, is shown in Fig. 8.14 for $N_1 \approx 10$ slits. Relative to Fig. 8.13(b) the visibility drops by about 10% to 87%, but otherwise the patterns are comparable. This demon-

[12]The wavelength distribution is actually given by $N(\lambda)\,d\lambda = C\lambda^{-7} \exp\left[-\left(\frac{\lambda-\lambda_0}{\Delta\lambda}\right)^2 \left(\frac{\lambda_0}{\lambda}\right)^2\right] d\lambda$, but the error is negligible for $\lambda_0/\Delta\lambda = 20$.

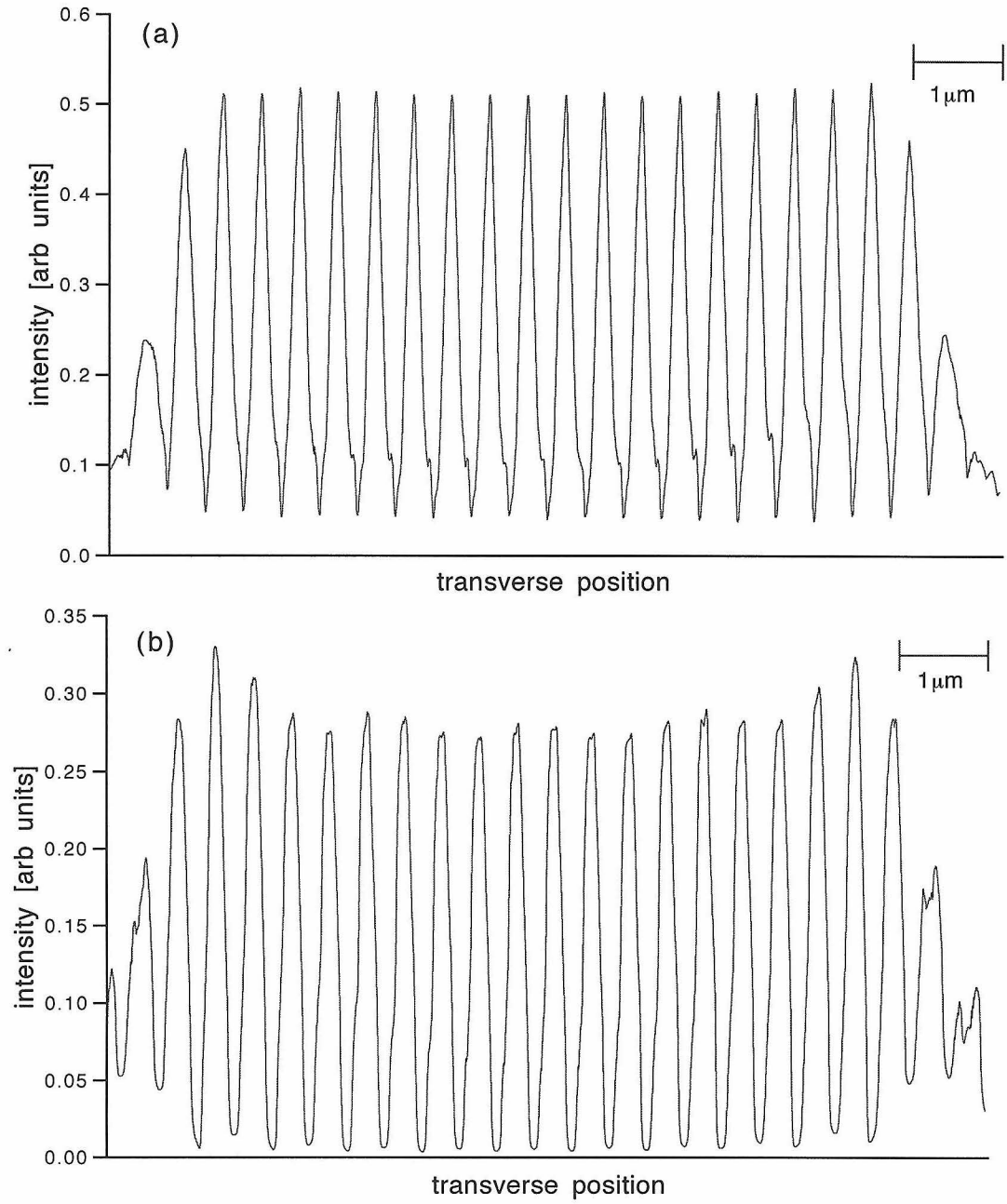

Figure 8.13: Results of the numerical simulations (numerical values set I) for $N_1 = N_2/2 \approx 20$ and a monochromatic source. a) Intensity distribution in the detector plane for $f_1 = f_2 = 1/2$ and b) for $f_1 = f_2/2 = 1/4$. The asymmetries are due to an arbitrary cutoff of the gratings on both sides (partial slits at both ends are possible).

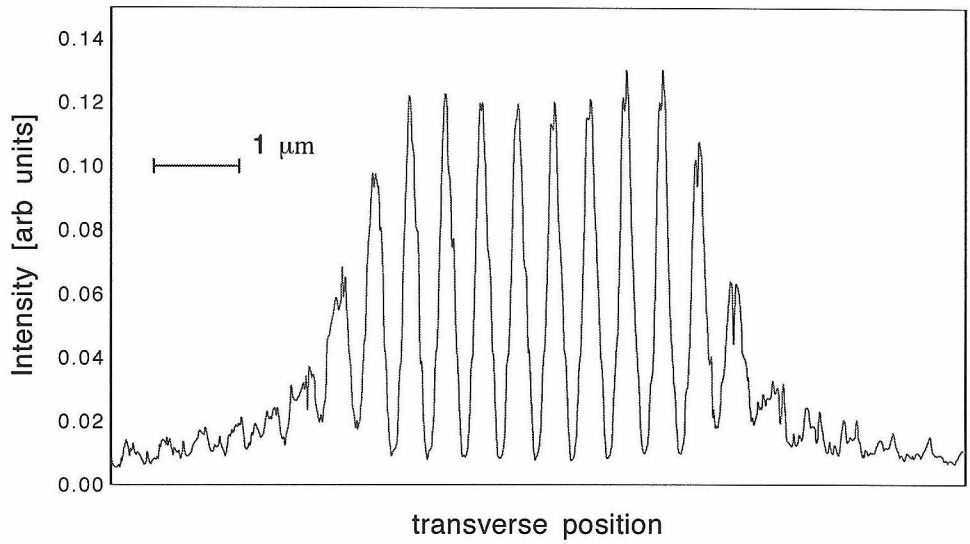

Figure 8.14: Numerical result (numerical values II) for a finite width in the velocity distribution such that $\lambda_0/\Delta\lambda = 20$. The parameters are from numerical values set II and $f_1 = f_2/2 = 1/4$. The visibility here is 87%.

strates that a supersonic beam is sufficient to suppress dispersion effects and that less-than-exact grating periods and separations are sufficient for good localization. For completeness, in Fig. 8.15 we show the self-imaging patterns for the above velocity distribution for various grating sizes. These results are for $N_1 = 5$ up to 20, showing that the visibility at the center of the pattern changes little when the number of slits is changed. The total relative number of atoms in the unstructured wings on both sides of the fringe pattern, however, decreases linearly with grating size. Large gratings are therefore more efficient for localization. In the actual experiment we will use gratings with $N_1 \approx 100$.

These two tests clearly show that the localization effect discussed in this paper is relatively robust to deviations from the ideal case and should be clearly observable in a realistic apparatus with high atomic flux.

8.4.7 Conclusions

We have shown that, even with an extended source, atomic patterns of high contrast with sub-micrometer resolution can be produced with a simple two-grating setup, where the grating period of grating 2 is approximately half that of grating 1 and

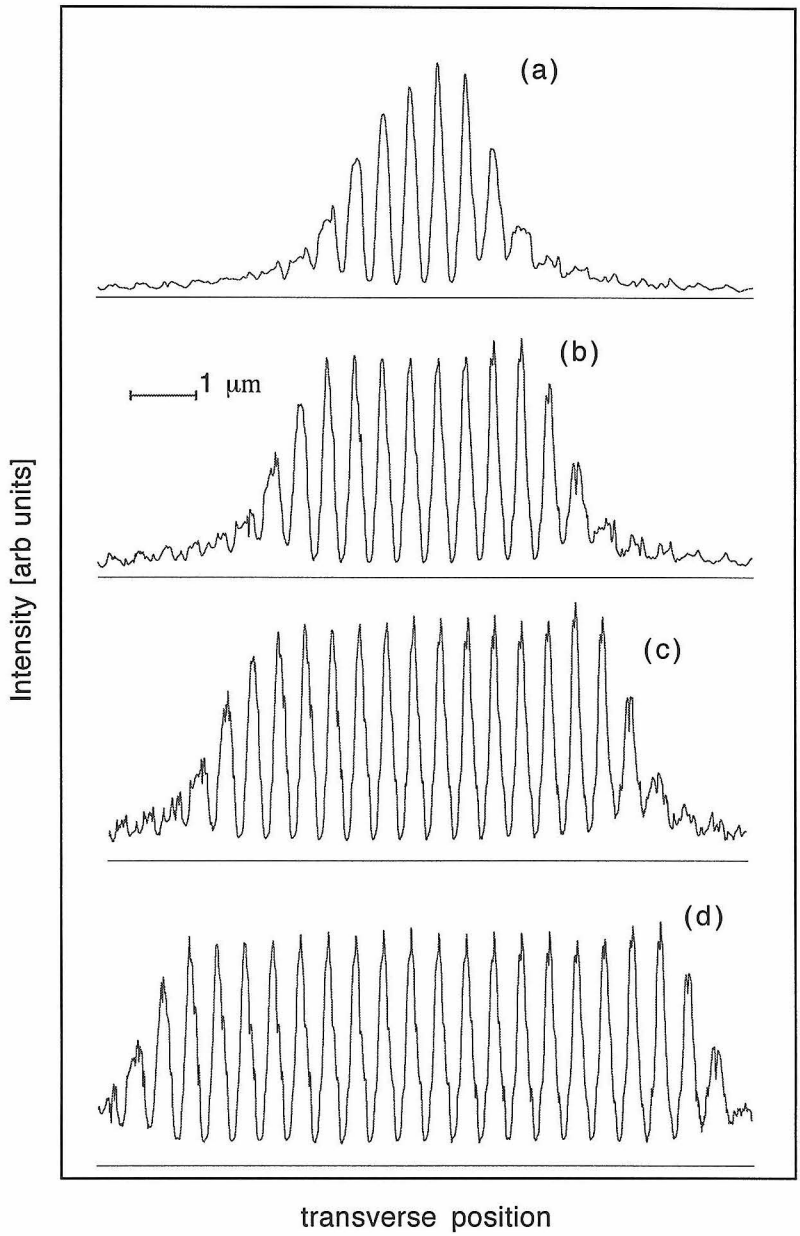

Figure 8.15: Same as in Fig. 8.14, but for a sequence of different grating sizes. a) $N_1 \approx 5$, b) 10, c) 15, d) 20. The relative number of atoms in the unstructured wings decreases with grating size, whereas the visibility stays almost constant. Note that Fig. (8.15b) is the same as Fig. (8.14).

the grating separation is approximately half the Talbot length of the first grating. This setup should not only allow significant atomic localization but should also yield high atomic fluxes and high mechanical stability due to grating separations in the centimeter range. Although we have restricted our analysis to the case of perfect rectangular gratings, the two-grating setup could also yield interesting results for phase gratings created by optical fields.

Chapter 9 Would-be cavity QED with stopped atoms

Another method at our disposal for controlling the position and timing of atoms in cavity QED makes use of a radio-frequency trapped ion. In this method, *external* rf and dc electric fields are used to confine an ion (in this case Yb II) within the cavity field. With additional and relatively straightforward laser cooling, the so-called Lamb-Dicke limit (localization to a region in space smaller than the optical wavelength) can be reached. So, independent of the cavity field, the atom will be fixed in space. If the energy spacing between levels of the trapping potential is larger than the atom-cavity interaction strength (strong confinement) (and the recoil frequency is smaller than this level spacing), then for all intents and purposes, the ion is rigidly fixed in space and will not be affected by the atom-cavity interaction.[1] This will be a valuable regime from the point of view of pure cavity QED, since it eliminates the need to use the cavity field itself as a trapping agent. One of the powers of ion-trapping is the exquisite control over the quantum-mechanical motion state, with virtually arbitrary motion state synthesis possible. With control over the external ionic wavefunction on wavelength scales, there are potentially interesting consequences of the quantization of both the internal and external degrees of freedom. In fact, it will likely be the case that in an initial demonstrative experiment, the coupling between internal and external degrees of freedom will be unavoidable, for better or for worse.

Apart from such considerations, the initial demonstration experiment will likely be something along the lines of a "one-dimensional" ion, as this is the atom-cavity parameter regime which can be accessed with present-day mirror technology. (The ionic transitions are in the near-UV.) The project is underway in a collaboration with Lute Maleki and Wo Yei of JPL.

[1] This ideal circumstance will be realized only as the mass of the ion goes to infinity.

9.1 Attainable atom-cavity parameters

9.1.1 Atom

We are using singly-ionized Ytterbium. The relevant levels are shown in Figure 9.1. The cavity QED transition will be the $4f^{14}6s\,^2S_{1/2} \rightarrow 4f^{14}6p\,^2P_{1/2}$ dipole-allowed transition at 369 nm. The lifetime of the $4f^{14}6p\,^2P_{1/2}$ state is 8 ns [246], which gives $\gamma_{\|} = 18$ MHz. Unfortunately, the excited state decays not only back to the ground state, but also to the $4f^{14}5d\,^2D_{3/2}$ level with a calculated branching ratio of 0.66 % [246]. If the ion falls into this metastable ($\tau = 52$ ms) $4f^{14}5d\,^2D_{3/2}$ state, it will be lost for an appreciable time. (Luckily, from there it is not likely to decay into the $4f^{14}6s^2\,^2F_{7/2}$ which has a measured lifetime of 10 years! [247]) The ground state can be repopulated via excitation out of the $4f^{14}5d\,^2D_{3/2}$ state to the configuration-mixing excited state $4f^{13}5d6s\,^2F_{3/2}\,^3D[1/2]_{1/2}$ at 609 nm. This (strange) excited state has a direct, fast decay channel to the ground state, with a lifetime on the order of 10 ns. There are other repopulating schemes, including driving the 2.4 μm $4f^{14}5d\,^2D_{3/2} \rightarrow 4f^{14}6p\,^2P_{1/2}$ directly [248], or by driving to another configuration mixing level ($4f^{1}35d6s\,^3D[3/2]_{1/2}$, lifetime 17–42 ns) at 935 nm [249]. The 935 nm line may be easier to reach with diode lasers than the 609 nm line.

It is somewhat unfortunate that the transition is not closed, but if we want to use a dipole transition from the ground state in Yb II, then we are stuck with the lower-lying $5d$ states. There are doubtless other good candidate ions out there, but an exhaustive search was not performed. The JPL group has experience with Yb^+ which does have several advantages. One of the advantages of this transition is its relatively long wavelength (for the primary ground-state line of an ion), which can be reached with a doubled Ti:Saph. Decent cavity mirrors are possible at 369 nm, as opposed to lines around 200 nm used in other commonly trapped species. As an added bonus, standard PMT's have excellent quantum efficiency near 400 nm.

Yb comes in a natural abundance consisting of: 3.1% ^{170}Yb, 14.3% ^{171}Yb, 21.9% ^{172}Yb, 16.2% ^{173}Yb, 31.7% ^{174}Yb, 17.7% ^{176}Yb. The even isotopes have nuclear spin $I = 0$ and are attractive since they have no hyperfine structure. ^{171}Yb has $I = 1/2$;

its simple ground-state hyperfine splitting of 12.6 GHz is considered a good candidate for a microwave clock transition [250]. ^{173}Yb has $I = 5/2$.

9.1.2 Cavity

At the 369 nm transition wavelength, mirror coatings tend to have high scattering losses, as scattering probability is inversely proportional to λ^4. The goal is, as usual to get mirrors with relatively low transmission but to keep scattering losses a small fraction of the transmission (see discussion of Section 2.1.1.1.3). With these criteria in mind, we have had $\delta_1 = \delta_2 = 200$ ppm, $\delta_0/2 = 25$ ppm mirrors manufactured. This is the smallest δ_0 we could be guaranteed which determined the choice of $\delta_{1,2}$. An initial measurement of the finesse of the cavity confirms the overall losses, though the distribution of losses has not been measured. In order to accommodate the electrodes of the ion trap, it is likely that the shortest cavity we will be able to make is on the order of 100 μm, with 3 mm substrates conically tapered to 1 mm at the mirror surface. We will use the tightest mirror radius available, which is 10 cm. These parameters give $(g_0, \gamma_\parallel, \kappa)/2\pi = (26, 18, 54)$ MHz, $(C_1, n_s) = (0.7, 0.16)$. This is state-of-the-art for a UV transition, but certainly not stellar relative to what we have seen in Parts I and II and Chapter 7. See Appendix B.1.3 for more details on the cavity and mechanical parameters for this experiment. It should be a good starting point for an experiment in which the transmission of the cavity with and without a trapped ion is monitored. Because the ion is stationary, some averaging can be used to boost S/N.

9.1.3 Trap parameters

An ion in an inhomogeneous rf electromagnetic field experiences an averaged *pseudopotential* Ψ given by [253]

$$\Psi(x, y, z) = \frac{q_e E_0(x, y, z)^2}{4m\Omega_t^2} \tag{9.1}$$

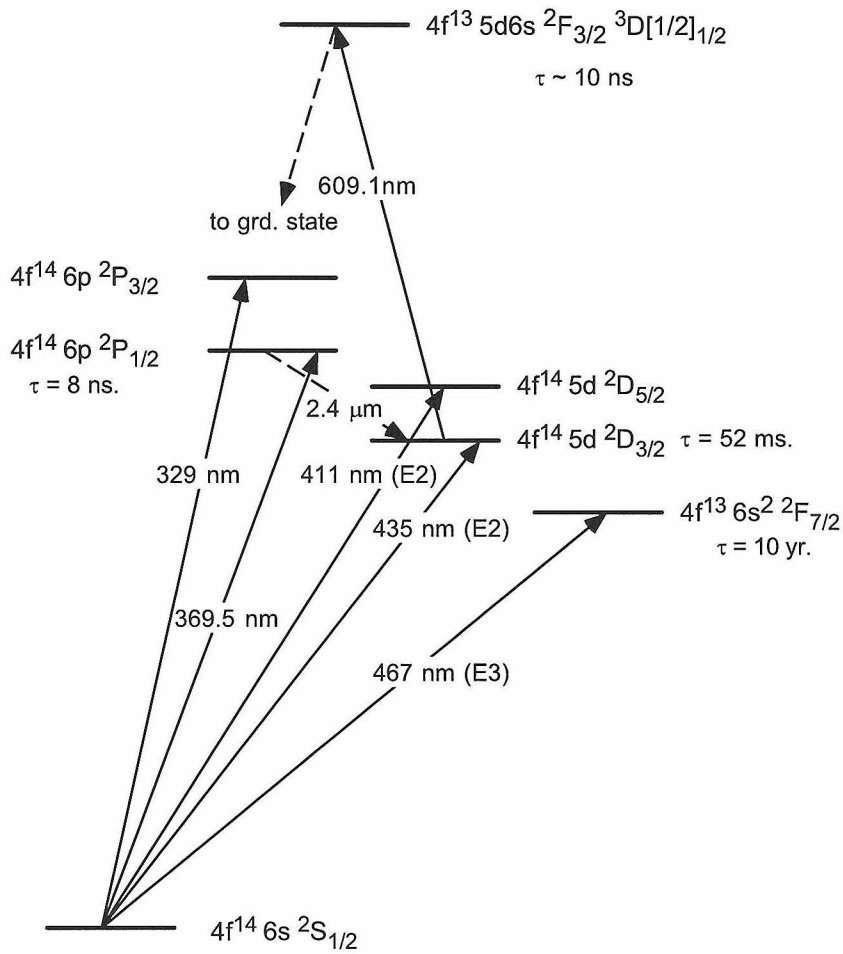

Figure 9.1: Yb^+ partial term scheme. The data are compiled from references [248, 249, 246, 251, 252, 247]. (E2): electric quadrupole transition, (E3) electric octupole transition.

where E_0 is the spatial part of the electric field which is oscillating at frequency Ω_t, q_e is the charge of the ion and m is its mass. The common configuration is for a pure quadrupolar field, in which case the pseudopotential is harmonic, with a trap *secular* frequency $2\pi\nu_{\rm trap} = (q_e^2 A_0^2/z_0^4)/(m^2\Omega_t^2)$ where A_0 is the amplitude of the applied rf potential (in Volts) and z_0 is a characteristic trap size (proportional to the spacing between trap electrodes). The size, applied trap voltage, and applied frequency are in practice determined by a stability criterion which demands that $2\pi\nu_{\rm trap}/\Omega_t \ll 1$; that is, the secular frequency should be significantly smaller than the trap drive frequency. In practice, a ratio of about 1/10 leads to a stable trap design [253, 254]. Without going to very small traps (as is done, e.g. in Ref. [255]) it is difficult to keep the secular frequency large for moderate applied voltages.

In order to obtain further estimates of secular frequencies, it is necessary to consider a specific geometry, since z_0 can be significantly different than the nominal spacing between electrodes. Let us look at the geometry in more detail. Consider the arrangement of trap electrodes in Figure 9.2, which is a simplified version of our trap. There is an applied potential either $+V$ or $-V$ at each electrode, which we take to be due to a point charge $q_{\rm eff} = \pm 4\pi\epsilon_0 V R_e$ located at the center of each electrode. (This is true for isolated electrodes, but not for the actual configuration. It is, however, a reasonable start.) The potential anywhere in the x-y plane is then given by

$$\phi(x,y) = \frac{q_{\rm eff}}{4\pi\epsilon_0}\left[\frac{1}{\sqrt{(x-a)^2+y^2}} + \frac{1}{\sqrt{(x+a)^2+y^2}} - \frac{1}{\sqrt{(y+a)^2+x^2}} - \frac{1}{\sqrt{(y-a)^2+x^2}}\right]. \tag{9.2}$$

(The anharmonic terms are down relative to the harmonic terms by a factor of 5 for distances from the center of the trap up to $a/10$.) From $\phi(x,y)$ we can find the electric field in the x and y directions, expand to first order in x and y (dropping terms that mix x and y) to find

$$E_0^2(x,y) \approx V^2 R_e^2 \left(\frac{16}{a^6}x^2 + \frac{16}{a^6}y^2\right). \tag{9.3}$$

Now if the electrodes are driven with rf, with the phase between electrodes preserved as in the figure, then this gives an harmonic pseudopotential

$$U = \frac{16 q_e V^2 R_e^2}{4 m \Omega_t^2 a^6}(x^2 + y^2) \tag{9.4}$$

and a secular frequency $2\pi\nu_{\rm trap} = (2/m)\sqrt{2} q_e V R_e/(\Omega_t a^3)$ For our configuration, $R_e \approx a/2$. With $a \approx 1$ mm the stability criterion from above gives some estimates on the attainable secular frequency: a 1 MHz secular frequency can be reached with 10 MHz drive at 500 V. In practice we will probably go to lower frequency and voltage, but I will continue to assume a 1 MHz secular frequency as the operating point. The depth of the trap (the most energetic ion that can be captured by the trap) can be taken to be $e\Psi(z_{max})$ evaluated at the edge of the trap, near the electrode (or much closer to the middle, where the trap is actually harmonic). The classical ion motion will extend to the classical turning point determined by the spring constant (or frequency for fixed mass) of the trap and the energy at which it was trapped. The depth is no more than a few tenths of an eV (0.3 eV at 100 μm), so it is difficult to trap hot ions. The Yb^+ ions are confined in the z-direction by applying the same small positive dc potential to two end-plates parallel to and above and below the x-y plane. With the cavity in place, the end-caps will be loops of wire around the mirror substrates. The cavity is oriented perpendicular to the plane of the electrodes defined in Figure 9.2.

We still need to quantify how well localized the atoms are within the trap. The Lamb-Dicke parameter is defined as[2]

$$\eta = k a_0 \quad k = 2\pi/\lambda, \tag{9.5}$$

where a_0 is the root-mean-square position extent of the quantum ground state of the harmonic well; $a_0 = \sqrt{\hbar/2m\omega_t}$, where $\omega_t = 2\pi\nu_{\rm trap}$. The goal is to get η small, so that the ion is confined to a region smaller than the optical wavelength. (Of course, a trap filled with hot ions will have a large position dispersion even if $\eta < 1$, so we also

[2]The definition of η seems to vary throughout the literature.

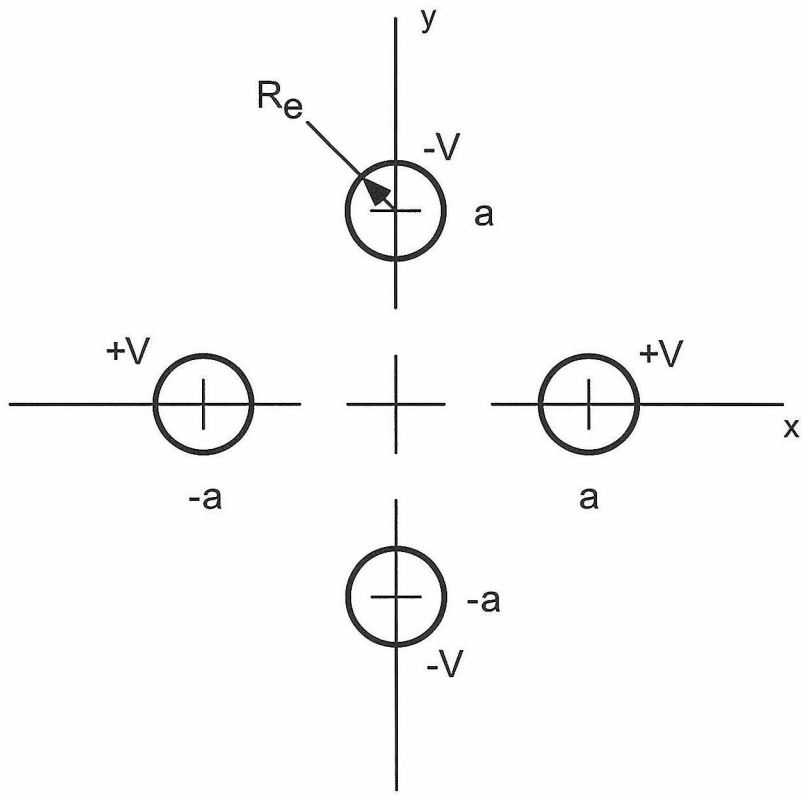

Figure 9.2: The trap electrodes, simplified. The electrodes actually extend away from the origin along all four directions $\pm x, \pm y$, and are cylindrical (see Figure 9.4).

have to cool the ions to near the ground state.) For a 1 MHz trapped Yb, $\eta \approx 0.1$.

9.1.4 Mechanical parameters

Finally, we can consider mechanical parameters of the system. Let us assume that we can trap a single ion at will, and that we can obtain a secular frequency $\nu_{\text{trap}} = 1$ MHz. This gives $\eta \approx 0.1$. Because we are in the weak-binding limit (motional sidebands not resolved on the natural linewidth, $\nu_{\text{trap}} < \gamma_{\|}$) the coldest that we can get the atoms with straightforward laser cooling is to the Doppler limit: $T_{\text{Doppler}} = \hbar\gamma_{\|}/2k_B$ which for the chosen transition (the cooling transition is the same as the cavity QED transition) is $T_{\text{doppler}} = 440\mu$K.[3] The temperature of the trap ground state $T_{\text{trap}} = \hbar\nu/k_B$ is $T_{\text{trap}} = 48$ μK, so Doppler-cooled ions will be populating at least the first 10 or so states of the trap. Laser cooling produces a thermal distribution with mean phonon number (in this case) $\bar{n}_{\text{trap}} = 9$. The position wavefunction for this situation is shown in Figure 9.3. The FWHM is reasonably well localized to the antinode of the standing wave ($\lambda/2$). This is good news for Doppler cooling, which should in principle be straightforward to achieve. In the experiment, a cycle of laser-cooling and cavity field monitoring will be needed to keep the ion confined. Cooling can be attained from a detuned cavity field, or from a beam injected through the side of the cavity.

9.2 Apparatus

We have designed an ion trap/cavity mount apparatus for this experiment, shown in Figure 9.4. The ion trap consists of an outer ring which holds four radial "pins" which form the trap rf electrodes. The end caps will be loops around the cavity mirrors. The mirrors for the cavity are mounted on supports which connect directly to the trap ring structure. The cavity mount is very similar to the design of Figure 2.2, with a different aspect ratio.

[3] Actually, since the ion will be in the cavity, it will experience an enhanced rate of spontaneous emission $\gamma_{\|}(1 + 2C_1)$, so that $T_{\text{Doppler}} \rightarrow T_{\text{Doppler}}(1 + 2C_1) \approx 900\mu$K.

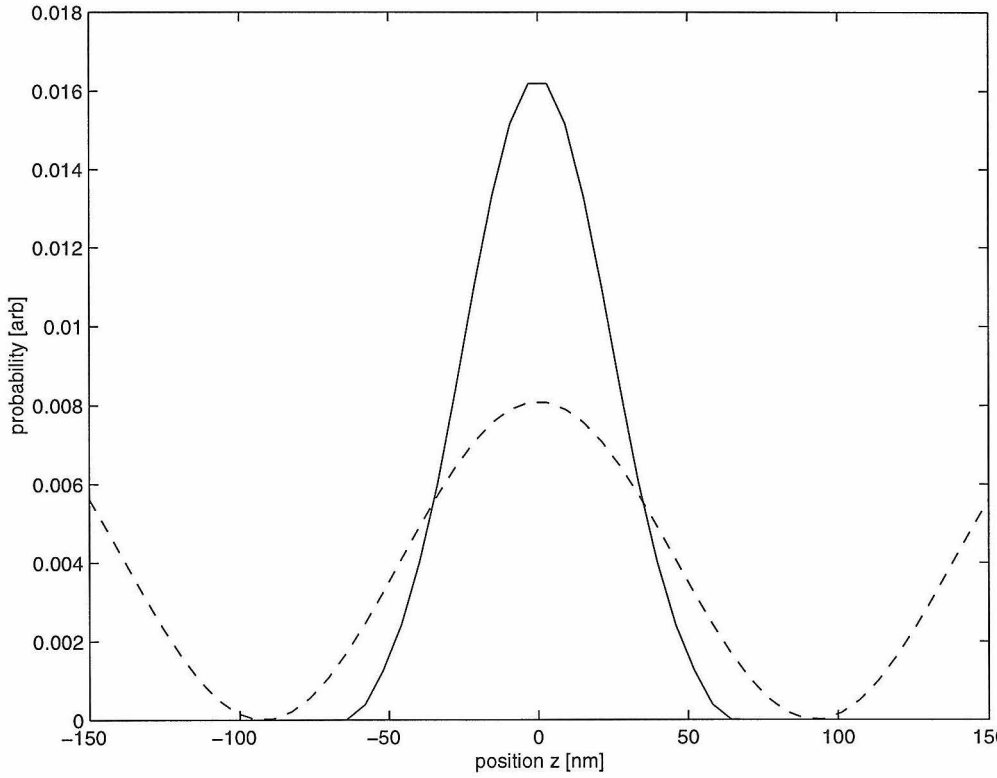

Figure 9.3: Position wavefunction for an ion cooled to a thermal state with $\bar{n} = 9, \eta = 0.03\pi, \lambda = 369$ nm. The dashed line is $\cos^2 kz$, the standing wave part of the cavity mode function. The phonon basis for the wavefunction calculation is truncated at $n_{\text{trap}} = 30$ at which point the probability of occupation is 5% of its maximum value.

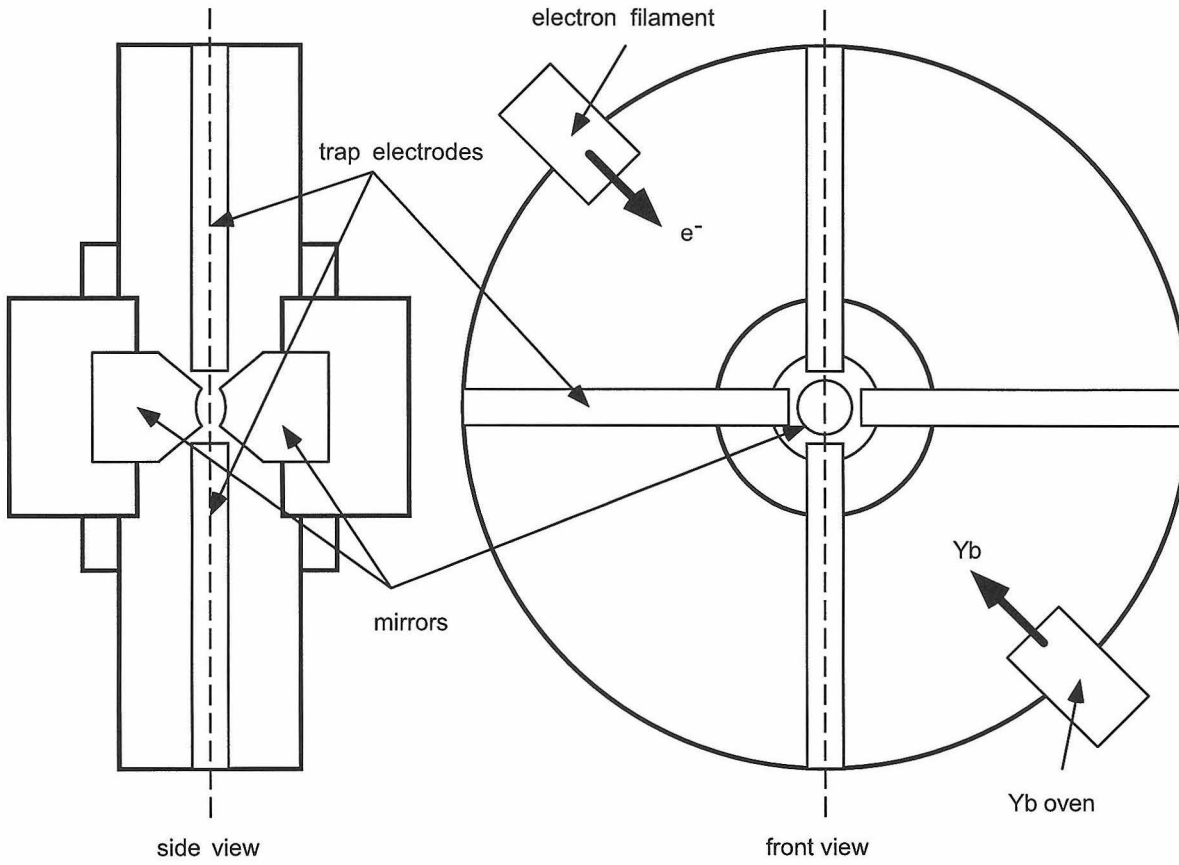

Figure 9.4: The ion-trap/cavity-mount apparatus. Not to scale. The cavity mirror substrates are 3 mm with a taper to 1 mm. The outer ring is 3 in. The trap electrodes are 1 mm across, but will eventually taper to a point 0.1 mm across. The dashed line through the "side view" indicates the plane of the "front view" cross-section and *vice versa*. The whole assembly will be in a vacuum chamber.

9.3 Some calculations on expected results

9.3.1 Fixed ion assumed

If we assume that the ion is rigidly fixed in space and that the atom-cavity interaction does not affect the motion, then all of the previous steady-state calculations are valid. In order to avoid locking the lasers and having complicated offset beams, etc., one of the easiest experiments will be to lock the cavity directly to the laser ($\omega_p = \omega_c$) and scan them both across the atomic resonance. For this arrangement of probe/cavity frequency, the probe transmission is shown in Figure 9.5. The transmission far off the atomic resonance is unity, since the probe is on the cavity resonance and the atom is effectively uncoupled. As the laser and cavity are brought near the atomic resonance, there is the characteristic dip in the probe transmission of the bad-cavity limit (note that this is not the same dip as, for example in Figure 1.3, since we are scanning *both* the probe and the cavity). In Figure 9.5 I show the transmission for two different strength drive fields. The curves are scaled so that the empty cavity in both cases is the flat line at 1 intracavity photon. The empty cavity drive for the solid curve is $n_s Y = 1$ and for the dashed curve $n_s Y = 0.001$. Thus the former is as strong a field as we are likely to use and the latter is weak field. The contrast for probe fields with intermediate power will always be less than or equal to the weak-field contrast. With a PMT dark count rate of hundreds of photons per second, and quantum efficiency $\eta_q \sim 60\%$, we should be able to resolve the transmission dip for fairly small drive fields. $\langle a^\dagger a \rangle = 1$ corresponds to an output flux of photons of $\kappa \langle a^\dagger a \rangle \approx 50 \times 10^6$ photons/sec.

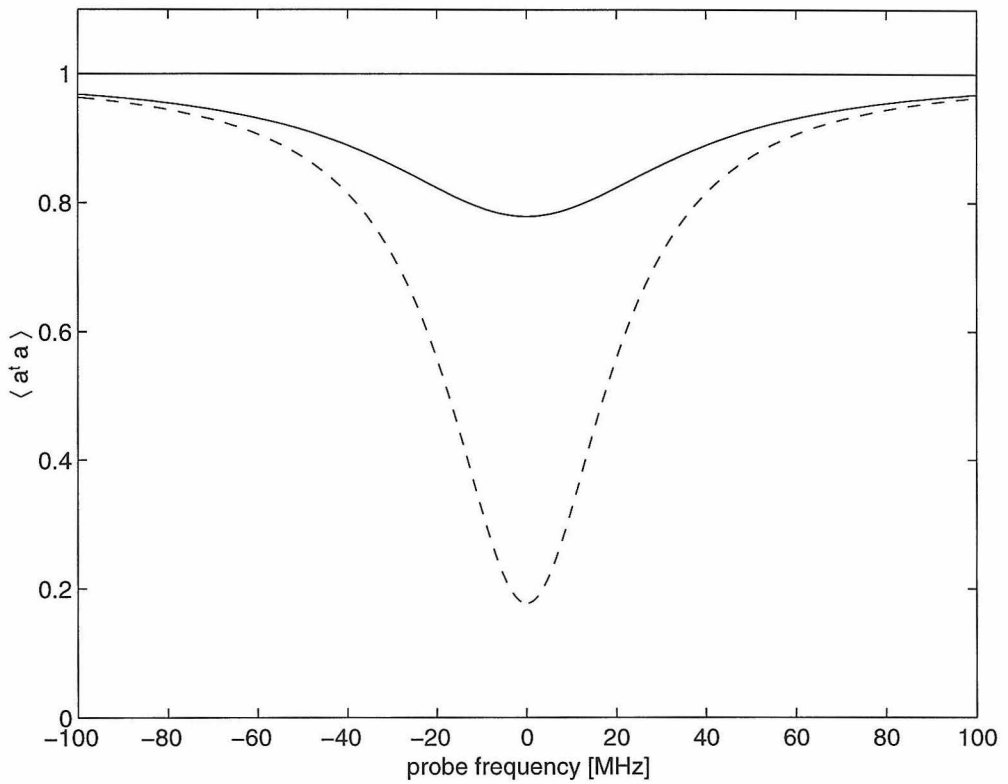

Figure 9.5: Quantum simulation of the transmission spectrum for coincident probe and cavity frequencies as the probe/cavity frequency is scanned. The solid curve is driven with $n_s Y = 1$ and the dashed curve with $n_s Y = 0.001$ and scaled by $(0.001)^{-1}$ to fit on the graph. The straight line at 1 intracavity photon is for the empty cavity. The parameters are as for the trapped-ion experiment: $(g, \gamma_{\|}, \kappa)/2\pi = (26, 18, 54)$ MHz, $(C, n_s) = (0.7, 0.16)$.

Appendix A Complicated expressions for $\gamma_{x,y,z}$ and $\Omega_{y,z}$

The expressions for $\gamma_{x,y,z}$ and $\Omega_{y,z}$ for the case of finite bandwidth squeezing that I promised in Section 3.2.2.2 follow. They are taken verbatim from a letter that Scott Parkins sent me, which begins at the next paragraph break. Note that Scott includes the effects of transit broadening by a modification of $\gamma_\perp \rightarrow \gamma_\parallel/2\,(1+2C) + \gamma_{\text{transit}}$. For the figure of Section 3.3.4 in which theory is compared to data (Fig. 3.24), a value of $\gamma_{\text{transit}} = 0.215\gamma_\parallel$ is used. In what follows, $\gamma \equiv \gamma_\parallel$. I am certainly not fully versed in the techniques involved, but briefly the expressions come from the following: There are a full set of stochastic Heisenberg equations for the evolution of the squeezing, cavity and atomic operators. The field mode is adiabatically eliminated as in the discussion of the bad-cavity limit in Section 1.3.2.1 to reduce these to a set of stochastic differential equations in the squeezing and atomic operators. Then a so-called decorrelation approximation [79] in which the noise (squeezing) operators and the atomic operators are factored upon averaging is applied. This allows some complicated integrals to be solved, truncates the hierarchy of operator moments and results in the OBEs for the atomic operators only (Eqs. 3.23) with the modified parameters that Scott has derived. Scott has compared this approximate treatment with an numerical integration of the full quantum master equation for the OPO/1-D atom system, and finds that the two approaches agree fairly well. In fact, the decorrelation approximation tends to underestimate the size of the modulation of the transmitted probe.

Here are the expressions for $\gamma_{x,y,z}$ and $\Omega_{y,z}$. Remember, they are derived under the assumption that Ω is sufficiently large that the parameter p is complex (note that

the $\gamma_{x,y,z}$ and $\Omega_{y,z}$ given below are all real). For completeness,

$$\lambda_\pm = -\frac{3}{4}\gamma(1+2C) - \frac{1}{2}\gamma_{\rm tr} \pm \frac{1}{2}p\,, \quad p = \sqrt{[(\gamma/2)(1+2C)-\gamma_{\rm tr}]^2 - 4\Omega^2}\,. \tag{A.1}$$

The coefficients are

$$\begin{aligned}
\gamma_x &= \frac{1}{2}\gamma(1+2C) + \gamma_{\rm tr} \\
&\quad +2\gamma C\eta(N \mp M)\frac{1}{p}b_\pm \times \\
&\quad \left[-\frac{\lambda_+ + (\gamma/2)(1+2C)+\gamma_{\rm tr}}{\lambda_+ - b_\pm} + \frac{\lambda_- + (\gamma/2)(1+2C)+\gamma_{\rm tr}}{\lambda_- - b_\pm}\right]
\end{aligned} \tag{A.2}$$

$$\begin{aligned}
\gamma_y &= \frac{1}{2}\gamma(1+2C) + \gamma_{\rm tr} \\
&\quad +\gamma C\eta(N \pm M)\frac{\Omega}{ip}b_\mp \times \\
&\quad \left[-\frac{1}{\lambda_+ - b_\mp + p/2} + \frac{1}{\lambda_+ - b_\mp - p/2} + \frac{1}{\lambda_- - b_\mp + p/2} - \frac{1}{\lambda_- - b_\mp - p/2}\right] \\
&\quad +\gamma C\eta(N \pm M)\frac{1}{p}b_\mp \times \\
&\quad \left\{-\left[\lambda_+ + (\gamma/2)(1+2C)+\gamma_{\rm tr}\right]\left(\frac{1}{\lambda_+ - b_\mp + p/2} + \frac{1}{\lambda_+ - b_\mp - p/2}\right)\right. \\
&\quad \left. + \left[\lambda_- + (\gamma/2)(1+2C)+\gamma_{\rm tr}\right]\left(\frac{1}{\lambda_- - b_\mp + p/2} + \frac{1}{\lambda_- - b_\mp - p/2}\right)\right\}
\end{aligned} \tag{A.3}$$

$$\begin{aligned}
\gamma_z &= \gamma(1+2C) \\
&\quad +\gamma C\eta(N \pm M)\frac{1}{p}b_\mp \times \\
&\quad \left\{-\left[\lambda_+ + (\gamma/2)(1+2C)+\gamma_{\rm tr}\right]\left(\frac{1}{\lambda_- - b_\mp + p/2} + \frac{1}{\lambda_- - b_\mp - p/2}\right)\right. \\
&\quad \left. + \left[\lambda_- + (\gamma/2)(1+2C)+\gamma_{\rm tr}\right]\left(\frac{1}{\lambda_+ - b_\mp + p/2} + \frac{1}{\lambda_+ - b_\mp - p/2}\right)\right\} \\
&\quad -\gamma C\eta(N \pm M)\frac{\Omega}{ip}b_\mp \times
\end{aligned}$$

$$\left(\frac{1}{\lambda_+ - b_\mp + p/2} - \frac{1}{\lambda_+ - b_\mp - p/2} - \frac{1}{\lambda_- - b_\mp + p/2} + \frac{1}{\lambda_- - b_\mp - p/2}\right)$$
$$+\gamma C\eta(N \mp M) b_\pm \times$$
$$\left\{\frac{1}{[(\gamma/2)(1+2C)+\gamma_{\rm tr}] + b_\pm - (p/2)} + \frac{1}{[(\gamma/2)(1+2C)+\gamma_{\rm tr}] + b_\pm + (p/2)}\right\} \tag{A.4}$$

$$\begin{aligned}
\Omega_z \;=\; & \Omega \\
& -\gamma C\eta(N \pm M)\frac{\Omega}{p} b_\mp \times \\
& \left[-\frac{1}{\lambda_+ - b_\mp + p/2} - \frac{1}{\lambda_+ - b_\mp - p/2} + \frac{1}{\lambda_- - b_\mp + p/2} + \frac{1}{\lambda_- - b_\mp - p/2}\right] \\
& +\gamma C\eta(N \pm M)\frac{1}{ip} b_\mp \times \\
& \left\{-[\lambda_+ + (\gamma/2)(1+2C) + \gamma_{\rm tr}]\left(\frac{1}{\lambda_+ - b_\mp + p/2} - \frac{1}{\lambda_+ - b_\mp - p/2}\right)\right. \\
& \left. + [\lambda_- + (\gamma/2)(1+2C) + \gamma_{\rm tr}]\left(\frac{1}{\lambda_- - b_\mp + p/2} - \frac{1}{\lambda_- - b_\mp - p/2}\right)\right\}
\end{aligned} \tag{A.5}$$

$$\begin{aligned}
\Omega_y \;=\; & \Omega \\
& +\gamma C\eta(N \pm M)\frac{1}{ip} b_\mp \times \\
& \left\{-[\lambda_+ + (\gamma/2)(1+2C) + \gamma_{\rm tr}]\left(\frac{1}{\lambda_- - b_\mp + p/2} - \frac{1}{\lambda_- - b_\mp - p/2}\right)\right. \\
& \left. + [\lambda_- + (\gamma/2)(1+2C) + \gamma_{\rm tr}]\left(\frac{1}{\lambda_+ - b_\mp + p/2} - \frac{1}{\lambda_+ - b_\mp - p/2}\right)\right\} \\
& +\gamma C\eta(N \pm M)\frac{\Omega}{p} b_\mp \times \\
& \left(\frac{1}{\lambda_+ - b_\mp + p/2} + \frac{1}{\lambda_+ - b_\mp - p/2} - \frac{1}{\lambda_- - b_\mp + p/2} - \frac{1}{\lambda_- - b_\mp - p/2}\right) \\
& -\gamma C\eta(N \mp M) i b_\pm \times \\
& \left\{\frac{1}{[(\gamma/2)(1+2C)+\gamma_{\rm tr}] + b_\pm - (p/2)} - \frac{1}{[(\gamma/2)(1+2C)+\gamma_{\rm tr}] + b_\pm + (p/2)}\right\}.
\end{aligned} \tag{A.6}$$

These expressions can be further manipulated to eliminate some factors, etc., but the resulting forms are probably not much more enlightening than those above.

Appendix B Experimental parameters code

B.1 Cavity Parameters: cavityq.mcd

B.1.1 The bad cavity

Units: $nm := 10^{-9}\cdot m$ $\mu m := 10^{-6}\cdot m$ $ppm := 10^{-6}$ $cm := 10^{-2}\cdot m$ $\mu s := 10^{-6}\cdot sec$ $ns := 10^{-9}\cdot sec$

Constants:

$\lambda := 852\cdot nm$ $c := 2.99\cdot 10^{8}\cdot\frac{m}{sec}$ $\gamma_{parl} := 2\cdot\pi\cdot 5\cdot 10^{6}\cdot\frac{rad}{sec}$ $\Gamma := 1$ $\gamma_{perp} := \frac{\gamma_{parl}}{2\cdot\Gamma}$

mirror properties:

$\delta_0 := 2\cdot ppm$ $\delta_1 := 1\cdot ppm$ $\delta_2 := 350\cdot ppm$ $\delta_c := \delta_0 + \delta_1 + \delta_2$ $\frac{1}{\gamma_{parl}} = 31.831\cdot ns$

$R_1 := 100\cdot cm$ $R_2 := 45\cdot cm$ $r := 3.5\cdot mm$

Cavity properties:

$l := 56\cdot\mu m$ $g_1 := 1 - \frac{l}{R_1}$ $g_2 := 1 - \frac{l}{R_2}$ $g_1 = 0.9999440000$ $g_2 = 0.9998755556$

(transverse mode spacing)

$TMS := \frac{acos\left(\sqrt{g_1\cdot g_2}\right)}{\pi}\cdot\frac{2\cdot\pi\cdot c}{2\cdot l}$

$\frac{TMS}{2\cdot\pi} = 11.415\cdot GHz$

the indentation of the mirrors:

$indent_1 := R_1 - \sqrt{R_1^2 - r^2}$ $indent_1 = 6.125\cdot\mu m$

$indent_2 := R_2 - \sqrt{R_2^2 - r^2}$ $indent_2 = 13.611\cdot\mu m$

$gap := l - indent_1 - indent_2$ $gap = 36.264\cdot\mu m$

cavity transmission and reflection:

$I_{trans} := \frac{4\cdot\delta_1\cdot\delta_2}{\delta_c^2}$ $I_{trans} = 0.011$

$I_{refl1} := \frac{\left(\delta_2 + \delta_0 - \delta_1\right)^2}{\delta_c^2}$ $I_{refl1} = 0.989$

$I_{refl2} := \frac{\left(\delta_1 + \delta_0 - \delta_2\right)^2}{\delta_c^2}$ $I_{refl2} = 0.966$

circulating intensity

$I_{circ1} := \frac{4\cdot\delta_1}{\delta_c^2}$ $I_{circ1} = 32.1$

$I_{circ2} := \frac{4\cdot\delta_2}{\delta_c^2}$ $I_{circ2} = 1.124\cdot 10^{4}$

cavity parameters:

$F := \frac{2\cdot\pi}{\delta_c}$ $FSR := \frac{c}{2\cdot l}$ $\kappa := \pi\cdot\frac{FSR}{F}$ $w_0 := \sqrt{\frac{l\cdot\lambda}{\pi}\cdot\sqrt{\frac{g_1\cdot g_2\cdot\left(1 - g_1\cdot g_2\right)}{\left(g_1 + g_2 - 2\cdot g_1\cdot g_2\right)^2}}}$ $V_m := \frac{\pi}{4}\cdot w_0^2\cdot l$

$F = 1.78\cdot 10^{4}$ $FSR = 2.67\cdot 10^{3}\cdot GHz$ $\frac{\kappa}{2\cdot\pi} = 74.993\cdot MHz$ $V_m = 4.972\cdot 10^{4}\cdot\mu m^3$

$w_0 = 33.624\cdot\mu m$

the next longitudinal mode

$$\left(\frac{c}{\lambda} + FSR\right)^{-1} \cdot c = 845.568 \cdot nm$$

atomic CQED parameters:

$$g := \sqrt{3 \cdot \frac{c}{8} \cdot \frac{\lambda^2}{\pi} \cdot \frac{\gamma_{parl}}{V_m}} \qquad C_1 := \frac{g^2}{2 \cdot \kappa \cdot \gamma_{perp}} \qquad n_s := \frac{2 \cdot \gamma_{perp} \cdot \gamma_{parl}}{3 \cdot g^2}$$

$$\frac{g}{2 \cdot \pi} = 20.362 \cdot MHz \qquad C_1 = 1.106 \qquad n_s = 0.02$$

$$\frac{1}{C_1} = 0.904$$

quality factor

additional stuff:

$$Q := \frac{2 \cdot \pi \cdot 2 \cdot l}{\lambda} \cdot \frac{1}{\delta_c} \qquad Q = 2.34 \cdot 10^6$$

$$\frac{1}{(1 + 2 \cdot C_1)^2} = 0.09696 \qquad \frac{g}{\gamma_{perp}} = 8.145 \qquad \frac{1}{g} = 7.816 \cdot ns \qquad \frac{1}{\kappa} = 2.122 \cdot ns$$

rate of spontaneous emmision to various places

$$rate_{cavity} := \frac{g^2}{\kappa} \qquad rate_{total} := \gamma_{perp} \cdot (1 + 2 \cdot C_1) \qquad \beta := \frac{rate_{cavity}}{rate_{total}}$$

$$\frac{rate_{cavity}}{2 \cdot \pi} = 5.529 \cdot MHz \qquad \frac{rate_{total}}{2 \cdot \pi} = 8.029 \cdot MHz \qquad \beta = 0.689$$

more units: $\mu K := 10^{-6} \cdot K$ $\qquad k := \frac{2 \cdot \pi}{\lambda}$ $\qquad eV := 1.602 \cdot 10^{-19} \cdot joule$ $\qquad gram := 10^{-3} \cdot kg$

constants:

$$k_B := 1.380658 \cdot 10^{-23} \cdot \frac{joule}{K} \qquad N_A := 6.0221367 \cdot 10^{23} \qquad m_{Cs} := \frac{133 \cdot gram}{N_A}$$

$$\varepsilon_0 := 8.854 \cdot 10^{-12} \cdot sec^2 \cdot \frac{coul^2}{kg \cdot m^3} \qquad hbar := \frac{6.6260755 \cdot 10^{-34} \cdot joule \cdot sec}{2 \cdot \pi} \qquad m_{Cs} = 0 \cdot kg$$

energy:

$$hbar \cdot g = 8.422 \cdot 10^{-8} \cdot eV \qquad hbar \cdot k = 0 \cdot kg \cdot m \cdot sec^{-1}$$

$$\nu := \frac{c}{\lambda} \qquad \nu = 3.5094 \cdot 10^8 \cdot MHz \qquad \omega := 2 \cdot \pi \cdot \nu$$

$$hbar \cdot \omega = 1.452 \cdot eV$$

electric field per photon $E := \sqrt{\frac{hbar \cdot \omega}{2 \cdot \varepsilon_0 \cdot V_m}}$ $\qquad E = 513.895 \cdot \frac{volt}{m}$ $\qquad E_{phot} := hbar \cdot 2 \cdot \pi \cdot \frac{c}{\lambda}$ $\qquad E_{phot} = 1.452 \cdot eV$

$pW := 10^{-12} \cdot watt$

for intracavity photon number of 0.1 $n := 10^{-4}$

the rate out the back side is

$R := \frac{c}{2 \cdot l} \cdot \delta_2$ $n \cdot R = 9.344 \cdot 10^4 \cdot sec^{-1}$

$R \cdot E_{phot} = 217.275 \cdot pW$

this corresponds to

$n \cdot R \cdot E_{phot} = 0.022 \cdot pW$

to attain the same intracavity photon number by driving from the backside, we need to put in 1/4(1+2*C)^2 of the power that is transmitted (see notes of 10-19-96)

$nsc := -4, -3.9 .. 0$

$nsc10(nsc) := 10^{nsc}$

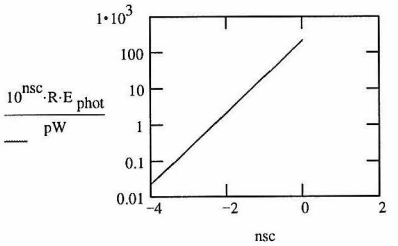

$F_b := \frac{(1 + 2 \cdot C_1)^2}{4}$

$n_s \cdot F_b \cdot R \cdot E_{phot} = 11.26 \cdot pW$

B.1.2 The falling atoms cavity

Units: $nm := 10^{-9}\cdot m$ $\mu m := 10^{-6}\cdot m$ $ppm := 10^{-6}$ $cm := 10^{-2}\cdot m$ $\mu s := 10^{-6}\cdot sec$ $ns := 10^{-9}\cdot sec$

Constants:

$\lambda := 852\cdot nm$ $c := 2.99\cdot 10^{8}\cdot\frac{m}{sec}$ $\gamma_{parl} := 2\cdot\pi\cdot 5\cdot 10^{6}\cdot\frac{rad}{sec}$ $\Gamma := 1$ $\gamma_{perp} := \frac{\gamma_{parl}}{2\cdot\Gamma}$

mirror properties:

$\delta_0 := 2\cdot ppm$ $\delta_1 := 15\cdot ppm$ $\delta_2 := 15\cdot ppm$ $\delta_c := \delta_0 + \delta_1 + \delta_2$ $\frac{1}{\gamma_{parl}} = 31.8310\cdot ns$

$R_1 := 100\cdot cm$ $R_2 := 100\cdot cm$ $r := 1.5\cdot mm$

Cavity properties:

$l := 108\cdot\mu m$ $g_1 := 1 - \frac{l}{R_1}$ $g_2 := 1 - \frac{l}{R_2}$ $g_1 = 0.9998920000$ $g_2 = 0.9998920000$

the indentation of the mirrors:

$indent_1 := R_1 - \sqrt{R_1^2 - r^2}$ $indent_1 = 1.1250\cdot\mu m$

$indent_2 := R_2 - \sqrt{R_2^2 - r^2}$ $indent_2 = 1.1250\cdot\mu m$

$gap := l - indent_1 - indent_2$ $gap = 105.7500\cdot\mu m$

(transverse mode spacing)

$TMS := \frac{acos\left(\sqrt{g_1\cdot g_2}\right)}{\pi}\cdot\frac{2\cdot\pi\cdot c}{2\cdot l}$

$\frac{TMS}{2\cdot\pi} = 6.4759\cdot GHz$

cavity transmission and reflection:

$I_{trans} := \frac{4\cdot\delta_1\cdot\delta_2}{\delta_c^2}$ $I_{trans} = 0.8789$

$I_{refl1} := \frac{\left(\delta_2 + \delta_0 - \delta_1\right)^2}{\delta_c^2}$ $I_{refl1} = 3.9063\cdot 10^{-3}$

$I_{refl2} := \frac{\left(\delta_1 + \delta_0 - \delta_2\right)^2}{\delta_c^2}$ $I_{refl2} = 3.9063\cdot 10^{-3}$

cavity parameters:

$F := \frac{2\cdot\pi}{\delta_c}$ $FSR := \frac{c}{2\cdot l}$ $\kappa := \pi\cdot\frac{FSR}{F}$ $w_0 := \sqrt{\frac{l\cdot\lambda}{\pi}\cdot\sqrt{\frac{g_1\cdot g_2\cdot\left(1 - g_1\cdot g_2\right)}{\left(g_1 + g_2 - 2\cdot g_1\cdot g_2\right)^2}}}$ $V_m := \frac{\pi}{4}\cdot w_0^2\cdot l$

$F = 1.9635\cdot 10^{5}$ $FSR = 1.3843\cdot 10^{3}\cdot GHz$ $\frac{\kappa}{2\cdot\pi} = 3.5250\cdot MHz$ $V_m = 1.6904\cdot 10^{5}\cdot\mu m^3$

$w_0 = 44.6414\cdot\mu m$

atomic CQED parameters:

$g := \sqrt{3\cdot\frac{c}{8}\cdot\frac{\lambda^2}{\pi}\cdot\frac{\gamma_{parl}}{V_m}}$ $C_1 := \frac{g^2}{2\cdot\kappa\cdot\gamma_{perp}}$ $n_s := \frac{2\cdot\gamma_{perp}\cdot\gamma_{parl}}{3\cdot g^2}$ $n_{sb1} := \frac{\gamma_{perp}\cdot\gamma_{parl}}{4\cdot g^2}$

$\frac{g}{2\cdot\pi} = 11.0438\cdot MHz$ $C_1 = 6.9200$ $n_s = 0.0683$ $n_{sb1} = 0.0256$

additional stuff:

$$\frac{1}{(1+2\cdot C_1)^2} = 4.54080\cdot 10^{-3} \qquad \frac{g}{\gamma_{perp}} = 4.4175 \qquad \frac{1}{g} = 14.4113\cdot ns$$

$$\frac{1}{\kappa} = 45.1505\cdot ns$$

the next longitudinal mode

$$\left(\frac{c}{\lambda} + FSR\right)^{-1}\cdot c = 848.6525\cdot nm$$

Mechanical parameters

units: $\mu K := 10^{-6}\cdot K$ $k := \frac{2\cdot\pi}{\lambda}$ $eV := 1.602\cdot 10^{-19}\cdot joule$ $gram := 10^{-3}\cdot kg$

constants: $k_B := 1.380658\cdot 10^{-23}\cdot\frac{joule}{K}$ $N_A := 6.0221367\cdot 10^{23}$ $m_{Cs} := \frac{133\cdot gram}{N_A}$

$\varepsilon_0 := 8.854\cdot 10^{-12}\cdot sec^2\cdot\frac{coul^2}{kg\cdot m^3}$ $hbar := \frac{6.6260755\cdot 10^{-34}\cdot joule\cdot sec}{2\cdot\pi}$ $m_{Cs} = 2.2085\cdot 10^{-25}\cdot kg$

velocities: $T_{doppler} := \frac{hbar\cdot\gamma_{parl}}{2\cdot k_B}$ $T_{doppler} = 119.9804\cdot\mu K$ $\frac{1}{2}\cdot a_g\cdot t^2 + v_0\cdot t - d$

$$v_t := \frac{1}{1}\cdot\sqrt{\frac{2\cdot k_B\cdot T_{doppler}}{m_{Cs}}} \qquad v_t = 12.2479\cdot\frac{cm}{sec} \qquad v_t = 0.1225\cdot\frac{\mu m}{\mu s}$$

$$\begin{bmatrix} \frac{1}{a_g}\cdot\left(-v_0 + \sqrt{v_0^2 + 2\cdot a_g\cdot d}\right) \\ \frac{1}{a_g}\cdot\left(-v_0 - \sqrt{v_0^2 + 2\cdot a_g\cdot d}\right) \end{bmatrix}$$

$d := 7\cdot mm$ $a_g := 9.8\cdot\frac{m}{sec^2}$ $\frac{\lambda}{2\cdot v_t} = 3.4781\cdot\mu s$

$$t_d := \frac{1}{a_g}\cdot\left(-v_t + \sqrt{v_t^2 + 2\cdot a_g\cdot d}\right) \qquad t_d = 0.0273\cdot sec$$

$$v_f := v_t + a_g\cdot t_d \qquad v_f = 39.0130\cdot\frac{cm}{sec}$$

$$\tau := \frac{2\cdot w_0}{v_f} \qquad \tau = 228.8540\cdot\mu s \qquad \frac{\tau^{-1}}{2\cdot\pi} = 6.9544\cdot 10^{-4}\cdot MHz \qquad g\cdot\tau = 5.0548\cdot 10^3\cdot\pi$$

energy:

$k_B\cdot T_{doppler} = 1.03403\cdot 10^{-8}\cdot eV$ $hbar\cdot g = 4.5678\cdot 10^{-8}\cdot eV$ $\frac{1}{2}\cdot m_{Cs}\cdot v_f^2 = 1.0491\cdot 10^{-7}\cdot eV$

recoil velocity

$\frac{hbar \cdot k}{m_{Cs}} = 3.5214 \cdot \frac{mm}{sec}$ $v_{recoil} := \frac{hbar \cdot k}{m_{Cs}}$ $g \cdot \tau = 5.0548 \cdot 10^{3} \cdot \pi$

"recoil frequency"

$\Omega_r := \frac{hbar \cdot k^2}{2 \cdot m_{Cs}}$

$hbar \cdot k = 7.7771 \cdot 10^{-28} \cdot kg \cdot m \cdot sec^{-1}$ $\nu := \frac{c}{\lambda}$ $\nu = 3.5094 \cdot 10^{8} \cdot MHz$

$\frac{\Omega_r}{2 \cdot \pi} = 2.0666 \cdot 10^{-3} \cdot MHz$

$\omega := 2 \cdot \pi \cdot \nu$

$hbar \cdot \omega = 1.4515 \cdot eV$ electric field $E := \sqrt{\frac{hbar \cdot \omega}{2 \cdot \varepsilon_0 \cdot V_m}}$ $E = 278.7180 \cdot \frac{volt}{m}$

$v_{recoil} \cdot \frac{1}{\gamma_{parl}} = 0.1121 \cdot nm$ $v_{recoil} \cdot \frac{1}{g} = 0.0507 \cdot nm$ $\frac{v_{recoil}}{\lambda} = 4.1331 \cdot KHz$

$\tau \cdot \gamma_{parl} = 7.1897 \cdot 10^{3}$ $\tau \cdot g = 1.5880 \cdot 10^{4}$ $\lambda \cdot 1 \cdot MHz = 85.2000 \cdot \frac{cm}{sec}$

standard quantum limit on position:

$v_{trans} := 1 \cdot \frac{cm}{sec}$ $B := 1000 \cdot Hz$ $\tau_{measB} := \frac{1}{B}$ $\tau_{measB} = 1.0000 \cdot 10^{-3} \cdot sec$

must guarantee with a given transverse velocity that the atom has not moved off a standing wave in the measurement time. this puts a limit of:

$\tau_{meas} := \left(\frac{\lambda}{8 \cdot v_{trans}} \right)$ $\tau_{meas} = 10.6500 \cdot \mu s$ $\frac{1}{\tau_{meas}} = 9.3897 \cdot 10^{4} \cdot Hz$

thus we need a bandwidth of at least 100 kHz and the SQL is:

$\delta x_{sql} := \sqrt{\frac{hbar \cdot \tau_{meas}}{m_{Cs}}}$ $\delta x_{sql} = 71.3120 \cdot nm$ $(\lambda/16)$

B.1.3 The proposed ion trap cavity

Units: $nm := 10^{-9}\cdot m$ $\mu m := 10^{-6}\cdot m$ $ppm := 10^{-6}$ $cm := 10^{-2}\cdot m$ $\mu s := 10^{-6}\cdot sec$ $ns := 10^{-9}\cdot sec$

Constants:

$\lambda := 369\cdot nm$ $c := 2.99\cdot 10^{8}\cdot \frac{m}{sec}$ $\tau_P := 8.8\cdot ns$ $\gamma_{parl} := \frac{1}{\tau_P}$ $\Gamma := 1$ $\gamma_{perp} := \frac{\gamma_{parl}}{2\cdot\Gamma}$

mirror properties:

$\delta_0 := 50\cdot ppm$ $\delta_1 := 200\cdot ppm$ $\delta_2 := 200\cdot ppm$ $\delta_c := \delta_0 + \delta_1 + \delta_2$ $\frac{\gamma_{parl}}{2\cdot\pi} = 18.0858\cdot MHz$

$R_1 := 10\cdot cm$ $R_2 := 10\cdot cm$ $r := \frac{1}{2}\cdot mm$

Cavity properties:

$l := 100\cdot\mu m$ $g_1 := 1 - \frac{l}{R_1}$ $g_2 := 1 - \frac{l}{R_2}$ $g_1 = 0.9990000000$ $g_2 = 0.9990000000$

the indentation of the mirrors:

(transverse mode spacing)

$TMS := \frac{\operatorname{acos}\left(\sqrt{g_1\cdot g_2}\right)}{\pi}\cdot\frac{2\cdot\pi\cdot c}{2\cdot l}$

$\frac{TMS}{2\cdot\pi} = 21.2835\cdot GHz$

$indent_1 := R_1 - \sqrt{R_1^2 - r^2}$ $indent_1 = 1.2500\cdot\mu m$

$indent_2 := R_2 - \sqrt{R_2^2 - r^2}$ $indent_2 = 1.2500\cdot\mu m$

$gap := l - indent_1 - indent_2$ $gap = 97.5000\cdot\mu m$

cavity transmission and reflection:

$I_{trans} := \frac{4\cdot\delta_1\cdot\delta_2}{\delta_c^2}$ $I_{trans} = 0.7901$

$I_{refl1} := \frac{\left(\delta_2 + \delta_0 - \delta_1\right)^2}{\delta_c^2}$ $I_{refl1} = 0.0123$

$I_{refl2} := \frac{\left(\delta_1 + \delta_0 - \delta_2\right)^2}{\delta_c^2}$ $I_{refl2} = 0.0123$

cavity parameters:

$F := \frac{2\cdot\pi}{\delta_c}$ $FSR := \frac{c}{2\cdot l}$ $\kappa := \pi\cdot\frac{FSR}{F}$ $w_0 := \sqrt{\frac{l\cdot\lambda}{\pi}\cdot\sqrt{\frac{g_1\cdot g_2\cdot\left(1 - g_1\cdot g_2\right)}{\left(g_1 + g_2 - 2\cdot g_1\cdot g_2\right)^2}}}$ $V_m := \frac{\pi}{4}\cdot w_0^2\cdot l$

$F = 1.3963\cdot 10^4$ $FSR = 1.4950\cdot 10^3\cdot GHz$ $\frac{\kappa}{2\cdot\pi} = 53.5357\cdot MHz$ $V_m = 2.0623\cdot 10^4\cdot\mu m^3$

$w_0 = 16.2042\cdot\mu m$

atomic CQED parameters:

$g := \sqrt{3\cdot\frac{c}{8}\cdot\frac{\lambda^2}{\pi}\cdot\frac{\gamma_{parl}}{V_m}}$ $\frac{g}{2\cdot\pi} = 26.0441\cdot MHz$

$C_1 := \frac{g^2}{2\cdot\kappa\cdot\gamma_{perp}}$ $C_1 = 0.7005$

$n_s := \frac{2\cdot\gamma_{perp}\cdot\gamma_{parl}}{3\cdot g^2}$ $n_s = 0.1607$

$n_{sb1} := \frac{\gamma_{perp}\cdot\gamma_{parl}}{4\cdot g^2}$ $n_{sb1} = 0.0603$

Q. Turchette
cavityqmYb.MCD
*e4pt 07:34

additional stuff:

$$\frac{1}{\left(1+2\cdot C_1\right)^2}=0.17345 \qquad \frac{g}{\gamma_{perp}}=2.8801 \qquad \frac{1}{g}=6.1110\cdot ns$$

$$d\lambda := \lambda^2\cdot\frac{FSR}{c} \qquad \frac{1}{\kappa}=2.9729\cdot ns$$

$$d\lambda = 0.6808\cdot nm$$

Mechanical parameters

units: $\mu K := 10^{-6}\cdot K$ $\quad mK := 10^{-3}\cdot K$ $\quad k := \frac{2\cdot\pi}{\lambda}$ $\quad eV := 1.602\cdot 10^{-19}\cdot joule$ $\quad gram := 10^{-3}\cdot kg$

constants: $k_B := 1.380658\cdot 10^{-23}\cdot\frac{joule}{K}$ $\quad N_A := 6.0221367\cdot 10^{23}$ $\quad m_{Yb} := \frac{173\cdot gram}{N_A}$

$\varepsilon_0 := 8.854\cdot 10^{-12}\cdot sec^2\cdot\frac{coul^2}{kg\cdot m^3}$ $\quad hbar := \frac{6.6260755\cdot 10^{-34}\cdot joule\cdot sec}{2\cdot\pi}$ $\quad m_{Yb}=2.8727\cdot 10^{-25}\cdot kg$

velocities: $T_{doppler} := \frac{hbar\cdot\gamma_{parl}}{2\cdot k_B}$ $\quad T_{doppler}=433.9880\cdot\mu K$

$v_t := \frac{1}{1}\cdot\sqrt{\frac{2\cdot k_B\cdot T_{doppler}}{m_{Yb}}}$ $\quad v_t=20.4244\cdot\frac{cm}{sec}$ $\quad v_t=0.2042\cdot\frac{\mu m}{\mu s}$ $\quad \frac{\lambda}{2\cdot v_t}=0.9033\cdot\mu s$

energy:

$$k_B\cdot T_{doppler}=3.74026\cdot 10^{-8}\cdot eV \qquad hbar\cdot g=1.0772\cdot 10^{-7}\cdot eV \qquad \frac{1}{2}\cdot m_{Yb}\cdot v_t^2=3.7403\cdot 10^{-8}\cdot eV$$

$$hbar\cdot\frac{g}{k_B}=1.2499\cdot mK$$

Q. Turchette
cavityqmYb.MCD
*e4pt 07:34

recoil velocity

$$\frac{hbar \cdot k}{m_{Yb}} = 6.2508 \cdot \frac{mm}{sec} \qquad v_{recoil} := \frac{hbar \cdot k}{m_{Yb}}$$

"recoil frequency"

$$\Omega_r := \frac{hbar \cdot k^2}{2 \cdot m_{Yb}}$$

$$hbar \cdot k = 1.7957 \cdot 10^{-27} \cdot kg \cdot m \cdot sec^{-1}$$

$$\nu := \frac{c}{\lambda} \qquad \nu = 8.1030 \cdot 10^{8} \cdot MHz$$

$$\omega := 2 \cdot \pi \cdot \nu$$

$$\frac{\Omega_r}{2 \cdot \pi} = 8.4699 \cdot 10^{-3} \cdot MHz$$

$$v_{recoil} \cdot \frac{1}{\gamma_{parl}} = 0.0550 \cdot nm \qquad v_{recoil} \cdot \frac{1}{g} = 0.0382 \cdot nm \qquad \frac{v_{recoil}}{\lambda} = 16.9398 \cdot KHz$$

$$\lambda \cdot 1 \cdot MHz = 36.9000 \cdot \frac{cm}{sec}$$

based on Fisk:

$$T_{cool} := 100 \cdot mK$$

$$E_{cool} := k_B \cdot T_{cool} \qquad E_{cool} = 8.6183 \cdot 10^{-6} \cdot eV$$

$$hbar \cdot \omega = 3.3515 \cdot eV$$

electric field $$E := \sqrt{\frac{hbar \cdot \omega}{2 \cdot \varepsilon_0 \cdot V_m}}$$

$$E = 1.2125 \cdot 10^{3} \cdot \frac{volt}{m}$$

Q. Turchette
cavityqmYb.MCD
*e4pt 07:35

for Yb trapped in harmonic potential of freq wt $\omega_t := 2\cdot\pi\cdot 1\cdot MHz$

$$v_0(x) := \left(\frac{m_{Yb}\cdot\omega_t}{\pi\cdot hbar}\right)^{\frac{1}{4}}\cdot\exp\left(-\frac{1}{2}\cdot m_{Yb}\cdot\frac{\omega_t}{hbar}\cdot x^2\right) \qquad x := -400\cdot nm, -399.9\cdot nm .. 400\cdot nm$$

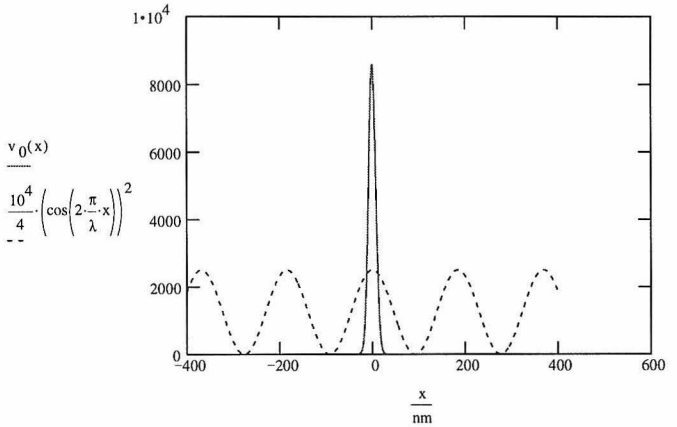

$$\Delta x(n) := \sqrt{\left(n+\frac{1}{2}\right)\cdot\frac{hbar}{m_{Yb}\cdot\omega_t}}$$

where can laser cooling get us?

$a_0 := \Delta x(0)$

$E_{trap} := hbar\cdot\omega_t$ $\quad E_{trap} = 4.1361\cdot10^{-9}\cdot eV$ $\quad a_0\cdot k = 0.0293\cdot\pi$

$T_{trap} := \frac{E_{trap}}{k_B}$ $\quad T_{trap} = 47.9922\cdot\mu K$ $\quad \Delta x(0) = 5.4049\cdot nm$

$\frac{T_{cool}}{T_{trap}} = 2.0837\cdot10^3$ $\quad \Delta x(2000) = 341.8770\cdot nm$

$\frac{T_{doppler}}{T_{trap}} = 9.0429$ $\quad \Delta x(9) = 23.5593\cdot nm$

Q. Turchette
cavityqmYb.MCD
*e4pt 07:35

B.2 Heterodyne Efficiency Calibration: beat.mcd

BEAT.MCD !

$BN := -21$ $\qquad P := 100 \cdot 10^{-9}$

$SN := -90$

$EN := -95$ $\qquad BW := 30 \cdot 10^{3}$

$$CSN := EN + 10 \cdot \log\left(10^{\frac{SN - EN}{10}} - 1\right) + 2.0$$

$$\delta := BN - CSN$$

$$S := -1 \cdot \log\left(\frac{P}{1.6 \cdot 10^{-19} \cdot 1.46 \cdot BW}\right) + \frac{\delta}{10}$$

$$\varepsilon 2 := 10^{S}$$

$\varepsilon 2 = 0.514$

$CSN = -89.651$

$\delta = 68.651$

B.3 Intracavity Photon Number from Beatnote: phot.mcd

$P := \frac{28.5}{.8} \cdot 10^{-9}$ calibration power $\quad W := 4.3 \cdot 10^{18} \quad c := 2.99 \cdot 10^{8}$

$BN := 12.5$ calibration BN (mV) $\quad BNQ := 30$ actual BN (μV)

$L := 52 \cdot 10^{-6} \quad T := 320 \cdot 10^{-6} \quad OPR := \frac{c}{2} \cdot \frac{1}{L} \cdot T \quad R := .19$ the reflectivity of the beam splitter in the output path

$OPR = 9.2 \cdot 10^{8}$

$BNC := \frac{BN^2}{P} \cdot \frac{10^6}{W}$

$BNC = 1.02 \cdot 10^{-3}$

$n1 := \frac{1}{BNC} \cdot \frac{1}{OPR} \cdot \frac{1}{1 - R}$

$n := BNQ^2 \cdot n1$

$n = 1.18406 \cdot 10^{-3}$ the inferred intracavity photon number

$n1 = 1.316 \cdot 10^{-6}$

Bibliography

[1] E. M. Purcell. Spontaneous emission probabilities at radio frequencies. *Phys. Rev.*, 69:681, 1946.

[2] E. T. Jaynes and F. W. Cummings. Comparison of quantum and semiclassical radiation theories with application to the beam maser. *Proc. IEEE*, 51:89, 1963.

[3] K. H. Drexhage. Interaction of light with monomolecular dye layers. In E. Wolf, editor, *Progress in Optics*, volume 12, pages 163–232. Elsevier Science Publishers B. V., Amsterdam, 1974.

[4] G. Rempe and H. Walther. Observation of quantum collapse and revival in a one-atom MASER. *Phys. Rev. Lett.*, 58:353, 1987.

[5] G. Rempe, F. Schmidt-Kaler, and H Walther. Observation of sub-poissonian photon statistics in a micromaser. *Phys. Rev. Lett.*, 64:2783, 1990.

[6] G. Rempe, R. J. Thompson, R. J. Brecha, W. D. Lee, and H. J. Kimble. Optical bistability and photon statistics in cavity quantum electrodynamics. *Phys. Rev. Lett.*, 67:1727, 1991.

[7] R. J. Thompson, G. Rempe, and H. J. Kimble. Observation of normal-mode splitting for an atom in an optical cavity. *Phys. Rev. Lett.*, 68:1132, 1992.

[8] M. Brune, F. Schmidtkaler, J. Dreyer, E. Hagley, J. M. Raimond, and S. Haroche. Quantum Rabi oscillation - a direct test of field quantization in a cavity. *Phys. Rev. Lett.*, 76:1800, 1996.

[9] K. An, J. J. Childs, R. R. Dasari, and M. S. Feld. Microlaser - a laser with one-atom in an optical-resonator. *Phys. Rev. Lett.*, 73:3375, 1994.

[10] M. Brune, E. Hagley, J. Dreyer, X. Maître, A. Maali, C. Wunderlich, J. M. Raimond, and S. Haroche. Observing the progressive decoherence of the 'meter' in a quantum measurement. *Phys. Rev. Lett.*, 77:4887, 1996.

[11] D. M. Meekhof, C. Monroe, B. E. King, W. M. Itano, and D. J. Wineland. Generation of nonclassical motional states of a trapped atom. *Phys. Rev. Lett.*, 76:1796, 1996.

[12] M. W. Noel and C. R. Stroud. Excitation of an atomic electron to a coherent superposition of macroscopically distinct states. *Phys. Rev. Lett.*, 77:1913, 1996.

[13] D. M. Eigler and E. K. Schweizer. Positioning single atoms with a scanning tunneling microscope. *Nature*, 344:524, 1990.

[14] K. Sugiyama and J. Yoda. Direct measurement of surface-diffusion using atom-tracking scanning-tunneling-microscopy. *Phys. Rev. Lett.*, 76:459, 1996.

[15] Y. Yamamoto. Squeezing and cavity QED in semiconductors. In M. Ducloy and D. Bloch, editors, *Quantum optics of confined systems*, Proceedings of the NATO Advanced Study Institute, page 202, Dordrecht, The Netherlands, 1996. Kluwer Academic Press.

[16] T. A. Fulton and G. J. Dolan. Observation of single-electron charging effects in small tunnel-junctions. *Phys. Rev. Lett.*, 59:109, 1987.

[17] M. H. Devoret, D. Esteve, and C. Urbina. Transfer of single electrons and single Cooper pairs in metallic nanostructures. In E. G. Beltrametti and J.-M. Levy-Leblond, editors, *Advances in Quantum Phenomena*, Proceedings of the NATO Advanced Study Institute, page 65, New York, 1996. Plenum Press.

[18] C. Livermore, C. H. Crouch, R. M. Westervelt, K. L. Campman, and A. C. Gossard. The Coulomb blockade in coupled quantum dots. *Phys. Rev. Lett.*, 274:1332, 1996.

[19] P. Meystre and M. Sargent III. *Elements of Quantum Optics.* Springer-Verlag, Berlin, 1991.

[20] M. G. Raizen, R. J. Thompson, and H. J. Kimble. Spectroscopy of the normal mode structure of two state atoms in an optical cavity. unpublished paper, 1990.

[21] H. J. Carmichael, L. Tian, W. Ren, and P. Alsing. Nonperturbative atom-photon interactions. In P. Berman, editor, *Cavity Quantum Electrodynamics*, pages 381–423. Academic Press, Boston, 1994.

[22] M. G. Raizen, R. J. Thompson, R. J. Brecha, H. J. Kimble, and H. J. Carmichael. Normal-mode splitting and linewidth averaging for two-state atoms in an optical cavity. *Phys. Rev. Lett.*, 63:240, 1989.

[23] H. J. Carmichael, R. J. Brecha, M. G. Raizen, H. J. Kimble, and P. R. Rice. Subnatural linewidth averaging for coupled atomic and cavity-mode oscillators. *Phys. Rev. A*, 40:5516, 1989.

[24] P. R. Rice and H. J. Carmichael. Single-atom cavity-enhanced absorption .1. photon statistics in the bad-cavity limit. *IEEE J. Quant. Elec.*, 24:1351, 1988.

[25] R. G. Hulet, E. S. Hilfer, and D. Kleppner. Inhibited spontaneous emission by a Rydberg atom. *Phys. Rev. Lett.*, 55:2137, 1985.

[26] P. Goy, J. M. Raimond, M. Gross, and S. Haroche. Observation of cavity-enhanced single-atom spontaneous emission. *Phys. Rev. Lett.*, 50:1903, 1983.

[27] K. G. Weyer, H. Widenmann, M. Rateike, W. R. MacGillivray, P. Meystre, and H. Walther. *Opt. Comm.*, 37:426, 1981.

[28] D. E. Grant and H. J. Kimble. Optical bistability for 2-level atoms in a standing-wave cavity. *Opt. Lett.*, 7:353, 1982.

[29] W. Jhe, A. Anderson, E. A. Hinds, D. Meschede, L. Moi, and S. Haroche. Suppression of spontaneous decay at optical frequencies—test of vacuum-field anisotropy in confined space. *Phys. Rev. Lett.*, 58:666, 1987.

[30] D. J. Heinzen and M. S. Feld. Vacuum radiative level shift and spontaneous-emission linewidth of an atom in an optical resonator. *Phys. Rev. Lett.*, 59:2623, 1987.

[31] L. A. Lugiato. Theory of optical bistability. In E. Wolf, editor, *Progress in Optics*, volume 21, page 71. Elsevier Science Publishers B. V., Amsterdam, 1984.

[32] A. T. Rosenberger, L. A. Orozco, H. J. Kimble, and P. D. Drummond. Absorptive optical bistability in two-state atoms. *Phys. Rev. A*, 43:6284, 1991.

[33] M. Weissbluth. *Photon-atom interactions.* Academic Press, Boston, 1989.

[34] P. D. Drummond. Optical bistability in a radially varying mode. *IEEE J. Quant. Elec.*, QE-17:301, 1981.

[35] C. M. Savage and H. J. Carmichael. Single-atom optical bistability. *IEEE J. Quant. Elec.*, 8:1495, 1988.

[36] P. Alsing and H. J. Carmichael. Spontaneous dressed-state polarization of a coupled atom and cavity mode. *Quantum Optics*, 3:13, 1991.

[37] D. J. Heinzen, J. L. Childs, J. Thomas, and M. S. Feld. Enhanced and inhibited visible spontaneous emission by atoms in a confocal resonator. *Phys. Rev. Lett.*, 58:1321, 1987.

[38] Y. Zhu, D. J. Gauthier, S. E. Morin, Q. Wu, H. J. Carmichael, and T. W. Mossberg. Vacuum Rabi splitting as a feature of linear-dispersion theory—analysis and experimental-observations. *Phys. Rev. Lett.*, 64:2499, 1990.

[39] S. E. Morin, C. C. Yu, and T. W. Mossberg. Strong atom-cavity coupling over large volumes and the observation of subnatural intracavity atomic linewidths. *Phys. Rev. Lett.*, 73:1489, 1994.

[40] K. J. Ebeling. Physics of semiconductor lasers. In M. Ducloy and D. Bloch, editors, *Quantum optics of confined systems*, Proceedings of the NATO Advanced Study Institute, page 283, Dordrecht, The Netherlands, 1996. Kluwer Academic Press.

[41] U. Mohideen and R. E. Slusher. In J. Rarity and C. Weisbuch, editors, *Microcavities and Photonic Bandgaps*, page 363. Kluwer, 1996.

[42] S. Haroche. Cavity quantum electrodynamics. In *Fundamental Systems in Quantum Optics*, pages 767–940. North Holland, Amsterdam, 1992.

[43] A. E. Siegman. *Lasers.* University Science Books, Mill Valley, CA, 1986.

[44] R. J. Thompson, Q. A. Turchette, O. Carnal, and H. J. Kimble. Nonlinear spectroscopy in the strong coupling regime of cavity qed. To be submitted to Phys. Rev. A, 1997.

[45] Q. A. Turchette, R. J. Thompson, and H. J. Kimble. One-dimensional atoms. *Appl. Phys. B*, 60:S1, 1995.

[46] H. Mabuchi, Q. A. Turchette, M. S. Chapman, and H. J. Kimble. Real-time detection of individual atoms falling through a high-finesse optical cavity. *Opt. Lett.*, 21:1393, 1996.

[47] G. Rempe, R. J. Thompson, H. J. Kimble, and R. Lalezari. Measurement of ultralow losses in an optical interferometer. *Opt. Lett.*, 17:363, 1992.

[48] R. J. Thompson. *Cavity Quantum Electrodynamics in the Optical Domain: Structure and Dynamics in the Strong Coupling Regime.* PhD thesis, The University of Texas at Austin, 1994.

[49] O. Schmidt, K.-M. Knaak, R. Wynands, and D. Meschede. Cesium saturation spectroscopy revisited: How to reverse peaks and observe narrow resonances. *Appl. Phys. B*, 59:167–178, 1994.

[50] J. L. Hall, L. Hollberg, T. Baer, and G. Robinson. Optical heterodyne spectroscopy. *Appl. Phys. Lett.*, 39:680, 1981.

[51] W. Demtröder. *Laser Spectroscopy: Basic concepts and instrumentation.* Springer-Verlag, Berlin, 1996.

[52] L. Wu, M. Xiao, and H. J. Kimble. Squeezed states of light from an optical parametric oscillator. *JOSA B*, 4:1465, 1987.

[53] M. H. Anderson, R. D. Jones, J. Cooper, and S. J. Smith. Errors in the measurement of non-Gaussian noise spectra using rf spectrum analyzers. *Rev. Sci. Instrum.*, 62:2828, 1991.

[54] H. J. Carmichael. Unpublished notes, 1994.

[55] C. W. Gardiner. Inhibition of atomic phase decays by squeezed light—a direct effect of squeezing. *Phys. Rev. Lett.*, 56:1917, 1986.

[56] G. J. Milburn. Interaction of a 2-level atom with squeezed light. *Optica Acta*, 31:671, 1984.

[57] G. J. Milburn. Atomic-level shifts in a squeezed vacuum. *Phys. Rev. A*, 34:4882, 1986.

[58] C. W. Gardiner and A. S. Parkins. Driving atoms with light of arbitrary statistics. *Phys. Rev. A*, 50:1792, 1994.

[59] R. Dum, A. S. Parkins, P. Zoller, and C. W. Gardiner. Monte-carlo simulation of master-equations in quantum optics for vacuum, thermal, and squeezed reservoirs. *Phys. Rev. A*, 46:4382, 1992.

[60] J. I. Cirac and L. L. Sanchezsoto. Analytic approximation to the interaction of a 2-level atom with squeezed light. *Phys. Rev. A*, 40:3743, 1989.

[61] M. L. Zou and G. C. Guo. Squeezed light interacting with a 2-level atom. *J. Phys. B*, 22:2205, 1989.

[62] C. W. Gardiner, A. S. Parkins, and M. J. Collett. Input and output in damped quantum-systems part 2 methods in non-white-noise situations and application to inhibition of atomic phase decays. *JOSA B*, 4:1683, 1987.

[63] S. H. An, M. Sargent, and D. F. Walls. Effects of a squeezed vacuum on probe absorption-spectra. *Opt. Comm.*, 67:373, 1988.

[64] H. Ritsch and P. Zoller. Absorption-spectrum of a 2-level system in a squeezed vacuum. *Opt. Comm.*, 64:523, 1987.

[65] P. Zhou, Z. Ficek, and S. Swain. Hole-burning and dispersive profiles at line center of the probe absorption-spectrum of a 2-level atom in a squeezed vacuum. *JOSA B*, 13:768, 1996.

[66] Z. Ficek and M. R. B. Wahiddin. Population-inversion and stationary lineshapes in a driven 2-atom system in a squeezed vacuum. *Quant. Semiclass. Opt.*, 7:41, 1995.

[67] Z. Ficek. Generalized bloch-siegert shift in a squeezed vacuum. *J. Mod. Opt.*, 40:2333, 1993.

[68] P. Zhou and S. Swain. The effects of squeezed field detunings on probe absorption-spectra. *Quant. Semiclass. Opt.*, 8:959, 1996.

[69] P. R. Rice and C. A. Baird. Interaction of a 2-level atom with a squeezed vacuum - photon statistics and spectra. *Phys. Rev. A*, 53:3633, 1996.

[70] S. Smart and S. Swain. Diagrammatic analysis of atom squeezed-light interactions. *Phys. Rev. A*, 45:6857, 192.

[71] H. Ritsch and P. Zoller. Atomic transitions in finite-bandwidth squeezed light. *Phys. Rev. Lett.*, 61:1097, 1988.

[72] A. S. Parkins and C. W. Gardiner. Effect of finite-bandwidth squeezing on inhibition of atomic-phase decays. *Phys. Rev. A*, 37:3867, 1988.

[73] M. Bosticky, Z. Ficek, and B. J. Dalton. Probe absorption-spectra for driven atomic systems in a narrow bandwidth squeezed vacuum. *Phys. Rev. A*, 53:4439, 1996.

[74] R. Vyas and S. Singh. Resonance fluorescence with squeezed-light excitation. *Phys. Rev. A*, 45:8095, 1992.

[75] H. J. Carmichael, A. S. Lane, and D. F. Walls. Resonance fluorescence in a squeezed vacuum. *J. Mod. Opt.*, 34:821, 1987.

[76] H. J. Carmichael, A. S. Lane, and D. F. Walls. Resonance fluorescence from an atom in a squeezed vacuum. *Phys. Rev. Lett.*, 58:2539, 1987.

[77] A. S. Parkins. Resonance fluorescence of a 2-level atom in a 2-mode squeezed vacuum. *Phys. Rev. A*, 42:6873, 1990.

[78] Z. Ficek and B. C. Sanders. Resonance fluorescence of a 2-level atom in an off-resonance squeezed vacuum. *J. Phys. B*, 27:809, 1994.

[79] A. S. Parkins. Rabi side-band narrowing via strongly driven resonance fluorescence in a narrow-bandwidth squeezed vacuum. *Phys. Rev. A*, 42:4352, 1990.

[80] S. Swain and P. Zhou. Nonclassical features in anomalous resonance fluorescence in a squeezed vacuum. *Opt. Comm.*, 123:310, 1996.

[81] S. Swain and P. Zhou. Conditions for anomalous resonance fluorescence in a squeezed vacuum. *Phys. Rev. A*, 52:4845, 1995.

[82] W. S. Smyth and S. Swain. Dressed states and resonance fluorescence of a 2-level atom in a squeezed vacuum. *Opt. Comm.*, 112:91, 1994.

[83] S. Swain. Anomalous resonance fluorescence-spectra in a squeezed vacuum. *Phys. Rev. Lett.*, 73:1493, 1994.

[84] S. Smart and S. Swain. Dispersive profiles in resonance fluorescence of a 2-level atom in a squeezed vacuum. *Phys. Rev. A*, 48:R48, 1993.

[85] S. Smart and S. Swain. Asymmetric 2-level resonance fluorescence-spectra and dressed state populations in a squeezed vacuum. *Quant. Opt.*, 5:75, 1993.

[86] S. Smart and S. Swain. Effect of laser linewidths and collisions on resonance fluorescence in a squeezed vacuum. *Phys. Rev. A*, 45:6863, 1992.

[87] C. M. Savage and D. F. Walls. Inhibition of tunneling in optical bistability by a squeezed vacuum. *Phys. Rev. Lett.*, 57:2164, 1986.

[88] A. S. Parkins. Optical-pumping with nonclassical light. *Phys. Rev. A*, 53:2893, 1996.

[89] A. S. Parkins and C. W. Gardiner. Photon-echoes with coherent and squeezed pulses. *Phys. Rev. A*, 40:2534, 1989.

[90] M. V. Satyanarayana, P. Rice, R. Vyas, and H. J. Carmichael. Ringing revivals in the interaction of a 2-level atom with squeezed light. *JOSA B*, 6:228, 1989.

[91] M. A. M. Marte, H. Ritsch, and D. F. Walls. Squeezed-reservoir lasers. *Phys. Rev. A*, 38:3577, 1988.

[92] M. A. M. Marte, H. Ritsch, and D. F. Walls. Quantum statistics of a squeezed-pump laser. *Phys. Rev. Lett.*, 61:1093, 1988.

[93] P. R. Rice, X. S. Yin, J. Walden, J. Geabanacloche, L. M. Pedrotti, and J. E. Mullen. Laser with injected squeezed vacuum - phase diffusion and intensity fluctuations. *Phys. Rev. A*, 50:4176, 1994.

[94] C. Ginzel, J. Geabanacloche, and A. Schenzle. Linewidth of a laser with a squeezed reservoir. *Phys. Rev. A*, 42:4164, 1990.

[95] C. Ginzel, R. Schack, and A. Schenzle. Dynamics and symmetry of a laser with a squeezed reservoir. *JOSA B*, 8:1704, 1991.

[96] C. Ginzel, J. G. Geabanacloche, and A. Schenzle. Dynamics and symmetry of a laser with a squeezed reservoir. *Acta Physica Polonica A*, 78:123, 1990.

[97] M. A. M. Marte and D. F. Walls. Quantum-theory of a squeezed-pump laser. *Phys. Rev. A*, 37:1235, 1988.

[98] Z. Ficek, W. S. Smyth, and S. Swain. Gain without population-inversion in a 2-level atom damped by a broad-band squeezed vacuum. *Opt. Comm.*, 110:555, 1994.

[99] Z. Ficek, W. S. Smyth, and S. Swain. Asymmetric probe-absorption spectrum and amplification without population-inversion in a squeezed vacuum. *Phys. Rev. A*, 52:4126, 1995.

[100] Z. Ficek and B. J. Dalton. Squeezing-induced transparency in a 2-level atom. *Opt. Comm.*, 102:231, 1993.

[101] J. I. Cirac and L. L. Sanchezsoto. Suppression of spontaneous emission by squeezed light in a cavity. *Phys. Rev. A*, 44:1948, 1991.

[102] T. A. B. Kennedy and D. F. Walls. Theory of intracavity atom-field interactions with squeezed inputs. *Phys. Rev. A*, 42:3051, 1990.

[103] A. S. Parkins and C. W. Gardiner. Inhibition of atomic phase decays by squeezed light in a microscopic fabry-perot cavity. *Phys. Rev. A*, 40:3796, 1989.

[104] J. Geabanacloche, R. R. Schlicher, and M. S. Zubairy. Emission-spectra of an atom in a cavity in the presence of a squeezed vacuum. *Phys. Rev. A*, 38:3514, 1988.

[105] C. Cabrillo and S. Swain. Interaction between 2-level atoms and a squeezed vacuum in a cavity - effect on the mean photon number. *Phys. Rev. Lett.*, 77:478, 1996.

[106] W. S. Smyth and S. Swain. Anomalous resonance fluorescence from an atom in a cavity with injected squeezed vacuum. *Phys. Rev. A*, 53:2846, 1996.

[107] Y. Benaryeh, C. A. Miller, H. Risken, and W. Schleich. Inhibition of atomic dipole collapses by squeezed light - a Jaynes-Cummings model treatment. *Opt. Comm.*, 90:259, 1992.

[108] P. R. Rice and L. M. Pedrotti. Fluorescent spectrum of a single atom in a cavity with injected squeezed vacuum. *JOSA B*, 9:2008, 1992.

[109] J. I. Cirac. Interaction of a 2-level atom with a cavity mode in the bad-cavity limit. *Phys. Rev. A*, 46:4354, 1992.

[110] A. S. Parkins, P. Zoller, and H. J. Carmichael. Spectral linewidth narrowing in a strongly coupled atom-cavity system via squeezed-light excitation of a vacuum Rabi resonance. *Phys. Rev. A*, 48:758, 1993.

[111] R. Graham, D. F. Walls, and W. P. Zhang. Laser cooling in a squeezed vacuum. *Phys. Rev. A*, 44:7777, 1991.

[112] J. I. Cirac and P. Zoller. Laser cooling of trapped ions in a squeezed vacuum. *Phys. Rev. A*, 47:2191, 1993.

[113] Y. Shevy. Laser cooling of atoms in squeezed vacuum. *Phys. Rev. Lett.*, 64:2905, 1990.

[114] Y. Shevy, B. Crosignani, and A. Yariv. Quantum fluctuations of the optical forces on atoms in a squeezed vacuum. *Phys. Rev. A*, 46:1421, 1992.

[115] J. Geabanacloche. 2-photon absorption of nonclassical light. *Phys. Rev. Lett.*, 62:1603, 1989.

[116] J. Javanainen and P. L. Gould. Linear intensity dependence of a 2-photon transition rate. *Phys. Rev. A*, 41:5088, 1990.

[117] Z. Ficek and P. D. Drummond. 2-photon population-inversion by squeezed-light in a fabry-perot microcavity. *Europhys. Lett.*, 24:455, 1993.

[118] M. R. Ferguson, Z. Ficek, and B. J. Dalton. Resonance fluorescence-spectra of 3-level atoms in a squeezed vacuum. *Phys. Rev. A*, 54:2379, 1996.

[119] M. R. Ferguson, Z. Ficek, and B. J. Dalton. Effect of a squeezed vacuum on coherent population trapping in a 3-level-lambda system. *J. Mod. Opt.*, 42:679, 1995.

[120] Z. Ficek and P. D. Drummond. 3-level atom in a broad-band squeezed vacuum field .1. general-theory. *Phys. Rev. A*, 43:6247, 1991.

[121] Z Ficek and P D Drummond. 3-level atom in a broad-band squeezed vacuum field .2. applications. *Phys. Rev. A*, 43:6258, 1991.

[122] P. Zhou and S. Swain. Atomic 2-photon excitation by an injected squeezed vacuum in a cavity. *Phys. Rev. A*, 54:2455, 1996.

[123] S. Smart and S. Swain. 3-level atom in a squeezed vacuum .1. the populations. *J. Mod. Opt.*, 40:1939, 1993.

[124] S. Smart and S. Swain. 3-level atom in a squeezed vacuum .2. resonance fluorescence. *J. Mod. Opt.*, 41:1055, 1994.

[125] S. Smart and S. Swain. Nonsecular effects in the resonance fluorescence of a 3-level atom in a squeezed vacuum. *Opt. Comm.*, 99:369, 1993.

[126] S. Smart and S. Swain. The optical double-resonance spectrum of an atom in a squeezed field. *Quant. Opt.*, 4:281, 1992.

[127] P. Galatola, L. A. Lugiato, M. G. Porreca, and P. Tombesi. Optical switching by variation of the squeezing phase. *Opt. Comm.*, 81:175, 1991.

[128] P. Galatola and L. A. Lugiato. Dynamic effects induced by the variation of the squeezing phase. *IOP Conf. Series*, 115:65, 1991.

[129] Z. M. Zhang, L. Xu, and J. L. Chai. Squeezing in the n-photon interaction of 2 atoms with squeezed light. *Phys. Lett. A*, 151:65, 1990.

[130] G. S. Agarwal and R. R. Puri. Cooperative behavior of atoms irradiated by broad-band squeezed light. *Phys. Rev. A*, 41:3782, 1990.

[131] Z. Ficek. Scattered and absorption-spectra of a system of atoms under squeezed vacuum excitation. *Opt. Comm.*, 88:494, 1992.

[132] Z. Ficek. Effect of a broad-band squeezed vacuum on 2-atom spontaneous emission. *Opt. Comm.*, 82:130, 1991.

[133] Z. Ficek. Pairwise atomic states - 2-atom system in a 3-dimensional squeezed vacuum field. *Phys. Rev. A*, 44:7759, 1991.

[134] Z. Ficek. Spontaneous emission from 2 atoms interacting with a broad-band squeezed vacuum. *Phys. Rev. A*, 42:611, 1990.

[135] H. Moyacessa and A. Vidiellabarranco. Interaction of squeezed light with 2-level atoms. *J. Mod. Opt.*, 39:2481, 1992.

[136] P. Zhou and S. Swain. Hanle effect in a squeezed vacuum. *Opt. Comm.*, 123:297, 1996.

[137] C. Cabrillo, W. S. Smyth, S. Swain, and P. Zhou. Sensitive response of a 2-level atom to a very weak squeezed vacuum. *Opt. Comm.*, 114:344, 1995.

[138] J. M. Courty and S. Reynaud. Dressed population trapping for a 2-level atom in a squeezed vacuum. *Europhys. Lett.*, 10:237, 1989.

[139] N. P. Georgiades, E. S. Polzik, K. Edamatsu, H. J. Kimble, and A. S. Parkins. Nonclassical excitation for atoms in a squeezed vacuum. *Phys. Rev. Lett.*, 75:3426, 1995.

[140] E. S. Polzik, J. Carri, and H. J. Kimble. Atomic spectroscopy with squeezed light for sensitivity beyond the vacuum-state limit. *Appl. Phys. B*, 55:279, 1992.

[141] E. S. Polzik, J. Carri, and H. J. Kimble. Spectroscopy with squeezed light. *Phys. Rev. Lett.*, 68:3020, 1992.

[142] H. J. Carmichael. Quantum trajectory theory for cascaded open systems. *Phys. Rev. Lett.*, 70:2273, 1993.

[143] C. W. Gardiner. Driving a quantum system with the output field from another driven quantum system. *Phys. Rev. Lett.*, 70:2269, 1993.

[144] M. W. Hamilton, D. S. Elliott, K. Arnett, and S. J. Smith. Saturation of an atomic transition by a phase-diffusing laser field. *Phys. Rev. A*, 33:778, 1986.

[145] M. W. Hamilton, K. Arnett, S. J. Smith, D. S. Elliott, M. Dziemballa, and P. Zoller. Saturation of an optical transition by a phase-diffusing laser field. *Phys. Rev. A*, 36:178, 1987.

[146] C. W. Gardiner. *Quantum Noise.* Springer-Verlag, Berlin, 1991.

[147] D. F. Walls and G. J. Milburn. *Quantum Optics.* Springer-Verlag, Berlin, 1994.

[148] H. J. Kimble. Quantum fluctuations in quantum optics: Squeezing and related phenomena. In *Fundamental Systems in Quantum Optics*, pages 545–674. North Holland, Amsterdam, 1992.

[149] A. S. Parkins. Modulation of the transmitted probe field. unpublished notes, April, 1996.

[150] N. Ph. Georgiades, R. J. Thompson, Q. A. Turchette, E. S. Polzik, O. Carnal, and H. J. Kimble. Spectroscopy with nonclassical light. In *IQEC Technical Digest*, volume 9, page 222, 1994.

[151] A. Ekert and R. Jozsa. Quantum computation and shor's factoring algorithm. *Rev. Mod. Phys.*, 68:733, 1996.

[152] D. P. DiVincenzo. Quantum computation. *Science*, 270:255, 1995.

[153] S. Lloyd. Quantum-mechanical computers. *Scientific American*, page 140, October 1995.

[154] C. H. Bennett. Quantum information and computation. *Physics Today*, page 24, October 1995.

[155] C. H. Bennett and D. P. DiVincenzo. Quantum computing: Towards an engineering era? *Nature*, 377:389, 1995.

[156] D. Deutsch. Quantum theory, the Church-Turing principle and the universal quantum computer. *Proc. R. Soc. London A*, 400:97, 1985.

[157] R. P. Feynman. Simulating physics with computers. *Int. J. Theor. Phys.*, 21:467, 1982.

[158] R. P. Feynman. Quantun mechanical computers. *Found. Phys.*, 16:507, 1986.

[159] S. Lloyd. Almost any quantum logic gate is universal. *Phys. Rev. Lett.*, 75:346, 1995.

[160] D. Deutsch, A. Barenco, and A. Ekert. Universality in quantum computation. *Proc. R. Soc. London*, 449:669, 1995.

[161] A. Barenco, D. Deutsch, A. Ekert, and R. Josza. Conditional quantum dynamics and logic gates. *Phys. Rev. Lett.*, 74:4083, 1995.

[162] P. W. Shor. In S. Goldwasser, editor, *Proceedings of the 35th Annual Symposium on the Foundations of Computer Science*, page 124, Los Alamitos, CA, 1994. IEEE Computer Society.

[163] C. Monroe, D. M. Meekhof, B. E. King, W. M. Itano, and D. J. Wineland. Demonstration of a fundamental quantum logic gate. *Phys. Rev. Lett.*, 75:4714, 1995.

[164] Q. A. Turchette, C. J. Hood, W. Lange, H. Mabuchi, and H. J. Kimble. Measurement of conditional phase shifts for quantum logic. *Phys. Rev. Lett.*, 75:4710, 1995.

[165] S. Lloyd. Universal quantum simulator. *Science*, 273:1073, 1996.

[166] P. W. Shor. LANL e-print quant-ph/9508027, 1996.

[167] S. Haroche and J.M. Raimond. Quantum computation: Dream or nightmare. *Physics Today*, page 51, August 1996.

[168] P. W. Shor. Scheme for reducing decoherence in quantum computer memory. *Phys. Rev. A*, 52:R2493, 1995.

[169] R. Laflamme, C. Miquel, J-P Paz, and W. H. Zurek. Perfect quantum error correcting code. *Phys. Rev. Lett.*, 77:198, 1996.

[170] A. M. Steane. Error correcting codes in quantum theory. *Phys. Rev. Lett.*, 77:793, 1996.

[171] A. Ekert and C. Macchiavello. Quantum error correction for communication. *Phys. Rev. Lett.*, 77:2585, 1996.

[172] J. I. Cirac, T. Pellizzari, and P. Zoller. Enforcing coherent evolution in dissipative quantum dynamics. *Science*, 273:1207, 1996.

[173] P. W. Shor. Fault-tolerant quantum computation. LANL e-print quant-ph/9605011, 1996.

[174] D. P. DiVincenzo and P. W. Shor. *Phys. Rev. Lett.*, 77:3260, 1996.

[175] V. Vedral, A. Barenco, and A. Ekert. Quantum networks for elementary arithmetic operations. *Phys. Rev. A*, 54:147, 1996.

[176] S. M. Tan, M. J. Holland, and D. F. Walls. Bell's inequality for systems with quadrature phase coherence. *Opt. Comm.*, 77:285, 1990.

[177] H. J. Kimble. Structure and dynamics in cavity quantum electrodynamics. In P. Berman, editor, *Cavity Quantum Electrodynamics*, pages 203–266. Academic Press, Boston, 1994.

[178] A. Ekert. In D. Wineland *et al.*, editor, *Proceedings of the 14th International Conference on Atomic Physics*, page 450. American Institute of Physics, 1995.

[179] A. S. Parkins, P. Marte, P. Zoller, and H. J. Kimble. Synthesis of arbitrary quantum states via adiabatic transfer of Zeeman coherence. *Phys. Rev. Lett.*, 71:3095, 1993.

[180] A. S. Parkins, P. Marte, P. Zoller, O. Carnal, and H. J. Kimble. Quantum state mapping between multilevel atoms and cavity light fields. *Phys. Rev. A*, 51:1578, 1995.

[181] C. K. Law and J. H. Eberly. *Phys. Rev. Lett.*, 76:1055, 1996.

[182] C. K. Law and H. J. Kimble. Deterministic generation of a bit-stream of single-photon pulses. Submitted to Phys. Rev. Lett., 1997.

[183] C. Monroe, D. M. Meekhof, B. E. King, S. R. Jefferts, W. M. Itano, and D. J. Wineland. Resolved-sideband Raman cooling of a bound atom to the 3D zero-point energy. *Phys. Rev. Lett.*, 75:4011, 1995.

[184] D. Meschede, H. Walther, and G. Muller. One-atom MASER. *Phys. Rev. Lett.*, 54:551, 1985.

[185] M. Brune, S. Haroche, V. Lefevre, J. M. Raimond, and N. Zagury. Quantum nondemolition measurement of small photon numbers by Rydberg-atom phase-sensitive detection. *Phys. Rev. Lett.*, 65:976, 1990.

[186] F. Bernadot, P. Nussenzveig, M. Brune, J. M. Raimond, and S. Haroche. *Europhys. Lett.*, 17:33, 1992.

[187] M. Brune, P. Nussenzveig, F. Schmidt-Kaler, F. Bernadot, A. Maali, J. M. Raimond, and S. Haroche. From Lamb shift to light shifts—vacuum and subphoton cavity fields measured by atomic phase-sensitive detection. *Phys. Rev. Lett.*, 72:3339, 1994.

[188] G. Raithel, O. Benson, and H. Walther. Atomic interferometry with the micromaser. *Phys. Rev. Lett.*, 75:3446, 1995.

[189] G. Rempe, R. J. Thompson, R. J. Brecha, Q. A. Turchette, and H. J. Kimble. Atoms in an optical cavity. In H. Walther, T. W. Hansch, and B. Neizert, editors, *Atomic Physics 13*, page 305, New York, 1992. American Institute of Physics.

[190] G. Rempe, R. J. Thompson, and H. J. Kimble. *Physica Scripta*, T51:67, 1994.

[191] H. J. Kimble, O. Carnal, N. Ph. Georgiades, H. Mabuchi, E. S. Polzik, R. J. Thompson, and Q. A. Turchette. Quantum optics with strong coupling. In D. Wineland, C. Wieman, and S. Smith, editors, *Proceedings of the International Conference on Atomic Physics 1994*, page 314. American Institute of Physics, 1995.

[192] J. J. Childs, K. An, M. S. Otteson, R. R. Dasari, and M. S. Feld. Normal mode line shapes for atoms in standing-wave optical resonators. *Phys. Rev. Lett.*, 77:2901, 1996.

[193] R. J. Brecha, L. A. Orozco, M. G. Raizen, M. Xiao, and H. J. Kimble. Observation of oscillatory energy exchange in a coupled-atom-cavity system. *JOSA B*, 3:238, 1986.

[194] R. J. Brecha, L. A. Orozco, M. G. Raizen, M. Xiao, and H. J. Kimble. Observation of oscillatory energy exchange in a coupled-atom-cavity system. *JOSA B*, 12:2329, 1995.

[195] M. Tavis and F. W. Cummings. Exact solution for an N-molecule-radiation-field Hamiltonian. *Phys. Rev.*, 170:379, 1968.

[196] P. R. Rice and H. J. Carmichael. Nonclassical effects in optical-spectra. *JOSA B*, 5:1661, 1988.

[197] H. J. Carmichael. Quantum fluctuations in absorptive bistability without adiabatic elimination. *Phys. Rev. A*, 33:3262, 1986.

[198] H. J. Carmichael. *An open systems approach to quantum optics.* Springer-Verlag, Berlin, 1993.

[199] G. V. Varada, M. Sanjay-Kumar, and G. S. Agarwal. Quantum effects of the atom-cavity interaction on 4-wave mixing. *Opt. Comm.*, 62:328, 1987.

[200] G. S. Agarwal, R. K. Bullough, and N. Nayak. Probing the dressed states of an atom interacting with a quantized field. *Opt. Comm.*, 85:202, 1991.

[201] L. Tian and H. J. Carmichael. Incoherent excitation of the Jaynes-Cummings system. *Quantum Optics*, 4:131, 1992.

[202] H. J. Carmichael, P. Kochan, and B. C. Sanders. Photon correlation spectroscopy. *Phys. Rev. Lett.*, 77:631, 1996.

[203] B. C. Sanders, H. J. Carmichael, and B. F. Wielinga. Photon correlation spectroscopy of the Jaynes-Cummings system. *Phys. Rev. A*, 55:1358, 1997.

[204] L. Tian and H. J. Carmichael. Unpublished notes, 1992.

[205] L. Tian and H. J. Carmichael. Quantum trajectory simulations of the 2-state behavior of an optical cavity containing one atom. *Phys. Rev. A*, 46:R6801, 1992.

[206] H. J. Kimble, G. Rempe, R. J. Thompson, and R. J. Brecha. Dissipative quantum dynamics in cavity quantum electrodynamics. In M. Ducloy, E. Giacobino, and G. Camy, editors, *Laser Spectroscopy: TENICOLS 1991*, page 211. World Scientific, 1992.

[207] O. S. Heavens. *JOSA*, 51:1058, 1961.

[208] O. Carnal, Q. A. Turchette, and H. J. Kimble. Near-field imaging with two transmission gratings for submicrometer localization of atoms. *Phys. Rev. A*, 51:3079, 1995.

[209] S. Haroche, M. Brune, and J.M. Raimond. Trapping atoms by the vacuum field in a cavity. *Europhys. Lett.*, 14:19, 1991.

[210] B.-G. Englert, J. Schwinger, A. O. Barut, and M. O. Scully. Reflecting slow atoms from a micromaser field. *Europhys. Lett.*, 14:25, 1991.

[211] D. J. Wineland, W. M. Itano, and J. C. Bergquist. *Opt. Lett.*, 12:389, 1987.

[212] W. E. Moerner and L. Kador. Optical-detection and spectroscopy of single molecules in a solid. *Phys. Rev. Lett.*, 62:2535, 1989.

[213] G. Rempe. One-atom in an optical cavity—spatial-resolution beyond the standard diffraction limit. *Appl. Phys. B*, 60:233, 1995.

[214] H. Mabuchi. Dynamical identification of open quantum systems. *Quant. Semiclass. Opt.*, 8:1103, 1996.

[215] T. Pellizzari, S. A. Gardiner, J. I. Cirac, and P. Zoller. Decoherence, continuous observation, and quantum computing: A cavity QED model. *Phys. Rev. Lett.*, 75:3788, 1995.

[216] J. I. Cirac, P. Zoller, H. J. Kimble, and H. Mabuchi. Quantum state transfer and entanglement distribution among distant nodes in a quantum network. To appear in Phys. Rev. Lett., 1997.

[217] D. W. Vernooy and H. J. Kimble. Quantum structure and dynamics for atom galleries. *Phys. Rev. A*, 55:1239, 1997.

[218] D. W. Vernooy and H. J. Kimble. Well-dressed states for wavepacket dynamics in cavity QED. Submitted to Phys. Rev. Lett., 1997.

[219] M. O. Scully, G. M. Meyer, and H. Walther. Induced emission due to the quantized motion of ultracold atoms passing through a micromaser cavity. *Phys. Rev. Lett.*, 76:4144, 1996.

[220] J. I. Cirac, A. S. Parkins, R. Blatt, and P. Zoller. Cooling of a trapped ion coupled strongly to a quantized cavity mode. *Opt. Comm.*, 97:353, 1993.

[221] P. Alsing, D.-S. Guo, and H. J. Carmichael. Dynamic Stark effect for the Jaynes-Cummings system. *Phys. Rev. A*, 45:5135, 1992.

[222] E. L. Raab, M. Prentiss, A. Cable, S. Chu, and D. E. Pritchard. *Phys. Rev. Lett.*, 59:2631, 1987.

[223] A. Doherty and S. Parkins. Unpublished notes, 1997.

[224] M. Ozawa. *Phys. Rev. Lett.*, 60:385, 1988.

[225] W. Lange and H. J. Kimble. Dynamic generation of maximally entangled photon multiplets by adiabatic passage. Unpublished manuscript, 1997.

[226] F. Talbot. *Philos. Mag.*, 9:401, 1836.

[227] M. S. Chapman, C. R. Ekstrom, T. D. Hammond, J. Schmiedmayer, B. Tannian, S. Wehinger, and D. E. Pritchard. *Phys. Rev. A*, 51:R14, 1995.

[228] P. R. Berman, editor. *Atom interferometry.* Academic Press, San Diego, CA, 1997.

[229] D.W. Keith, R.J. Soave, and M.J. Rooks. *J. Vac. Sci. Technol. B*, 9:2846, 1991.

[230] P. P. Wegener, editor. *Molecular beams and low density gasdynamics.* M. Dekker, New York, 1974.

[231] N. Ramsey. *Molecular beams.* Oxford, Clarendon Press, Oxford, England, 1956.

[232] E. Lau. *Ann. Phys.*, 6:417, 1948.

[233] F. Gori. *Opt. Comm.*, 31:4, 1979.

[234] L. Liu. *JOSA A*, 5:1709, 1988.

[235] K. Patorskii. In E. Wolf, editor, *Progress in Optics Volume XXVII*, pages 1–108. Elsevier, 1989.

[236] J. M. Cowley and A. F. Moody. *Proc. Phys. Soc.*, B70:486,497,505, 1957.

[237] J. F. Clauser and M. W. Reinsch. *Appl. Phys. B*, 54:380, 1992.

[238] J. F. Clauser and S. Li. *Phys. Rev. A*, 49:R2213, 1994.

[239] J.J. McClelland, R.E. Scholten, E.C. Palm, and R.J. Celotta. *Science*, 262:877, 1993.

[240] V. Sears. *Neutron Optics.* Oxford University Press, New York, 1989.

[241] M. Born and E. Wolf. *Principles of Optics.* Pergamon Press, 1989.

[242] Q. A. Turchette, D. E. Pritchard, and D. W. Keith. Numerical model of a multiple-grating interferometer. *J. Opt. Soc. Am. A*, 9:1601, 1992.

[243] O. Carnal, A. Faulstich, and J. Mlynek. *Appl. Phys. B*, 53:88, 1991.

[244] B.J. Chang, R. Alferness, and E.N. Leith. *Appl. Opt.*, 14:1592, 1975.

[245] R. Sudol and B.J. Thompson. *Opt. Comm.*, 31:105, 1979.

[246] B. C. Fawcett and M. Wilson. Computed oscillator strengths, lande g-values and lifetimes in Yb II. *At. Data Nucl. Data Tables*, 47:241, 1991.

[247] M. Roberts, P. Taylor, G. P. Barwood, P. Gill, H. A. Klein, and W. R. C. Rowley. Observation of an electric octopole transition in a single ion. *Phys. Rev. Lett.*, 78:1876, 1997.

[248] H. A. Klein, A. S. Bell, G. P. BArwood, and P. Gill. Laser cooling of trapped Yb^+. *Appl. Phys. B*, 50:13, 1990.

[249] A. S. Bell, P. Gill, H. A. Klein, A. P. Levick, Chr. Tamm, and D. Schnier. Laser cooling of trapped ytterbium ions using a four-level optical-excitation scheme. *Phys. Rev. A*, 44:R20, 1991.

[250] R. Blatt, R. Casdorf, V. Enders, W. Neuhauser, and P. E. Toschek. New frequency standards based on Yb^+. In A. DeMarchi, editor, *Frequency standards and metrology*, page 306. Springer Varlag, Berlin, 1989.

[251] R. W. Berends and L. Maleki. Hyperfine structure and isotope shifts of transitions in neutral and singly ionized Ytterbium. *JOSA B*, 9:332, 1992.

[252] P. T. H. Fisk, M. A. Lawn, and C. Coles. Laser cooling of $^{171}Yb^+$ ions in a linear Paul trap. *Appl. Phys. B*, 57:287, 1993.

[253] H. G. Dehmelt. Radiofrequency spectroscopy of stored ions I: Storage. *Adv. At. Mol. Phys.*, 3:53, 1967.

[254] R. K. Melbourne, J. D. Prestage, and L. Maleki. Analytic potential in a linear radio-frequency quadrupole trap with cylindrical electrodes. *J. Appl. Phys.*, 69:2768, 1991.

[255] S. R. Jefferts, C. Monroe, E. W. Bell, and D. J. Wineland. Coaxial-resonator-driven rf (Paul) trap for strong confinement. *Phys. Rev. A*, 51:3112, 1995.